Investigation of the Mixing Energy Consumption Affecting Coagulation and Floc Aggregation

by

Yamuna Srinivasan Vadasarukkai

Submitted in partial fulfilment of the requirements
for the degree of Doctor of Philosophy

at

Dalhousie University
Halifax, Nova Scotia
August 2016

Dedication

To my beloved grandmother, my source of inspiration to achieve this and many milestones in my life—I know you would be thrilled to hear Doctor after my surname. My abilities are a true reflection of your sacrifices and hard work. Love you always!

Table of Contents

List of Tables

List of Figures

Abstract

Energy is an essential commodity invariably used for proper performance of major processes used in municipal water treatment. This research was primarily driven by the potential rise in energy demand in the water sector. In particular, the research focuses on rapid mix system, continuous-flow stirred tanks specifically designed for chemical dispersion in the coagulation process. Energy-intensive rapid mixing is often practiced in treatment plants for chemical-particle interactions, which is assumed essential for particle aggregation. The central hypothesis of this thesis was that removal of targeted impurities from drinking water supplies (e.g., natural dissolved organic matter) was achievable at a much lower mixing velocity during the rapid mix stage of coagulation. Insoluble precipitates (e.g., floc aggregates) resulting from coagulation can be effectively separated from drinking water in subsequent solid-liquid separation processes, including flocculation, clarification, and filtration.

This thesis integrates water quality and floc characterization techniques to evaluate the influence of mixing energy utilized during coagulation. Mixing energy was quantified from the root mean square velocity gradient (i.e., the G-value). A modified mixing arrangement was used to set the coagulation G-value ranging from 0 to 1450 s^{-1}, keeping chemical (coagulant dose, pH) and physical conditions (temperature) similar. An in-line holographic microscopy technique was used for a non-destructive, direct measurement of floc characteristics (e.g., floc counts, sizes, relative floc velocities) on a laboratory workbench and in a full-scale flocculation tank. Major experimental findings from this present study confirmed that reduced coagulation mixing energy not only removed targeted impurities from the water but also produced enough flocs, which were effectively removed during settling. Specifically, the results presented offered a new range of reduced mixing intensities ($110\ s^{-1} < G < 450\ s^{-1}$) during rapid mixing for a combined effective removal of total organic carbon, turbidity, and floc aggregates. Both water quality and macroscopic analyses support the contention that more mixing energy was expended than necessary in coagulation, which are typically designed at 600-1000 s^{-1} in treatment plants. It is anticipated that this research will contribute to a boarder conversation related to reducing energy footprints in the water sector.

List of Abbreviations and Symbols Used

A	Area of the identified floc (μm^2)
ATR	Attenuated total reflectance
CFD	Computation fluid dynamics
DI	Deionized water
DIHM	Digital inline holographic microscopy
DOM	Dissolved organic matter
DOC	Dissolved organic carbon (mg L^{-1})
D50	Median equivalent floc diameter (μm)
d	Equivalent diameter (μm)
d_f	Maximum floc size
dV	Volume fraction of flocs
E	Energy consumption of a coagulation mixing system (kW-h day^{-1})
ECD	Equivalent circular diameter (μm)
EDS	Energy dispersive X-Ray spectrometry
EVD	Equivalent volumetric diameter μm)
Fe	Iron
FT-IR	Fourier transform infrared spectroscopy
G-value	Root-mean-square velocity gradient or energy input rate (s^{-1})
JDKWSP	J.D. Kline Water Supply Plant
MFI™	Micro-flow Imaging
n	Number concentration of particles in a sample volume (m^{-3})
OCC	Optimal coagulant concentration (mg L^{-1})
P	Power transferred to the water in a mixing tank (J s^{-1})
P_{avg}	Average power supplied in a mixing tank (J s^{-1})
pH_{zpc}	Zero point charge
Q_{avg}	Average daily plant flow rate (m^3 s^{-1}),
SEM	Scanning electron microscopy
SUVA	Specific ultraviolet absorbance (L mg^{-1} m^{-1})
TOC	Total organic carbon

t	Time (s)
t_m	Mean hydraulic retention time (s).
V	Volume of mixing tank (m^3)

Greek Letters

α	Collision efficiency factor ($0 < \alpha < 1$)
$\beta(i,j)$	Collision frequency function ($m^3 s^{-1}$)
ρ	Fluid density ($kg\ m^{-3}$)
ε	Turbulent kinetic energy dissipation per unit mass for vessel ($m^2\ s^{-3}$)
η	Kolmogorov microscale (μm)
$\tau_{Kolmogorov}$	Kolmogorov time scale (s)
μ	Dynamic viscosity of water ($kg\ m^{-1} s^{-1}$)
ν	Kinematic viscosity of water ($m^2\ s^{-1}$)

Acknowledgements

For me, writing this section is the most enjoyable part, as it allows me to take a moment to cherish and treasure the paths I have taken in this Ph.D. marathon.

Firstly, I would like to acknowledge Halifax Water and the Natural Sciences and Engineering Resource Council of Canada (NSERC) for the financial support to the NSERC/Halifax Water Industrial Research Chair. Being a part of this program has provided me with an opportunity to present my research work to water utilities, and it has helped me in structuring this dissertation applicable to water treatments. I would like to extend my sincere thanks to the support team (John Samson) at 4-Deep Inwater Imaging and Dr. Manfred H. Jericho from Physics dept. at Dalhousie University for the invaluable help rendered during the initial design and implementation of holography microscope.

I am extremely honoured, excited, and thankful to Dr. Peter Jarvis for agreeing to be my external examiner. I am glad to have a dynamic supervisory committee (Dr. Tetjana Ross, Dr. Mysore Satish, Dr. Walsh, and Dr. Gagnon), their guidance and constant encouragements has allowed me to think critically about my research right from my comprehensive exam to publishing research articles. All these wonderful opportunities that I have experienced were not possible without the guidance and optimistic encouragement from my supervisor, Dr. Graham Gagnon. I owe him the researcher that I have shaped into today. This may sadly change our student-supervisor relationship; I look forward to have a professional collaboration in many more water networking events yet to unfold.

This thesis would be considered incomplete without a proper acknowledgement to a fantastic technical team at various departments of Dalhousie University: our tireless research chemists (Heather Daurie, Elliott Wright), technical and in-kind supports during SEM analysis (Patricia Scallion, IRM) , TEM analysis (Dr. Ping Li, biology Dept.), FT-IR analysis (Jon-Paul Sun, Ph.D. student, Physic department), amazing friendly folks at Mineral engineering center (Daniel Chevalier and Gerald Fraser) for Malvern Mastersizer analysis, CHN analyzer (Claire Normandeau, Biology Dept.). I would also like to thank the Louisbourg water treatment plant authority (Nova Scotia, Canada) for supplying water to conduct the research.

I am grateful to the doctoral students (Dr. Lee, Dr. Kot, Ben, Jordan, Amina, Sean, Lindsay, Leili) and post-doctoral researchers (Dr. Parker, Dr. Mackie) at the CWRS for their valuable suggestions that was crucial during manuscripts and thesis writing. I would like to thank Dr. Bohan and Dr. S. J. Payne for always providing me with sufficient time to discuss about the art of writing, which has tremendously improved my writing abilities over the years. My nerdy research life was balanced by many wonderful friends (Matt, Leah, Angus, Dr. Judy Guernsey, Naorin, Rowe, Dr. Bhatawadekar, Kristi, Karan, Madhu, Sukh, Vj, Shailesh & Bhabhi, Amitabh, Sandra, Dr.Krkosek, Dr. Younker, Jess, SJ, all D230 office-mates), among many others who came along during this course of journey, both personally and professionally. I would not have been able to effectively co-ordinate meetings, organize paperwork and signatures, remember to fill GSIS etc. without these lovely administrative staffs (Tarra, June, Shelley, Alicia).

Lastly, I feel truly blessed to have a wonderful family (Srinivasan & Komala Srinivasan, Srinivasan & Chitra Parthasarthy, my lovely sis—Rukmani, Srivatsan & Supraja, Ramji), who

have always been endlessly patient and encouraging to pursue my dreams. Thank you all for the moral support, it means a lot to me! I would not have realized my potential without the sacrifices & initiatives of my lovely mother, Komala Srinivasan, who put a brave face and sent me to Halifax! I am extremely lucky to share this journey with my dearest hubby, Kannan Srinivasan—I have accomplished more than a degree by having you next to me!

Chapter 1 Introduction

In municipal water treatment, several energy-intensive processes are used in order to provide safe drinking water and reliable wastewater services to their customers (Leiby and Burke, 2011). Energy is required for extraction and conveyance of raw water; treatment and distribution of drinking water; for heating water for residential end-uses such as showering, dish and clothes washing; and for wastewater collection, treatment, and discharge (Leiby and Burke 2011, Mass 2010, Plappally and Lienhard 2012). The use of service pumps for the transportation of drinking water through distribution systems is directly associated to the largest onsite consumption of energy in a utility, accounting for 63-80% of the total energy consumed (Leiby and Burke 2011, Santana et al. 2014). The energy cost associated with pumping and transportation alone can represent a significant percentage of a utilities' operational cost (Leiby and Burke 2011, Mass 2010). In addition, the anticipated rise of energy-intensive treatment processes due to stringent regulations, along with the need to pump water to greater distances and depths due to projected population growth (Mass 2010), suggest an exponential increase in the energy needed to provide water services. Moreover, the U.S. Environmental Protection Agency has estimated a projected 20% rise in water and wastewater energy usage by 2023 (USEPA 2008).

Concern over the impact of this predicted increase in energy demand has led to a significant increase in life cycle analysis studies to assess energy performance of a municipal treatment (e.g., Mo et al. 2014, Plappally and Lienhard 2012, Santana et al. 2014, Stokes and Horvath 2006). Energy usage is determined starting from extraction of water supply, treatment, use, and disposal. Common energy benchmarks are used to quantify the energy consumed at each stage, such as kilowatt-hour (kW-h) of electricity consumed per unit volume of treated water (NYSERDA 2010). Breakdown of total energy has demonstrated that the annual electrical energy required for pumping and treatment purposes in Ontario were approximately 20 PJ/yr (i.e., 5,556 mega kilowatt-hour/yr) (Mass 2010). This energy was said equivalent to the energy that could light every home in Ontario (Mass 2010). In Nova Scotia, the annual energy use for providing water services among different communities was calculated between 400 - 1200 MJ/yr (i.e., 112 - 334 kilowatt-hour/yr) (West 2015).

Energy is an essential commodity invariably used at different scales in various regions of the world. Energy consumption of a utility can significantly vary depending on several factors, which may include demographic and topography of the service area, treatment size and processes, operation and maintenance of equipment used. An anticipated rise in energy demand relates to an obvious increase in energy cost for a utility. It can also indicate an increase in greenhouse carbon emissions associated with the primary energy (e.g., fossil fuels, nuclear energy, renewable energy) used in the production of electricity for the operation of these systems. This suggests a need for a systematic evaluation of energy utilization for a better understanding of energy-water dependency and to develop effective energy management programs.

1.1 Research Statement

This research was primarily driven by the potential rise in energy demand in the water sector. In particular, an interest in identifying opportunities for sustainable design and operations of treatment processes in water utilities that could lead to a more efficient management of energy. The research focuses on rapid (or flash) mixing systems specifically designed for chemical dispersion in the coagulation process, as it represent the second largest energy consumption in a conventional drinking water treatment (EPRI 2002).

1.1.1 Potential to Improve Energy Efficiency through Coagulation Process Optimization

A rapid mix system is a component of a conventional treatment, dissolved air flotation treatment, direct filtration treatment, and a few membrane technologies. Rapid mix is a continuous-flow, stirred tank reactor (CSTR) (Lang 2002). It is practiced in treatment plants to quickly disperse chemical in water and to bring about chemical and physical interactions between the added chemical (iron or aluminium salts), particles, organics, and other contaminants in water. The effectiveness of coagulation governs the successful removal of stable particles by forming large precipitates (i.e., floc aggregates) that can be separated from drinking water in subsequent solid-liquid separation processes, including flocculation, clarification, and filtration.

Standard rapid mixing systems seen in treatment plants may contain mechanical impellers or paddles, hydraulic, and static mixers to achieve a uniform mixing of chemicals in a short time.

The root mean square velocity gradient (i.e., the G-value), proposed by Camp and Stein (1943), remains as the standard design parameter used by engineers to characterize the measure of mixing intensity, and for scaling up purposes in treatment plants (Bridgeman et al. 2008, Crittenden et al. 2005, Edzwald 2013, Letterman et al. 1999, Stanley & Smith 1995). The input power supplied is the only variable required in order to calculate a specific G-value, as given in Equation 1.1.

$$\mathbf{G} = \left(\frac{\mathbf{P}}{\mu \mathbf{V}} \right)^{0.5} \tag{1.1}$$

where, P is the average power transferred to the water in a mixing tank (J s^{-1}), μ is the dynamic viscosity of water (kg $m^{-1}s^{-1}$), and V is the volume of a mixing tank (m^3).

Common guidelines call for an energy-intensive mixing process in coagulation. These guidelines are typically designed at an average velocity gradient (G-value) of 600-1000 s^{-1} and a short hydraulic residence time of 10-60 s (AWWA-ASCE 2012). The Ten State Standards (2012) recommends a maximum residence time of 30 s with mixing equipment capable of imparting a minimum G of at least 750 s^{-1}.The average power supplied is proportional to the square of G (refer Equation 1), there is an exponential increase in the power and hence, energy consumption at $G \geq 600$ s^{-1}. For instance, sample calculations demonstrate that for a representative plant flow of 120 MLD at least 341 kW-h/day is daily expended for mixing at 600 s^{-1}, which was 4 times the calculated energy utilized at 300 s^{-1}. Energy consumed was calculated as a product of average power supplied to continuously mix suspension for 24 hour of operation. Clearly, it is evident that a large amount of energy is expended to operate at a designed G-value in coagulation process.

Previous studies have identified various disadvantages in rapid mixing tank designs, and have specified that the practice of intense mixing in coagulation is largely overemphasized (Allerdings et al. 2015; Edzwalds 2013). The G-value is an average measure of velocity gradient in a complex flow, and therefore does not account for a considerable variation in mixing that can occur within a system (Edzwald, 2013). For instance, the distribution of velocity gradients closer to the impeller was shown several orders of magnitude in excess of the rest of the tank, which

supports the argument that the G-value to represent a complex flow is flawed (Bridgeman et al. 2008; Hopkins and Ducoste 2003, Vadasarukkai and Gagnon 2010).

Notably, none of the particle-coagulant interaction mechanisms are accounted for in the theoretical G-value calculations. In a coagulation process, there are several pathways of interactions that may occur simultaneously during the removal process of certain particles from drinking water. Neutralization of particles' surface charge and adsorption (or sweep floc) of particles onto the surface of metal hydroxide precipitates are considered as the important coagulant mechanisms (Duan and Gregory 2003). In practice, a few experimental investigations have shown coagulation by adsorption mechanism is indifferent to rapid mixing operations (Allerdings et al. 2015, Amirtharajah and Mills 1982). The interpretations from these studies suggest it is plausible that the energy input in the rapid mixing tanks is not optimized for effective organics and particle removal.

1.2 Research Hypothesis and Objectives

Previous research has indicated that sustainable designs for coagulation mixing are plausible with less energy input, in particular for adsorption (or sweep floc) coagulation. The research hypothesis of the present study extends this practice for the removal of natural dissolved organic matter (DOM) in coagulation.

This thesis integrates water quality and floc characterization techniques to evaluate the influence of mixing energy during coagulation. In order for an energy saving, the key objective was to understand the influence of operating at a low-mixing intensity (i.e., G-value) during coagulation on the resulting precipitates (e.g., floc aggregates) and their settling characteristics. The experiments were designed to address the following specific objectives:

1. Conduct jar test experiments to determine optimal coagulant concentration required for maximum removal of DOM (as measured by total organic carbon) at different pHs.
2. Investigate the effects of varying mixing energy during coagulation on water quality, keeping coagulant dose, pH, temperature, and flocculation G-value similar conditions.

3. Examine the applicability of an in-line tool to measure floc size distributions at different scales (a batch reactor and a full-scale flocculation tank).
4. Investigate the effect of varying mixing energy on physical and chemical characteristics of floc sizes, following rapid mixing and flocculation in a batch reactor.

These objectives were met by the following approach. The experiments were conducted in a laboratory set up using a square beaker of 1 L capacity. A modified mixing arrangement was proposed in the present study to overcome the limitation of the standard jar test apparatus, which could only achieve $G \leq 300\ s^{-1}$. A compact digital mixer (Cole-Parmer, Vernon Hills, Illinois), with a mixing capacity ranging from 46 to over 1450 s^{-1}, was used to mix the water sample during the rapid mix process. A digital in-line holographic microscope (DIHM) was used to measure floc size distributions during slow mixing in the flocculation stage.

1.3 Organization of Thesis

This thesis has been presented in publication format, with versions of Chapters 4 and 5 have been published elsewhere. The author of this thesis is also the first author of these publications and performed the required research, designed, implemented, and conducted laboratory investigations, interpreted the resulting data, and wrote the manuscripts. The co-author(s) of these publications contributed in developing laboratory procedures and participated in reviewing and editing of manuscripts.

Chapter 1-provides the research motivation and justification for the thesis, along with the theory and practice of mixing in coagulation. The research objective and outlines are stated in this chapter.

Chapter 2-has a comprehensive review of theory and practice of mixing energy concepts applied in coagulation and flocculation for particle-coagulant interactions. A brief overview of coagulation and flocculation processes for removal of natural dissolved organic matter (DOM) in water, along with a highlight on common floc properties measured in water treatment can be found in this chapter.

Chapter 3- the method applied to measure floc size distributions using an inline holographic microscopy at bench-scale jar test beaker is described in this chapter.

Chapter 4- a submersible model of holographic microscopy was applied to measure floc sizes with respect to spatial variation in flow velocities at a full-scale flocculation tank is illustrated in this chapter.

Chapter 5- describes the water quality analysis of two types of raw waters at two different pH conditions. Also, the influence of the rapid mixing process on water quality was evaluated.

Chapter 6- examines the surface and morphological analyses of floc aggregates using a Fourier transform infrared (FT-IR) spectroscopy, and a scanning electron microscopy (SEM) combined with an energy dispersive X-Ray spectrometry (EDS).

Chapter 7- provides the influence of mixing energy input on floc growth and aggregation.

Chapter 8- discusses using a curvilinear approach regarding the role of G-values.

Chapter 9- summarizes the results of each chapter, explaining the main conclusion of this doctoral dissertation and also, provides recommendation for future work.

Chapter 2 Application Review of Relevant Literature

This chapter provides an overview of the relevant background literature in order to understand the effects of mixing energy on the dynamic of coagulation and flocculation. Topics reviewed include an overview of coagulation and flocculation process, mixing concepts applied in coagulation for particle-coagulant interactions, natural dissolved organic matter (DOM) and their characteristics in water, coagulant hydrolysis reactions and their interactions with DOM, and variables influencing the characteristics of the resulting precipitates, in particular DOM-coagulant flocs.

Coagulation and flocculation is two-stage treatment process followed in both drinking water and wastewater for removal of impurities. The root mean square velocity gradient (i.e., the G-value) gives a global measure of mixing in both coagulation and flocculation (Edzwald 2013). For the purpose of this study, the two types of mixing energies applied in coagulation and flocculation processes are distinguished. First, coagulation is defined as a system operated at a high mixing velocity, referred to as rapid mixing, to achieve quick dispersal of coagulant and bring about particle-coagulant interactions. The next step followed is the flocculation process, wherein slow or gentle mixing is delivered for about 20-30 min. This operation change is supposed to improve the attachment of two or more aggregates, which can grow into a large cluster of aggregates. These insoluble aggregates are of irregular shape and size, collectively referred to as flocs (or floc aggregates) in this study. Settling and filtration methods are then used to separate flocs (e.g., sludge) from drinking water and treated wastewater effluents.

2.1 Overview of Coagulation and Flocculation

Coagulation and flocculation remain critical treatment steps in most surface water treatment plants to facilitate in an effective reduction of a broad range of suspended and colloidal impurities in water supplies (Edzwald 1993). Such impurities in general are relatively stable under pH conditions of most surface waters, and characterized with a net negative surface charge in the range of 0.1 to 1 μeq/mg (Thurman 1985). Their removal from drinking water supplies is necessary as they can (a) reduce the clarity of potable water, causing turbidity in suspensions, (b) impart colour and odour issues (aesthetic reasons), (c) cause microbial contaminants (e.g., algae,

bacteria, protozoa, viruses), and (d) adsorb (trace metals) toxic compounds and control their stability (Crittenden et al. 2005). Conventionally, in coagulation, aluminium or iron salt is added as coagulant to surface waters. However, in recent years, polymeric coagulants (e.g., polyaluminium chloride (PACl), polyaluminium sulphate (PAS)) have gained popularity due to lower dose requirement and less sludge production (Matilainen et al. 2010). These salts possess high positive charges on their surfaces.

When aluminum or iron salt is added to water, in acidic solution each trivalent metal ion is surrounded by six coordinated water molecules, forming aquometal complexes (Crittenden et al. 2005, Davis and Edwards 2014). In the pH range used in water treatment (~ 4.5-8), these complexes undergo a series of rapid, complex hydrolysis and precipitation reactions (Davis and Edwards 2014), as illustrated in Equations 2.1-2.3. A negatively charged hydroxyl (OH^-) ligand substitutes for coordinated water molecules, forming mononuclear compounds (Davis and Edwards 2014, Jiang and Graham 1998). The release of hydrogen ions tends to lower the pH in such reactions. This is often counterbalanced by the addition of caustic soda, CO_2 or hydrated lime in treatment plants, depending on the source water buffering capacity.

$$\mathbf{Fe(H_2O)_6^{3+} \rightarrow Fe(OH)(H_2O)_5^{2+} + H^+} \quad (2.1)$$

$$\vdots$$

$$\mathbf{\left(Fe(OH)_2(H_2O)_4\right)^{1+} \rightarrow \left(Fe(OH)_3(H_2O)_3\right)^{0} + H^+} \quad (2.2)$$

$$\vdots$$

$$\mathbf{2Fe(H_2O)_6^{3+} + 2H_2O \rightarrow \left(Fe_2(OH)_2(H_2O)_{12}\right)^{4+} + 2H^+} \quad (2.3)$$

The type of hydrolysis and precipitation reactions in aqueous iron solutions is highly dependent on their pH (Stumm and Morgan 1995). For example, the equilibrium-solubility diagram of Fe(III) suggests that soluble monomeric species Fe^{3+}, $Fe(OH)^{2+}$ and $Fe(OH)_2{}^+$ are favoured below pH 7. While the vast majority of ferric coagulant is in an amorphous precipitated form between pH 7 and 9, with traces of soluble $Fe(OH)_2{}^+$ and $Fe(OH)_4{}^-$ species. The minimum solubility for iron hydroxides in water occurs typically around pH 8, although iron (oxy)hydroxide has a much lower solubility at pH 6.0 (Davis and Edwards 2014). Elevated concentrations of residual metal ions are undesirable in drinking water supplies. Hence, the

coagulant concentration and pH in water treatment are optimized to form largely insoluble amorphous precipitates. As shown in Equation 2.3, a condensation reaction can occur in which two hydrolysis species can form a bridge with its neighbours by the –OH and –O bridges (Stumm and Morgan 1995).

2.1.1 Coagulation Mechanisms for Particle Removal

The principal mechanism by which surface properties of particles in a stable suspension are modified to increase their tendency to attach to one another is termed as destabilization (Letterman et al. 1999). One method of destabilizing particles is to add counter ions (opposite charged particles), such as an electrolyte (e.g., sodium chloride) to the suspension. An increase in the ionic strength of counter ion will compress the thickness of the diffuse layer surrounding the particle, resulting in a reduction in repulsive forces between the particles (Crittenden et al. 2005, Letterman et al. 1999). Thereby, van der Waals attractive forces can dominate between particles that can result in successful attachment of particles. This concept is applied in coagulation process in water treatment. Their mode of action is generally explained in terms of two distinct mechanisms—(a) neutralization of negatively charged surfaces of particles by adding an equivalent amount of positively charged coagulant species, they have a tendency to adsorb on to particle surfaces to produce a net surface charge of zero, referred as charge neutralization and (b) addition of excess amount of coagulant until amorphous hydroxide precipitates are formed, which can entrap impurities on to their surfaces, referred as sweep flocculation (Duan and Gregory 2003, Pernitsky and Edzwald 2006).

The idea of mixing energy applied in coagulation is necessarily to increase contacts between particle and hydrolyzed coagulant species in order to achieve high rate of destabilization of particles (Edzwald 2013). The role of intense mixing gradient (G-value) to achieve this objective of particle-coagulant or particle-particle interactions has been constantly questioned in the literature (Benjamin and Lawler 2013, Han and Lawler 1992, Li 1996). In practice, a few experimental investigations have shown coagulation by sweep flocculation is indifferent to rapid mixing operations (Allerdings et al. 2015, Amirtharajah and Mills 1982). As a result, an understanding of mixing theory is necessary to undermine the practical applicability of mixing energy on the dynamic of coagulation.

2.2 Theory and Practice of Mixing Energy Input in Coagulation:

In municipal water treatment, turbulent flow is often used as an external source of energy to accomplish mixing of chemicals with incoming water and to transport particles in a process train, which includes pre-mixing treatments (e.g., pH control, oxidation), coagulation, flocculation, disinfection. Turbulent flows are characterized by high Reynolds number ($Re > 10^4$) (Oyegbile et al. 2016). Particles in suspension will experience a fluctuation in fluid motion due to rapid changes in velocity as a function of both time and space in turbulent flows (Oyegbile et al. 2016). Large-scale actions (e.g., mechanical mixers, inlet of a jet, flow over a weir) causes particle transport in treatment processes, which can lead to possible collision of particles by virtue of local variations in velocity over distance. Short ranged spatial flow patterns called eddies are generated due to large-scale actions, wherein a high degree of correlation exists between velocities at a particular direction (Benjamin and Lawler 2013). Large eddies can be of size of the order of the diameter of reactors (Benjamin and Lawler 2013), representing the macro scale of turbulence or integral length scale (L) (Oyegbile et al. 2016). A scale of motion less than the macro scale is responsible for convective transfer of kinetic energy to smaller eddies until it is dissipated at small scales (Crittenden et al. 2005, Letterman et al. 1999, Stanley and Smith 1995).

Smaller scale eddies occur close to the Kolmogorov micro scale (η), where both viscous energy dissipation and inertial convection subrange are active (Parker et al. 1972). After this scale, the flow is dominated by viscous effects. That is, the turbulent kinetic energy is dissipated in terms of heat due to frictional effects. In typical mixing conditions, the separation length between micro and macro scales is considered between 100 and 1000 μm, respectively (Oyegbile et al. 2016).

The Kolmogorov microscales of length and time are of particular interest in practical applications, computed on a dimensional analysis as given below (Benjamin and Lawler 2013):

Length: $$\eta = \left(\frac{\nu^3}{\varepsilon}\right)^{0.25} \quad (2.4)$$

$$\text{Time:} \quad \tau_{\text{Kolmogorov}} = \left(\frac{\nu}{\varepsilon}\right)^{0.5} \tag{2.5}$$

Here, η is the Kolmogorov micro-scale (μm), $\tau_{\text{Kolmogorov}}$ is the time scale (s), ε is the turbulent kinetic energy dissipation per unit mass for vessel ($m^2\ s^{-3}$), ν is the kinematic viscosity of water ($m^2\ s^{-1}$)

In coagulation and flocculation, mixing intensity is usually described by the root mean square velocity gradient, G-value, with a dimension of inverse time. A velocity gradient is a derivative of velocity u, v and w over distance in x, y, and z directions (Benjamin and Lawler 2013), given in Equation 2.6.

$$G_{\text{abs}} = \left\{\left(\frac{\partial u}{\partial y} + \frac{\partial v}{\partial x}\right)^2 + \left(\frac{\partial u}{\partial z} + \frac{\partial w}{\partial x}\right)^2 + \left(\frac{\partial v}{\partial z} + \frac{\partial w}{\partial y}\right)^2\right\}^{0.5} \tag{2.6}$$

Calculations of absolute velocity gradient require computational fluid dynamics to predict local variations in velocity gradient within the mixing reactor (Bridgeman et al. 2008, Vadasarukkai and Gagnon 2010, Vadasarukkai et al. 2011), and may involve measurements of fluid velocities (Ducoste et al. 1997) (e.g., using laser Doppler velocimetry (LDV), particle image velocimetry (PIV), acoustic Doppler velocimetry (ADV) techniques). Therefore, in treatment practice, the average value of G-value in a tank is more conventionally used as a design parameter by engineers to compute the energy supplied to a system (Equation 2.7). The average rate at which the energy supplied (i.e., power supplied) is assumed equal to the energy dissipated per unit time throughout the system (Crittenden et al. 2005).

$$G = \frac{1}{\tau_{\text{Kolmogorov}}} = \frac{1}{\left(\frac{\nu}{\varepsilon}\right)^{0.5}} \simeq \left(\frac{P}{\mu V}\right)^{0.5} \tag{2.7}$$

Here, P is the power transferred to the water in a mixing tank ($J\ s^{-1}$), μ is the dynamic viscosity of water ($kg\ m^{-1}s^{-1}$), and V is the volume of a mixing tank (m^3). For turbulent flow, the G-value is an inverse of the Kolmogorov timescale by dimensional reasoning (Benjamin and Lawler 2013). This means the smallest characteristics time scale for mixing ($\tau_{\text{Kolmogorov}}$) is of the order of 0.0017 - 0.001 s for the design parameter recommended in rapid mix from 600-1000 s^{-1}, respectively.

Benjamin and Lawler (2013) recommended small values of $\tau_{Kolmogorov}$ in rapid mix to ensure ultimate interactions of particles and chemical occurs within the microscale.

Most rapid tanks are designed for a theoretical hydraulic residence time in the range of 10-60 s (AWWA-ASCE 2012), which is at least 10^4 times greater than $\tau_{Kolmogorov}$, and substantially greater than the chemical reaction times. Also, the characteristics reaction times for the formation of metal hydroxide precipitates are less than 10^{-4} s (Dempsey et al. 1984). The need for a lengthy residence time is questionable as this time can allow for aggregation of unstable particles to form small precipitates (i.e., floc aggregates) in the rapid mix itself.

Floc resulting from coagulation and flocculation may adversely impacted by the mixing energy, leading to floc breakage as well (Spicer et al. 1998, Yukselen and Gregory 2004). On a similar note, particle size relative to the Kolmogorov length scale (η) has been shown by an empirical relation in Equation 2.8, which indicates floc breakage mechanisms to dominate above a critical value of applied G (Jarvis et al. 2005a, Parker et al. 1972).

$$\mathbf{d_f = C(G)^{-\gamma}} \tag{2.8}$$

Here, d_f is the maximum floc size, G is the average velocity gradient, C and γ are constants for particles larger or smaller than the Kolmogorov microscale (η). The microscale of turbulence predominates in a typical laboratory mixing settings, wherein particle collisions are promoted by eddy size similar to those of the colliding particles (Thomas et al. 1999). While particles smaller than this length scale (η) are more likely to experience pressure force, particle shear, and surface drag (Stanley and Smith 1995) since viscous forces dominates below the microscale. Alternatively, particles are entrained in eddies whose sizes are sufficiently larger than the micro scale, promoting particle transport within the inertial subrange. This reflects a balance of the mixing energy in coagulation is critical for adequate particle-chemical interactions while energy must not be expended in substantial breakage of flocs. Breakage of hydroxide precipitates are often considered as an irreversible phenomenon (Yu et al. 2016), which can lead to an adverse impact on solid-liquid separation processes.

2.3 Dissolved Organic Matter (DOM)

For the purpose of this study, primary particles was chosen as natural dissolved organic matter (DOM) that are ubiquitously found in freshwater and marine systems, and in terrestrial environments. In such ecosystems, DOM is a broad term applied to a complex mixture of naturally occurring aromatic and aliphatic hydrocarbon that have functional groups attached to their structure (Leenheer and Croue 2003). These organic constituents are derived largely from degradation of plant and animal remains (Davis and Edwards 2014). These remains are deposited on soil surfaces or deep within soil sediments, and gradually disseminated with mineral particles, water, and living organisms (Hedges and Oades 1997).

The transport of DOM from land to aquatic systems occurs by soil-water movement. The release of potential DOM is susceptible to seasonal changes. An increase in DOM release to surface waters has been indicated to occur at the onset of rainfall and snow melt, events that are associated with the late summer or early autumn period (Scott et al. 2001). Straw or tea-colored water results from the leaching of organic acids from plant and soil organic matter (Thurman 1985). Humic and fulvic acids derived from the degradation of plant-based biopolymers (e.g., lignin), are considered as the predominant class of dissolved organic constituents in fresh aquatic systems (Leenheer and Croue 2003).

DOMs are rich reservoirs of bioactive elements (C, N, P), which act as building blocks and a source of substrate for aquatic biota (Minor et al. 2014). They play an integral part of biogeochemical cycles in these ecosystems. In the drinking water sector, DOMs in source waters are considered undesirable as it significantly influences many aspects of treatment processes, including the performance of coagulation, membrane filtration, and distribution systems (Edzwald 1993, Hong and Elimelech 1997, Owen et al. 1995). Specific components of DOM have shown to react with chlorine to form disinfection by-products (DBPs) in drinking water, a class of compounds considered to cause potential health risks to humans (Health Canada 2010). As a result of the associated risks, DOM removal continues as a primary target in water treatment plants. In terms of energy perspective, the influent total organic carbon (TOC) concentration, a bulk measurement of DOM, was shown responsible for 11% of total operation energy consumption of a drinking water treatment plant (Santana et al. 2014). These findings

strongly suggest DOM has an influence on direct and indirect (e.g., chemical consumption) energy demand of a treatment plant. Therefore, a need to assess the effects of mixing energy consumption on DOM removal is essential from an energy management perspective.

2.3.1 Treatment Options for DOM Removal

Coagulation and flocculation processes have been extensively applied as a treatment option for removal of DOM constituents from portable water supplies. Coagulation is also used in combination with other treatment processes for DOM removal, which may include oxidation, physical separation using membrane processes, and ion exchange resin (Matilainen et al. 2010). A large volume of literature is available regarding DOM removal by various coagulants, at different pH levels, and for different water source characteristics. However, when applying coagulation, it is still difficult to quantitatively predict DOM removal efficacy.

2.3.2 Enhanced Coagulation

A range of factors such as composition of surface waters, coagulation pH, and coagulant dose influence the range of hydrolysis species formed and the removal mechanisms (Jiang and Graham 1998). The presence of dissolved natural organic matter (DOM) in surface waters, particularly aquatic humic and fulvic acid, is shown to affect greatly the chemistry of coagulation (Vanbenschoten and Edzwald 1990). These aquatic humic substances are larger molecular weight, hydrophobic (or non-polar) organic ligands that have a great affinity to get adsorbed and form complexes on metal hydroxide surfaces (Bose and Reckhow 1998). Other characteristic properties of DOM that are used to quantify their adsorption affinity on metal surfaces may include molecular weight distribution, charge density, total organic carbon, and specific ultraviolet absorbance (Bose and Reckhow 1998, Edzwald 1993, Jarvis 2008).

Total organic carbon (TOC), dissolved organic carbon (DOC), and specific UV absorbance at 254 nm (SUVA) are often used as surrogate parameters to quantify DOM removal from surface waters. Many investigations in the past have shown a substantial removal of 30- 70% of DOC reduction during coagulation, depending on aquatic humics concentrations in water matrix (Edzwald 1993). This process of application of optimized coagulant doses to minimize DOM and thereby, control the formation potential of disinfection byproducts (DBPs) in drinking water

treatments or distribution systems is termed as enhanced coagulation (Edzwald 1993, Xie et al. 2012). Table 2.1 provides the compliance target set by the USEPA (1999) to meet the required total organic carbon (TOC) removal by enhanced coagulation in conventional water treatment plants.

Table 2.1 Recommended total organic carbon (TOC) removal by enhanced coagulation and enhanced softening for plants using conventional treatment[a]

Source water total organic carbon (TOC) (mg/L)	Source water Alkalinity (mg/L as $CaCO_3$)		
	0 to 60	>60 to 120	>120*
>2.0 – 4.0	35.0%	25.0%	15.0%
>4.0 – 8.0	45.0%	35.0%	25.0%
>8.0	50.0%	40.0%	30.0%

*Plants practicing precipitative softening must meet the TOC removal requirements in this column

[a]adapted from USEPA (1999)

2.3.3 Removal Mechanism of DOM during Coagulation

The coagulation mechanisms of DOM removal have been extensively studied in order to improve organics removal and to control disinfection by-products (DBPs) in drinking water systems. However, the specific interactions involved in DOM removal by coagulation are not conclusive due to the nature of metal hydrolysis species and water matrix. Earlier research has favored rapid precipitation reactions of metal salts when added to water at a pH range typically operated in treatment plants, which largely formed amorphous metal hydroxide precipitates (floc aggregates) as a dominant end product (Davis and Edwards 2014, Jiang and Graham 1998). Here, humic sorption on metal hydroxide surfaces is thought to occur via ligand exchange reactions (Davis and Edwards 2014). At lower pH, the mechanisms ascribed are mainly complexation of DOM with dissolved metal ions, followed by a direct precipitation and possible adsorption of the complex material on metal hydroxide precipitates (Pernitsky and Edzwald 2006). Figure 2.1 illustrates the possible mechanisms of DOM removal during coagulation.

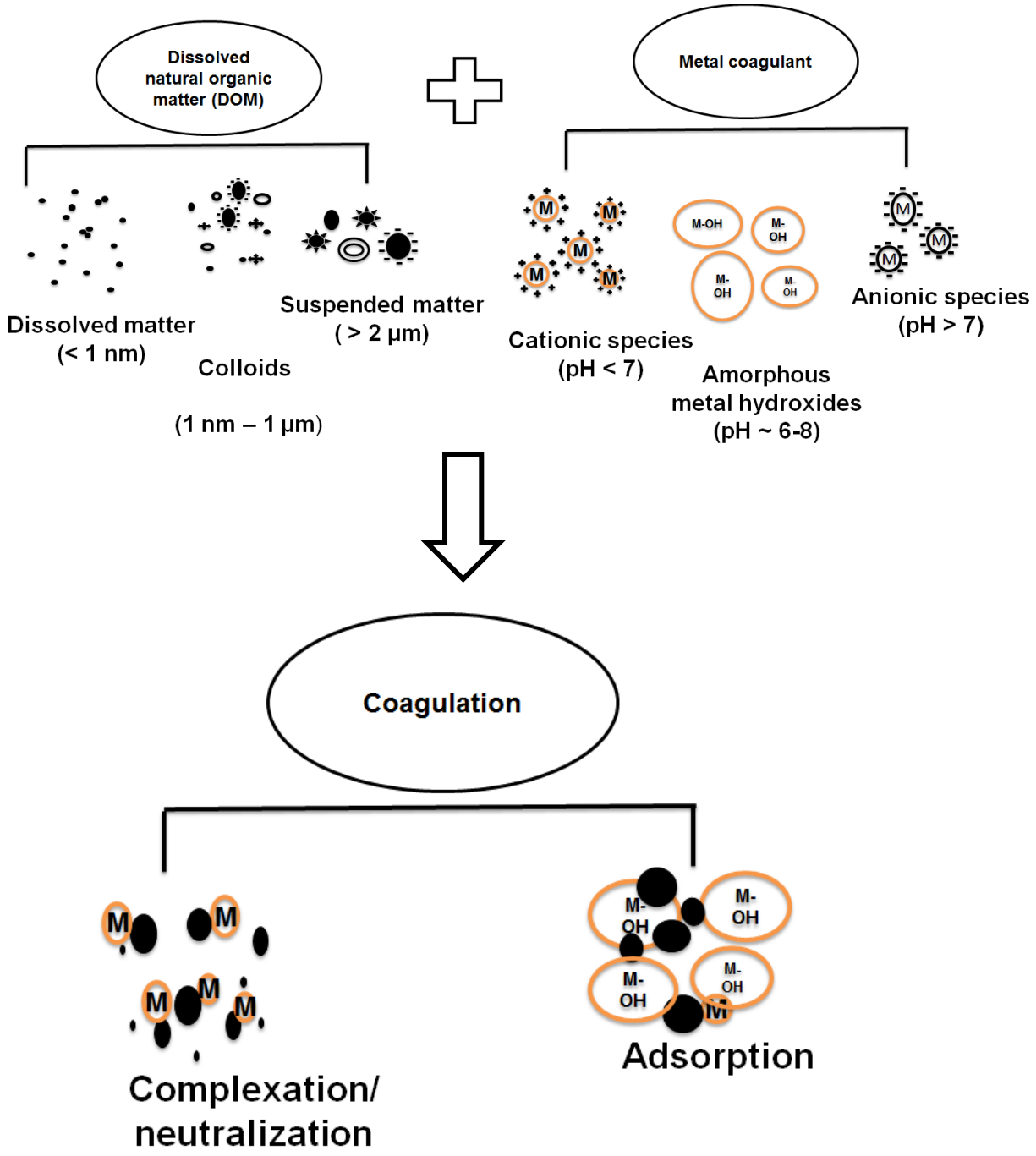

Figure 2.1 Possible mechanisms of DOM removal during coagulation

2.3.4 Characteristics of DOM Floc Aggregates

Insoluble precipitates resulting from chemical interactions between DOM, coagulant and other primary particles are collectively referred to as DOM floc aggregates. In general, flocs are described as highly irregular in shape but with fractal features (Spicer et al. 1996), i.e., they have

recurring structural features at different magnification levels. A multilevel structural model is used to describe such arrangements (Gorczyca and Ganczarczyk 1999), which suggests that primary particles in water form compact floccules, which then assemble themselves into microflocs. Microflocs bind together to form large and highly porous floc aggregates, which occurs predominantly during slow mixing in flocculation. The porosity of floc aggregates is shown to increase with their size, which affects their settling rate, their volume and the dewatering characteristics of the sludge (Gorczyca and Ganczarczyk 1999).

DOM has a significant impact on floc structural characteristics (Jarvis et al. 2005b, Jarvis et al. 2006). Association of humic substances with metal ions is shown to produce netlike floc structures (Myneni et al. 1999, Sieliechi et al. 2008); other studies have shown DOM flocs has a low settling velocity as highly branched and loosely bound, open structures are formed (Jarvis et al. 2006, Zhong et al. 2011). Slightly above a mass ratio of 1:1 organic carbon to coagulant dose, Jarvis et al. (2005b) showed a significant decrease in floc properties, including floc size, settling rate, strength and degree of compaction. While Zhong et al. (2011) suggested the adsorbed humic acid modified the surface characteristics of clay particles and caused poor floc regrowth. A comprehensive review of strength analysis of DOM floc structures suggest humic flocs had the least strength to resist external force; the degree of repulsion was hypothesized to increase due to existence of some negatively charged portion of DOM within a floc (Jarvis et al. 2005b).

2.3.5 Floc Properties and their Measurements

Floc aggregation and breakup are both dynamic phenomena in nature. Segregated models such as the population balance approach are often used in the literature to describe the instantaneous aggregation and breakage rates of flocs (Nopens et al. 2002, Samaras et al. 2010). Experimental methods to capture such dynamic variations require real-time monitoring devices to determine and characterize floc size distributions (Yao et al. 2014).

Several direct and indirect ways of measuring floc sizes has been reported in the literature. Microscopy is a traditional direct method of analysing an individual floc or a small sample of floc suspension at a high magnification by placing onto a microscopic slide (Allen 1997). Semi-automatic to fully automatic aids (e.g., digital photography, image analysis) has improved the

tedious manual way of counting and sizing floc images (Gibbs and Konwar 1982, Gorczyca and Klassan 2008, Spicer and Pratsinis 1996). For instance, Gorczyca and Klassan (2008) used the Brightwell MFI (Brightwell Technologies, Ottawa, Canada), an automated particle analyzer, in which floc samples were pumped through a flow cell. A digital camera captured and analyzed data for particle counts, area, diameter and perimeter. Instead of pumping the samples, Chakraborti et al. (2000) used a high intensity light source coupled with a CCD camera that was mounted facing the jar test beakers, which captured high resolution of floc samples through a controlled light source.

Indirect methods are used to obtain floc size distributions by measuring optical and electrical properties of flocs. Light scattering techniques (e.g., Malvern Mastersizer) are frequently used in many water laboratories to analyze floc properties (Biggs and Lant 2000, Jarvis et al. 2004b, Gonzalez-Torres et al. 2014, Wu and Wheatley 2011). Light scattered from different sizes of particles. For example, large particles absorb light and scatter at a smaller angle than smaller particles. Measurements of the degree of scattering from various particles provide an indirect measurement of floc sizes. Alternatively, the light transmission technique is used in other studies (e.g., Yu et al., 2016; Yukselen and Gregory 2004). It measures the average light intensity transmitted (dc value) and the root mean square value (rms) of the fluctuating component. Although a strong correlation was shown between the flocculation index (rms/dc) and floc sizes (Yukselen and Gregory 2004), limited quantitative information about floc sizes can be gathered from this approach.

2.3.5.1 Statistical Parameters Used in Floc Size Analysis

Standardization of irregular flocs shapes is essential to compare different floc measuring techniques. Different statistical average diameters are used in the literature to represent the irregular structures of flocs. A simple one dimensional (1D) measurement is to calculate the longest dimension of a floc image (Spicer and Pratsinis 1996). A similar approach is extended to the two dimensional (2D) measurements in other research (e.g., Chakraborti et al. 2000), where both the horizontal and vertical dimensions are measured. Floc characteristics such as height, width and aspect ratios are determined from these measurements. These parameters provide

information about the shape of flocs. The orientation of particles themselves to a particular plane has however limited the applicability of such measurements (Allen 1997).

2.3.5.1.1 Equivalent Circular Diameter (ECD)

The equivalent circular diameter (ECD) is an important statistical parameter that is frequently used in numerous investigations to represent floc size distributions (Chakraborti et al. 2000, Gorczyca and Klassen 2008). ECD allows the diameter of irregular particles to be defined as the diameter of a circle that would have an equivalent projected area as that of the particle (Allen 1997). Equation 2.9 is used to calculate the equivalent circular diameter:

$$\mathbf{d = 2\sqrt{\frac{A}{\pi}}} \tag{2.9}$$

where, d is the floc diameter (μm), A is the area of the identified floc (μm^2), and π is the numerical constant (3.1416).

Magnified images of the floc structure are captured using various optical techniques (e.g., microscopy method, a digital camera). For instance, the projected area measured from a randomly oriented particle using an image analysis is as shown in Figure 2.2. The area is expressed in terms of the total number of pixels that has been activated for that particular image (MFI^{TM} micro-flow imaging, 2011). Image analyzing software (e.g., BIOQUANT IV, NIH-Image, Global Lab Image v.2.0) scans pixel by pixel from top left to bottom right corners of the image. Using specialized algorithms, the pixels belonging to the existing particle is converted to represent the projected area of the floc in two dimensions. A similar process is performed to the next new particle captured by the camera.

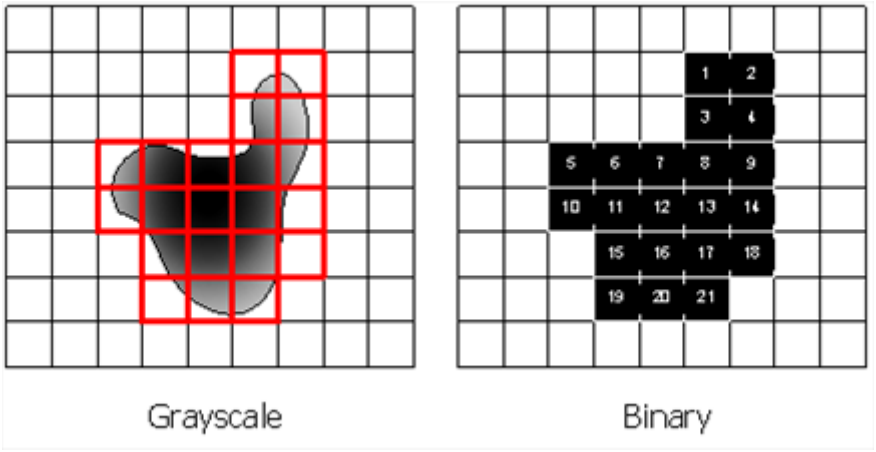

Figure 2.2 Projected area of an object (e.g., floc) measured using imaging analysis (Source: MFI™ micro-flow imaging, 2011)

2.4.5.1.2 Equivalent Volumetric Diameter (EVD)

The volume and mass distribution of flocs is important for the control of floc sizes in solid-liquid separation process. The equivalent volumetric diameter (EVD) is a common quantity used in earlier studies to report floc size measurements in water (Biggs and Lant 2000, Gonzalez-Torres et al. 2014, Jarvis et al. 2004b), especially from the light scattering technique (e.g., Malvern Mastersizer). A steady-state average value can be obtained from the floc size distributions, for example—volume mean diameter (i.e., d[4,3]=ratio of diameters raised to the exponents 4 and 3), surface mean diameter (i.e., d[3,2]= ratio of diameters raised to the exponents 3 and 2), most probable diameter, median diameter. Although the median equivalent diameter has been used in many studies to represent floc sizes (e.g., Gonzalez-Torres et al. 2014, Jarvis et al. 2004b), a single value may not effectively represent the distribution of the sample population in terms of skewness, standard deviation, and variations in the width of distribution. Another approach in volume-based floc analysis is to express floc sizes in terms of the percentile values at D10, D50 (median), and D90.

2.3.5.2 Factors Affecting Floc Properties

The following section discusses the importance of proper sampling procedures and highlights some of the physical, chemical, and biological factors that may affect the structural characteristics of flocs.

2.3.5.2.1 Sampling

Several earlier investigations have shown the sampling protocol followed as a crucial step in obtaining a true representative of floc size distribution (Gibbs and Konwar 1982, Spicer et al. 1998). The number of flocs to measure per sample is one such critical criterion. For instance, Spicer et al. (1998) have suggested samples for image analysis must contain at least 500 particle numbers to accurately determine the actual floc size distribution. The British Standard for quantitative microscope counting suggests a minimum of 625 particles to obtain a representative size distribution (BSI 1963).

Flocs have irregular, amorphous morphology, which are shown to experience rupture (breakage) during sampling events (Gibbs and Konwar 1982). Previous findings indicate small pipette tips or narrow nozzles used for floc sampling had a negative impact on floc sizes, it showed a reduction in the steady-floc size distribution (Gibbs and Konwar 1982, Spicer and Pratsinis 1996). The effect of shear on steady floc size distribution was studied by Biggs and Lant (2000), who demonstrated that flowrates lower than 180 mL/min had significantly minimized the effect of shear on floc sizes. The pump is usually located downstream after the sample cell to avoid any floc rupture before analysis. Peristaltic pumps are preferred for sampling of flocs in many particle size analyses (e.g., Jarvis et al. 2004b). In-line techniques offer a non-intrusive method to obtain reliable floc data since they require little to no sample handling, or dilution of samples. Only few studies have used such technology, for instance, Chakraborti et al. (2000) have highlighted the suitability of an in-line image based photographic technique to study alum floc aggregates.

Apart from human incurred sampling error, there are several physical, chemical and biological parameters as illustrated in Figure 2.3 that may affect floc properties. Turbulence and organic composition has been discussed earlier. In the following section, a few other physical and chemical properties are highlighted.

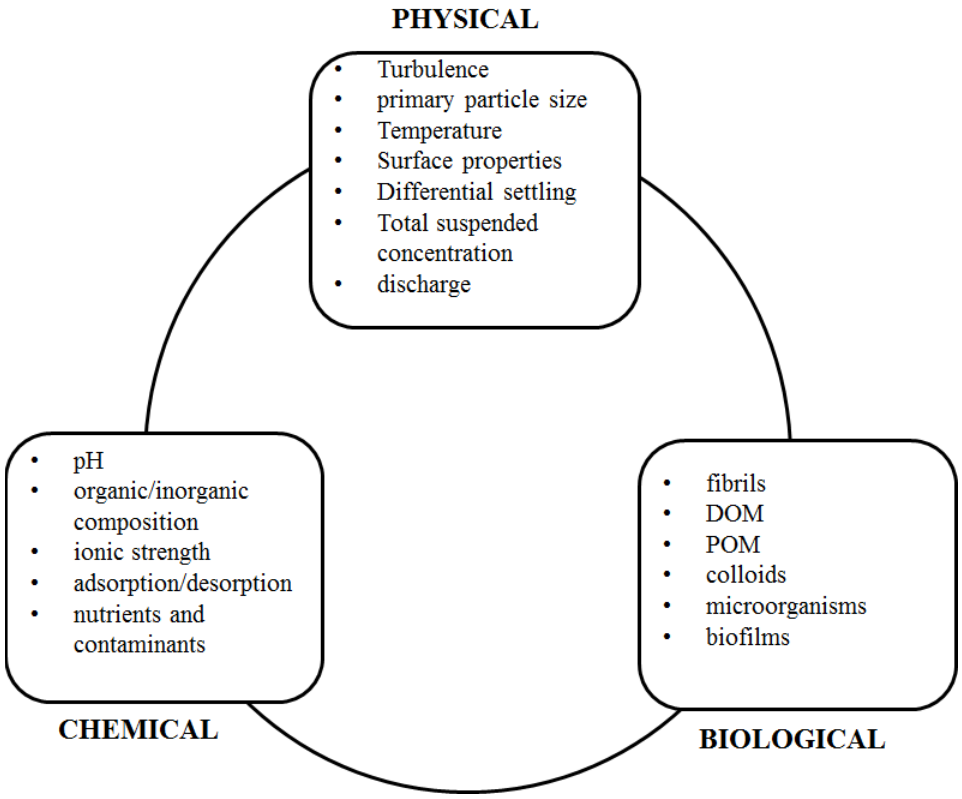

Figure 2.3 Physical, chemical and biological factors influencing floc development (adapted from Droppo et al. 1997)

2.3.5.2.2 Coagulant Type, Dose, and pH

Aluminum (Al) hydroxide flocs are in general transparent. These flocs are considered extremely fragile in nature (Chakraborti et al. 2000). Ferric flocs are consistently shown to grow at a faster rate and have larger average floc size distributions in comparison to Al hydroxide flocs (Gonzalez-Torres et al. 2014, Xiao et al. 2010). Floc strength analysis has indicated that iron flocs experience a quick decrease in size at an increased mixing intensity (Xiao et al. 2010). The findings of Parsons et al. (2007) agreed well with the previous finding. In their study, ferric sulfate flocs had a poor regrowth recovery factor of 18, which was considerably lower than the recovery factors of 40 for alum and 32 for polymer flocs. Jarvis et al. (2008) ranked the floc strength from different coagulated system in the following order: MIEX (resin) + Fe > polymer > Fe > Fe + polymer > Al.

The characteristics of flocs formed from various coagulation mechanisms are fundamentally different (Chakraborti et al. 2000, Kim et al. 2001, Li et al. 2006). Kim et al. (2001) found that flocs formed under sweep-floc coagulation were larger and more compact than those formed under charge neutralization. Contrary to this finding, Li et al. (2006) showed that the floc strength formed under sweep-floc coagulation were weaker due to the aluminum hydroxide bond formed. The effect of pH on binding between particles and/or precipitate and their surface charge determines the growth of flocs (Lin et al. 2014). Coufort et al. (2005) showed a low aggregate strength when the pH was raised from 3.5 to 5, which may be due to weakened interparticle forces between primary particles that constituted the flocs. Conversely, Lin et al. (2014) showed the floc strength to increase as the pH was changed from 5.2 to 6.0, implying a significant change in the floc structure. It is likely that the differences seen in the floc characteristics between the coagulated systems are attributed to various bonding mechanism that can differ depending on experimental conditions. As yet, there is no detailed understanding of the internal composition and bonding that can occur within a floc aggregate. This may include a systematic investigation of the number of bonds, location of points of attachment, and internal attractive and repulsive forces within the structure (Parsons et al. 2007).

2.3.5.2.3 Primary Particle Size and Concentration

Initial turbidity or particle concentration in source water is indicated to affect the rate of collision between particles and aggregates (Chakraborti et al. 2003, Xiao et al. 2010). Chakraborti et al. (2003) did not find any significant differences in the fractal dimensional analysis conducted for different particle concentrations. It is likely because of a relatively small variation in particle concentration between the experiments investigated, i.e., 220 and 366 particles/mL. Contrary to their finding, Coufort et al. (2005) found different initial populations in suspensions to strongly influence significant changes in floc size distributions. Floc characteristics of algogenic organic matter (AOM) were shown to grow larger than DOM and kaolin flocs (Gonzalez-Torres et al. 2014). Xiao et al. (2010) demonstrated that an increase in initial turbidity can accelerate the floc growth, in turn reducing the flocculation time required to achieve a steady-state distribution. Due to limited work seen in literature, it is difficult to make a conclusive remark on the effects of initial turbidity or initial particle concentration on floc growth.

2.4 General Summary

The dynamics of floc aggregation and breakup in coagulation and flocculation is complex. The phenomenon of decrease in floc sizes with increasing mixing intensity (G-values) is well-accepted in the literature. Notably, restructuring of flocs to form a more compact arrangement at an increased shear is a common interpretation observed in such studies (e.g., Yukselen and Gregory 2004). Although most of the literature findings are applicable for a fully developed floc following flocculation, little is understood about the role of rapid mixing typically designed at high G-values of 600-1000 s^{-1} in coagulation (AWWA-ASCE 2012). The above review also indicate many other factors influence floc growth, including coagulant, pH, surface chemistry of particles/organics, and initial particle concentration. For a sustainable energy design and operations, more research is required to investigate the influence of coagulation mixing energy on water quality parameters and on the resulting floc characteristics. The relevant literature reviewed for this dissertation has provided with the following interpretations that has formed the basis for the development of Chapters 3-8:

- **Dissolved organic matter:** Coagulation and flocculation is primarily used for the removal of large molecular mass, hydrophobic (or non-polar) DOM compounds. The influence of coagulation mixing energy is not conclusive for interactions of coagulant and organic probably due to heterogeneous mixtures of organic constituents in DOM. One way is to conduct a systematic investigation at different coagulation G-values to understand the effect of mixing energy on organic removal and floc formation.
- **Floc size measurements:** Many direct and indirect ways of measuring floc sizes following coagulation and flocculation are available in the literature; however, a vast discrepancy among those measurement techniques exist due to differences in the principle of measurements (by number or volume), different raw water types, and coagulation mechanism. Therefore, it was considered appropriate to take necessary measures to ensure that floc size measurements are repeatable at both laboratory and full-scale models using the inline holographic microscopy tool in this study.
- **DOM-floc aggregates composition:** The chemical compositions of resulting DOM-floc aggregates are less focused in the literature, which may provide a better insight on the resulting floc aggregates from particle-coagulant interactions. A combination of surface

and elemental analyses, along with physical characterization of flocs can advance our knowledge to understand the fate, transport, and removal of such contaminants.

Chapter 3 Characterization of Floc Size Distributions using a Digital Inline Holographic Microscopy (DIHM)

Measurement of floc size distributions is of prime importance for understanding the formation and breakage process in a dynamic system, such as coagulation and flocculation processes. In this Chapter, the applicability of an inline holographic microscopic technique was examined for characterizing natural dissolved organic matter (DOM) in a jar test apparatus.

3 .1 Introduction

The average size of particles (less than micron or sub-micron size range) is increased during coagulation and flocculation processes to enhance solid removal (Spicer and Pratsinis 1996). The resulting insoluble form of precipitates is referred to as flocs. Previous studies have confirmed the growth of floc sizes as a discontinuous process (Ducoste et al. 1997, Spicer et al. 1996, Spicer and Pratsinis 1996). As flocculation continues, aggregates become more susceptible to breakage even when the mixing velocity (measured as the G-value) remains unchanged. The overall growth rate was limited due to floc breakage and a steady floc size distribution was attained (Spicer and Pratsinis 1996). This phenomenon of evolution of floc size is conceptually shown as in Equation 3.1. Accordingly, floc size attains a limiting value when the aggregation and breakage rates are equal (Bridgeman et al. 2008, Manning and Dyer 1999). Determining this steady floc size distribution is of high operational importance. It has significant consequence with respect to settling and contaminant transport properties in engineered and natural systems (Droppo et al. 1997).

$$\textbf{Net rate of floc growth} = \textbf{Rate of aggregation or formation of flocs} - \textbf{Breakage rate growth} \quad (3.1)$$

In-line techniques are an ideal way to measure floc sizes. It is possible to get a true representation of a sample floc population as it avoids any external sampling procedures that can cause deformation and breakage to floc structures (Chakraborti et al. 2000, de Oliveira et al.

2015). Yao et al. (2014) analyzed the dynamic variations in particle size distribution by using an on-line particle counter. A high speed camera was applied by de Oliveira et al. (2016) to acquire morphology, particle size (by number) distributions, and particle size (by volume) distributions for kaolin-alum flocs. Likewise, Chakraborti et al (2000) using an in-line camera and image analysis measured sizes of floc aggregates formed in lake water coagulated with alum. A vast discrepancy among the inline floc measurement techniques are seen in the literature, which may be due to differences in the principle of measurements (by number or volume), different raw water types, and coagulation mechanism.

In this study, a non-intrusive approach was used to count and measure floc size distributions using a digital holographic microscope. Holography is capable of recording three-dimensional information of a sample volume on a plane (Sheng et al. 2006), which can be numerically reconstructed to get recorded "object" details. This technique has been previously applied for identifying dead and living cell cultures (Missan and Hrytsenko 2015), tracking motion of microscopic organisms (Garcia-Sucerquia et al. 2006), and in measurements of micrometer and submicrometer particles in dense liquid suspensions (Sheng et al. 2006). This technique was applied for measurement of flocs sizes following coagulation and flocculation experiments. Experiments were designed to address the following objectives:

- Quality control steps to process and acquire particle count and size distributions of floc aggregates from the recorded holograms (diffraction patterns).
- Determine the repeatability of floc size analysis using this technique
- Compare floc size distributions obtained from DIHM to other standardized technique (e.g., laser particle size analysis)

3.2 Materials and Methods

3.2.1 Water Source

Synthetic humic water was used as a model DOM for the organic floc characterization in this study. The solution was prepared by dissolving 0.030 g of humic acid, sodium salt (Alfa Aesar, Haverhill, Massachusetts) in a liter of deionized (DI) water, producing a total organic concentration (TOC) of (8.75± 0.64) mg/L. Alkalinity was introduced by adding 20 mg/L of 1 N

sodium bicarbonate to the stock solution. The prepared stock solution was continuously mixed using a magnetic stirrer for approximately 2 hours prior to the start of the experiment. Some general water quality parameters are provided in Table 3.1. A detailed summary of humic water characteristics is available in Chapter 5.

The particle size distribution of humic water after the addition of sodium bicarbonate was measured using a dynamic light scattering instrument (Zetasizer Nano-ZS, Malvern, UK), which had a detection size range from 0.6 nm to 6 μm. The angle of detection was set at 173 degree of backscatter. All results were reported as intensity weighted average (Z-average) size. A colloidal size range of 122-220 nm was measured for the prepared solution.

Table 3.1 Water quality characteristics of synthetic humic water

Water quality parameter	Value
pH	(7.66± 0.35)
Turbidity	(6.88± 0.02) NTU
Colour	392 Pt-Co
Dissolved organic carbon	(6.51± 0.11) mg/L
UV absorbance at 254 nm	(0.538± 0.02) cm^{-1}
Zeta potential	(-57± 0.78) mV

3.2.2 The Set-Up

Coagulation and flocculation experiments were carried out for the prepared synthetic humic water. Ferric sulfate, MP Biomedicals (Fisher Scientific, Pittsburgh, Pennsylvania) was used as the coagulant. Two pH set points were selected to form iron-DOM floc aggregates—pH 4.5 and 6.8. Two coagulant doses, 8 mg/ L of Fe (i.e., 0.26 mM Fe) and 14 mg/L of Fe (i.e., 0.47 mM Fe), were chosen for floc investigations at the selected pHs. These doses were determined from jar test analyses. A detailed explanation on the determination of optimal coagulant concentration (OCC) can be referred to Sections 5.3.4 and 5.4.2 in Chapter 5. In this method, an optimal coagulant concentration (OCC) of ferric sulphate was chosen as a dose that resulted in minimum

values of TOC, turbidity, and metal concentration in the treated water. Table 3.2 shows a summary of organic carbon and turbidity removal for humic water at different coagulant doses.

All coagulation and flocculation experiments were conducted at room temperature (21 ± 1°C) in a 1-L square jar test beaker. A compact digital mixer (Cole-Parmer, Vernon Hills, Illinois) was used for mixing purposes. For floc characterization, the optimal coagulant dose and chemicals for pH adjustment (i.e., 1M sodium hydroxide and 1N nitric acid) were added simultaneously during the rapid mixing stage at a G-value of 175 s^{-1} for 90 s. Images of flocs were recorded only during the slow mixing stage during flocculation, which was rotated at 46 s^{-1} for 20 min.

Table 3.2 Settled water quality results for the optimal coagulant concentration at pHs 4.5 and 6.8

Coagulant dose (mg/L as Fe)	pH	Turbidity (NTU)			Total Organic Carbon (mg/L)		
		Raw water	Settled water	Removal (%)	Raw water	Settled water	Removal (%)
4		6.2	12.4	--	9.4	9.1	3.3
8	**4.5**	**6.2**	**0.49**	**92**	**9.6**	**0.38**	**96**
12		6.2	2.7	56	9.14	0.47	94.8
8		6.2	15.4	--	8.28	8.97	--*
14	**6.8**	**6.2**	**0.53**	**92**	**8.32**	**0.58**	**93**
20		6.2	0.44	90.9	8.32	0.71	91.5

* Note: Only three coagulant doses were selected for clarity purposes. Total organic carbon (TOC) in the settled water was found greater than the initial TOC concentration at a lower coagulant dose, resulting in a negative percentage removal of organic carbon. This may be possibly due to an increased turbidity that may have interfered with the organic carbon measurements in the TOC analyzer (Shimadzu Corporation, Kyoto, Japan).

3.2.3 Analytical Methods

A laboratory model of a digital inline holographic microscopy (DIHM) (4Deep Imaging, Canada) was used to characterize flocs resulting from the coagulation and flocculation experiments. The microscope was vertically mounted on to one of the corners of a jar test beaker. A customized u-shaped arrangement allowed the laser light (λ= 640 nm) to travel through the

sampling volume. The image volume was situated at a few centimeters above the stirrer to ensure a proper circulation was provided for water samples to move in and out of the imaging volume. A sensor (CCD camera) with a pixel size equivalent to 0.7 micron and a direct shutter exposure of 1 ms was used as the recording medium. The distance between the point source (laser light) and the camera was kept at a 65 mm distance. The image size was 2048 x 2048 pixels (i.e., 1434 μm x 1434 μm). Each pixel was recorded using an 8-bit resolution.

Holography technique uses the intensity of light to record images. That is, a floc or cluster of aggregates that passes through the image volume can scatter the path of a reference beam of light, in this case a monochromatic light of a wavelength of 640 nm. The recorded interference of reference wave and scattered light intensity by different floc sizes will produces dark and light fringes (speckles), called as holograms (Sheng et al. 2006). For example, opaque particles appeared as dark objects, and transparent particles were bright in the light background. Samples of such diffraction patterns (holograms) recorded by the camera are shown in Figure 3.1.

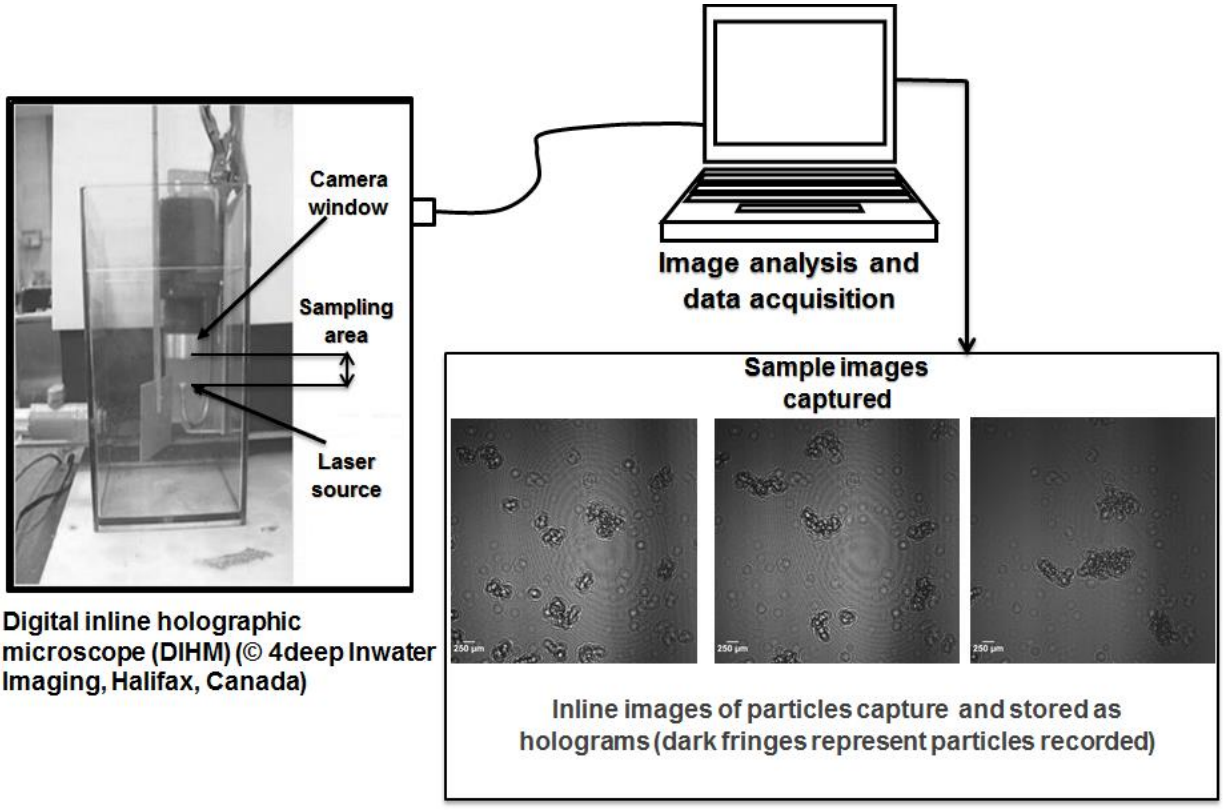

Figure 3.1 A schematic diagram illustrating (a) the set-up of a digital inline holographic microscopy (DIHM) in a jar test (b) holograms recorded

Preliminary tests were performed to determine the sampling frequency required to capture a true representative sample of floc aggregates. Three frequencies at a frame rate of 2, 10, and 15 fps were tested during the 20 min flocculation mixing at 46 s^{-1}. At higher frequencies of 10 and 15 fps, particle counts were overestimated due to multiple recording of a floc image. Therefore, the sampling frequency was set at a minimum frequency of 2 fps. That is, 2400 holograms were recorded for 20 min flocculation period. This frequency value was subjective to the mixing condition set in this study, and thus, it requires adjustment for other mixing velocities, especially at higher G-values. Recorded holograms were stored as bitwise images for the numerical reconstruction step. A two dimensional integral, Kirchhoff Helmholtz transform, was used to numerically reconstruct the acquired floc images from the experimentally measured diffraction patterns or holograms (Garcia-Sucerquia et al. 2006). Pairwise numerical reconstruction resulted in a dark background containing only particle information after a pixel by pixel comparison of consecutive hologram pairs. A stack of reconstructed holograms of floc aggregates were processed using the software (Holosuite, 4deep Inwater Imaging) to get the morphological details of flocs, which included floc counts and size distribution.

A laser dynamic diffraction instrument (Malvern Mastersizer 3000, Worcestershire, UK) was used to compare an equivalent floc diameter measured from the DIHM analysis. The humic water sample after coagulation was passed through the optical unit of Malvern Mastersizer and the water was recirculated back to the beaker using a peristaltic pump at a flow rate of 25 mL/min, similar to the set-up used by other studies (e.g., Biggs and Lant 2000, Jarvis et al. 2004b, Spicer et al. 1998).The pump was located after the Mastersizer to avoid any floc breakage prior to the analysis. Floc analysis was conducted for a total period of 20 min and floc size measurements was recorded at a time-step of 10 min. The floc size distribution was expressed as volume equivalent diameter.

3.3 Results and Discussion

3.3.1 Measurements of Floc Size Distributions

Recorded images of floc aggregates were used to count number of individual flocs, calculate area and diameter of those flocs. Unless explicitly specified, examples used in this section were from

the coagulation and flocculation experiments carried out at a coagulant dose of 8 mg/L of Fe and at a pH 4.5. An adjustable threshold value was set to define contrast between a floc image and the background (Wu and Wheatley 2010). For instance, for a threshold of 45 in Figure 3.2, only those images were counted as "objects" if their pixel value was greater than the adjustable threshold value, otherwise they were assigned as "background" pixels.

Previous studies have identified from microscopic investigations that floc morphology had a cloudy or dispersed network surrounding electron-dense areas of slightly smaller size (Myneni et al. 1999, Sieliechi et al. 2008). As seen from the Figure 3.2, the threshold values of 75 and 100 represented only the dense portion of flocs and did not identify those transparent (less dense) films that surrounded the inner structure (refer to the original hologram in Figure 3.2a). Dilation and erosion factors were used for the purpose to enhance the quality of identified flocs, especially those less dense areas. Although the threshold value of 45 was able to identify both the features fairly well, dilation caused an overlap of a floc boundary with other adjacent flocs in many images. Besides, many small flocs were counted by the program without having a dilation factor. This was because a boundary was split into several individual flocs instead of assigning it as one large floc.

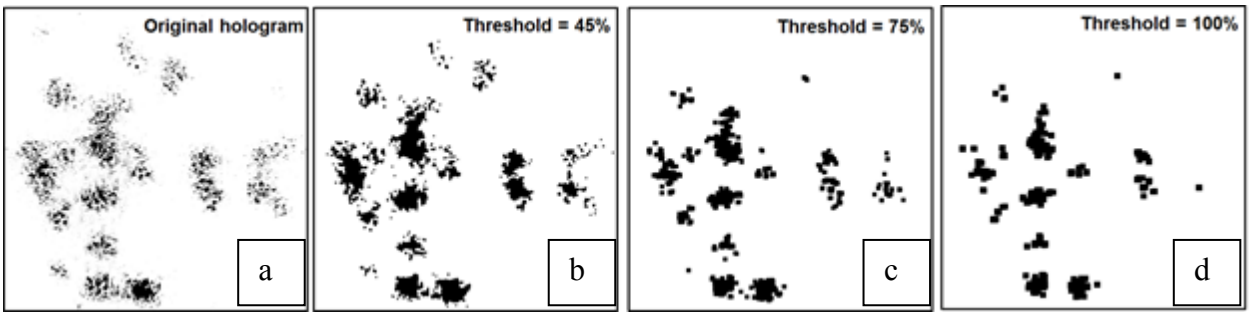

Figure 3.2 Illustration of a sequence of steps used to remove background noise from an original hologram using different thresholding factors.

Note: Flocs appear as dark spots on the lighter background, the background was changed to a lighter color for better visibility

Therefore, the threshold value of the original image was adjusted between 70 and 100% by manually examining it for at least 5-10 reconstructed images. A dilation factor of 4- 5 and erosion of 0-1 were the best suitable values for measuring flocs. These parameters defined the boundary of individual floc or cluster of aggregates. For cases where the quality of reconstructed

image was poor (e.g., blurred images or overlapping images), the threshold was increased up to 135% to reduce the noise. If the poor quality was still an issue even after applying those corrections, the image was deleted for quality control purposes. Pixel area of identified floc "objects" was automatically calculated by the software based on the number of pixels selected, which was then used to measure the equivalent circular diameter of floc size. This statistical diameter is equivalent to the diameter of a circle with the same projected area measured from imaging analysis (Allen 1997), given in Equation 3.2.

$$\mathbf{d = 2\sqrt{\frac{A}{\pi}}} \tag{3.2}$$

where, d is the floc diameter (μm), A is the area of the identified floc (μm^2), and π is the numerical constant (3.1416).

Flocs larger than 50 μm in diameter are considered as the major source contributing towards total surface area, volume, and mass of flocs; however, they are generally outnumbered by small size counterparts (Li and Ganczarczyk 1991, Wu and Wheatley 2010). Three threshold cut-off areas were tested in this present study: 0%, 0. 015% and 0.1%, which were equivalent to removing floc of diameters 0, 20, and 51 μm, respectively. Figure 3.3 (a-c) shows a typical histogram of floc size distributions that was determined from the particle counting program. In general, the number of floc counts decreased with an increase in floc equivalent diameter, which resulted in a highly skewed distribution to the right. The particle count was well above the minimum of 625 particles recommended in the British Standard for quantitative microscope counting (BSI 1963).

The particle count was greater than 200,000 and nearly 30% of floc populations were at 25 μm or less, without having a cut-off of floc area. Yet, the median floc diameter was still comparable to that of removing flocs less than 20 μm (i.e., 0.015% cut-off area), which signified most of the resulting floc population was in the micron scale larger than 20 μm. However, exclusion of less than 51 μm floc diameter resulted in a dramatic increase of median diameter to 100 μm. Li and Ganczarczyk (1991) showed small flocs between the size ranges of 2-16 μm had a negligible contribution to the total volume of flocs. On the other hand, the authors showed moderate flocs at 16-256 μm range resulted in as high as 80% of total volume and biomass distribution. This

portion of particle size range represents a significant role in the separation processes, and it should not be ignored. Therefore, a cut-off area of approximately 500 pixels of the image area (2048 x 2048 x 0.012%) was selected in the present study to exclude floc sizes below 17 µm from the analysis.

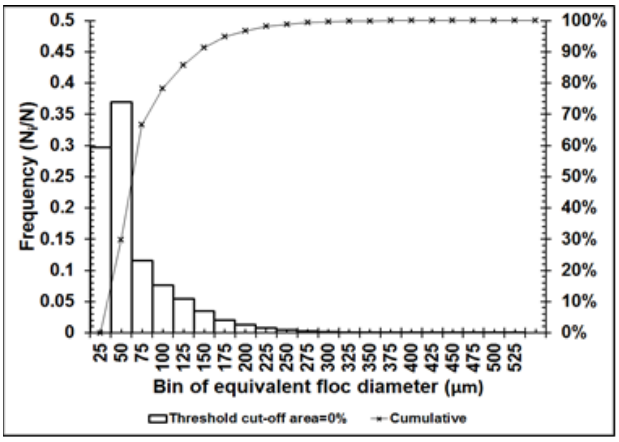

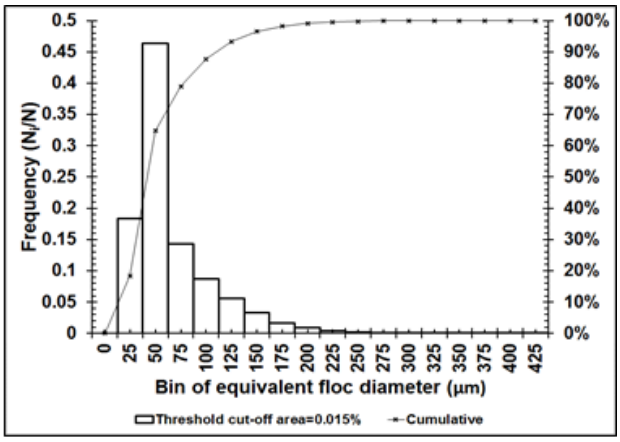

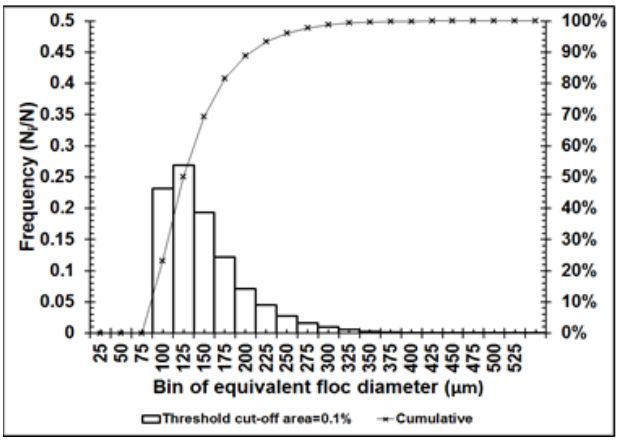

Threshold cut-off area (%)	Particle counts	Median (D50)
0	215,083	39
0.015	166,169	42
0.1	61,129	100

Figure 3.3 An example of floc size measurements with different cut-off areas.
(a) 0%, (b) 0. 015% and (c) 0.1% (d) floc count and median floc diameter for respective cut-off areas

Determination of volume fractions of flocs is an important operational parameter for solid-liquid separation process. For example, large flocs may be present in a small number; however, they can occupy a significant volume of filter bed, which may lead to shortening of filter run time. The equivalent volumetric diameter is another commonly used statistical quantity to report floc size measurements in water treatment (e.g., Gonzalez-Torres et al. 2014, Jarvis et al. 2004b), especially from the light scattering technique (e.g., Malvern Mastersizer). Therefore, for a comparison purpose with other techniques, floc sizes measured from the DIHM analysis was expressed as a volume fraction of floc diameter in each bin using Equation 3.3.

$$dV_i = \frac{(\frac{\pi d_i^3}{6}) * (\frac{dN_i}{N})}{V} \quad (3.3)$$

Here, dV_i is the volume fraction of flocs in the i^{th} class interval, the term $\left(\frac{\pi d_i^3}{6}\right)$ is the average volume of flocs in the i^{th} class interval based on spherical shape assumption, the term $\left(\frac{dN_i}{N}\right)$ is the frequency of occurrence for the i^{th} class interval with dN_i number of flocs, V is the total floc volume.

The transformation of data to a volume equivalent floc diameter as shown in an example case in Figure 3.4 resulted in a broad distribution of floc diameter between 25 and 500 µm. The median floc diameter was 170 µm, which was 44 µm for the original floc size distribution by number (data not shown). Flocs with diameter larger than 100 µm occupied at least 8% of the total volume fraction of flocs. Thus, represented a major source towards the total floc volume, which supports the findings of earlier studies (e.g., Li and Ganczarczyk 1991; Wu and Wheatley 2011).

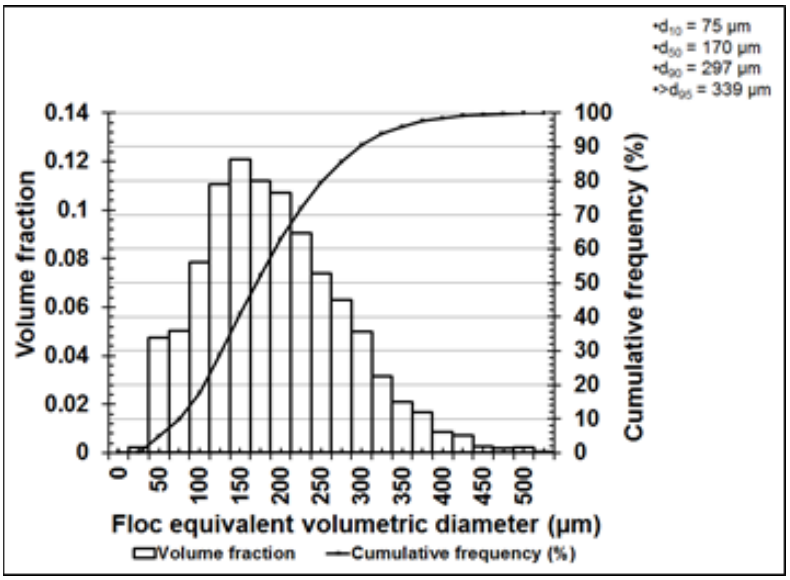

Figure 3.4 Example of a volume equivalent floc diameter distribution resulting from the transformation of number to volume fraction.
(using a threshold cut-off area = 0.012%)

3.3.1.1 Quality Control Step

Three sequential steps were taken in the present study to measure floc sizes from the DIHM analysis. First, the threshold, dilation, and erosion factors were adjusted by manually examining the values for at least 5-10 reconstructed images. That is, the diameter of a floc boundary can be manually estimated by using the image cuts tool that was available in the software. Here, a chord was drawn through the center point of a floc; the measure of this chord provided an approximate measurement of the equivalent floc diameter. This value was then used as a reference to verify the diameter that was calculated by the counting program for different threshold values and/or dilation factors. This procedure was carried out for at least at least 5-10 reconstructed images to ensure that the samples can be considered as a true representative of flocs in water treatment. A second step was to exclude flocs below 17 μm from the analysis. The last step was to represent floc size distributions as a volume fraction of flocs.

3.3.2 Repeatability of the DIHM Data

Floc experiments were repeated at least two times. The sequence of steps explained in the previous section was followed to acquire the distribution of equivalent floc diameters at pHs 4.5 and 6.8. Box plots and quantile-quantile plots displayed in Figure 3.5 provides comparison of a quantiles of floc population between the two replicates. Although box plots showed a good agreement between the median floc diameters (D50) at both the pHs, there was some deviation noted at the right tail (whisker). This discrepancy was clearly visible from the quantile plots for flocs larger than 500 μm diameter at the selected pHs. A solid line in the quantile-quantile plot represents a situation when the percentile of floc diameters was alike between the two replicate experiments (i.e., y=x). The deviation from a linear estimate was shown by quantiles located either below or above the solid line. At pH 4.8, quantiles of floc diameter measured in an experiment had a slightly larger distribution when compared to the other one. While most of the quantiles agreed well with one another until the 95^{th} percentile value at pH 6.8.

Kolmogorov-Smirnov (K-S) test, applied to compare floc size distributions, indicated there was no significant differences in floc diameter measured between the two groups at a significance level of $\alpha=0.05$ (Figure 3.6). This suggests reproducibility of the experimental data was possible

using the DIHM technique. Specifically, the median floc diameter (D50) showed a consistent value for comparison between the replicate experiments. This quantity was often chosen as an appropriate parameter to express the positively skewed distributions and to compare percentiles in many other floc investigations (e.g., Gonzalez-Torres et al. 2014, Yu et al. 2014).

3.3.3 Comparison between Particle Measuring Methods

Floc size distributions from the replicate DIHM experiments were combined to produce a histogram that represented the average of floc data. Figure 3.7 compares floc size distributions measured using the inline holographic (e.g., DIHM) and the laser dynamic diffraction (e.g., Malvern Mastersizer) methods. Although both the methods represented a positively skewed floc distribution profile, the data from the Malvern Mastersizer had a much longer tail than the DIHM—suggesting the detection of larger flocs in the Malvern Mastersizer. This difference in larger floc size measurements between the two methods was clearly evident for the experiments carried out at pH 6.8. The Malvern Mastersizer seemed to detect larger flocs up to 1200 μm, which can be explained by a wider size detection of this method (0.02 to 2000 μm). Also, the normalized volume-weighted distribution produced a smoother curve at larger floc sizes (near the tail) in this method (Govoreanu et al. 2004). Similar interpretation of a broad profile of volume-based floc size distributions has been explained using the laser diffraction technique by other researchers (Govoreanu et al. 2004, Zhong et al. 2011).

There are few measures recommended in previous studies for comparing floc size distributions from one or more different techniques. For instance, Wu et al. (2010) showed an improved agreement between image analysis and laser diffraction techniques when smaller flocs < 50 μm were ignored. The geometric mean obtained from the log-normal fitted transformation data of the Malvern Mastersizer has shown to correlate well with other number or volume measurements (Govoreanu et al. 2004). Accordingly, a log-normal distribution fit was assumed as it was recommended for comparison of data in the middle of a distribution from the two size analysis. Notably, Figure 3.8 illustrates a better fit between the log-normal data from the two methods for floc diameter less than 600 μm. The cumulative frequency distributions in Figure 3.8 showed a consistent trend of results in terms of percentiles (e.g., D10, D50, and D90) at pH 4.5.

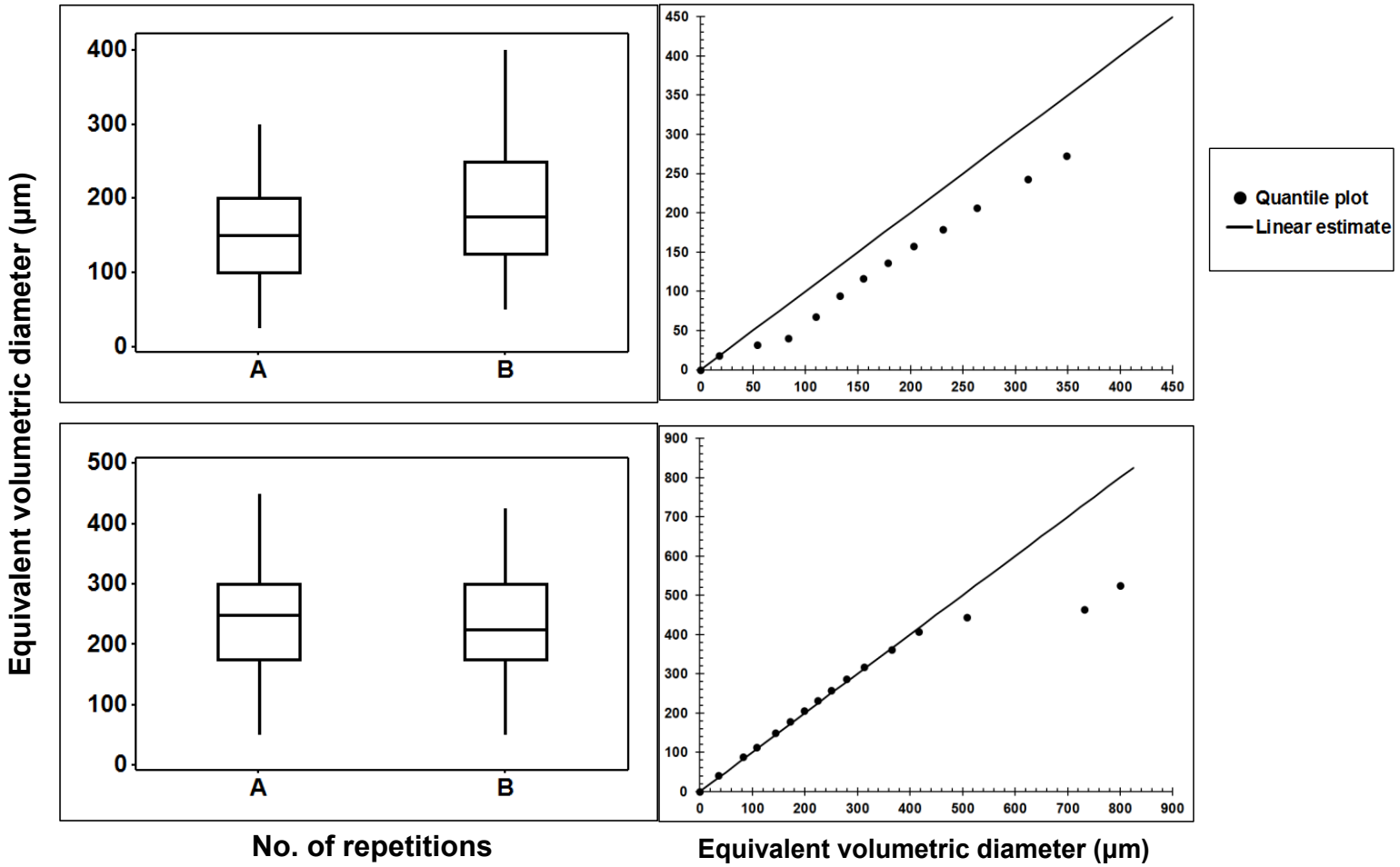

Figure 3.5 Comparison of a volume equivalent floc size distribution using box plots and quantile-quantile plots at pHs 4.5 (*top panel*) and 6.8 (*bottom panel*).

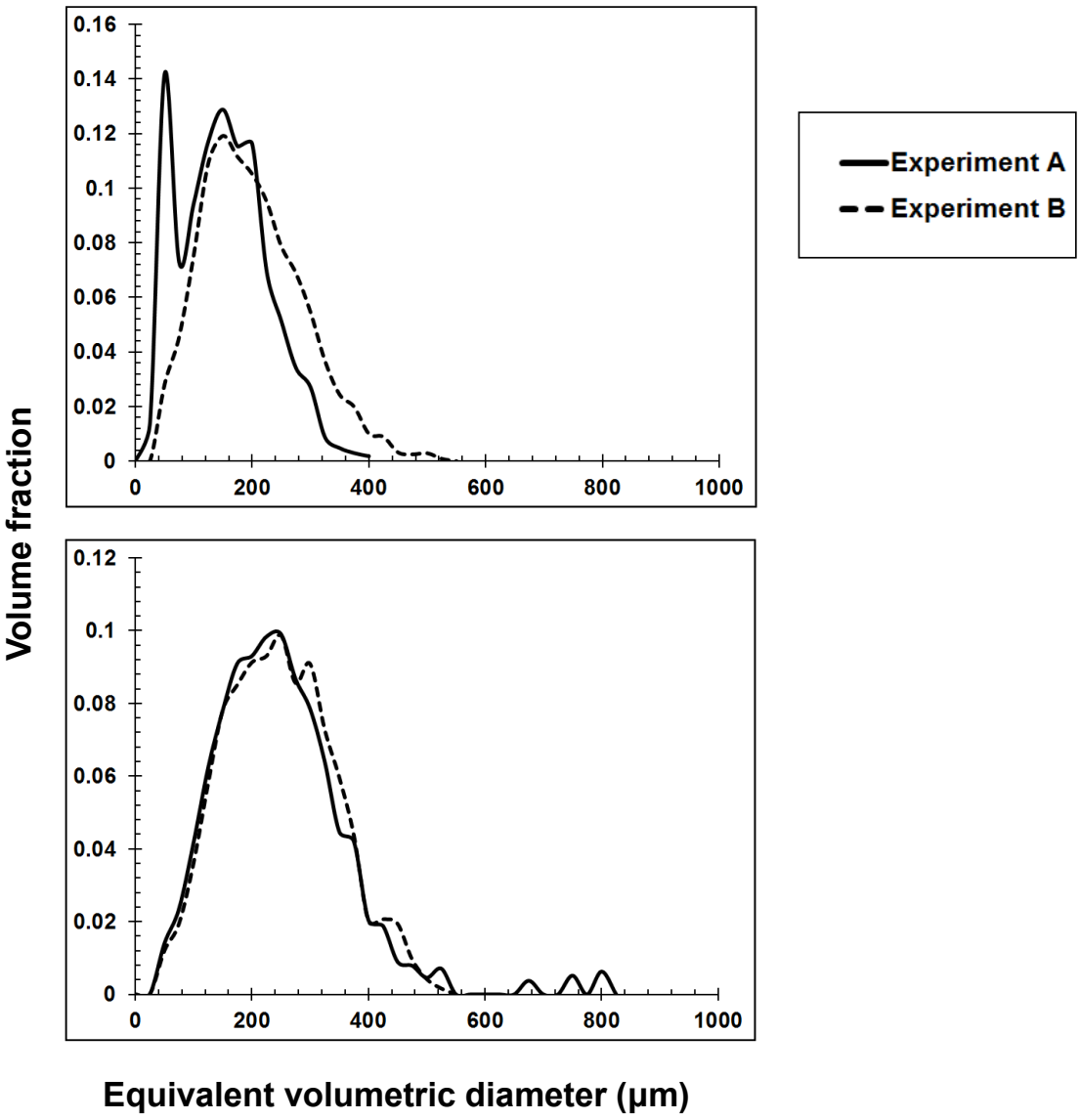

Figure 3.6 Histogram of floc size distributions (by volume) shown using smooth curve for the experiments carried out at pHs 4.5 (*top panel*) and 6.8 (*bottom panel*).

On the other hand, the Malvern Mastersizer still showed a much wider distribution than the DIHM at pH 6.8.

Flocs are expected to grow into larger aggregates at a higher pH due to amorphous hydroxide precipitates at an increased coagulant dose (Duan and Gregory 2003) (e.g., 14 mg/L of Fe in this case). Even though this trend was observed in the holographic method, only few flocs have been detected in a higher range (>600 μm). Flocs may experience breakage passing through the

sampling area or this could be partly attributed to the limited detection range of the software program. For these reasons, the DIHM was considered more suitable to effectively detect equivalent floc diameter in the range of 25-600 μm. Enhancing the threshold factor was an option that was available to compare larger flocs for the present case. Although biased measurements were expected during the enhancement process since it can merge adjacent floc boundaries and measure it as single floc "object". This shortcoming can be possibly overcome by improving the software program to select only large particles for the enhancement features.

3.4 Conclusion and recommendations

The present study has demonstrated the applicability of an inline holographic microscopic technique for characterization of natural dissolved organic matter (DOM) flocs resulting from coagulation and flocculation processes. The results presented here provide an insight into organic flocs formed by the addition of ferric sulphate coagulant in a jar test beaker at the selected pHs, 4.5 and 6.8. Reliability of the data was examined by conducting replicate experiments. Also, floc size distribution from the DIHM was compared to a standardized floc measuring method (e.g., the Malvern Mastersizer). The following conclusions can be drawn from this study:

- Floc size distributions were expressed in terms of volume fraction to represent the total volume of flocs formed during coagulation and flocculation experiments.
- Flocs smaller than 17 μm diameter were excluded from the analysis as the amount of volume occupied was less than 0.3%. Alternatively, when number distributions are of interest, these flocs can contribute up to 20.2% of the total number of flocs.
- Repeatability of the experimental data was shown possible using the DIHM technique at a significant level of α=0.05. It is highly recommended to repeat the floc experiments at least once, and combine the floc data to generate a histogram that represents the average of floc data.
- Comparison of floc data with the Malvern Mastersizer showed that equivalent floc diameter in the range of 25-600 μm can be effectively detected and measured using the DIHM. While larger floc sizes can be measured by enhancing the threshold factor without causing errors in the distribution.

- The three sequential steps followed in this study can be used as a guideline to obtain representative floc information for different water sources. That is, (a) adjusting threshold and dilation factors by manually estimating floc diameter using the image cuts tool, (b) exclusion of small floc data, and (c) expressing floc diameter as a volume fraction of floc diameter in each bin (Equation 3.3). Although this introduces a limitation in processing time, as a longer time was required to process and acquire a reliable statistical estimate of floc size distributions from the recorded holograms.

Few recommendations for future work are highlighted below:

1. Overlapping of holograms of highly concentrated flocs is possible, for example when analyzing wastewater sludge. In such cases, dilution may be required.
2. Since this technique measures floc sizes based on flow through the sample volume, it may not be suitable for stationary measurements or experiments conducted at a very low mixing velocity, such as $< 10\ s^{-1}$. In those cases, an external pump should be used for proper circulation. Alternatively, higher mixing velocities $> 450\ s^{-1}$ should be avoided during floc measurements as it can cause bubble formations in the sampling area.
3. The use of an equivalent circular or volumetric diameter may result in an overestimation of floc sizes as it assumes the area or volume as a solid floc. Although in reality, floc aggregates produced are permeable and have a non-uniform mass distribution (Li and Logan 1997). Therefore, size of flocs do not necessarily represent the fractal nature of flocs, which depicts whether the aggregates are densely packed as a large cluster or loosely arranged.
4. Image analysis from the DIHM was not directly compared to another method that works on a similar principle of particle counting. The Micro-flow imaging technique of Brightwell that was available in the Centre for water resources studies (Dalhousie University, Canada) had a maximum floc detection of 200 μm only, which can cause significant breakage to floc sizes measured in this present case.

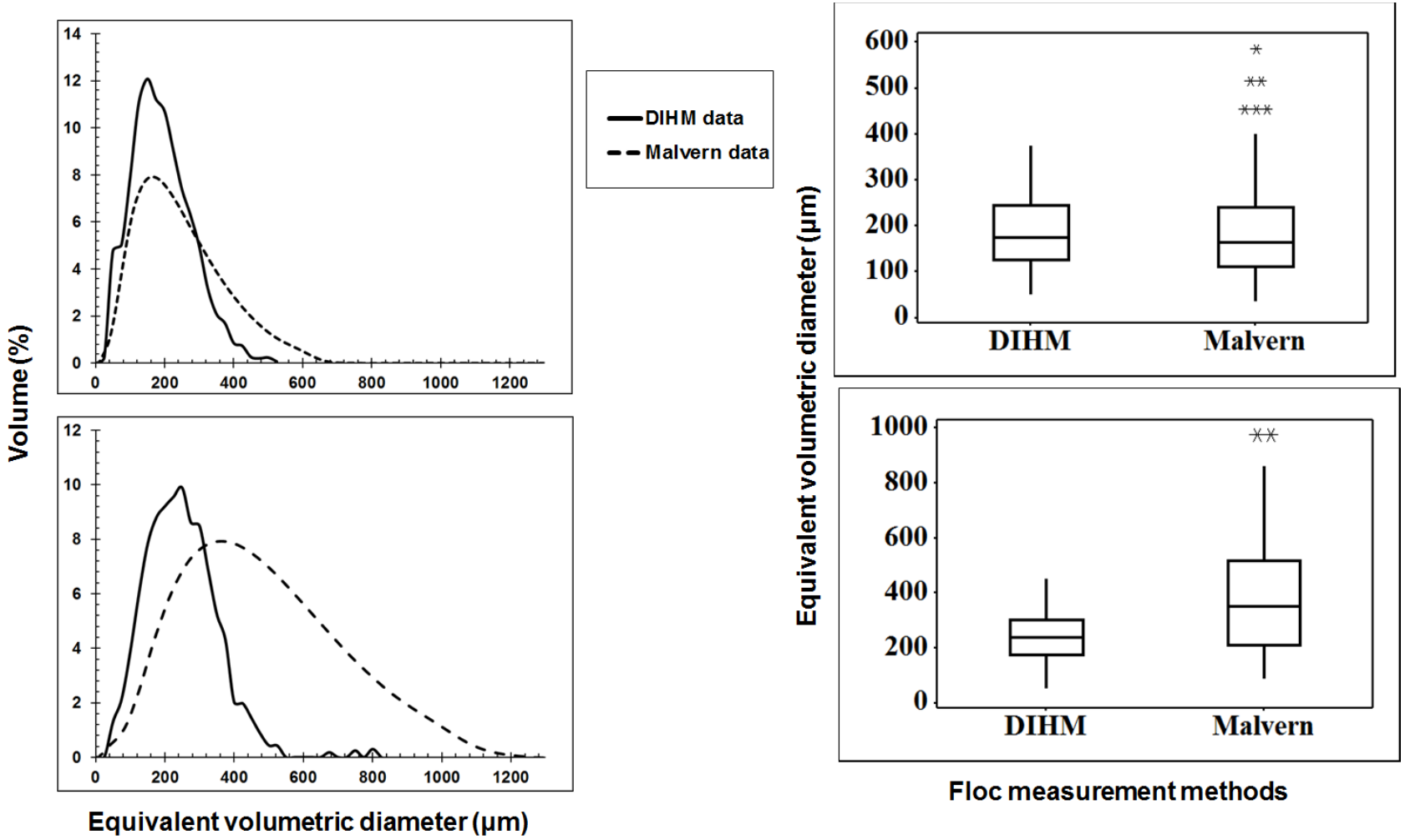

Figure 3.7 Floc size distributions (by volume) measured using the inline holographic technique and the laser dynamic diffraction technique at pHs 4.5 (*top panel*) and 6.8 (*bottom panel*).

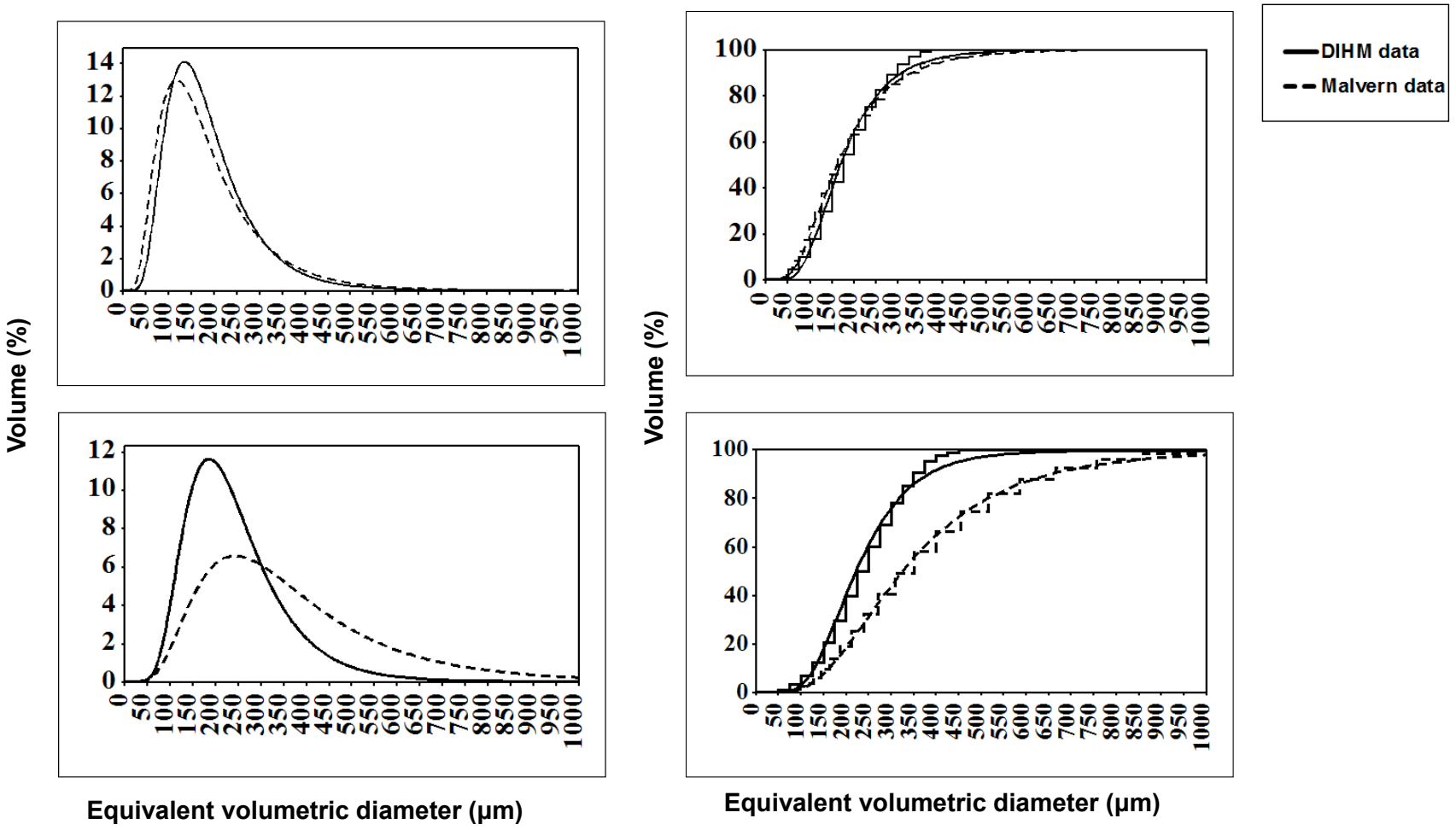

Figure 3.8 Log-normal fitted distribution for floc size distributions (by volume) measured using the inline holographic technique and the laser dynamic diffraction technique at pHs 4.5 (*top panel*) and 6.8 (*bottom panel*).

Chapter 4 Characterization, Fate and Transport of Floc Aggregates in Full-Scale Flocculation Tanks[1]

4.1 Abstract

Floc size distribution is of high operational importance as it governs the transport and removal of contaminants from drinking water. The complex nature of turbulent flow in treatment plants has limited the research to quantify the dynamics of flocculation. This paper describes the use of a submersible digital in-line holographic microscopy (DIHM) technique for the measurement of the spatial distribution of floc sizes in a direct filtration treatment facility. The DIHM tool was positioned at thirteen different locations in a flocculation tank and holograms were recorded for at least 10 minutes at each location. The acquisition of morphological details of flocs (e.g., floc counts, size distributions and floc velocities relative to the fluid motion) from the reconstructed DIHM images is discussed. The results of the spatial distribution of floc sizes indicated that the volume equivalent floc diameter measured in the flocculation tank was mostly of large-sized aggregates greater than 100 μm, which can have adverse impacts on the performance of a direct filtration process. The relative motion of flocs calculated from the DIHM analysis ranged from 0.002 to 0.008 m/s. Results showed that the investigated DIHM technique could be used as an operational tool to evaluate flocculation performance in terms of floc sizes, which is otherwise difficult to characterize in most treatment plants. The information acquired from this tool is important to understand the fate and transport of flocs during flocculation for process optimization that can lead to minimize chemical and energy usage in treatment plants.

4.2 Environmental Impact

The ability to obtain details on floc morphology from in-line measurements will significantly advance our understanding of the fate and transport of flocs with their associated contaminants in treatment plants. In this study floc counts, floc size distributions, and floc velocities are

[1] **Vadasarukkai, Y.S**., and Gagnon, G.A. (2016). Characterization, fate and transport of floc aggregates in full-scale flocculation tanks. Environmental Science: Water Research and Technology. **2**(1), 223-232

characterized relative to hydrodynamics in a hydraulic flocculation tank. The results demonstrated that large, irregular shaped floc aggregates were formed in flocculation due to limited supply of active mixing in the tank. Accumulation of large flocs on filters has an economical impact on the plant performance. In a boarder context, the ability to understand floc formation in real-time has potential to assist in other environmental applications (e.g., wastewater treatment, algal detection).

4.3 Introduction

Coagulation is an important treatment process for the removal of mineral and organic particles in water supplies that are typically stable in water.[1] Inorganic metal salts added in coagulation causes a change to the surface chemistry of constituent particles in source water mainly by charge neutralization or enmeshment of particles within metal hydroxide precipitates.[2] Flocculation that follows coagulation is the gentle mixing phase used to achieve contact between unstable particles in suspension, promoting their aggregation.[3] Particles grow in flocculation often leading to aggregates of highly porous, loosely connected, irregular shaped structures, described as flocs.[3, 4] High molecular weight polymers are at times added as a flocculant aid to increase floc strength and size by adsorption and interparticle bridging mechanisms.[5]

Flocs represent a complex matrix of microbial communities, colloids and suspended materials, and organic and inorganic constituents.[6] The size and strength of the developed flocs determines the efficiency of solids removal processes. Preferred floc characteristics differ depending on the solids removal processes used-for instance, relatively small, dense and low-volume flocs are recommended for direct filtration (i.e., no sedimentation step) in order to enhance the effective use of the media depth.[8] In contrast, large and dense aggregates with high resistance to breakage are preferred for sedimentation.[9] Although the porosity of aggregates often increases with floc size, which affects their settling rates, their volume, and dewatering characteristics of the sludge.[10] Therefore a compromise between sedimentation efficiency and sludge filtration characteristics has to be achieved in industrial practice.

Flocculation is a dynamically active process which is directly influenced by its hydrodynamic conditions.[9, 11] The flow conditions are driven by localized fluid turbulence that depends on both

the geometry of the flocculation tank and the impeller speed and type.[12] Flocs are transported between zones of varying levels of energy dissipation in a turbulent flow; this results in a continuous process of aggregation and breakage of flocs.[11] Hopkins and Ducoste[13] showed that the average floc size varied spatially in a flocculation reactor at low mixing speeds with larger flocs sizes and growth rates in the bulk region and a larger variance in the impeller discharge region. A simulation study by Samaras et al.[14] showed no large flocs in the region close to the impeller and floc growth in regions of high residence time. Data on spatial variations in floc size distribution is an important parameter to understand the transport and removal of particles in flocculation, sedimentation and filtration of suspensions.[15]

Measuring floc physical characteristics (e.g. size and morphology) can be achieved by using a number of different techniques such as optical microscopy[16], automated image analysis system[17], coulter counters[18], laser diffraction techniques[19], and photometric dispersion analyzer[20]. Most of these techniques (including microscopy, imaging analysis, and laser diffraction) require withdrawal of floc samples through pipetting or pumping and/or dilution of floc samples prior to the measurement. Such sampling procedures can disrupt the floc structure, causing floc breakage.[21] In-line methods are advantageous for floc analysis as it eliminates sample collection and/ preparation issues. Only a few studies have used in-line techniques (e.g., Oliveira et al.[22], Chakraborti et al.[23])- for instance, Chakraborti et al.[23] used a non-intrusive photographic technique coupled with a digital image processing system to characterize alum floc aggregates formed in a jar test. But all these aforementioned techniques are limited to laboratory workbench only.

Holographic microscopy is a technique that can be used for the characterization of marine particulates and tracking particle motion, such as the swimming behaviour of microscopic organisms[24], and spatial distribution of micrometer and sub-micrometer particles in dense liquid suspensions.[25] In the current study, a submersible digital in-line holographic microscopy (DIHM) was used for the non-destructive, direct measurement of floc characteristics (e.g., floc counts, sizes, relative floc velocities) in a three-stage hydraulic flocculation tank at the J.D. Kline Water Supply Plant in Halifax, Canada. The flow characteristics of the flocculation tank were previously modelled using computational fluid dynamics (CFD), as described by Vadasarukkai

et al.[12]. In the previous study, the predicted average velocity gradient (i.e., the G- values) ranged from 2 to 40 s^{-1} at various inflow conditions in the flocculation tank, which was significantly below the recommended design criteria of 20 to 75 s^{-1}.[8]

The purpose of the current study was to obtain in-line measurements of floc size distributions and floc velocities relative to the prevailing turbulent flow in hydraulic flocculation tanks. The potential implications of identified floc characters on filter performance are also discussed. It was hypothesized that the use of DIHM tool will improve the understanding of flocs transport in flocculation as it is capable of counting particles, conducting image analysis and tracking particle motion. The present study is its first application to the authors' knowledge in the drinking water industry.

4.4 Materials and Methods

4.4.1 Overview of the Study Site

The study was carried out at the J.D. Kline Water Supply Plant in Halifax, Canada. The design capacity of the plant is about 220 ML/d, with an average daily intake of 95 ML/d. Raw water is pumped into the direct filtration facility through a 1.2 m (48") inlet pipe, and flows under gravity into the subsequent treatment processes. As seen in Fig. 4.1, the treatment process consists of three rapid mix tanks in series, four parallel units of a three-stage tapered hydraulic flocculation tanks, eight direct dual-media filtration units in parallel, and chlorination. Calcium hydroxide (lime) is added for pH adjustment in the first of three premix tanks. Water then passes to the second premix tank, where additional mixing takes place, and then to the final premix tank where carbon dioxide is used to adjust to the coagulation pH of 5.5–6 and an average alum dose of 8 mg/L of aluminum sulfate is added for coagulation.[26]

Flow distributes the water after coagulation into four identical hydraulic flocculation tanks. Each flocculation tank contains three rows of two parallel sets of chambers (i.e., total six). The inlet pipe is located primarily below grade at the site, which divides the incoming water into the first set of chambers (Fig. 4.1). The length, width, and depth of each flocculation chamber are 5.0 m, 5.0 m, and 8.3 m, respectively. Two tapered vertical shafts are provided for the water to transfer

between the three rows of flocculation chambers. Each shaft has a capacity of 11.95 m^3 and 18.68 m^3 respectively. The water enters at an inclined angle into the first chamber due to the inlet design. After mixing in the first chamber it flows over a weir, then through a vertical shaft, and enters the next cell from the bottom. The design of an up-and-down flow arrangement in the subsequent second and third flocculation chambers provides the tapered G-value for mixing purposes.[12] After the flocculation process, the water is distributed to filter units through a floc water conduit.

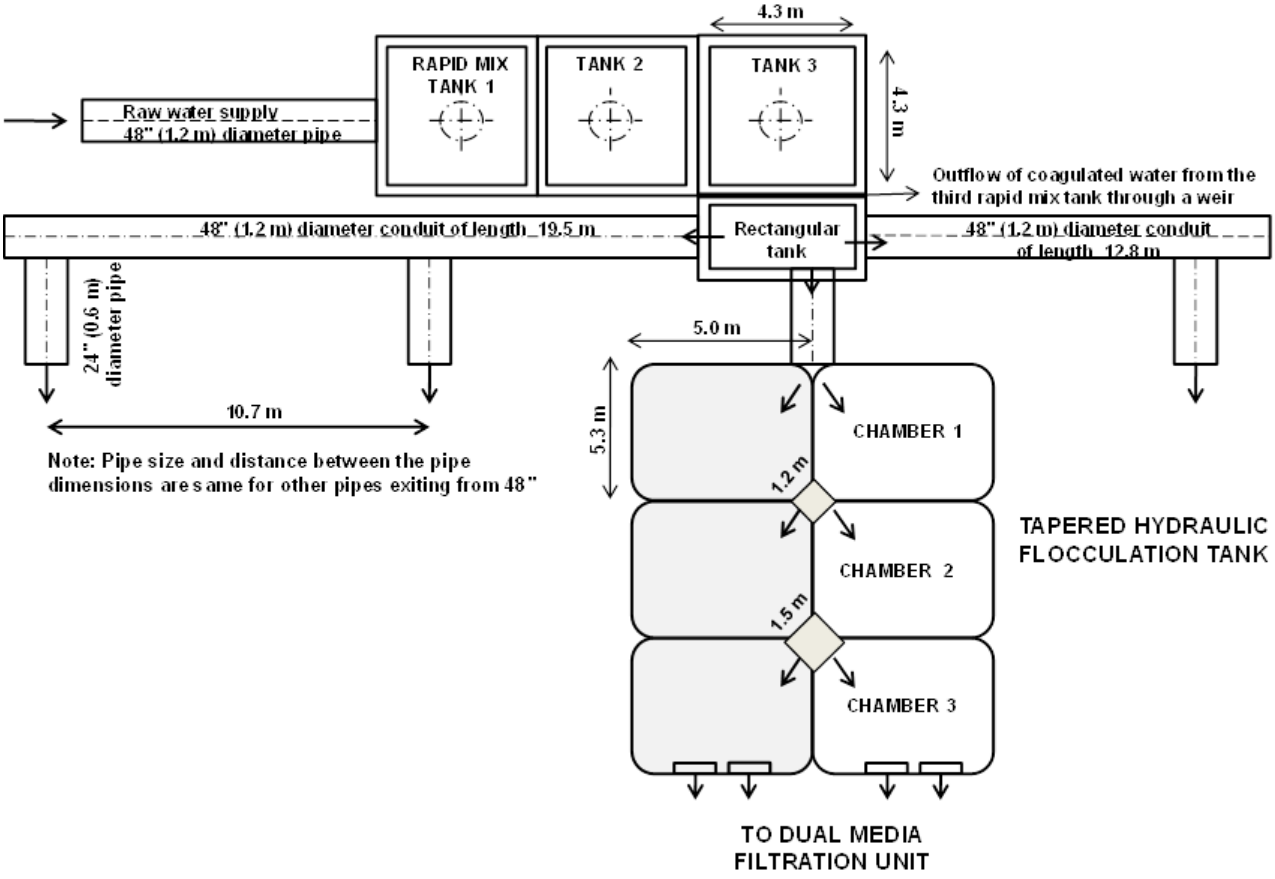

Figure 4.1 Schematic overview of the treatment processes of a direct filtration system at the J.D. Kline Water Supply Plant (Halifax, Canada)
(adapted from Vadasarukkai et al.[9])

Note: Not to scale

4.4.2 DIHM Set-up and Acquisition of Images

Fig. 4. 2 shows the main components of the submersible digital in-line holographic microscopy (4deep Inwater Imaging, Halifax, Canada). It consists of a laser source that directs the light (λ= 365 nm) through a 500 nm pinhole. A spherical wave emanates through the pinhole, which acts as the point source. As seen in the schematic in Fig. 4.2, it has two pressure chambers, one of which houses the laser and the other has a CCD camera (JAI PULNIX Inc., Sunnyvale, CA) connected to a computer source and a power supply. A 3 mm sampling space was provided between the two chambers to allow free circulation of water (medium) between them. The sampling space can be adjusted up to an 8 mm range depending on floc sizes to measure. Interference between the reference wave with a known phase distribution and light scattered from various size range of floc aggregates in the water was recorded as holograms.[25] The records of interference patterns contain spatial information about flocs within the imaged volume.

The present study was conducted on one parallel set of chambers of a hydraulic flocculation tank. The flow characteristics predicted in the previous CFD study[12] were used to select different sampling locations to position the submersible microscope in the tank. According to the model, three distinct regions were identified in the tank – namely, short circuiting, recirculation and stagnant (non-mixing) zones as shown in Fig. 4.3. The short circuiting path was created by a jet velocity of flow near the inlet which caused some portion of the incoming flow to rapidly exit into the second flocculation chamber. An intense recirculation region was formed at the interior of the first flocculation chamber, where 10.4% of simulated particles were shown trapped in that region for a longer residence time from the particle tracking analysis.[12] Stagnant (or non-mixing) zones depicted in Fig. 4.3 represented those regions in the second and third flocculation chambers where the flow path of particles never visited.

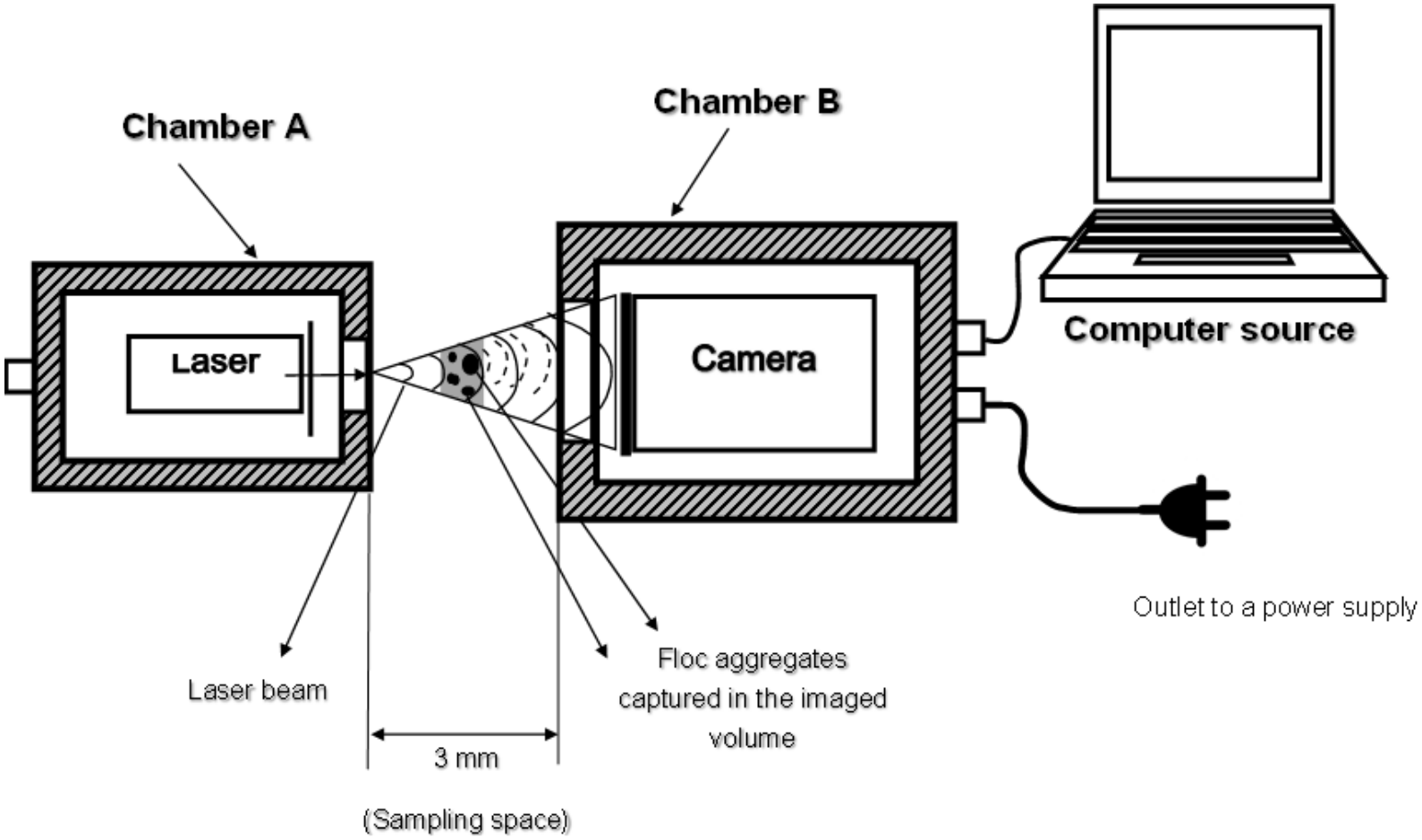

Figure 4.2 A schematic diagram of a submersible digital inline holographic microscope (DIHM).

Two pressure chambers-A & B, a 365 nm laser light source, imaged volume, camera sensor, and computer source are shown.
Note: Not to scale

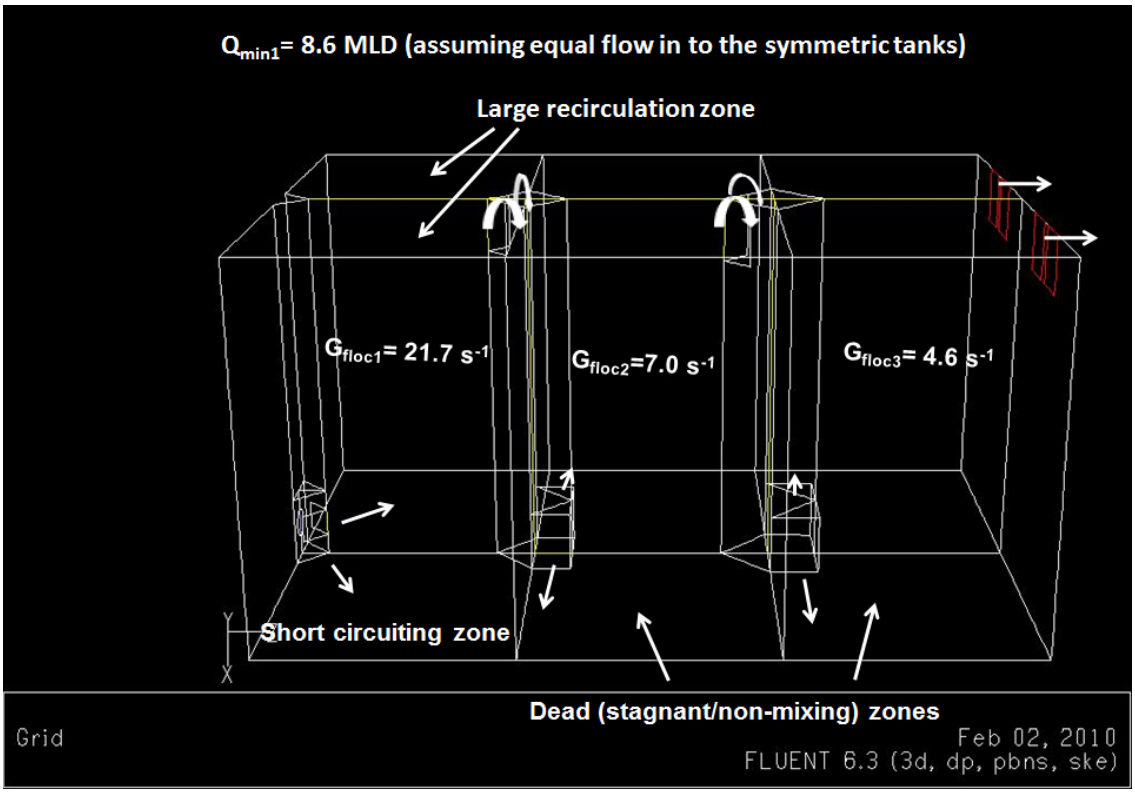

Figure 4.3 A three dimensional geometry of the three-stage tapered hydraulic flocculation tank along with the flow characteristics.

G_{floc1}, G_{floc2}, G_{floc3}- the average velocity gradient in the first, second and third flocculation chambers, respectively.

* The average G-value was 21.7, 7 and 4.6 s^{-1} in the first, second and third flocculation chambers at a plant flow of 90 MLD was computed from the numerical analysis (Vadasarukkai et al.[9]).

As illustrated in Fig. 4.4, the DIHM tool was positioned at thirteen different sampling locations in the flocculation tank to acquire a true representation of the spatial distribution of floc sizes in a turbulent flow. Specifically, eleven locations in section X-X in the first chamber and two locations in section Y-Y in the last chamber were chosen. These locations were selected based on the three regions identified from the flow characteristics described previously. For instance, 1B and 2B were the locations that represented the short circuiting path near the inlet in the first tank; locations 4M and 4B at the center denoted the recirculation region. No sampling location was selected for the second flocculation chamber as the fluid velocity was low in the stagnant zones

(Fig. 4.3). Only two locations, 6T and 6B, were selected for the last (third) flocculation chamber, where location 6T was situated near the peripheral outflow.

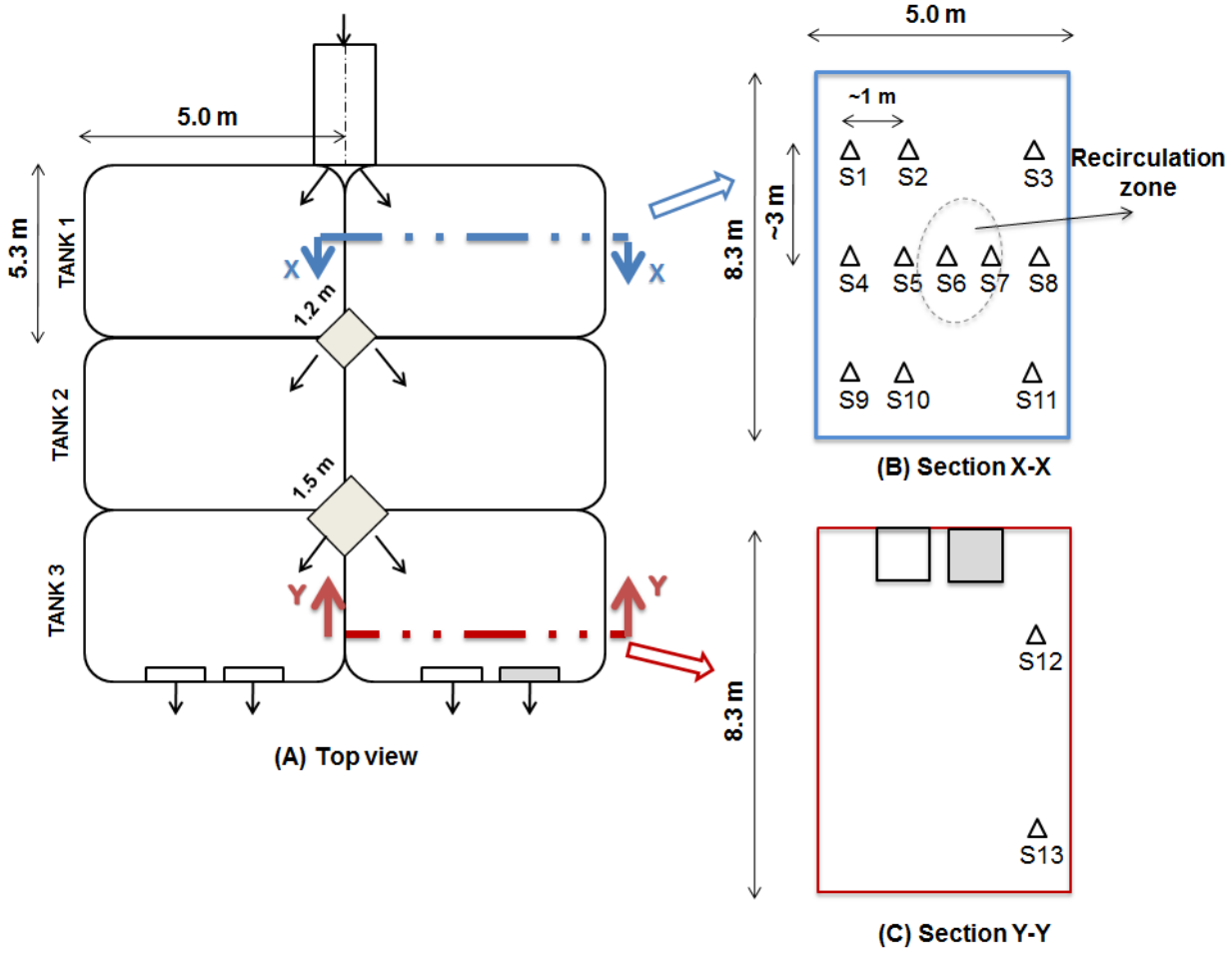

Figure 4.4 Thirteen sampling locations selected in one parallel set of a flocculation tank for the digital inline holographic microscope (DIHM) analysis

(A) top view of the entire tank (B) sectional view X-X of chamber-1 and B) sectional view Y-Y of chamber-3.

At each selected location, the DIHM was placed perpendicular to the fluid motion to allow free circulation of water through the sampling space. The instrument was held firmly using a rope, and the holograms were recorded continuously for 10 minutes at 15 fps by the CCD camera as illustrated in Fig. 4.5. Data was transmitted from the camera to the computer via an underwater cable. All the recorded holograms were stored as bitwise digital images in the computer for further analysis.

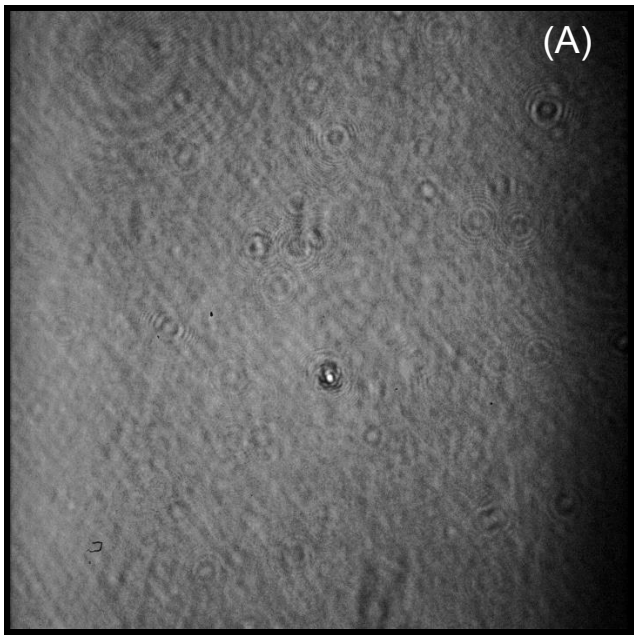

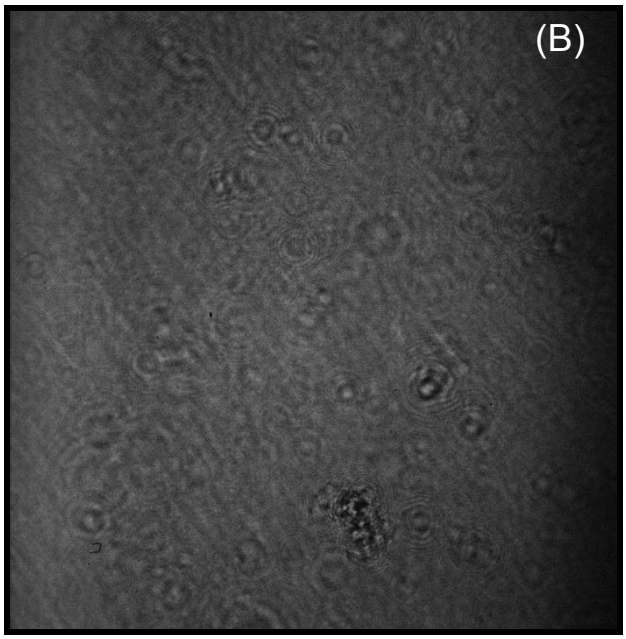

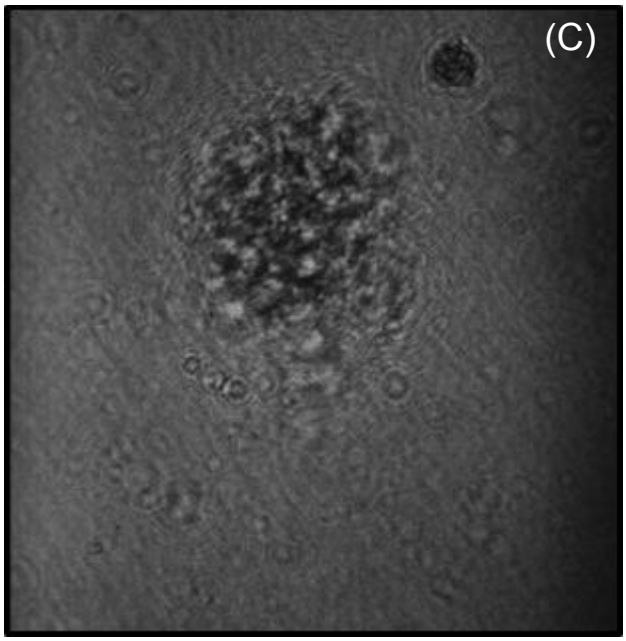

Figure 4.5 Illustration of holograms recorded at (A) 1B, (B) 1M and (C) 1T locations using the DIHM technique.

Note: Scale: 100 nm

4.4.3 Image Processing- Hologram Reconstruction and Measuring the Floc Aggregates

Stored holograms were reconstructed numerically to obtain images of floc aggregates within the imaged volume. Software (Holosuite, 4deep Inwater Imaging) was used to reconstruct each batch of holograms acquired at a sampling location. An example of reconstruction step is illustrated in Fig. 4.6. Here, two consecutive holograms were paired to remove the background noise. This combined file, called the difference hologram, was then reconstructed with the Kirchhoff-Helmholtz transform[27] to obtain images at a particular depth plane in the sample volume.

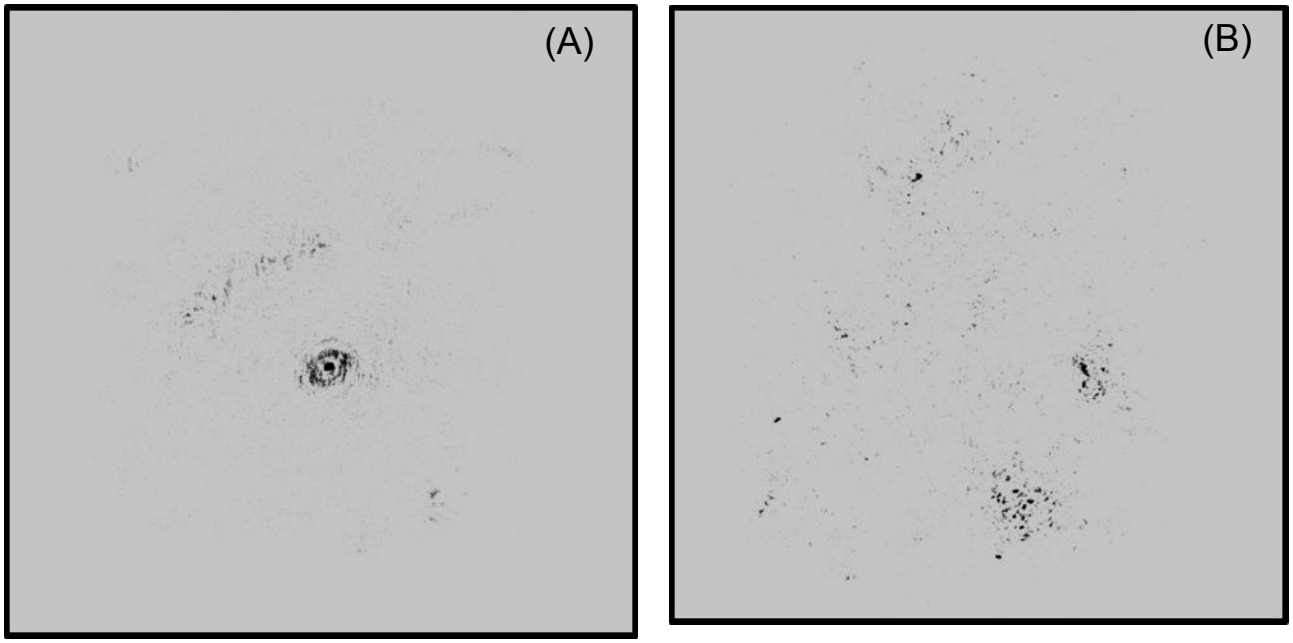

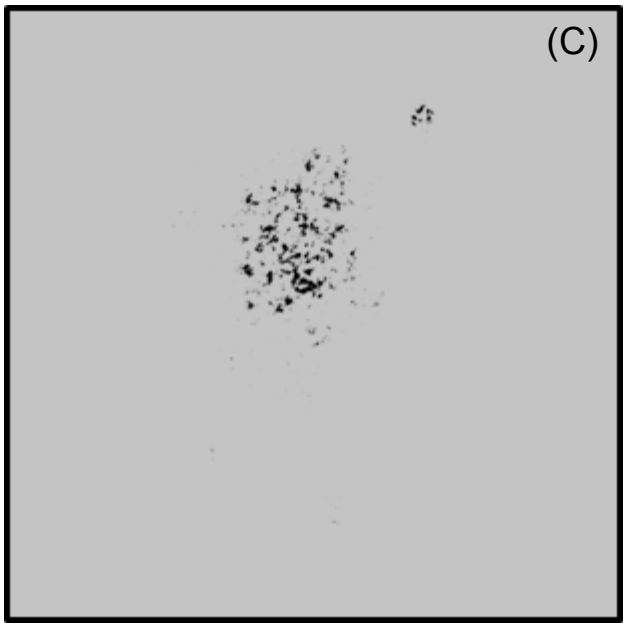

Figure 4.6 Example of reconstruction step- a difference hologram reconstructed after subtracting the background noise from consecutive hologram pairs at locations 1B, 1M and 1T.
(Scale: 100 nm)

Note: Flocs appear as dark spots on the lighter background, the background was changed to a lighter color for better visibility.

The morphological details of flocs, including floc counts and size distribution, were processed from the reconstructed DIHM images. The pixel value of the image was enhanced using the threshold tool to detect the floc aggregates from the background noise. Typically, the pixel value varied between 0 and 255, where 0 was considered as black and 255 signified the white color. Those images with pixel values greater than the adjustable threshold value were recognized as "floc aggregates"; the rest of the image was inferred as background pixels, as suggested by Wu et al., 2010. The threshold value of the original image was adjusted between 110 and 120% by manually examining it for at least 5-10 reconstructed images. The dilation and erosion factors were used to enhance the identified flocs. It was seen that a 10- 12 of dilation and 1-3 of erosion were the best suitable values for measuring flocs. The entire sequence of reconstructed DIHM images was then automatically counted, based on the parameter values that were manually adjusted for the first image.

Eq. 4.1 was used to measure the equivalent circular diameter, d (μm), from the projected area (A in μm^2) of a floc detected using the DIHM analysis. The volume and mass distribution of flocs is important for the control of floc sizes in solid-liquid separation process. Thus, floc size distribution was expressed as the volume fraction of floc diameter in each bin using Eq. 4.2.

$$\mathbf{d} = \sqrt{\frac{\mathbf{4A}}{\boldsymbol{\pi}}} \tag{4.1}$$

$$\mathbf{dV_i} = \frac{(\frac{\boldsymbol{\pi}\mathbf{d_i^3}}{\mathbf{6}}) * (\frac{\mathbf{dN_i}}{\mathbf{N}})}{\mathbf{V}} \tag{4.2}$$

Here, dV_i is the volume fraction of flocs in the i^{th} class interval, the term $\left(\frac{\boldsymbol{\pi}\mathbf{d_i^3}}{\mathbf{6}}\right)$ is the average volume of flocs in the i^{th} class interval by assuming flocs are spherical, the term $\left(\frac{\mathbf{dN_i}}{\mathbf{N}}\right)$ is the frequency of occurrence for the i^{th} class interval with dN_i number of flocs, V is the total floc volume.

4.4.4 Floc Velocity Measurements

Floc velocity was calculated by overlaying two subsequent holograms. Overlaying the reconstructed holograms highlighted only the floc motion relative to the fluid (water) velocity, while the rest of the stationary features were deducted during this process. The distance travelled was manually measured (Fig. 4.7). The relative magnitude of velocity of a floc was calculated as the ratio of distance travelled and the time between frames. Nearly, 30-50 flocs were tracked to obtain a statistically significant velocity magnitude profile. It was challenging to track flocs, and to calculate their velocities at locations that had minimum fluid velocity (e.g., stagnant zones).

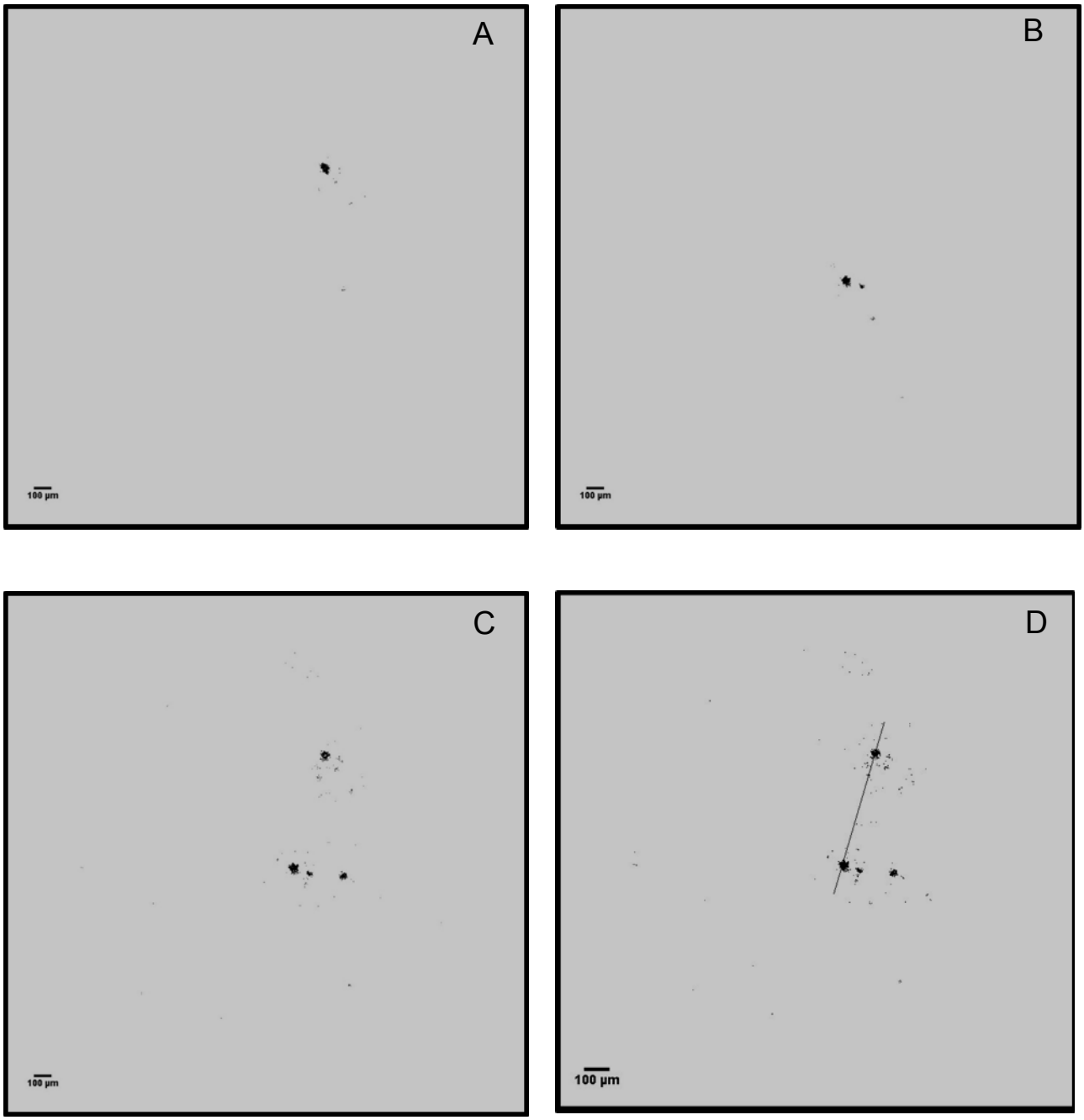

Figure 4.7 Illustration of the relative floc velocity measurement

(A-B) trajectories of a floc aggregate captured using two successive reconstructed holograms (C) superimposing of the two reconstructed holograms to obtain the path travelled by a floc aggregate (D) measurement of the distance travelled.

(Scale: 100 nm)
Note: Flocs appear as dark spots on the lighter background, the background was changed to a lighter color for better visibility.

4.5 Results of Full-Scale Data

4.5.1 Floc Size Distribution

The floc size distribution was evaluated for the thirteen locations in the flocculation tank. Fig. 4.8 illustrates the volume-based floc equivalent diameter measured at one such sampling location (1B in the first flocculation chamber). The value of the median equivalent diameter was 188 µm at this location, with a 90th percentile of 300 µm. Similar information about the floc size distribution was acquired from the data collected at the remaining locations (1M to 6B). Box and whisker plots were used to demonstrate spatial variations in the equivalent floc diameter as shown in Fig. 4.9 (A) and (B). In Fig. 4.9 (A), the data in the section X-X was arranged into four groups (A, B, C and D) with reference to the flow trajectory. Most distributions were positively skewed, with the median equivalent floc diameter varying from 175 to 225 µm at these locations. A log-normal distribution (α=0.01) was a suitable fit for the size distribution of floc aggregates, the finding which is in agreement with earlier studies.[18] Although five sampling locations (i.e., 1B, 2M, 5B, 5M, and 5T) did not fit any of the models tested, including Weibull, log-normal, exponential, and gamma distributions.

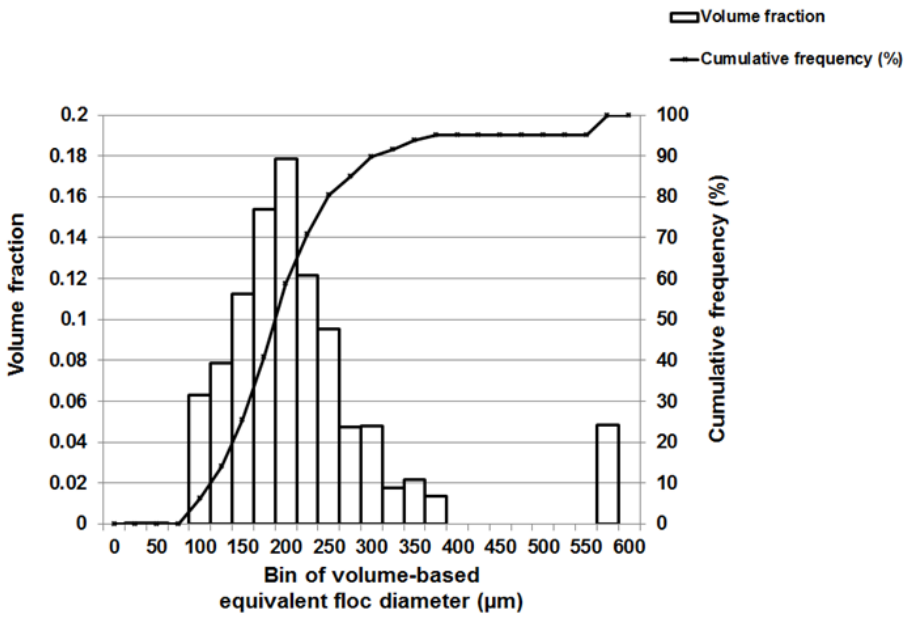

Figure 4.8 Illustration of the floc size distribution (by volume) calculated at the location, 1B, in the flocculation chamber-1.

Levene's test (α=0.05; N >16) was used to assess the variation in floc size distribution within each group; it showed no significant difference in floc aggregate sizes formed in the section X-X, except for locations in Group B (i.e., 2T, 2M and 2B). The spatial distribution of floc size was related to the local velocity of the fluid phase, and the turbulent energy dissipation, as described in previous studies.[14, 28, 29] A detailed description of the predicted velocity distribution for the sections X-X and Y-Y is illustrated in Fig. 4.A (1) in the supplementary information. Initially, flocs followed the trajectory of the main inlet flow stream, which was the main source of mixing intensity for flocs to interact in the hydraulic flocculation tank. The actual floc growth was observed more towards the upper middle and top portions of the tank. A few floc aggregates of larger than 550 μm in diameter, identified as outliers in Fig. 4.9 (A), were prominent in Group A (i.e., 1T, 1M and 1B) and Groups B (i.e., 2T, 2M and 2T). 3M and 4M, situated at the interior of the flocculation tank, had a narrow distribution of floc aggregates with median values between 175 and 200 μm. In these recirculation zones, lower velocities (0 to 0.015 m/s) were observed, causing fewer particle interaction(s) and limiting floc size.

In the last flocculation chamber, a broader distribution of floc sizes ranging from 100 to 750 μm was observed, as shown in Fig. 4.9 (B). This resulted in a heterogeneous floc suspension near the peripheral outflow, with 95% percent of the volume fraction of floc sizes less than or equal to 674 μm.

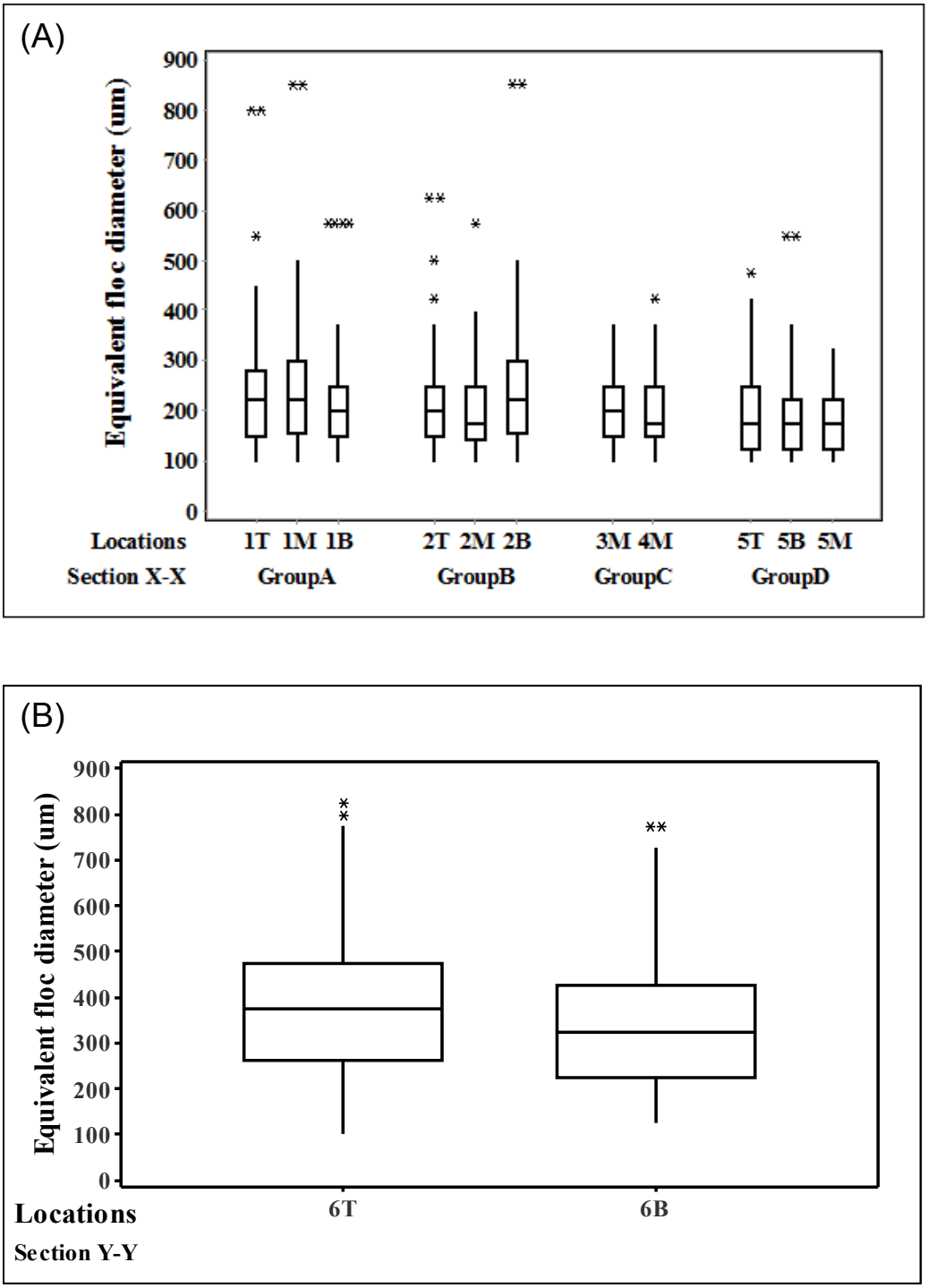

Figure 4.9 Box and whisker plots of the spatial distribution of the volume-based floc equivalent diameter measured at different floc monitoring stations

(A) represents floc sizes formed in chamber-1 and (B) represents floc distribution in chamber-3.

4.5.2 Measurements of Relative Velocity of Floc Aggregates

The relative motion of individual floc aggregate with respect to the fluid motion was tracked using the recorded holograms. As shown in Fig. 4.10, median values of the relative velocity of flocs varied significantly from 0.003 to 0.009 m/s at each location. A jet inflow velocity of approximately 0.1-0.16 m/s near the entrance caused flocs at 1B, 2B and 5B locations to experience a relative floc velocity of up to 0.016 m/s, following the trajectory of the fluid motion. The sampling locations 5B, 5M and 5T in Group D had a clear trend of decreasing values of median floc velocities from 0.007 to 0.004 m/s along the depth. This suggested the upward flow of water to the rest of the tank appeared to reduce the floc velocity at the middle and top locations. But, this trend was not consistent in the sampling locations of Group A and B, which were situated in a high velocity profile location with the local velocity magnitude ranging between 0.03 and 0.08 m/s. These locations (1T, 1M, 1B, 2T, 2M and 2B) had median floc velocities ranging between 0.006 and 0.008 m/s. The low fluid velocity profile of less than 0.015 m/s in the recirculation regions (3M and 4M) had the interquartile relative floc velocities ranging from 0.005 to 0.006 m/s.

The relative motion of flocs calculated from the DIHM analysis was in reasonable agreement with the fluid flow. At large, the predicted fluid velocities (0.02 to 0.055 m/s) from the CFD analysis were approximately an order of magnitude larger than the DIHM calculated particle velocity (0.002 to 0.008 m/s). The variation in the average relative velocity of flocs to the fluid motion is attributable to two possible reasons- (i) the actual plant flow was 86.72 ML/d at the time of floc analysis, which was less than the modelled flow rate of 90 MLD (ii) floc velocities were tracked for a wide range of flocs sizes from 20 to over 500 μm measured in the flocculation chamber. Saffman and Turner[30] found that small agglomerates (<15 μm) in water treatment plants follow the fluid motion completely. The larger floc sizes predominantly found in the flocculation tank exhibited inertia with respect to turbulent flow fluctuations leading to a motion of particles different from that of the fluid, as suggested in Abrahamson's[31] work.

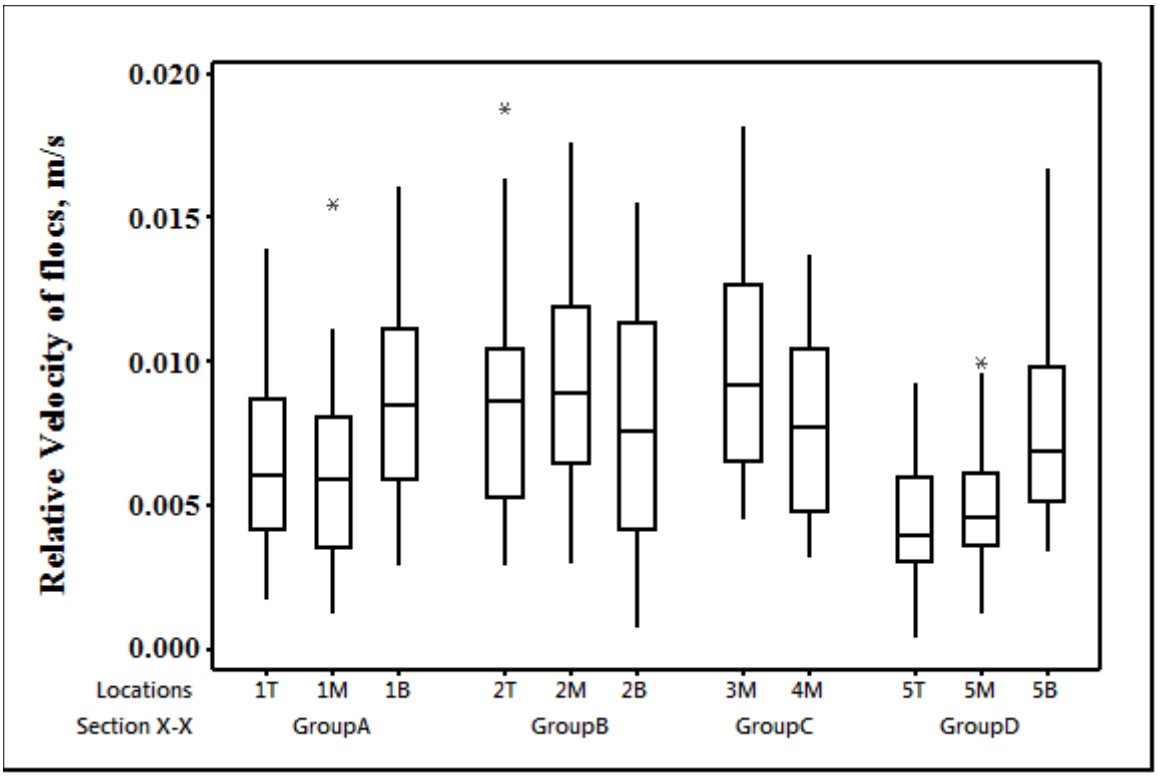

Figure 4.10 Box and whisker plots of the relative velocities of flocs with respect to the fluid motion calculated at the sampling locations in the flocculation chamber-1.

4.6 Practical Implications

The DIHM analysis demonstrated a relatively quiescent condition in the flocculation process, which was in agreement with the earlier CFD findings.[12] Flocs formed in the hydraulic flocculation tank received a limited supply of active mixing in the chambers, aside from the inlet and small openings in weir columns between the chambers. Median floc sizes of 200-225 µm were formed in the regions that had the local velocity range of 0.035 to 0.07 m/s. Flocs that were entrained in the recirculation region in locations 3M and 4M of high residence time[12] had a narrow distribution of floc aggregates. These regions are recognized to contribute less to floc sizes in the peripheral outflow and are thus less connected to the solid-liquid separation processes (e.g., sedimentation, filtration).[14] Approximately 25% of volume fractions of floc sizes measured near the outflow in the present study was larger than 500 µm. As a consequence, bulky and irregular shaped floc aggregates represented the overall floc morphology in the hydraulic flocculation tank.

In direct filtration, as the entire solid-liquid separation takes place in the filter itself, the floc size is an important operational parameter.[32] Filter beds in direct filtration processes are designed with a large floc holding capacity[8] that can retain a considerable volume of floc sizes larger than the effective filter pore size. Alternatively, fine flocs sizes of the order of 1 μm are not readily captured by typical filter grains.[33] Their small sizes are more likely to bypass the filters along with the treated effluent, which can pose potential risks to the drinking water quality. The volume equivalent floc diameter measured in the flocculation tank was larger than the optimum sizes recommended in the literature. For instance, the simulation results of Ngo et al.[32] indicated that a mean floc diameter of 62 μm was the optimal size for direct filtration. Similar results by Pivokonsky et al.[9] demonstrated that small, highly compact and regular aggregates of most probable diameter of 50 μm displayed the best filterability. In the present case, over 98% of the particle count near the peripheral outflow was tied to flocs larger than 100 μm.

The open structure of large floc aggregates can have adverse impacts on the performance of a direct filtration process. Such floc structures are susceptible to breakage during transportation through the floc tunnel to the filtration unit, potentially leading to filter performance issues such as turbidity breakthrough. Jarvis et al.[19] showed consistent decrease in floc sizes in three different floc suspensions when exposed to increased rotational speeds, with little re-growth potential after the breakage. Large floc sizes can also reduce the effective filter run times in a direct filtration plants. Pivokonsky et al.[9] showed that a high proportion of large (i.e., 155-1330 μm) floc aggregates formed during coagulation/flocculation processes caused a high pressure drop in deep-bed filtration and thereby, significantly shortened filter run time.

4.7 Conclusions

This study demonstrated the applicability of the submersible digital in-line holographic microscopy (DIHM) technique for the measurement of the spatial distribution of floc sizes in full-scale flocculation tanks. The spatial distribution of floc sizes indicated that the volume equivalent floc diameter measured in the flocculation tank was mostly large-sized aggregates of greater than 100 μm, which was larger than the optimum floc size (~50 μm) recommended for direct filtration by other studies (e.g., Pivokonsky et al.[9]). In direct filtration, large flocs can

quickly cover the top surface of the filter media, reducing the effective use of the entire media depth. Practical issues of operating at such conditions in a direct filtration facility are rapid clogging of filters, resulting in excessive backwashing due to a high rate of head loss development.

The performance of a hydraulic flocculation tanks was evaluated using in-line measurements of floc size distributions, which is otherwise difficult to characterize in treatment plant with respect to the prevailing turbulent flow. The motion of individual floc aggregate tracked in the DIHM showed relative velocities ranging from 0.002 to 0.008 m/s. At large, the velocity magnitude of fluid motion (0.02 to 0.055 m/s) from the CFD predictions was approximately an order of magnitude larger than the DIHM calculated particle velocity. Regularly acquiring critical information on the type of flocs formed in flocculation can assist water utilities to take corrective actions (e.g., adjust coagulant dosage, pH, mixing) to improve filter performance. The information from this study is important for understanding the fate and transport of flocs during the flocculation process for process optimization that can lead to minimize chemical and energy usage in treatment plants. The ability of DIHM to measure particles sizes and to compute the relative particle velocities is likely to contribute to the advancement of new technologies for the water and wastewater industry in other environmental applications (e.g., algal, microbial detections).

4.8 Acknowledgements

The authors acknowledge the support of the Natural Sciences and Engineering Resource Council of Canada (NSERC) and 4deep Inwater Imaging through an NSERC Engage Grant, as well the financial support of both NSERC and Halifax Water through the NSERC/Halifax Water Industrial Research Chair program. The authors also acknowledge the technical and in-kind support of Dr. Manfred H. Jericho, Stefan Jericho and John Samson from the department of Physics at Dalhousie University during the initial design and implementation phase of the study. The authors also thank the J.D. Kline water supply plant authority, Nova Scotia, Canada for providing access to conduct sample collections in the hydraulic flocculation tanks.

4.9 Bibliographic References & Notes

1. J. K. Edzwald, *Water Science and Technology*, 1993, **27**, 21-35.

2. J. M. Duan and J. Gregory, *Advances in Colloid and Interface Science*, 2003, **100**, 475-502.

3. J. Bridgeman, B. Jefferson and S. Parsons, *Chemical Engineering Research & Design*, 2008, **86**, 941-950.

4. S. H. Kim, B. H. Moon and H. I. Lee, *Microchemical Journal*, 2001, **68**, 197-203.

5. R. D. Letterman, A. Amirtharajah and C. R. O'Melia, *Coagulation and flocculation.*, American Water Works Association, McGraw Hill,New York, 5th edn., 1999.

6. I. G. Droppo, G. G. Leppard, D. T. Flannigan and S. N. Liss, *Water Air and Soil Pollution*, 1997, **99**, 43-53.

7. AWWA, *Operational control of coagulation and filtration processes*, American Water Works Association, Denver, CO, 2nd edn., 2000.

8. AWWA and ASCE, *Mixing, coagulation, and flocculation.*, McGraw Hill, American Water Works Association and American Society of Civil Engineering, New York, 5th edn., 2012.

9. M. Pivokonsky, P. Bubakova, L. Pivokonska and P. Hnatukova, *Environmental Technology*, 2011, **32**, 1355-1366.

10. B. Gorczyca and J. Ganczarczyk, *Water Quality Research Journal of Canada*, 1999, **34**, 653-666.

11. A. J. Manning and K. R. Dyer, *Marine Geology*, 1999, **160**, 147-170.

12. Y. S. Vadasarukkai, G. A. Gagnon, D. R. Campbell and S. C. Clark, *Journal American Water Works Association*, 2011, **103**, 66-80.

13. D. C. Hopkins and J. J. Ducoste, *Journal of Colloid and Interface Science*, 2003, **264**, 184-194.

14. K. Samaras, A. Zouboulis, T. Karapantsios and M. Kostoglou, *Chemical Engineering Journal*, 2010, **162**, 208-216.

15. M. C. Kavanaugh and J. O. Leckie, *Particulates in water: characterization, fate, effects, and removal.*, American Chemical Society, Washington D.C., 1980.

16. B. Gorczyca and J. Ganczarczyk, *Environmental Technology*, 1996, **17**, 1361-1369.

17. B. Gorczyca and P. Klassen, *Water Quality Research Journal of Canada*, 2008, **43**, 239-247.

18. D. H. Li and J. Ganczarczyk, *Research Journal of the Water Pollution Control Federation*, 1991, **63**, 806-814.

19. P. Jarvis, B. Jefferson and S. Parsons, *Water Science and Technology*, 2004, **50**, 63-70.

20. M. A. Yukselen and J. Gregory, *International Journal of Mineral Processing*, 2004, **73**, 251-259.

21. R. J. Gibbs and L. N. Konwar, *Environmental Science & Technology*, 1982, **16**, 119-121.

22. A. L. de Oliveira, P. Moreno, P. A. G. da Silva, M. De Julio and R. B. Moruzzi, *Desalination and Water Treatment*, 2015, 1-12.

23. R. K. Chakraborti, J. F. Atkinson and J. E. Van Benschoten, *Environmental Science & Technology*, 2000, **34**, 3969-3976.

24. J. Garcia-Sucerquia, W. B. Xu, S. K. Jericho, P. Klages, M. H. Jericho and H. J. Kreuzer, *Applied Optics*, 2006, **45**, 836-850.

25. J. Sheng, E. Malkiel and J. Katz, *Applied Optics*, 2006, **45**, 3893-3901.

26. A. K. Stoddart and G. A. Gagnon, *Journal American Water Works Association*, 2015, **107**, E638-E647.

27. K. Nakamura, H. J. Kreuzer and A. Wierzbicki, *Quantum Control and Measurement*, 1993, 271-276.

28. D. L. Marchisio, R. D. Vigil and R. O. Fox, *Chemical Engineering Science*, 2003, **58**, 3337-3351.

29. O. P. Prat and J. J. Ducoste, *Chemical Engineering Science*, 2006, **61**, 75-86.

30. P. G. Saffman and J. S. Turner, *Journal of Fluid Mechanics*, 1956, **1**, 16-30.

31. J. Abrahamson, *Chemical Engineering Science*, 1975, **30**, 1371-1379.

32. H. H. Ngo, S. Vigneswaran and H. B. Dharmappa, *Environmental Technology*, 1995, **16**, 55-63.

33. J. Gregory, *Filtration & Separation*, 1998, **35**, 367-371.

4.A Supplementary Information

The data on the distribution of predicted velocity magnitude for the sections X-X and Y-Y at 90 ML/d was extracted from the previous study (Vadasarukkai et al.[9]) using the post-processing tool in ANSYS-FLUENT. As illustrated in Figure A1, it was evident that the spatial distribution of velocity magnitude was non-uniform. A local increase in velocity magnitude of approximately 0.1 - 0.16 m/s was observed closer to the inlet. A decreasing trend in the velocity magnitude was observed as moved towards the upper portion of the tank; the predicted velocity was at minimum closer to wall locations due to the no slip boundary condition. Recirculation region was observed largely in the interior, and to some extent close to the inlet in the first flocculation chamber as shown in Fig. A(1). Section Y-Y had an overall velocity magnitude less than 0.05 m/s.

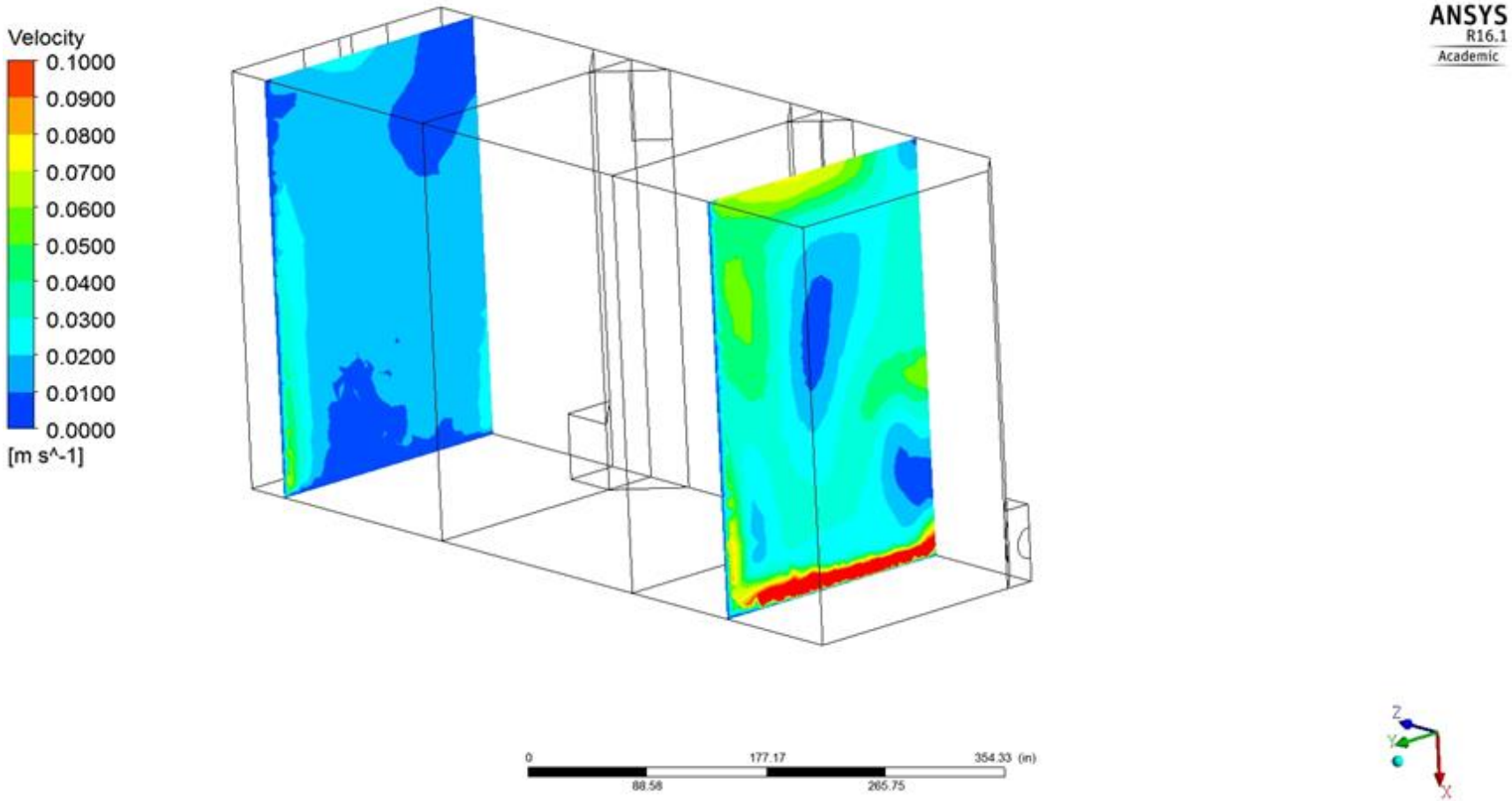

Figure 4.A(1) Contour of the predicted velocity magnitude for sections X-X and Y-Y in the flocculation chambers-1 and 2 at a plant inflow rate of 90 MLD.

Chapter 5 Application of Low- Mixing Energy Input for the Coagulation Process[2]

5.1 Abstract

Rapid-mixing tanks with mechanical mixers are a common design used in treatment plants. Yet, the role of such rapid-mixing systems on the effectiveness of the coagulation performance is unclear. This study looked at optimizing the direct energy used in the coagulation process for removal of natural dissolved organic matter (DOM). The role of coagulation mixing intensity (G-value) on total organic carbon (TOC) and turbidity removal was examined for the water types with high organic content, with a specific ultraviolet absorbance (SUVA) of at least 2-2.5 units of m^{-1} of absorbance per mg/L. A standard jar test using ferric sulfate coagulant was performed to optimize the chemical condition in coagulation for removal of dissolved organics as well as particles. The jar test analysis at an acidic pH (4.5 ± 0.3) required an iron dose <0.3 mM to arrive at an optimal coagulant concentration and resulted in above 75% of TOC removal. The influence of coagulation mixing on TOC and turbidity removal was evaluated at G varying from 0 to 1500 s^{-1} at the optimized coagulant dose and pH conditions for enhanced coagulation. In this study, a combined effective removal of TOC and turbidity was achieved at a low-mixing intensity range of 110 s^{-1} < G < 450 s^{-1}. Coagulation operated at G greater than 450 s^{-1} showed negligible improvement in TOC removal. Minimizing energy consumption in enhanced coagulation is feasible at the proposed mixing intensity range (i.e., 110 s^{-1} < G < 450 s^{-1}), without sacrificing the effectiveness of DOM removal by coagulation. These findings represent an opportunity for energy savings for the water industry without sacrificing quality.

Keywords: coagulation; mixing intensity; dissolved organic matter; energy optimization

---

[2] **Vadasarukkai, Y.S**., and Gagnon, G.A. (2015). Application of low-mixing energy input for the coagulation process. Water Research. **84**, 333-341

5.2 Introduction

The water sector relies highly on energy-intensive processes to provide safe drinking water and reliable wastewater services to their customers (Leiby and Burke, 2011). Energy consumption in the water and wastewater utility accounts for approximately one-third of a city's total energy bill (USEPA, 2008), and by 2023 energy demand is estimated to increase by 20% due to projected population growth and more stringent water quality regulations (USEPA, 2008). There are ways to reduce the energy consumption of water utility operations. One example is the modification of several processes at the Metropolitan Syracuse Wastewater Treatment Plant (New York), including retrofitting motors and upgrading impellers, that resulted in improved energy efficiency and an annual electricity savings of about 2.8 million kWh (EERE, 2005). Therefore, a thorough assessment of the energy performance of water treatment processes is important to optimize system efficiency and to achieve gains in energy conservation.

Energy usage in the water sector can be quantified in terms of power and cost per unit volume of treated water. Previous research on the David L.Tippin water treatment plant in Tampa, Florida (Santana et al., 2014) quantified the energy consumed at that facility through the calculation of the operational embodied energy. The authors defined it as the sum of the direct and indirect energies used exclusively during the operation and maintenance life stage. Direct energy is mostly related to the onsite consumption of fuel and electricity for pumping and process operations. It amounts to the use of high service pumps for transportation of water in and out of the treatment plant, power associated with mixing of motors and impellers, operation of processes (e.g. ozonation), and other equipment used onsite on a daily basis. The authors (Santana et al., 2014) estimated about 62.9% of the total operational embodied energy was primarily the direct consumption of energy at the plant. The remaining 37.1% was indirect energy associated with the chemicals used in the treatment process.

The direct energy used in treatment plants is the largest contributor of the embodied energy. The current study examines one such application of direct energy in the coagulation process for removal of natural dissolved organic matter (DOM). Coagulation is a critical process used commonly in the surface treatment plants and facilitates the reduction of turbidity, pathogens, dissolved organic matter and inorganic particles from drinking water (Davis and Edwards, 2014).

Humic substances, the major class of organic compounds in natural waters, comprise higher than 50% of dissolved organic carbon (Thurman, 1985). The removal of DOM during drinking water treatment is significantly important for water utilities due to the potential health risks associated with the formation of chlorinated disinfection byproducts (Amirtharajah et al., 1993). Presence of DOM in potable water is also linked to aesthetic issues, increased oxidant demand, membrane fouling, corrosion, and bacterial regrowth in the distribution systems (Davis and Edwards, 2014; Owen et al., 1995). Coagulation is often optimized to provide a substantial removal of DOM as well as particles (Volk et al., 2000). This process of application of effective coagulant doses to minimize residual DOM after coagulation in drinking water supplies is termed as enhanced coagulation (Xie et al., 2012).

Removal of DOM in coagulation occurs either by charge neutralization or by adsorption on precipitated metal hydroxide (Duan and Gregory, 2003). The primary mechanism of DOM removal is strongly related to the concentration of DOM, the coagulant dose and pH that controls the speciation of coagulant metal salts (Dempsey et al., 1984). Cationic hydroxyl species of aluminum or iron-based coagulants are predominant at pH less than 6.0 (Amirtharajah et al., 1993; Amirtharajah and Mills, 1982). In charge neutralization mechanism, the cationic species are suggested to chemically react with the soluble humic anions and give rise to strong association of complexes that form precipitation (Narkis and Rebhun, 1977). Alternatively, the rate of amorphous metal hydroxide precipitates is favored at pH greater than 6.0 and at a relatively high coagulant dose (> 0.03 mM as Fe or 0.05 mM as Al) (Jiang and Graham, 1998). This mechanism of rapid precipitation of metal hydroxides at a sufficient metal coagulant dose is referred as sweep-floc coagulation (Edzwald, 2013). Under such conditions, adsorption of DOM complexes on metal hydroxide precipitates and/ direct adsorption of DOM onto the surface of precipitates is proposed to play a major role in removal of humic substances (Van Benschoten and Edzwald, 1990; Dempsey et al., 1984).

Rapid (or flash) mixing is used in coagulation to uniformly disperse the coagulant with the incoming water and to promote subsequent collision rates between the charge neutralized particles. Further aggregation of such particles is promoted in a flocculation stage to form large floc aggregates, which are removed from drinking water in subsequent solid-liquid separation

processes (e.g. sedimentation/flotation, filtration) (Jiang and Graham, 1998). Design guidelines call for an intense mixing during coagulation with an average mixing intensity, measured as G-value, of 600 - 1000 s^{-1} and a short detention time of 10-60 s (AWWA-ASCE, 2012). The Ten State Standards (2012) recommends a maximum detention time 30 s with mixing equipment capable of imparting a minimum G of at least 750 s^{-1}. However, previous research suggests such a high-intense mixing operation is not necessary for the coagulation mechanism by precipitation (Edzwald, 2013; Amirtharajah and Mills, 1982). Amirtharajah and Mills (1982) found a low G of 300 s^{-1} made no significant differences in the settled water turbidity as that of operating at a high G of 750 s^{-1} for the optimal sweep-floc coagulation. Edzwald (2013) showed a reduction of one-tenth in power costs with the incorporation of low-mixing operations, which suggests that the size of rapid mixing tanks should be based on average daily flow rather than the maximum plant design flow.

Extensive research has focused on DOM removal by enhanced coagulation; there is a little understanding as to how a change in the coagulation mixing may influence the removal of humic substances. Siéliéchi and colleagues (2008) showed a drastic decrease in sediment volumes under low mixing intensity, suggesting the shrinkage of the humic/hydrolyzed-iron complexes. In the current study, the pH and coagulant dose were predetermined using jar test analysis to optimize the removal of total organic carbon (TOC), a surrogate parameter measured to quantify DOM removal. At the optimized coagulant dose and pH conditions for enhanced coagulation, we investigated the role of coagulation mixing on TOC removal at a range of G-values. This study focuses on minimizing the direct energy consumption in coagulation by determining the feasibility of using low-mixing intensity, without compromising the removal efficiency of DOM by enhanced coagulation.

5.3 Materials and Methods

5.3.1 Water Source

Two water types were used in the coagulation experiments: synthetic humic water and raw water from a lake source. Both waters have a high organic content, with a specific ultraviolet

absorbance (SUVA) of at least 2-2.5 units of m^{-1} of absorbance per mg/L. Detailed characterization of the water quality parameters for the two source water is outlined in Table 5.1.

5.3.1.1 Preparation of the Synthetic Humic Water

Commercially available humic acid, sodium salt (containing 50-60% as humic acid) was purchased from Alfa Aesar (Haverhill, Massachusetts). Elemental analysis of humic acid in the ECS 4010 CHNSO analyzer (Costech Analytical Technologies Inc., Valencia, California) indicated of the composition of 38.4% carbon (C), and 0.73% nitrogen (N). For the purposes of this study, hydrogen (H) was not analyzed. A stock solution was prepared by dissolving 0.030 g of humic acid in a liter of deionized (DI) water to produce a TOC concentration of (8.75± 0.64) mg/L. Alkalinity was introduced by adding 20 mg/L of 1 N sodium bicarbonate to the stock solution. The prepared stock solution was continuously mixed using a magnetic stirrer for approximately 2 hours prior to the start of the experiment.

5.3.1.2 Freshwater Source

Approximately 30 L of raw water was collected from the intake at the Louisbourg water treatment plant (Nova Scotia, Canada). The plant withdraws raw water from Kelly Lake, a protected watershed area located approximately a kilometer from the water treatment plant. The plant has a capacity of three million liters per day (MLD).

5.3.2 Chemicals Used in the Coagulation Process

Ferric sulfate, MP Biomedicals (Fisher Scientific, Pittsburgh, Pennsylvania) was used as the coagulant. Fresh stock solution of 1 g/L of ferric sulfate was prepared prior to the coagulation and flocculation experiments. The stock solution was replaced every day to minimize aging or any metal precipitation. The concentration of iron in the stock solution was measured as 5 mM of iron (Fe), according to the Standard Method 3125 (APHA, 2012). Stock solutions of 0.2 N nitric acid and 1 M sodium hydroxide were used to adjust the pH to the desired pH condition.

Table 5.1 Summary of the water quality characteristics of (a) Synthetic humic water and (b) Raw lake water from Louisbourg water treatment plant (Nova Scotia, Canada).

Water Type	pH	Turbidity (NTU)	UV_{254} (cm^{-1})	TOC (mg/L)	DOC (mg/L)	SUVA (L/mg m)	Colour (Pt-Co)	Sulfate (mg/L)	TIC (mg/L)	ZP (mV)	Total Fe (mg/L)
Synthetic humic water	7.66 (0.35)	6.88 (0.02)	0.538 (0.02)	8.75 (0.64)	6.51 (0.11)	8.27 (0.03)	392	6	0.51	-57 (0.78)	ND
Raw lake water [a]	6.02 (0.32)	0.43 (0.12)	0.146 (0.02)	3.80 (0.32)	3.63 (0.31)	4.02 (0.18)	> MLD	ND	0.60	-24 (0.42)	0.06 (0.002)

[a] Data represents the average water quality parameters for the raw lake water from June to October, 2014

()-Parentheses give standard deviation of the data

MLD- true colour of the sample was greater than the maximum detectable limit of 500 Pt-Co units in the HACH DR 5000 UV/Vis spectrophotometer (Hach Company, Loveland, Colorado).

ND- iron concentration and sulfate concentration of the samples was below the detection lime of 0.006 mg/L in the inductively coupled plasma-mass spectrometry (ICP-MS) (Thermo Scientific XSeries II ICP-MS, Waltham, Massachusetts) and 0 mg/L in the HACH DR 5000 UV/Vis spectrophotometer (Hach Company, Loveland, Colorado), respectively.

$$\mathrm{SUVA} = \frac{\mathrm{UV}_{254}(\mathrm{cm}^{-1}) \times 100}{\mathrm{DOC(mg/L)}}$$

5.3.3 Jar Test Apparatus

The coagulation and flocculation experiments were conducted at room temperature (21 ± 1°C) in a 1-L square beaker using a variable speed jar tester (Phipps & Bird, Richmond, Virginia) and a compact digital mixer (Cole-Parmer, Vernon Hills, Illinois). The digital mixer was used to rapidly mix the water sample during the coagulation process, which had a mixing capacity ranging from 50 to 2500 rpm. The coagulated water was transferred soon after the rapid mixing process to the variable speed jar tester to achieve the slow stirring phase in flocculation. The sampling tap provided in the square beaker was used as the outlet, which was positioned at approximately 10.3 cm from the water level. A flat paddle impeller (76 x 25 mm) was used to facilitate the mixing process. The center of the impeller was positioned at approximately $1/3^{rd}$ the height of the beaker. The impeller was set to rotate at a specific rotational speed and the corresponding G-value was determined from the laboratory velocity gradient calibration chart (G-curve) of Cornwell and Bishop (1983).

5.3.4 Determination of the Zero Point Charge (pH_{zpc}) and Coagulant Dose for Enhanced Coagulation

Preliminary experiments were conducted on the synthetic humic water samples to determine the point of zero charge, which corresponds to a pH value having no net surface charges. A multiple purpose autotitrator (MPT-2, Malvern Instruments Ltd., Worcestershire, UK) was connected to the Zetasizer Nano series (Malvern Instruments Ltd., Worcestershire, UK) to measure the surface charge of the water samples over a pH range of 2.5 to 8.5 at 25°C. Ferric sulfate dose was varied from 0.2 to 0.7 mM as Fe to determine the optimal pH_{ZPC}. A calibrated pH probe was used to record the pH reading during the titration sequence. Three titrants of 0.25 M sodium hydroxide, 0.25 N and 0.5 N hydrochloric acid were used to adjust the pH. Samples were initially adjusted to an acidic pH of 2 and the zeta potential was automatically measured for every 0.2 unit increment in pH until the value reached to a pH of 8.0 ± 0.5.

Jar test experiments were conducted to determine the optimal coagulant dose for both the source waters at the selected pHs. The coagulant dose was varied in each experiment at the chosen pH value. The coagulation experiment was initiated by rapidly agitating the suspension at an

arbitrary G of 175 s^{-1} for 1.5 min, followed by a low-mixing intensity of 46 s^{-1} at 50 rpm to facilitate flocculation process for 20 min. At the end of mixing, a quiescent period of 60 min, with a calculated overflow rate of 0.17 cm/min, allowed the floc aggregates to settle. During the initial start of rapid mixing, a known dose of coagulant and a calculated volume of pH adjusting chemicals were added simultaneously into the eye of the mixer. A 180 mL of sample was collected from the outlet of the jar test beaker at the end of the rapid mixing and settling period. The optimal coagulant concentration (OCC) was considered as that the coagulant dose at which there was maximum removal of total organic carbon (TOC). Other water quality parameters including residual turbidity, total metal concentration, UV absorbance (at 254 nm) in the settled water were benefitted or remained unaltered at that OCC.

5.3.5 Determination of the Influence of Mixing Intensity on the Coagulation Performance

To investigate the influence of mixing intensity on the coagulation performance, the rapid mixing process was varied using the compact digital mixer from a G of 0 to 1500 s^{-1} for 1.5 min at the predetermined chemical conditions for enhanced coagulation. The coagulation and flocculation experiments were carried out using the procedure described in Section 2.4, except the flocculation of aggregates was kept at a constant, low G of 6 s^{-1} at 10 rpm for 20 min. The coagulated water was transferred immediately to the variable speed jar tester to achieve the slow mixing at 6 s^{-1}. Samples of 180 mL were collected soon after at the end of rapid mixing and settling periods.

5.3.6 Calculation of Energy Usage in the Coagulation Process

In treatment plants, energy is continuously transmitted to a unit volume of water at a constant rate (power) over a period of time. The direct energy associated with the coagulation process is expressed in kilowatt-hours, which was calculated as the product of power supplied in kilowatts and the time in hours. In this study, the root mean square velocity gradient (G-value) was used to determine the average power supplied by the mechanical mixer to stir a unit of volume of water, as given in Equation 5.1.

$$\mathbf{G} = \left(\frac{\varphi_m}{\mu}\right)^{0.5} = \left(\frac{\mathbf{P}}{\mu \mathbf{V}}\right)^{0.5} \tag{5.1}$$

Here, φ_m is the mean value of the work input per unit of time per unit of volume (J s^{-1} m^{-3}), P is the power transferred to the water in a mixing tank (J s^{-1}), μ is the dynamic viscosity of water (kg $m^{-1}s^{-1}$), and V is the volume of a mixing tank (m^3).

The V in Equation 5.1 is calculated as the product of plant flow rate in m^3 s^{-1} and the hydraulic retention time in seconds. It is assumed the mechanical mixer is operated for 24 hours with a motor efficiency of 85%. A water temperature of 15°C, a 20 s of retention time in the rapid mixing tanks, and a power cost of $0.12 per kW-h is used as the plant design conditions (Edzwald, 2013).

5.3.7 Analytical Methods

Both the samples collected at the end of rapid mixing and settling periods were analyzed for the following water quality parameters.

5.3.7.1 General Water Quality Parameters

All methods, unless otherwise stated, were conducted according to the procedure described in the Standard Methods (APHA, 2012). The pH measurements were taken using an Accumet electrode and Accumet Excel XL50 (Dual channel pH/ion/conductivity) meter (Fisher Scientific, Singapore), and calibrated using standard buffer solutions to three sets of calibration points (i.e. pH of 4, 7 and 10). Residual turbidity was measured using a HACH 2100AN laboratory turbidimeter (Hach Company, Loveland, Colorado). Total organic and inorganic carbon (TOC and TIC) were analyzed using a TOC analyzer (Shimadzu Corporation, Kyoto, Japan). The TOC samples were poured into a 50 mL headspace free glass vial, and acidified to a pH below 2 with phosphoric acid. No acid was added to the TIC samples. Sample vials were capped and stored at 4°C until analysis. All the metal samples were acidified to a pH below 2 using nitric acid, TraceMetal™ Grade (Fisher Scientific, Pittsburgh, Pennsylvania), and the samples were digested for 2 hours. The cooled, acidified samples were then measured for the total iron concentration using the inductively coupled plasma-mass spectrometry (ICP-MS) (Thermo Scientific XSeries II ICP-MS, Waltham, Massachusetts), having a detection limit of 0.68 µg/L for iron.

UV absorbance at 254 nm wavelength (UV_{254}) was measured using a HACH DR 5000 UV/Vis spectrophotometer (Hach Company, Loveland, Colorado). The concentration of sulfate was measured using SulfaVer 4 method (Hach, 2005) at 450 nm wavelength, and the true colour was measured using the platinum cobalt method (Hach, 2005) at 455 nm wavelength using a HACH DR 5000 UV/Vis spectrophotometer (Hach Company, Loveland, Colorado). The maximum detection limit was 70 mg/L and 500 Pt-Co units for sulfate and colour, respectively. Samples were filtered through a 0.45 μm polysulfone filter membrane (GE Water & Process Technologies, Trevose, Pennsylvania) to remove any suspended solids prior to the UV_{254}, sulfate, and colour analyses.

5.3.7.2 Zeta Potential Measurements

Conductivity and zeta potential of the samples was measured using the Zetasizer Nano series at 25°C. The zeta potential was calculated by determining the electrophoretic mobility of the particles using Laser Doppler Velocimetry (LDV) and then applying the Henry equation with 1.5 as the Smoluchowski approximation. The zeta potential was measured at various stages of the jar test analysis; samples were collected and analyzed immediately at the end of rapid mixing and settling periods. Triplicate measurements were performed on the unfiltered samples for the zeta potential analysis.

5.4 Results and Discussion

5.4.1 Determination of the Zero Point of Charge (pH_{zpc})

Fig. 5.1 illustrates the zeta potential measurements of the synthetic humic water as a function of pH. The synthetic humic water was highly stable for pH ranges between 2.5 and 8.5. The raw water was characterized by an overall net negative surface charge of approximately -40 mV at a pH 2.6 and -58 mV at a pH 8.6 without any coagulant dose. However, with the addition of coagulant, the zeta potential shifted to a more positive value for pH below 4.5, and had a net negative surface charge for pH above 7.0 (as indicated in Fig. 5.1). This obvious trend of compression of the electrostatic potential between the particles with the addition of a cationic coagulant is noted elsewhere in the literature (Davis and Edwards, 2014).

The point of zero charge (pH_{ZPC}) was determined as 4.7, 5.2 and 6.6 in correspondence to the iron doses of 0.26, 0.47, 0.66 mM as shown in Fig. 5.1. The observed pH_{ZPC} values were within the pH of 4.5 to 7.0 at the coagulant doses examined. In line with the zeta potential findings of this study, and in comparison with the equilibrium-solubility diagram of Fe(III) (Amirtharajah et al., 1993), this study used an acidic pH of 4.5 ± 0.3 and a near neutral pH of 6.7 ± 0.3 as the preferred pH ranges to ensure both the charge neutralization and sweep-floc coagulation mechanisms were examined.

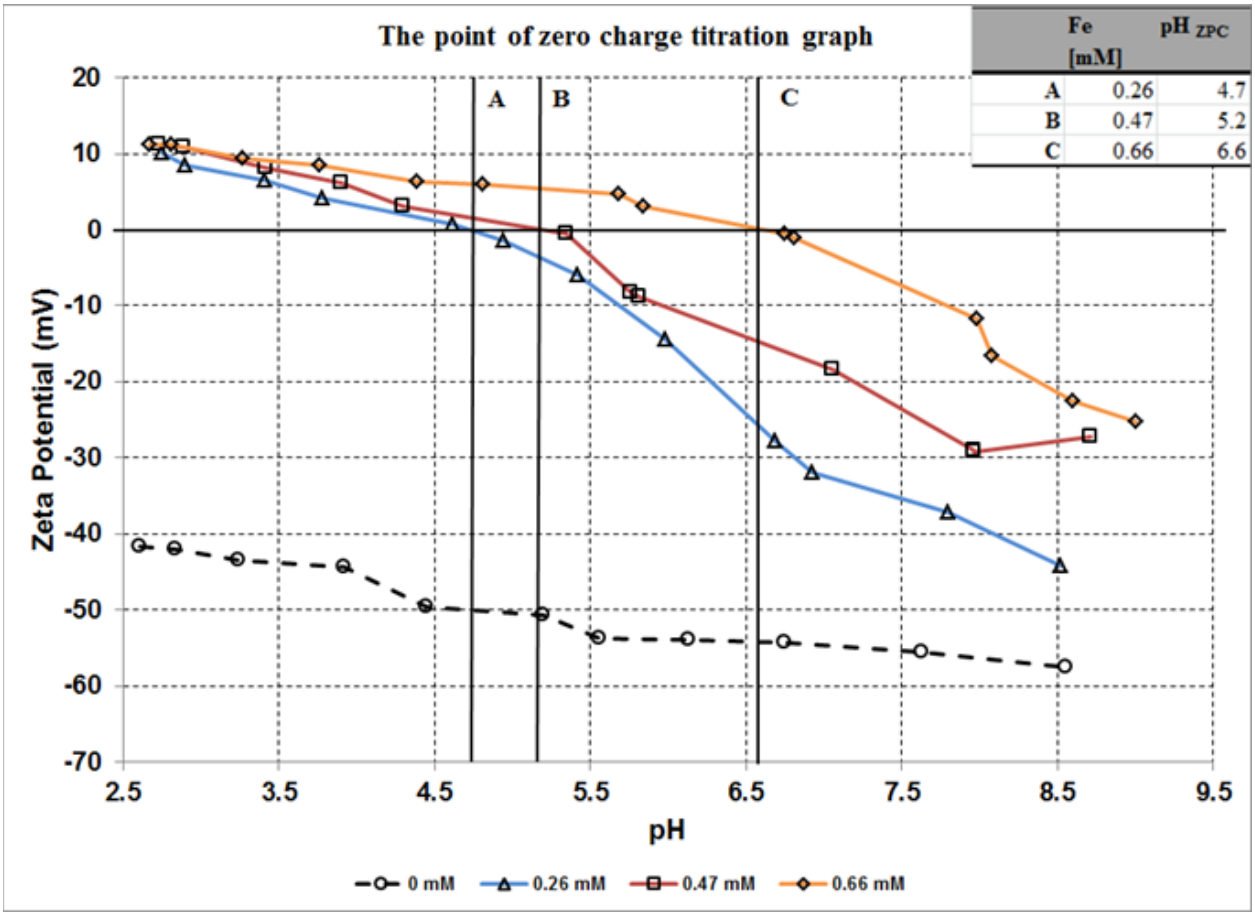

Figure 5.1 Variations in the zeta potential of synthetic humic water as a function of pH at ferric sulfate doses of 0 mM, 0.26 mM, 0.47 mM, and 0.66 mM as Fe.

pH_{ZPC}- the zero point of charge indicated by solid black line
A,B,C- represents the pH values of 4.7, 5.2 & 6.6 exhibiting the zero point of charge (pH_{ZPC})

5.4.2 Determination of the Optimal Coagulant Concentration (OCC)

Jar test data indicated a good correlation between the settled water turbidity and total iron concentration for the synthetic humic water (Fig. 5.2a and 5.2c). At low coagulant doses as illustrated in Fig. 5.2a and 5.2c, the hydrolysis of iron and the formation of humic-hydrolyzed Fe complexes caused a peak increase in both the residual turbidity and iron concentration. However, with further increase in the coagulant dose, there was a steep decline in both the parameters, signifying the formation of settleable aggregates. This dose (as shown by dotted line in Fig. 5.2) was selected as the optimal coagulant concentration (OCC), wherein the fraction of TOC, residual turbidity, and the total iron concentration reached a minimum in the settled water. At a coagulant dose beyond 0.8 mM as Fe, a restabilization zone was observed in Fig. 5.2a by a sharp increase in the residual turbidity from 0.48 to 4.3 NTU. This zone was more pronounced for the experiments conducted at the acidic pH, which is also documented in other studies (Siéliéchi et al., 2008; Amirtharajah et al., 1993).

As shown in Fig. 5.2b at the acidic pH of 4.5 ± 0.3, the zeta potential was near -2.5 ± 0.7 mV at the OCC of 0.26 mM as Fe. In this experimental condition, a possible combination of charge neutralization and adsorption on amorphous precipitates was considered as mechanisms responsible for the removal of humic substances. At higher iron dose of > the OCC of 0.26 mM as Fe, an asymptotical effect of zeta potential in Fig. 5.2b implied that adsorption on hydroxide precipitates was the dominant coagulant mechanism (Duan and Gregory, 2003). As shown in Fig. 5.2d, the zeta potential was -30.2 ± 2.5 for the coagulation experiments conducted at the near neutral pH of 6.7 ± 0.3 under a high iron concentration of 0.47 mM. Angelico et al. (2014) suggest the negative charge generation of Ferrihydrite-humic acid co-precipitates was attributed to the dissociation of the phenolic group at neutral-alkaline pH. In this current study, the negative surface charge did not seem to have an adverse effect on the turbidity and organics removal as shown in Fig. 5.2c and 5.2d. Duan and Gregory (2003) mentioned sweep-floc coagulation to influence dissolved organics removal at a sufficiently high ratio of coagulant dose to TOC concentration (i.e. > 1.0 mg of metal/mg of TOC), which was the case for the experiments conducted at the near neutral pH in the present study. The removal of humic substance under these conditions was entirely by adsorption on precipitated hydroxide.

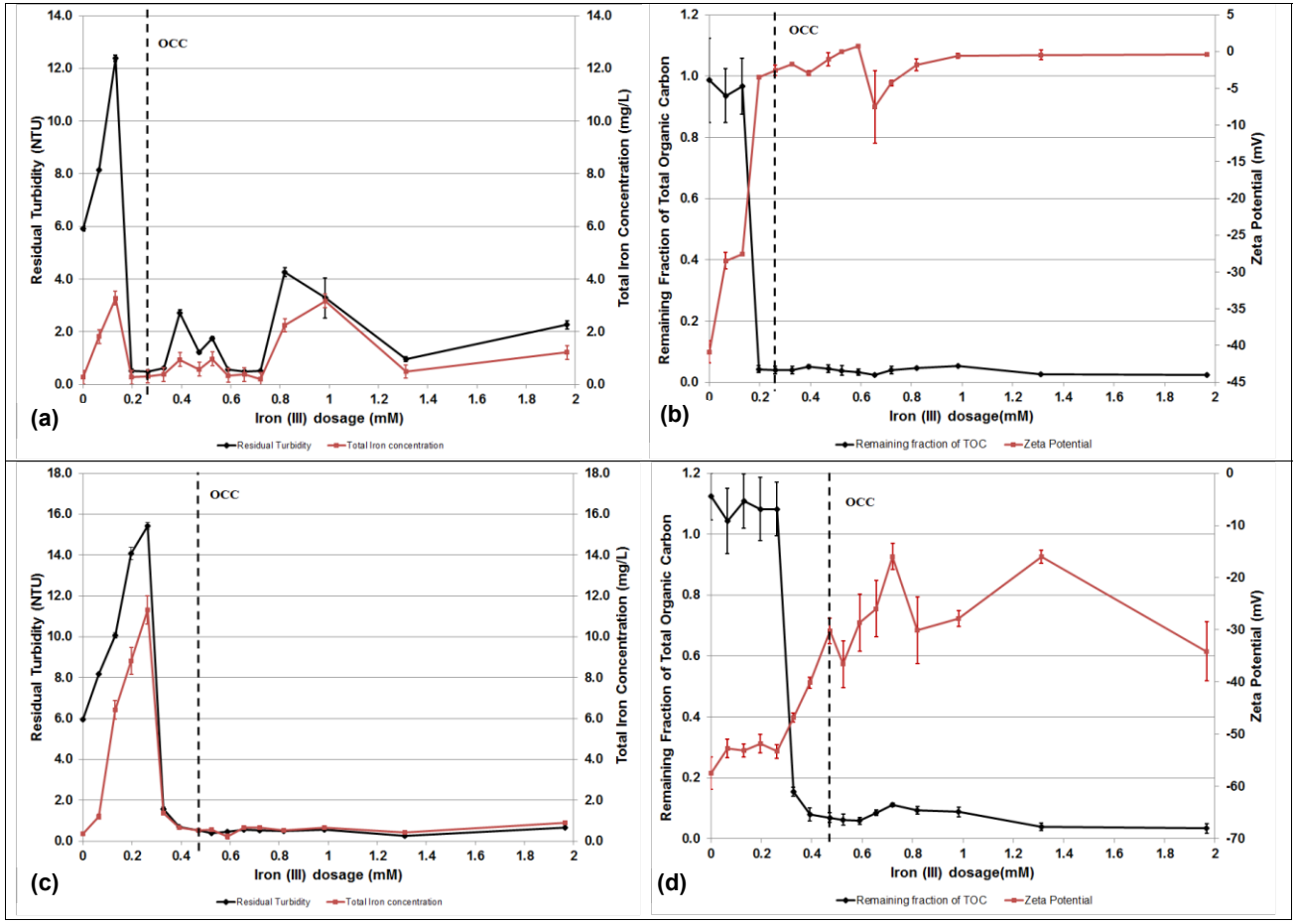

Figure 5.2 Dose response curve displaying the settled water characteristics of the coagulation-flocculation experiments conducted for the synthetic humic water samples at (a,b) pH 4.5 ± 0.3and (c,d) pH 6.7 ± 0.3
(a) Residual turbidity and total iron concentration and (b) Fraction of TOC and associated zeta potential at pH 4.5 ± 0.3;
(c) Residual turbidity and total iron concentration and (d) Fraction of TOC and associated zeta potential at pH 6.7 ± 0.3
OCC- Optimal coagulant concentration indicated by the dotted line; error bar if available represents the standard deviation of the data

Similar coagulation behaviour was observed for the raw lake water and the OCC were comparable to that of the synthetic humic water at the selected pHs of 4.5 ± 0.3 and 6.7 ± 0.3. Table 5.2 provides the settled water characteristics of both waters at the enhanced coagulation conditions. As expected, more than 91% removal of turbidity and TOC was achieved for the synthetic humic water at the acidic and near neutral pH. Coagulation of the raw lake water had an overall removal efficiency of approximately 68%. The residual TOC fractions of approximately 25-30% that remained in the lake water after the treatment were suspected as the hydrophilic organic fractions, which were less amenable to removal by coagulation (Sharp et al., 2006). The TOC removal in this study was in compliance with the 50% requirement specified in the Stage 1 disinfection by-product Rule (USEPA, 1999) for enhanced coagulation of low alkalinity (< 60 mg/L as $CaCO_3$) and high TOC (> 8 mg/L) source waters. Overall, the jar test experiments conducted at an acidic pH of 4.5 ± 0.3 required a coagulant dose < 0.3 mM to arrive at an optimal coagulation condition and resulted in a superior TOC removal. These findings are supported by previous work for DOM removal, which also showed improved removal of organics at a slightly acidic pH (e.g. Lin et al., 2014; Jarvis et al., 2005; Amirtharajah et al., 1993).

5.4.3 Effect of the Mixing Process in Coagulation on the Settled Water Quality

The results of the influence of the coagulation G-value on the settled water characteristics at the optimal coagulant condition for the synthetic humic water and raw lake water are provided in Fig. 5.3. Notably, the mixing intensity had a negligible role in improving TOC removal for the experiments conducted at G > 450 s^{-1} for both water types at the selected pHs of 4.5 ± 0.3 and 6.7 ± 0.3. Unlike TOC removal, the G had a major impact on residual turbidity of the settled water as illustrated in Fig. 5.3a and 5.3c. Effective turbidity removal was achieved at an optimal G range of 110 to 450 s^{-1} for both the synthetic humic water and raw lake water at their respective optimal coagulant dose and pH. A steep decline in residual turbidity below 110 s^{-1} indicated an insufficient supply of mixing energy to form settleable aggregates. When the mixing operation exceeded 450 s^{-1}, it also resulted in a high residual turbidity, except this trend was not evident for the lake water at the pH 6.85.

Table 5.2 Optimal coagulant doses of ferric sulfate determined for synthetic humic water and raw lake water at the selected pH of 4.5 ± 0.3 and 6.7 ± 0.3 along with the settled water quality data.

Water Type	Pre-dominant coagulation mechanism (assumed)	Initial water quality parameters		Enhanced coagulation conditions[a]		Settled water quality			
		Turbidity (NTU)	TOC (mg/L)	pH	Optimal coagulant concentration (mM as Fe)	Turbidity removal (%)	TOC removal (%)	ZP (mV)	pH
Synthetic humic water	Charge neutralization and/ adsorption	6.19 (0.14)	9.57 (0.14)	4.5	0.26	92.1	96.0	-2.6 (0.7)	4.48
	Sweep-floc coagulation	6.15 (0.08)	8.32 (0.06)	6.8	0.47	91.4	93.1	-30.2 (2.5)	7.03
Raw lake water	Charge neutralization and/ adsorption	0.65 (0.03)	3.71 (0.07)	4.8	0.33	68.7	74.8	-2.5 (1.0)	4.68
	Sweep-floc coagulation	0.68 (0.03)	4.82 (0.09)	6.8 5	0.66	68.1	69.8	-9.8 (0.9)	6.53

[a] Mixing conditions- an arbitrary G-value of 175 s^{-1} for 1.5 min for coagulation; followed by a low-mixing intensity of 46 s^{-1} to facilitate flocculation for 20 min

()-Parentheses give standard deviation of the data

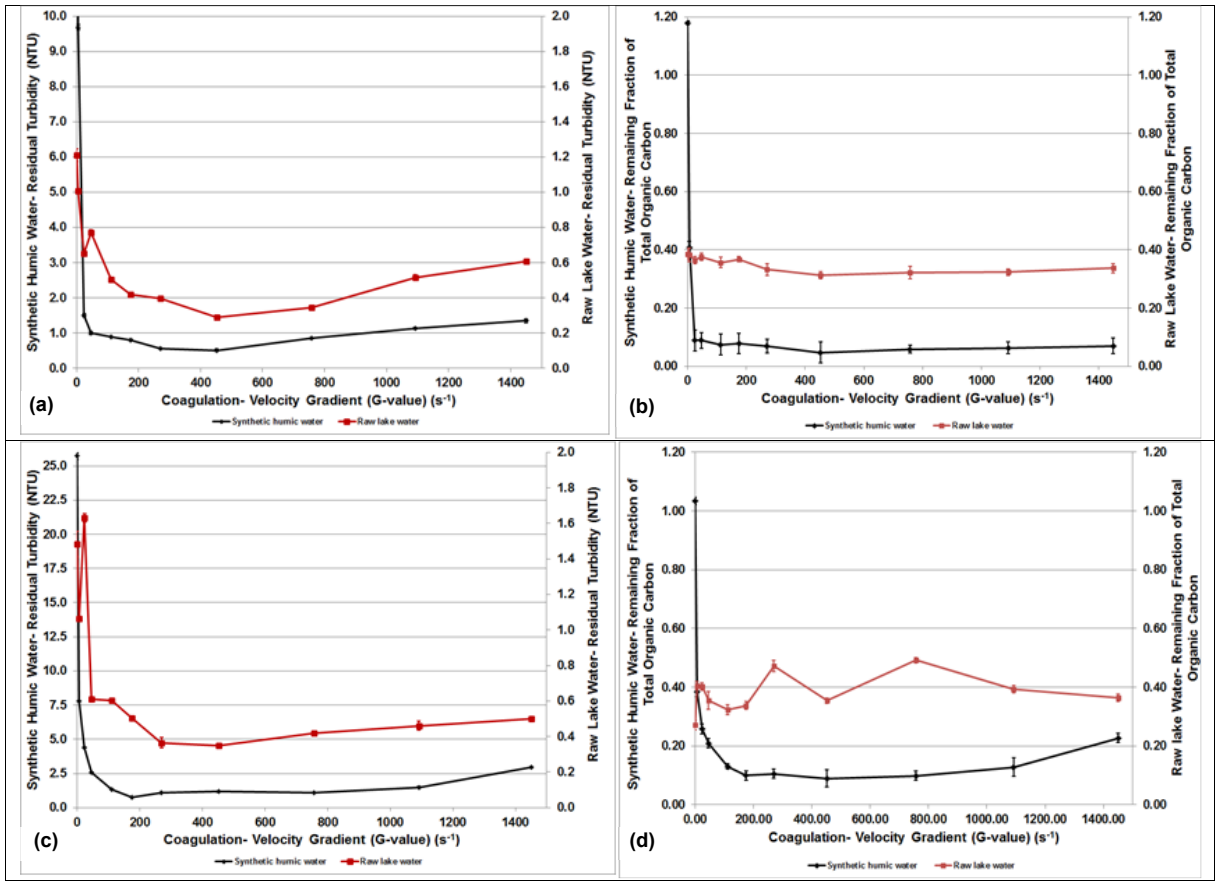

Figure 5.3 Influence of the coagulation mixing intensities (G-value) on the settled water characteristics of the coagulation-flocculation experiments conducted for the synthetic humic water and raw lake water at (a,b) 4.5 ± 0.3 and (c,d) pH 6.7 ± 0.3
(a) Residual turbidity and (b) Fraction of total organic carbon (TOC) at pH 4.5 ± 0.3;
(c) Residual turbidity and (d) Fraction of total organic carbon (TOC) at pH 6.7 ± 0.3
Note: Flocculation was kept at a constant low G-value of 6 s^{-1} for 20 min; Error bar if available represents the standard deviation of the data.

The residual turbidity plots indicate breakup of aggregates during the rapid mixing stage at G > 450 s^{-1} (Fig. 5.3a and 5.3c), which signifies an increase in the distribution of small size aggregates with increasing G values (Pivokonsky et al., 2011). Earlier studies have characterized the dynamic relationship between turbidity and particle size distribution (Yao et al., 2014, Yukselen and Gregory, 2004). Yao et al. (2014) correlated a linear increase in the total number of particles to an increase in water turbidity in the range of 0- 40 NTU. Kan et al. (2002) related turbidity removal to the state of particle aggregation, suggesting the rise in residual turbidity in sweep-floc coagulation was attributed to the breakage of microflocs formed during the rapid mixing.

The effectiveness of coagulation in TOC removal was independent of the mixing intensity. This effect is due to the nature of chemical interaction(s) of humic substances with the hydrolyzed-Fe species in the coagulation process. Previous microscopic investigations have suggested that such interaction(s) at optimal coagulant dose results in an overall shrinkage of anionic humic network to form a dense, spheroid-like structure of humic aggregates, approximately 300 nm in size (Siéliéchi et al., 2008; Myneni et al., 1999). Such compact and nano sizes of DOM/hydrolyzed-Fe colloids are more likely to be entrained within eddies at increased agitation and thus, these colloids may not experience enough surface stress to cause rupture (Stanley and Smith, 1995).

Alternatively, the physical attachment of microflocs onto other microflocs and/or ferric hydroxide precipitates is susceptible to breakage at increased mixing intensities. The mode of attachment of microflocs may also result in differences in the size distribution and rearrangement of floc structures that can result in a variation in the removal efficiency. This hypothesis requires further examination of aggregate structures through microscopic measurements, which is not included in the scope of this study.

5.4.4 Evaluation of Minimization of Energy Usage in the Coagulant Process

The empirical findings from the present study suggest that a low-mixing intensity of 110 s^{-1} < G < 450 s^{-1} is the optimal operating range for coagulation of high organic content source waters, with a SUVA of at least 2-2.5 units of m^{-1} of absorbance per mg/L. The finding is supported by previous studies, which have recommended a low G of 300 s^{-1} for rapid mixing tanks (Edzwald,

2013; Kawamura, 2000; Amirtharajah and Mills, 1982). Edzwald (2013) identified a major disadvantage of rapid mixing tank design is their relatively large volume, which requires more power to achieve a specified design G-value. Other sustainable design alternatives including in-line and open channel static mixers, use of Venturi meters, Parshall flumes and weirs as hydraulic methods are preferred for effective coagulation mixing (Edzwald, 2013; Kawamura, 2000). Similarly, in the current study, a cost-effective modification to the operational design parameter at a low G of $110\ s^{-1} < G < 450\ s^{-1}$ is recommended.

The energy consumption of a coagulation mixing system at the proposed operating G range (i.e., $110\ s^{-1} < G < 450\ s^{-1}$) was evaluated. Fig. 5.4 illustrates the energy usage associated with the mixing process in coagulation at different plant flow rates, along with the efficiency of TOC removal at different G-values for the raw lake water. The chemical condition was at the optimal coagulant dose, and pH conditions for enhanced coagulation: 0.33 mM as Fe at the acidic pH of 4.8 and 0.66 mM as Fe at the near neutral pH of 6.85. As seen in Fig. 5.4, the energy consumption was relatively large for treatment plants operated at a typical G of $750\ s^{-1}$ since the average power supplied is proportional to the square of G as in Equation (5.1). For an average flow of 120 MLD, the energy usage was in the range of 11 to 181 kW-h for the optimal G range proposed in this study, while the consumption markedly increased to almost 2.77 times (i.e., 502 kW-h) at $750\ s^{-1}$. Fig. 5.4 shows that, at different coagulation G ranging from 6 to $1500\ s^{-1}$, the raw lake water had an average TOC removal of 65% and 60% at the acidic pH of 4.8 and the near neutral pH of 6.85, respectively. Fig. 5.4 clearly indicates that operating the coagulation process at high-mixing intensities has a negligible role in the improvement of TOC removal, especially at $G > 450\ s^{-1}$. Optimization of the mixing intensity is necessary to achieve significant improvement in plant energy performance. As shown, operating the mixers at the optimal G-values proposed in this study minimizes the direct energy used in the coagulation process without compromising TOC removal.

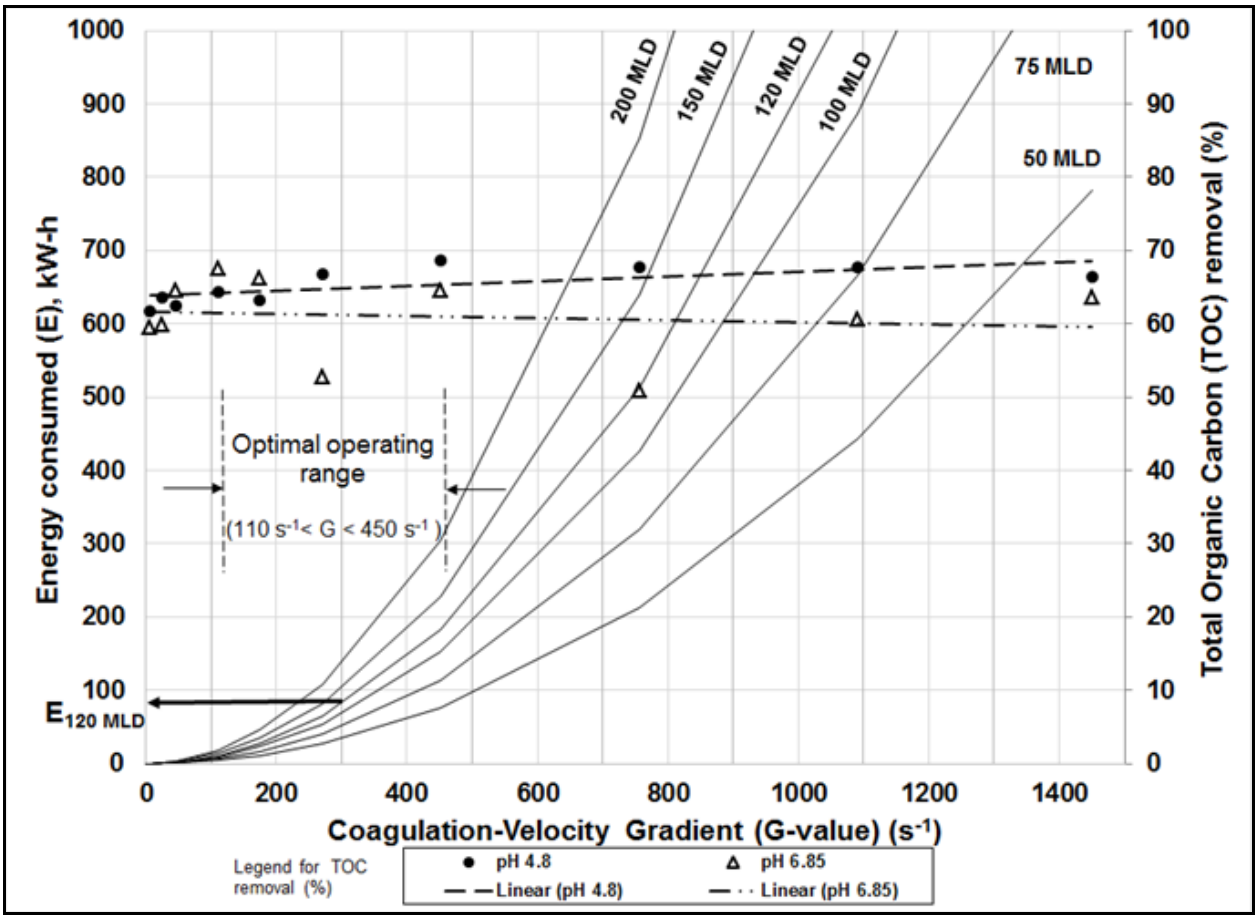

Figure 5.4 The coagulation mixing intensities (G-value) vs. the energy consumption at various flow conditions in a treatment plant and the percentage removal of total organic carbon (TOC) at the enhanced coagulant condition* for the raw lake water at pH 4.8 and 6.85.

* Enhanced coagulant condition for the raw lake water was (●) 0.33 mM as Fe at the acidic pH of 4.8 for an initial TOC of 4.9 ± 0.2 mg/L and (▲) 0.66 mM as Fe at the near neutral pH of 6.85 for an initial TOC of 4.4 ± 0.2 mg/L

$E_{120\ MLD}$- Estimated energy consumption at a flow rate of 120 MLD and the arrow represents the scale of the data.

5.5 Conclusions

An intense mixing of 600- 1000 s^{-1} and a short detention time of 10-60 s is often the design criteria recommended for the coagulation mixing. Earlier studies (Siélièchi et al., 2008) indicate agitation has less influence on the coagulation demand and, in particular, that coagulation by precipitation method is indifferent to mixing intensities (Edzwald, 2013; Amirtharajah and Mills,

1982). This study emphasized that, for both the sweep-floc and charge neutralization mechanisms of coagulation, varying the mixing intensities in coagulation made no substantial improvement in TOC removal. However, at $G > 450\ s^{-1}$, there was a rise in the residual turbidity after settling period, which signifies an increase in suspended particle concentration. Our study suggests that the microflocs formed during the rapid mixing process are susceptible to breakage at increased mixing intensities and may also result in differences in the size distribution and rearrangement of aggregate structures. Additional microscopic investigations are being conducted to understand the structural configuration of humic/hydrolyzed-iron colloids at the acidic pH (4.5 ± 0.3) and the near neutral pH (6.7 ± 0.3).

The current study extends the knowledge of implementation of low-mixing intensity in the coagulant process for high organic content source waters with a specific ultraviolet absorbance (SUVA) of at least 2-2.5 units of m^{-1} of absorbance per mg/L. A low-mixing intensity range of $110\ s^{-1} < G < 450\ s^{-1}$ was sufficient for a combined effective removal of two key contaminants: turbidity and natural dissolved organic matter (DOM). Sample calculations demonstrated that for a plant flow of 120 MLD reducing the G-value from $750\ s^{-1}$ to $300\ s^{-1}$ would reduce energy consumption from 500 kW-h to less than 100 kW-h, without sacrificing water quality in terms of turbidity and DOM removal. From a design standpoint, this study demonstrates that enhanced coagulation can be practiced in water treatment using lower energy inputs, contributing to valuable energy and cost savings, without negatively impacting the coagulation performance.

5.6 Acknowledgements

The authors would like to acknowledge Halifax Water and the Natural Sciences and Engineering Resource Council of Canada (NSERC) for the financial support to the NSERC/Halifax Water Industrial Research Chair. The authors also acknowledge the technical and in-kind support of Heather Daurie and Elliott Wright, research chemists at Dalhousie University's Clean Water lab. The authors also thank the Louisbourg water treatment plant authority, Nova Scotia, Canada for providing access to the water treatment for sampling. Lastly, the authors are grateful to the doctoral students at the Center for Water Resources Studies at Dalhousie University for the valuable suggestions provided for the possible submission of this manuscript.

5.7 References

American Public Health Association (APHA), 2012. Standard methods for the examination of water and wastewater. 22nd ed. American Public Health Association, American Water Works Association and Water Pollution Control Federation, Washington D.C.

American Water Works Association (AWWA), American Society of Civil Engineering (ASCE), 2012. Mixing, coagulation, and flocculation. In: Water Treatment Design. 5th ed. (S.J. Randtke and M.B. Horsley, editors). McGraw Hill, American Water Works Association and American Society of Civil Engineering, New York.

Amirtharajah, A., Dennett, K. E., Studstill, A., 1993. Ferric chloride coagulation for removal of dissolved organic matter and trihalomethane precursors. Water Sci. Technol. 27 (11), 113-121.

Amirtharajah, A., Mills, K. M., 1982. Rapid-mix design for mechanisms of alum coagulation. J. Am. Water Works Assoc. 74 (4), 210-216.

Angelico, R., Ceglie, A., He, J. Z., Liu, Y. R., Palumbo, G., Colombo, C., 2014. Particle size, charge and colloidal stability of humic acids coprecipitated with ferrihydrite. Chemosphere. 99, 239-247.

Cornwell, D. A., Bishop, M. M., 1983. Determining velocity-gradients in laboratory and full-scale systems. J. Am. Water Works Assoc. 75 (9), 470-475.

Davis, C. C., Edwards, M., 2014. Coagulation with hydrolyzing metal salts: mechanisms and water quality impacts. Crit. Rev. Environ. Sci. Technol. 44 (4), 303-347.

Dempsey, B. A., Ganho, R. M., O'melia, C. R., 1984. The coagulation of humic substances by means of aluminum salts. J. Am. Water Works Assoc. 76 (4), 141-150.

Duan, J. M., Gregory, J., 2003. Coagulation by hydrolysing metal salts. Adv. Colloid Interface Sci. 100-102, 475-502.

Edzwald, J. K., 2013. Coagulant mixing revisited: theory and practice. J. Water Supply: Res. Technol. -AQUA. 62 (2), 67-77.

Energy Efficiency and Renewable Energy (EERE), 2005. Onondaga county department of water environment protection: process optimization saves energy at metropolitan Syracuse wastewater treatment plant. DOE/GO-102005-2136. Energy Efficiency and Renewable Energy, U.S. Department of Energy, Washington, D.C.

Hach, 2005. DR 5000 Spectrophotometer procedures manual. 2nd ed. Hach Co., Loveland, Colorado.

Jarvis, P., Jefferson, B., Parsons, S. A., 2005. How the natural organic matter to coagulant ratio impacts on floc structural properties. Environ. Sci. Technol. 39 (22), 8919-8924.

Jiang, J. Q., Graham, N. J. D., 1998. Pre-polymerised inorganic coagulants and phosphorus removal by coagulation - A review. Water SA. 24 (3), 237-244.

Kan, C. C., Huang, C. P., Pan, J. R. S., 2002. Time requirement for rapid-mixing in coagulation. Colloids Surf. A Physicochem. Eng. Asp. 203 (1-3), 1-9.

Kawamura, S., 2000. Integrated design and operation of water treatment facilities. 2nd ed. John Wiley & Sons, New York.

Leiby, V., M., Burke, M., E., 2011. Energy efficiency best practices for North American drinking water utilities. ISBN 978-1-60573-159-9. Water Research Foundation and New York State Energy Research and Development Authority, U.S.A.

Lin, J. L., Huang, C., Dempsey, B. A., Hu, J. Y., 2014. Fate of hydrolyzed Al species in humic acid coagulation. Water Res. 56, 314-324.

Myneni, S. C. B., Brown, J. T., Martinez, G. A., Meyer-Ilse, W., 1999. Imaging of humic substance macromolecular structures in water and soils. Science. 286 (5443), 1335-1337.

Owen, D. M., Amy, G. L., Chowdhury, Z. K., Paode, R., McCoy, G., Viscosil, K., 1995. NOM - characterization and treatability. J. Am. Water Works Assoc. 87 (1), 46-63.

Pivokonsky, M., Bubakova, P., Pivokonska, L., Hnatukova, P., 2011. The effect of global velocity gradient on the character and filterability of aggregates formed during the coagulation/flocculation process. Environ. Technol. 32 (12), 1355-1366.

Santana, M. V. E., Zhang, Q., Mihelcic, J. R., 2014. Influence of water quality on the embodied energy of drinking water treatment. Environ. Sci. Technol. 48 (5), 3084-3091.

Sharp, E.L., Parsons, S.A., Jefferson, B., 2006. Seasonal variations in natural organic matter and its impact on coagulation in water treatment. Sci. Total Environ. 363(1-3), 183-194.

Siéliéchi, J. M., Lartiges, B. S., Kayem, G. J., Hupont, S., Frochot, C., Thieme, J., Ghanbaja, J., de la Caillerie, J. B. D., Barrès, O., Kamga, R., Levitz, P., Michot, L. J., 2008. Changes in humic

acid conformation during coagulation with ferric chloride: implications for drinking water treatment. Water Res. 42 (8-9), 2111-2123.

Stanley, S. J., Smith, D. W., 1995. Measurement of turbulent flow in standard jar test apparatus. J. Environ. Eng. ASCE. 121 (12), 902-910.

Ten State Standards of the Great Lakes-Upper Mississippi River Board of State and Provincial Public Health and Environmental Managers, 2012. Recommended standards for water works. Health Research Inc., Health Education Services Division, Albany, New York.

Thurman, E. M., 1985. Organic geochemistry of natural waters. ISBN: 978-94-010-8752-0. Martinus Nijhoff/Dr W. Junk Publishers, Dordrecht.

U.S. Environmental Protection Agency (USEPA), (2008). Ensuring a sustainable future: an energy management guidebook for wastewater and water utilities. U.S. Environmental Protection Agency, Washington, D.C.

U.S. Environmental Protection Agency (USEPA), (1999). Enhanced coagulation and enhanced precipitative softening guidance manual. EPA 815-R-99-012. U.S. Environmental Protection Agency, U.S.A.

Van Benschoten, J. E., Edzwald, J. K., 1990. Chemical aspects of coagulation using aluminum salts-II. Coagulation of fulvic-acid using alum and polyaluminum chloride. Water Res. 24 (12), 1527-1535.

Volk, C., Bell, K., Ibrahim, E., Verges, D., Amy, G., Lechevallier, M., 2000. Impact of enhanced and optimized coagulation on removal of organic matter and its biodegradable fraction in drinking water. Water Res. 34 (12), 3247-3257.

Xie, J. K., Wang, D. S., van Leeuwen, J., Zhao, Y. M., Xing, L. N., Chow, C. W. K., 2012. pH modeling for maximum dissolved organic matter removal by enhanced coagulation. J. Environ. Sci-China. 24 (2), 276-283.

Yao, M., Nan, J., Chen, T. 2014. Effect of particle size distribution on turbidity under various water quality levels during flocculation processes. Desalination. 354, 116-124.

Yukselen, M. A. and Gregory, J., 2004. The reversibility of floc breakage. Int. J. Miner. Process. 73 (2-4), 251-259.

Zumstein, J., Buffle, J., 1989. Circulation of pedogenic and aquagenic organic-matter in an eutrophic lake. Water Res. 23 (2), 229-239.

Chapter 6 Investigation of Chemical Composition and Structure of Floc Aggregates

6.1 Abstract

A synthetic humic acid was used in the study as a natural dissolved organic matter (DOM) reference model found in natural waters. In general, the infrared (IR) spectra of humic acid had a broad peak ranging from 3600 to 2500 cm^{-1} (-OH stretch of phenolic and carboxylic groups) , two distinct peaks at 2910 to 2930 cm^{-1} (aliphatic C-H), and two broad peaks between 1650-1540 cm^{-1} and 1450-1360 cm^{-1} ($-COO^-$ stretch of carboxylate salts), which confirms the aliphatic and aromatic characteristics. Complex heterogeneous humic acid and the presence of other elements resulted in an overlap of many spectral bands. However, this method in conjunction with a scanning Electron Microscopy (SEM) and an energy Dispersive X-Ray Spectroscopy (EDS) provided an insight into formation of humic floc aggregates. The interpretation from the Fourier transform infrared spectroscopy (FT-IR) and SEM-EDS data in the present study supports surface complexation, where protonated weaker carboxylic groups were proposed to bind on to the surfaces of iron at both the pHs, 4.5 and 6.8. Iron-DOM complexes resulting from this reaction grew into larger aggregates during the slow mixing stage in flocculation, which had a ratio of iron to carbon greater than 1.

6.2 Introduction

Floc aggregates play an important role in the fate, transport of sorbed organic constituents and inorganic impurities trapped in their matrix, and their subsequent removal in solid-liquid separation processes. Various growth phases of floc occur during coagulation and flocculation that are described using a multilevel structural model (Gorczyca and Ganczarczyk 1999). According to this model, primary particles in water form compact flocculi which assemble themselves into microflocs. Microflocs bind together to form large and highly porous floc aggregates. Experimental investigation by Gorczyca and Ganczarczyk (1999) has confirmed three distinctive floc populations during coagulation with alum coagulant: flocs with small pore sizes of less than 2.5 μm^2, medium sizes ranging from 2.5-10 μm^2, and large pores of >10 μm^2 were formed.

Experimental investigations have consistently shown floc breakage to occur with increasing the mixing intensity (G-value), resulting in an overall rapid reduction in floc size (e.g., Biggs and Lant 2000, Spicer et al. 1998, Pivokonsky et al. 2011, Yukselen and Gregory 2004). This change in floc sizes has been related to floc compactness by fractal analysis (Jarvis et al. 2005b, Spicer et al. 1998). This implies that the multilevel floc structure (i.e., flocculi-microflocs-aggregates) proposed earlier undergoes a significant change in their structural arrangement after experiencing a breakage. Earlier studies have described rupture in floc structures in terms of fragmentation and surface erosions (Jarvis et al. 2005a, Parker et al. 1972). Fragmentation splits a floc into many fragments as a result of pressure forces; while small particles are thought to erode from floc surfaces due to viscous forces resulting from surface erosions, causing an increase in small size distributions (Jarvis et al. 2005a, Thomas et al. 1999).

In general, floc breakage are quantified based on size, shape, and fractal dimensions using imaging analysis (e.g., Pivokonsky et al. 2011) and laser scattering techniques (e.g., Jarvis et al. 2008, Jarvis et al. 2004). As yet, there is no detailed understanding of the internal composition and bonding that can occur within a floc aggregate. Only few studies have used spectroscopic surface analysis to probe into the sorption mechanisms involved in floc formations (El Samrani et al. 2004, Jung et al. 2005, Sari and Chellam 2015). Similar elemental analyses combined with physical characterization are essential to have a better understanding on the formation mechanisms of micro- and macro-floc aggregates and their structural arrangements.

The main objective of this study was to examine the characteristics of floc aggregates that were formed during coagulation and flocculation processes at two pH set points. A synthetic humic acid was used as a model compound for natural dissolved organic matter (DOM) in drinking water sources. Surface analyses of flocs resulting from coagulation and settled flocs were characterized using a Fourier transform infrared spectroscopy (FT-IR). This was performed to obtain specific information on the main functional groups present in the humic acid source and their interaction(s) with the hydrolyzed coagulant species. Additionally, morphology of flocs formed during rapid mixing stage were investigated using a scanning electron microscopy (SEM) combined with an energy dispersive X-Ray spectrometry (EDS).

6.3 Materials and Methods

6.3.1 Materials

Ferric sulfate ($Fe_2(SO_4)_3$) was used as the coagulant, which had 2.71% water content (MP Biomedicals, USA). Fresh stock solution was prepared at a concentration of 5 mM (calculated as Fe). Stock solutions of 0.2 N nitric acid and 1 M sodium hydroxide were used to adjust the pH to a desired set point. All the reagents used were of analytical grade and stock solutions were prepared using deionized (DI) water.

A synthetic sodium salt of humic acid obtained from Alfa Aesar (USA) was used as a DOM model in the jar test experiments. It had a composition of 38.4% carbon (C), and 0.73% nitrogen (N) as measured from the ECS 4010 CHNSO analyzer (Costech Analytical Technologies Inc., California). Approximately 30 mg of humic acid was dissolved in a liter of de-ionized water to produce a stock solution at a concentration of (8.75± 0.64 mg/L) of total organic carbon (TOC). Alkalinity was introduced by adding 20 mg/L of 1 N sodium bicarbonate to the stock solution. The prepared suspension was continuously mixed for approximately 2 hours prior to the start of the experiment. Table 6.1 provides an elemental analysis of the synthetic humic acid analyzed using the inductively coupled plasma-mass spectrometry (ICP-MS) (Thermo Scientific XSeries II ICP-MS, USA).

6.3.2 The Set-Up

Coagulation and flocculation experiments were tested at the two pH set points, an acidic pH of 4.5 and a near neutral pH 6.8, following a procedure described in Chapters 3. In that study, an iron dose of 8 mg/ L (i.e., 0.26 mM) at pH 4.5 and 14 mg/L (i.e., 0.47 mM) at pH 6.8 was shown as the optimal coagulant concentration (OCC) that resulted in the removal of more than 91% of turbidity and TOC from the humic water. These optimal conditions were used in the present study to form humic floc aggregates.

Table 6.1 Inductively coupled plasma-mass spectrometry (ICP-MS) data of the humic water

Elemental Analysis	Value (mg/L)
Magnesium (Mg)	(0.102± 0.01)
Iron (Fe)	0.165
Sodium (Na)	11.91
Aluminum (Al)	(0.145± 0.04)
Calcium (Ca)	(0.631± 0.08)
Potassium (K)	0.023

Floc experiments were conducted at room temperature (21 ± 1°C) in a 1-L square jar test beaker. A compact digital mixer (Cole-Parmer, USA) was used for mixing purposes. The coagulant and pH adjustment chemicals (i.e., 1M sodium hydroxide and 0.2N nitric acid) were added simultaneously during the rapid mixing operation at a G-value of 175 s^{-1}. This G-value was well within the optimal operating range (i.e., 110 s^{-1} < G < 450 s^{-1}) of mixing energy input required for the coagulation process, as illustrated in Chapter 4 (Vadasarukkai and Gagnon 2015). A settling period of 60 min was provided for flocs to settle in the jar test beaker. The operating conditions used in this study were well within the recommended design standards for water treatment plants (Ten State Standards, 2012), except for the coagulation experiments. A low G-value of 175 s^{-1} and a slightly longer detention time of 90s was set for the rapid mixing stage of coagulation. This additional detention time was applicable in the present case since more than one chemical (e.g. ferric sulphate and 1N sodium hydroxide) was used for forming floc aggregates (AWWA-ASCE, 2012).

6.3.3 Sample Preparations

6.3.3.1 Scanning Electron Microscopy and Energy Dispersive X-Ray Spectroscopy

Morphology of flocs formed soon after rapid mixing was characterized mainly using a scanning Electron Microscopy (SEM) and an energy Dispersive X-Ray Spectroscopy (EDS). It was noted that the sample preparation played a key role in SEM analyses. For example, drying the samples at 30-45^0 C in crucibles led to a non-uniform formation of flat structures (data not shown), significantly affecting the floc morphology. Goodwill et al. (2015) indicated drying at 104^0 C for surface analyses can possibly cause transformation of amorphous iron hydroxides ($Fe(OH)_3$) to iron (oxy)hydroxide (FeOOH) by dehydration and crystallization processes. As amorphous type of morphology was considered predominant in the pH ranges seen in water treatment (Davis and Edwards 2014), SEM samples were air-dried for at least 24 hour at room temperature (21 ± 1°C). Approximately 50 mL of samples was drawn soon after the rapid mixing stage and a droplet was carefully placed on a SEM specimen stub using a wide-mouth pipette (e.g., 10 mL pipette). The samples were coated with gold palladium using a Polaron SC7620 Mini Sputter Coater (Quorum Technologies, Lewes, U.K.), with a plasma current of 18 mA for 120s. SEM and EDS analyses were performed using a Hitachi S-4700 FEG Scanning Electron Microscope (Hitachi, Tokyo) with an accelerating voltage of 20 kV and an emission current of 8.5 μA. Each EDS spectrum was ran for at least 30s scan time.

6.3.3.2 Attenuated Fourier Transform Infrared Spectroscopy (FTIR)

An attenuated total reflectance module (ATR) of the Fourier Transform Infrared Spectroscopy (FT-IR), along with the EDS data, was used to determine the characteristics of functional groups in the humic acid and their interaction(s) with the iron hydrolysis species. All the infrared analysis was carried out using the Cary 630 ATR FT-IR (Agilent Technologies, Santa Clara, California) in the absorption mode. An ATR module with a zinc selenide (Zn-Se) crystal was used for this purpose.

Sample preparation often used for identifying functional groups present in organic compounds requires a high concentration of organics and preferably, low in salt concentrations (Minor et al. 2014). Water molecules absorb a significant portion of the infrared (IR) band due to the hydroxyl

group (-OH). A strong signal at 3700-3000 cm^{-1} and 1700-1600 cm^{-1} are largely reported due to residual water (Sari and Chellam 2015), which was identified for the IR spectra of deionized (DI) water in Figure A.1. The interference from water bands has to be reduced for a successful, quantitative estimation of functional groups in humic substances that yield strong IR signals in those regions (e.g., carboxylic, phenolic groups). For this reason, many studies have concentrated natural dissolved organic matter (DOM) and dried the samples (El Samrani et al. 2004, Goodwill et al. 2015, Sari and Chellam 2015). Few studies have preferred a diffuse reflectance infrared Fourier transform (DRIFT) spectroscopy for investigations of aquatic humic substances (Niemeyer et al. 1992). Other adsorption studies have applied a thin layer of metal oxides on the crystal surface and then filled the ATR cell with organic acid solutions (Guan et al. 2007, Guan et al. 2006).

Three sampling procedures were tested to concentrate and collect humic floc aggregates: direct freeze-drying at -20 ^{0}C (El Samrani et al. 2004), oven drying at 35-40 ^{0}C, and filtration on a glass fiber filter (glass microfibers, 0.7 μm porosity, Whatman Co.) (Tremblay et al. 2011). It was found from the preliminary investigation of spectral data that all the four drying procedures examined in this present study had some influence on the FT-IR spectra generated for DOM-metal complexes. The highest intensity of most spectral regions was obtained by the oven-drying method at 35-40 ^{0}C. The findings from oven-dried samples showed comparable results to the freeze-dried samples, which has been commonly used to preserve coagulated sediments (El Samrani et al. 2004).Hence, this method was selected for further analysis. Detailed information on different sample preparation methods is provided in Appendix A.1.

The oven-dried floc aggregates in the crucibles were scraped and placed on the surface of the crystal, and the dial was lowered to lock into place. The Happ-Genzel method was used with 200 scans at a resolution of 2 cm^{-1} was collected from a spectral range of 650-4000 cm^{-1}. Backgrounds were taken with the crystal alone.

6.4 Results and Discussion

6.4.1 Characteristics of the Synthetic Humic Acid

Figure 6.1 and 6.2 shows the mid-IR spectra of synthetic humic acid and ferric sulphate that were used in the jar test experiments as received from the manufacturers. The diagnostic spectral range from 3000 to 1500 cm^{-1} was used to identify few important functional groups that may be present in these compounds. Unless specified, most peaks were assigned from handbooks for IR spectra of organic (Bellamy 1968, Lin-Vien et al. 1963, Smith 1999) and inorganic compounds (Nakamoto 1963).

In general, the IR spectra the humic acid (HA) showed similar characteristics behaviour to the commercial potassium salt of humic acid extracted from Leonardite, a reference humic model from the International Humic Substances Society (U.S. Geological Survey, Denver, CO). The two distinct peaks at 2920 and 2851 cm^{-1} (C-H stretch of CH_2 groups) in Figure 6.1 (*top panel*) were also shown in the spectra of leonardite HA(Niemeyer et al. 1992), indicating the presence of aliphatic components. While a broad spectrum from approximately 3600 to 2500 cm^{-1} in Figure 6.1 (*top panel*) represents a stretch in the hydroxyl (i.e., -OH) functional group of organic components (e.g., phenolic, carboxylic acid groups) and water molecules.

The two broad peaks found in 1650-1540 cm^{-1} and 1450-1360 cm^{-1} (this region splits into several small shoulder peaks) were mostly assigned to the carboxylate ions (COO^-) stretch of carboxylate salts. The presence of alkali metal salts such as sodium in the synthetic humic acid was also reflected from the elemental analyses (Table 6.1). It is possible to have carboxylate group associated to metal salts during resin extraction of humic acid (Leenheer 1981), and similar observation were also made by other researcher. For instance, Vinkler et al. (1976) showed for humic and fulvic acids containing alkaline metals the asymmetric and symmetric COO^- stretches occurred between 1600-1580 cm^{-1} and 1390-1378 cm^{-1}, respectively. Likewise, Niemeyer et al. (1992) showed carboxylate peaks at 1585 and 1385 cm^{-1} for the commercial potassium salt of humic acid extracted from Leonardite.

Complex chemical structure of humic acid and the presence of other elements as impurities may have resulted in an overlap of many spectral bands for the fingerprinting region below 1100 cm^{-1}. For instance, different substitution pattern can occur at out of plane C-H bending between 710 and 860 cm^{-1}. This suggests the aromatic C-H out of plane bending at 1000- 700 cm^{-1}. Identification of aromatic hydrocarbon stretch is typically shown around 3100-3000 cm^{-1} and ring modes at 1620-1400 cm^{-1}. However, confirmation for an aromatic ring structure in the humic acid was masked by the broad carboxylate bands in these regions. Whereas, a broad band near 1120-980 cm^{-1} with a peak at 1030 cm^{-1} was typically assigned to C-O stretch in carbohydrate and polysaccharide groups (Ribeiro et al. 2001).

Micrographs of humic acid showed irregular fibrillar (elongated rod-like) structures, containing a rich amount of carbon, oxygen and sodium (Figure 6. 1 (*bottom panel*)). It was also associated with other elements, such as calcium, potassium, sulphur and aluminium. The presence of these elements was also confirmed in the elemental analysis (Table 6.1).

6.4.2 Characteristics of Ferric Sulphate

The IR spectra of ferric sulphate had three main spectral regions as shown in Figure 6.2 (*bottom panel*): the first two regions were assigned to water molecules in the structure of ferric sulfate that had contributed to a symmetric and an asymmetric H-O-H stretching modes in 3500-2600 cm^{-1} and a H-O-H bending mode at 1640 cm^{-1}, respectively (Nakamoto, 1986). While peaks at 1078 and 1013 cm^{-1} in the third region were assigned to the asymmetrical vibrational mode of S-O of sulphate, as it was found to contribute the strongest IR peaks in this spectral region 1400-400 cm^{-1} (Ling and Wang 2010) and S-O bends occurred in the region 680-610 cm^{-1}. Notably, the SEM micrographs of ferric sulphate had crystalline plate structures, with few clusters were formed as shown in Figure 6.2 (*top panel*). Using spectral mapping, these clusters were assigned to sulfate groups containing 54, 12 and 11% (by weight) of oxygen, sulphur and carbon, respectively. This suggests the structural arrangement of ferric sulphate—that is SO_4 tetrahedra were connected to iron by sharing an oxygen atom (Ling and Wang 2010).

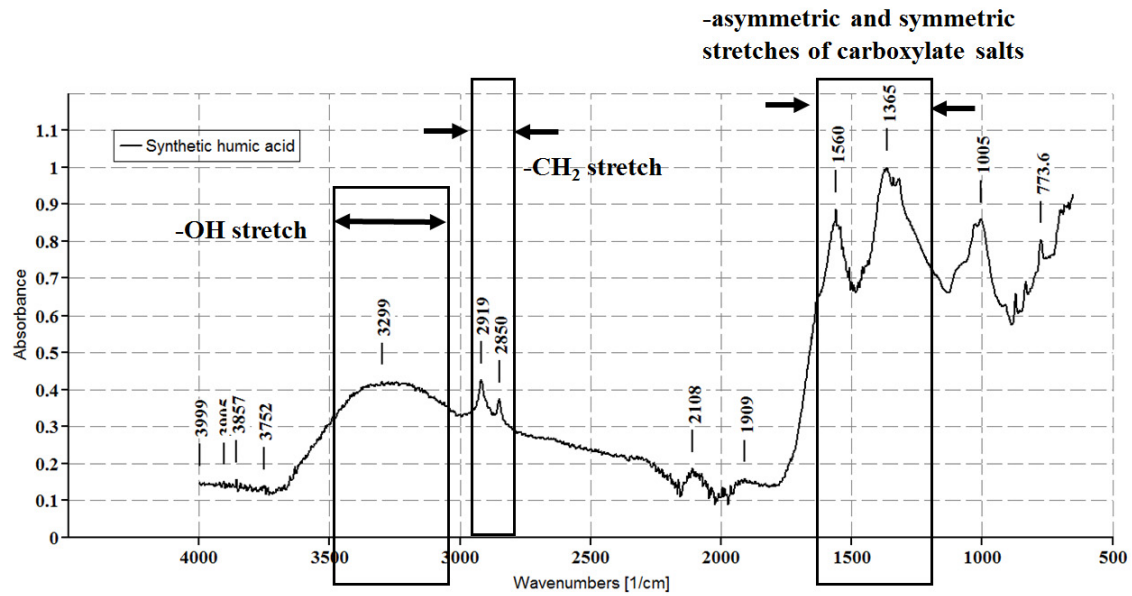

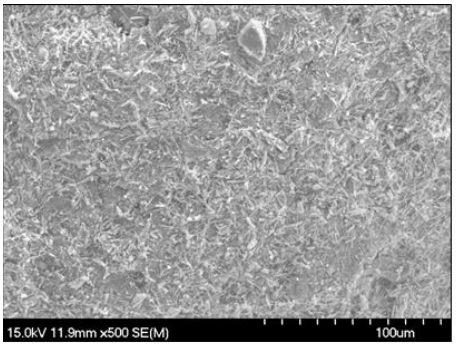

Element	Weight %
C K	47.41
O K	41.82
Na K	6.26
Mg K	0.11
Al K	0.27
Si K	0.42
Cl K	0.42
K K	0.23
Ca K	2.06
Fe L	1.06
Totals	100.00

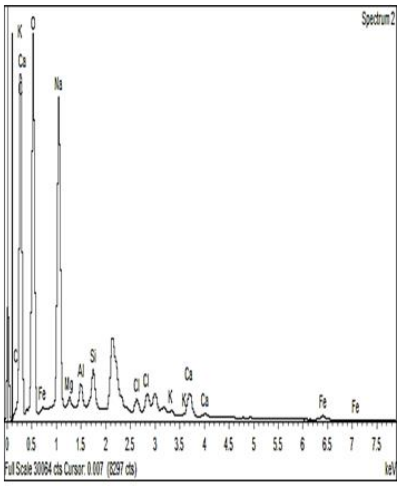

Figure 6.1 FTIR spectra *(top panel)* and SEM-EDS *(bottom panel)* of the synthetic HA in its orginal solid forms

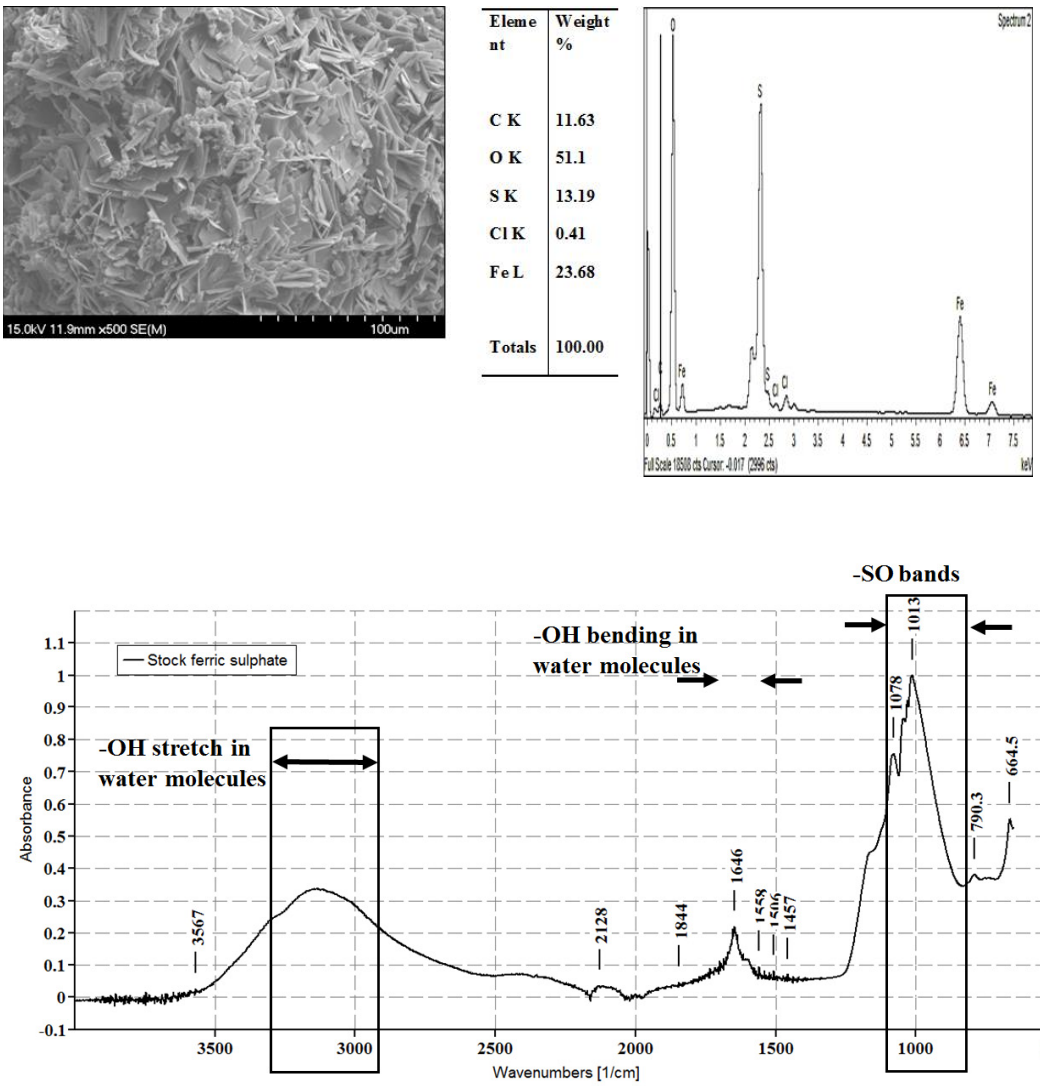

Figure 6.2 SEM-EDS *(top panel)* and FTIR spectra *(bottom panel)* for ferric sulphate coagulant in its orginal solid forms

(note: Each reported values are average of at least 4 EDS spectras carried out at different spots)

6.4.3 Surface Analysis of Flocs by FT-IR

Figure 6.3 presents the IR spectrum of floc aggregates following coagulation and flocculation experiments. The diagnostic spectral range from 3000 to 1500 cm^{-1} for both the rapid mix and settled water flocs showed features similar to that of the synthetic humic acid at a relatively reduced peak intensities. This signified the process efficiency of coagulation and flocculation

process in removal of soluble organic impurities by forming precipitates. Reduced peak intensities at 2920 and 2851 cm^{-1} of the saturated alkane hydrocarbon (-CH_2 groups) may indicate deformation in their aliphatic structure with the iron addition (El Samrani et al. 2004). The two peaks that were previously assigned to the stretches of carboxylate salt in the humic acid were identified in floc samples; however, these peaks had a very slight shift from 1560 to 1559 cm^{-1} and 1365 cm^{-1} to 1363 cm^{-1} at both the selected pHs. Also, several small yet sharp peaks were formed along 1800- 1616 cm^{-1}, 1570 -1470 cm^{-1} and 1470-1362 cm^{-1}.

These peaks can be explained due to probable variations in the solution pH, which is shown to affect the position and the number of bands in the IR spectrum (Tejedor-Tejedor et al. 1990). The spectral changes was interpreted in terms of the acid-base titration curve. Since the pK_a values for humic acid were 2.8 and 6.4 (Appendix A2), the FT-IR spectrum at pH 4.5 should correspond to a mixture of weak carboxylic acid and disassociated anion (e.g., carboxylate ions (COO^-)). When the pH was at 6.8, loss of a second proton was expected. Disassociation of the COO^- group was indicated to affect the vibration of the benzene ring, which may have caused peaks at 1504-1466 and 1466-1422 cm^{-1} (Varsanyi and Szoke 1969). These disassociated carboxylate group were available for interaction and possible associations with the iron coagulant species(El Samrani et al. 2004), forming complexes or chemical bonds between them. Likewise, (Lu et al. 1997) showed loss of intensities at 1720 and 1200 cm^{-1}, with an increasing absorption at 1630 and 1400 cm^{-1} due to conversion of -COOH to COO^- groups in iron-humate complexes. This chemical reaction of release of carboxylate ion is termed as decarboxylation, which occurs during metal humic complexation. The reaction is usually accompanied with a release of CO_2 as shown by the band the absorption peak around 2300 cm^{-1} in Figure 6.6 (Liu and Huang 2001)..

It was seen from the SEM-EDS data that the elemental ratio of sodium to carbon (Table 6.3) reduced with an increase in iron to carbon ratio, following coagulation. This indicated that the carboxylate group that was initially associated to sodium salt, as interpreted from the FTIR analysis, was exchanged for other cations (e.g., iron) during the process. Such findings were consistent with previous elemental analysis of coagulated sediments (Jung et al. 2005), showing that the association of iron-coagulant species were predominantly with the carboxylate group of

humic colloids, and that this interaction was induced by a release of previously complexed calcium ions.

Several earlier studies have identified complexes by the appearance of new peaks and peak shifts in the FT-IR spectra; Table 6.2 summarizes examples of the peak assignment results from the literature. Their findings support this present study's interpretation of surface complexation between hydrolyzed iron species and functional groups of humic acid. The presence of cation, such as Ca, Mg, Na and Al, were expected to compete with iron. Since the ranges for different metal-COO^- stretching peaks can greatly overlap, the definite assignment of these bands was difficult. In fact, Alberts and Filip (1998) work showed similar spectral regions for the calcium, magnesium, aluminum, and iron complexes, suggesting these ions bind to humic acids primarily through carboxyl functional groups; while association of gold and lead occur through carboxyl- and alcoholic moieties.

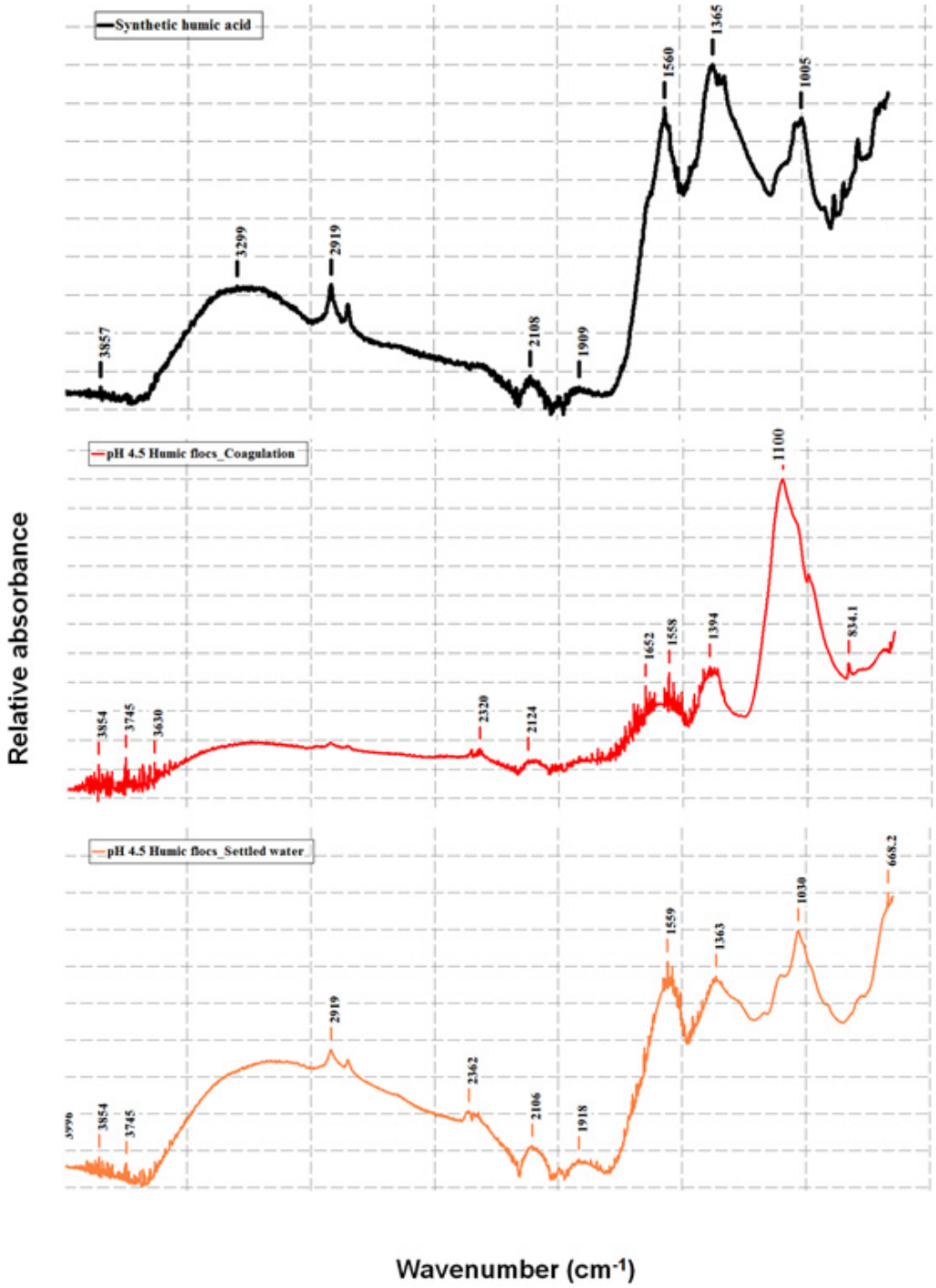

Figure 6.3 FT-IR spectra of HA flocs at an acidic pH of 4.5 and an optimal coagulant iron dose of 8 mg/L

Table 6.2 Summary of peaks resulting from metal-organic complexes

Peak positon (cm^{-1})	Peak assignment	Organic and metal interactions	Reference
1580-1524	Asymmetric vibration (ν_{as} COO^-) in bidentate or binuclear complexes	Dihydroxybenozic acid and aluminum hydroxide	(Guan et al. 2006)
1442-1366	Symmetric vibration (ν_s COO^-) in bidentate mononuclear complexes		
1411-1373	ν_s COO^- in bridge complexes		
1645	C=O stretching in monodentate complexes	Salicylic acid and aluminum hydroxide	(Guan et al. 2007)
1607-1609 and 1566	Asymmetric vibration of C-O bond in the bidentate or bridging complexes		
1439	Symmetric vibration of C-O bond		
1544 and 1410	Asymmetrical and symmetrical stretching of C=O in complex carboxylate group, respectively	Sewage water with ferric chloride coagulant	(El Samrani et al. 2004)
1600-1615	Ionic-covalent complex;	Metal-humate	(Vinkler et al. 1976)
1615-1630	Covalent complexes		
1616,	vibration of carboxylate group and aromatic C=C double bond conjugated with C=O groups;	Catechol on iron oxide	(Liu and Huang 2001)
1253	C-O stretch of COOH;		
1381	symmetric stretch of COO^-;		
1469	bending vibration of aliphatic group due to complexation catechol with Fe oxide		

It was interesting to note some key differences between the fingerprinting region below 1100 cm^{-1} for flocs following coagulation and settled flocs (Figure 6.3). The IR spectra for rapid mix floc sample had an intense peak at 1100 cm^{-1}, with a small shoulder at 990 cm^{-1}. This was attributed to the asymmetrical vibrational mode of S-O of sulphate, which was previously identified in ferric sulphate structure at pH 6.8 due to distortion in SO_4 tetrahedra (Figure B.3). Notably, this peak at 1100 cm^{-1} was weaker with a new peak formed at 1030 cm^{-1} for the settled floc sample. Although this region resembled to those bands found in humic acid, the C-O stretch assigned to carbohydrate and polysaccharide groups at 1005 cm^{-1} was absent. The region at 1070-1040 cm^{-1} can be due to S=O stretches of aliphatic sulfoxides with one or two bands. Alternatively, the bands at 1020/1110 cm^{-1} may also be assigned to preferentially adsorption of the -OH functional groups on iron oxide surface (Gu et al. 1995). Two sharp peaks at 871 and 833 cm^{-1} that was previously observed in the humic spectrum had disappeared completely for the settled water, which denotes possible deformation in the ring structure with the iron addition.

6.4.4 Influence of pH on the FT-IR Results and Floc Morphology

The optimum iron concentration was increased from a dose of 8 to 14 mg/L with increasing pH to 6.8, which also increased the measured sulphate concentration in the settled water from 20 to 44 mg/L. It was noted from jar test data that surface charge for settled water changed from -2.57 ± 0.7 to a more negative value of -30.2 ± 2.5. This reconfirmed the increase in anions (e.g., sulphate, hydroxyl ions) at higher pH. When the pH value of a system was higher than the pKa values for humic acid, for instance in the case of pH 6.8, the disassociated anions (which carried negative charges) of humic acid was shown to replace the positively charged $–OH_2$ functional groups on iron oxide surfaces (Liu and Huang 2001); while the hydroxyl (-OH) groups were left behind on their surfaces. This also explains the observed trend of more negative zeta potential values.

Notably, the region containing peaks at 1559 and 1363 cm^{-1} was similar for pHs 4.5 and 6.8, as seen in Figure 6.4. A closer comparison of those regions (Figure A.4) in revealed relatively low absorbance intensity for peaks formed at pH 6.8 than those at pH 4.5 and the signature of those peaks experienced a slight shift by 1 cm^{-1} to higher wavelength at pH 6.8. However, this minimal change between the IR spectra did not provide any substantial evidence for any differences in the

adsorption mechanism that was proposed in the previous section, indicating the surface adsorption by ligand exchange between iron and carboxylate group of organic compounds was prevalent for both the pHs. At higher pH, more protons were disassociated and may have formed complexes with iron, which may explain the asymmetric and symmetric COO^- vibrations at 1559 and 1363 cm^{-1} in those complexes.

The change in pH caused some changes to the fingerprinting region below 1100 cm^{-1}, which was similar to the observed changes in Figure 6.3. The S-O stretch and S-O bands of sulphate was noticeable at 1140-1080 cm^{-1} and 680-610 cm^{-1} for pH 6.8, respectively (Figure 6.4). Interestingly, this intense band at 1100 cm^{-1} was noticed during the rapid mixing phase for pH 4.8 experiments (Figure 6.3). It is suspected that these changes were attributed to the association of sulfur/oxygen bonds with hydrocarbons in the humic network. SEM-EDS analyses were probed to get an insight on adsorption mechanisms.

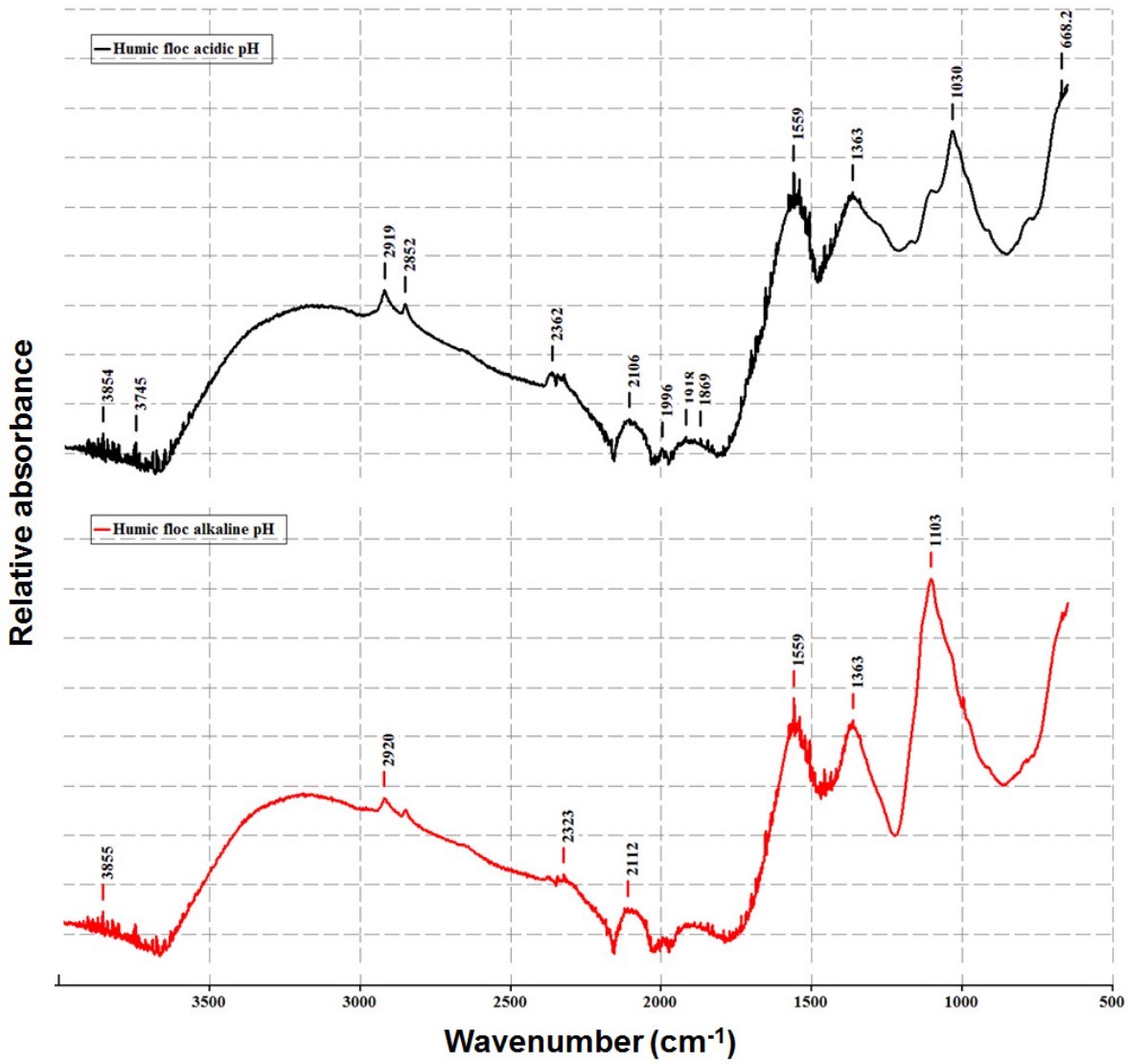

Figure 6.4 Comparison of FT-IR spectra of humic acid flocs at the two selected pHs

(a) an acidic pH of 4.5 and an optimal coagulant iron dose of 8 mg/L (b) a near neutral pH of 6.8 and an optimal coagulant iron dose of 14 mg/L of Fe

6.4.4.1Morphology of Flocs

Structural variation was observed between images for pHs 4.5 and 6.8; however, it could be an artefact of the natural drying procedure selected for preparing SEM samples. SEM images combined with an EDS analysis provided some insight on floc formation at different pHs.

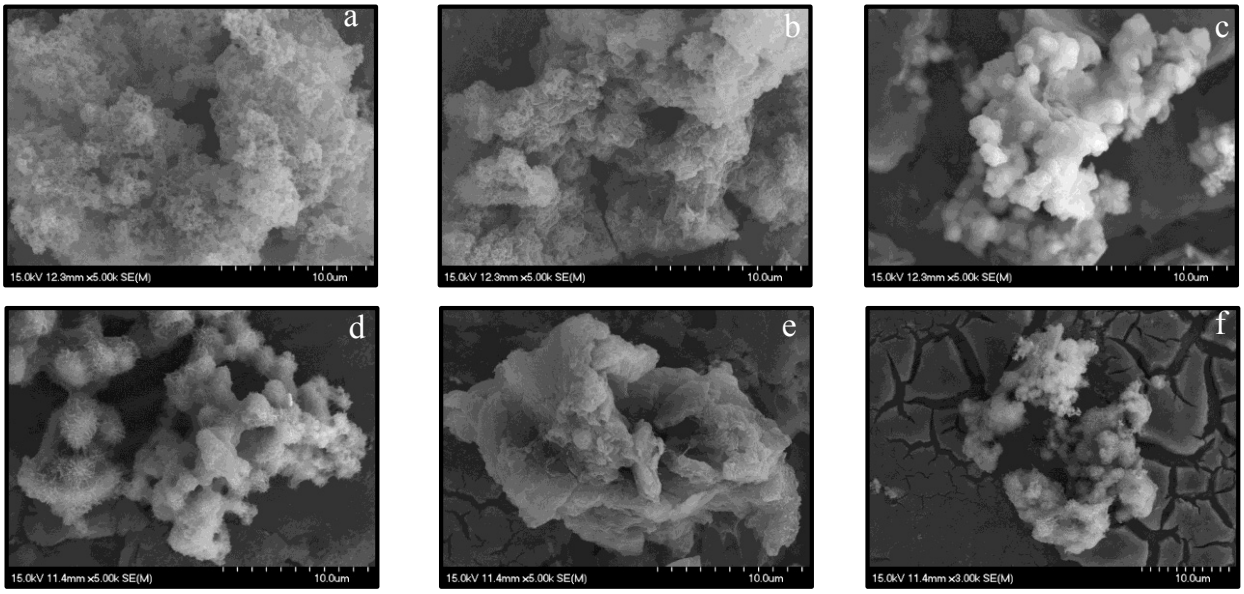

Figure 6.5 Comparison of micrograph images of humic acid flocs at the two selected pHs

Acidic pH 4.5 and an optimal coagulant iron dose of 8 mg/L: (a) rapid mix- Image 1 (b) rapid mix- Image 2 (c) after settling process

Near neutral pH of 6.8 and an optimal iron dose of 14 mg/L: (d) rapid mix- Image 1 (e) rapid mix- Image 2 (f) rapid mix- Image 3

Note: Each reported values are average of at least 4 EDS spectras carried out at different spots

Table 6.3 SEM-EDS analysis of microfloc structures at the two selected pHs

SEM-EDS Sample ID	Ratio of normalized weight (%) O/C	Ca/C	Na/C	Mg/C	Al/C	Fe/C	S/C
(a) pH 4.5 and 8 mg/L of Fe							
Rapid mix	**6.31(2.83)**	**0**	**-0.02(0.02)**	**1.09(0.83)**	**ND**	**0.51(0.37)**	**0.86(0.78)**
Settled water	**1.04(0.29)**	**0**	**0**	**0.03(0.03)**	**0.07(0.01)**	**1.16(0.61)**	**0.02(0.01)**
(b) pH 6.8 and 14 mg/L of Fe							
Rapid mix	**2.36(1.34)**	**0.01(0.00)**	**0.45(0.29)**	**0.09(0.05)**	**0.53(0.30)**	**1.38(0.92)**	**0.15(0.10)**
Supernatant	**1.95(0.15)**	**0.05**	**0.27(0.11)**	**ND**	**2.07(1.15)**	**0.37(0.42)**	**0.10(0.04)**

Note: Each reported values are average of at least 6-8 EDS spectra carried out at different spots on various images

Micrographs of SEM images in Figure 6.5 showed the presence of fibrillar (or filament-like) aggregates of size approximately 10 μm or less formed at both the selected pHs. Such filament-like structures were formed in abundant during the initial rapid mixing stages (e.g., in Figure 6.5 a,b, & e), with the ratio of iron to carbon correlated well with the calculated theoretical ratio of 0.8 and 1.6 mg of Fe/ mg of TOC for pH 4.5 and 6.8, respectively. After the settling process, the precipitates had a rich source of iron and oxygen, along with the presence of carbon, aluminum and other impurities that were initially present in humic acid (Figure 6.1 (*bottom panel*)). Many of the settled SEM images resembled spheroid-like structures that had a high iron content, along with other elements such as magnesium and aluminum. Notably, these precipitates were also identified in the rapid mix flocs samples for pH 6.8 experiments. This is partly attributed to a relative high theoretical iron to carbon ratio (i.e., 1.6 mg of Fe/mg of TOC) used in those jar test experiments that may have resulted in their formation at early stages of microfloc growth (Figure 6.5d & 6.5f).

Figure A.5 shows that the portion of humic macromolecules that remained after settling process (i.e., supernatant). They were small granular aggregates that appeared to have bridged into elongated/branched structures, having a less Fe/C ratio (Table 6.3). This finding is consistent with the electron energy loss spectroscopy investigation (Jung et al. 2005), wherein the supernatant was characterized by a higher calcium content and carboxylic group, with lesser amount of hydrolyzed Fe species.

Most of the images had a fairly detectable range of percentage of aluminum (Al) to carbon ratio (Table 6.3). Both the trivalent metal ions were shown to have a greater affinity to bind to humic acid (Alberts and Filip 1998). The rate of competing reactions involving aluminum and fulvic acid was expected less than 1 s (Dempsey et al. 1984). This implies aluminum that was present originally in the humic acid may have competed with iron for binding sites. Even though aluminum was measured in both rapid mix and settled floc sludge, it was not conclusive since Al in the SEM specimen material may have interfered with the analysis. Isolated adsorption studies are required to confirm about interferences of other metals during coagulation process.

The sulphur to carbon ratio varied among floc types (Table 6.3), this can be related to a large distortion indicated in the FT-IR analysis to the SO_4 tetrahedra during coagulation. In particular, the settled water flocs formed at pH 4.5 had a S/C ratio less than 0.03%; while S/C ratio was over 0.1%, which indicates probable influence of sulphates on sorption process of organic compounds. Webster et al. (1998) showed ternary complexes between oxide surface, SO_4, and the metal ion enhanced adsorption of copper onto goethite. Further adsorption study are recommended to get an insight on preferential interactions of sulphur with DOM in the presence of iron.

6.4.5 Sorption Mechanism of DOM Removal during Coagulation

The data from FT-IR and SEM-EDS analyses in previous sections may be used to draw some inferences on the nature of associations between hydrolyzed iron and natural dissolved organic matter during coagulation. Although a combination of soluble and insoluble complexes may exist in the experimental conditions, hydrolysis was assumed to largely result in the formation of amorphous precipitates at an iron to carbon ratio of 0.8-2.3 calculated from EDS analyses in this study (Bose and Reckhow 1998). In fact, The experimental values of aluminum/TOC ratio from Bose and Reckhow (1998) were 1-2 orders of magnitude higher than theoretical calculation, indicating much of the aluminum-DOM complex formed was composed of aluminum hydroxide flocs, which was a valid argument for the present case. The acid-base titration curve also provided a quantitative explanation on the formation of soluble and insoluble precipitates, suggesting precipitation of soluble complexes to insoluble precipitates may have occurred near pH 5.1 and 9 (Figure B.6).

The SEM analysis showed no clear evidence of crystallinity in floc structures, supporting the above interpretation. It had more irregular surfaces resembling amorphous morphology of precipitates, which are typically expected in coagulation of water treatment (Davis and Edwards 2014, Sari and Chellam 2015). Most of the SEM-EDS samples analyzed had a higher oxygen content (Table 6.3). This could be partly due to the drying procedure followed during SEM preparation that could have resulted in transformation of amorphous iron hydroxides ($Fe(OH)_3$) to iron (oxy)hydroxide (FeOOH); however, this type of structural transformation was suggested to occur at a high temperature of 104 ^{0}C (Goodwill et al. 2015). Other possible explanation was

air-dried samples may still contain water molecules in floc structure that can result in a highly disordered arrangement floc structures. X-ray powder diffraction (XRD) analysis of floc surfaces to prove the dominance of (oxy)hydroxides was not successful due to irregular structural arrangements.

Ferrihydrite (iron (oxy)hydroxides) and Schwertmannite (iron (oxy)hydroxy sulfate) precipitates are known for poor crystalline structures (Ramimoghadam et al. 2014), which are likely to have formed in this study. For instance, few aggregates displayed in Figure 6.7 (c, d, & f) contain needle-like structures on their surface to provide a pin-cushion morphology, which was recognized as the characteristics of Schwertmannite (iron-oxy hydroxysulfate) precipitates (Bigham et al. 1994). These spheroid-like structures had high iron content, along with other elements such as sodium, aluminum, calcium, and magnesium. Schwertmannite are characterized by a high surface area in the range of 55 to 200 m^2/g (Bigham et al. 1994, Webster et al. 1998), which may explain adsorption of small aggregates on to iron (oxy)hydroxide precipitates during settling process.

Many studies have agreed upon humic acid being capable of binding to metal oxides or hydroxides and form insoluble precipitates (Bose and Reckhow 1998, Narkis and Rebhun 1977, Sieliechi et al. 2008). The interpretation from FTIR and SEM-EDS data in the present study supports surface complexation, where protonated weaker carboxylic groups were proposed to bind on to the surfaces of iron. The resulting iron-DOM complexes from a site specific adsorption via ligand exchange are suggested to have formed inner-sphere complexes (Guan et al., 2006, Lu et al. 1997). Neutralization of surface charges in surface complexation reactions indicated precipitation of soluble complexes and/or strong adsorption onto (solid) iron precipitates as the dominant mechanism responsible for DOM removal (Pernitsky and Edzwald 2006), at both the selected pHs presented.

Precipitated hydroxides contain the remaining surface active hydroxyl groups, including –OH and $–OH_2$, which can form chemical bridging between other iron hydroxide sites, containing at least one water molecule in their structure (i.e., $HOH^{\cdots}OH$) (Rustad and Casey 2006, Yu et al. 2016). An increase in the stretching band at 3700-3500 cm^{-1} of free surface –OH groups in the

FTIR spectra (Nakamoto, 1986) supported this theory of presence of more hydroxyl linkage. The participation of hydroxyl group in the adsorption process of humic substances was signified from the shift in the –OH stretch at 3173 cm^{-1} in ferric sulfate coagulant to a higher wavenumber, approximately 3300 cm^{-1} in both the pHs. This type of adsorption formed through a nonspecific adsorption (e.g., electrostatic attraction) are termed as outer-sphere surface complex (Goldberg 2013). This process may have caused flocs to grow during flocculation. Future work on adsorption studies are recommended to validate this theory by conducting experiments at different pH, iron, and DOM concentrations.

6.5 Practical Implications and Concluding Remarks

Understanding the mechanism of formation of floc aggregates in coagulation and flocculation is of environmental importance, as the fate and transport of sorbed organic contaminants and trace metals are dependent on type of flocs formed. The multilevel structure of flocs was examined by conducting surface analyses on flocs, following coagulation and settling process. Sample preparation played a key role in both FT-IR and SEM analyses. It was found from the preliminary investigation of spectral that the drying procedures examined had some influence on the FT-IR spectra generated for DOM-metal complexes. Drying may have also resulted in some morphological changes to floc as supposed to a wet floc. Dehydration indicated a large distortion to SO_4 tetrahedra in ferric sulfate structure (Ling and Wang, 2010). When a trivalent metal ion reacts with both carboxylic and phenolic group (chelating structure), a strain on such metal-humate complexes are suggested to cause thermal decompositions (Lu et al. 1997). Therefore, it is recommended to use a wet procedure for both surface (e.g., DRIFT spectroscopy) and morphological analyses (e.g., Transmission electron microscopy coupled with an energy dispersive X-ray spectroscopy).

The results presented in this study can be treated as exploratory. Nevertheless, the conclusion drawn from this study adds to the growing body of literature probing into mechanisms of DOM removal and floc aggregations. In this study, using FT-IR and SEM-EDS analysis, the sorption mechanisms for DOM removal was suggested to have formed from primary and secondary interactions during the coagulation and flocculation experiments. Floc aggregates were composed of micro-aggregates of less than 10 μm (SEM images), following coagulation. These

flocs appeared to have formed from surface complexation reactions between carboxylate ions of humic acid and iron hydrolyzed species. Large aggregates following the settling process appeared to have formed from the chemical bridging between iron hydroxides, a secondary interaction that may have formed an outer-sphere complex. Surface water containing impurities and dissolved inorganic constituents that are likely to show similar floc complexation reactions.

Chapter 7 Influence of the Mixing Energy Consumption Affecting Coagulation and Floc Aggregation

7.1 Abstract

The operational use of energy-intensive rapid mixing process remain unaddressed in coagulation and during aggregation of insoluble precipitates (flocs), which play an important role in the removal of impurities from drinking water supplies. In this study, the influence of rapid mixing and its associated mixing energy on floc aggregation was examined for a surface water source, characterized with a high fraction of aquatic humic matter. Infrared spectral analyses showed that the colloidal complexes resulting from ligand exchange between iron and dissolved natural organic matter (DOM) were less influenced by the mixing energy input. This signified DOM removal by coagulation can be achieved at reduced energy consumption. In contrast, macroscopic investigations showed the coagulation mixing energy affected floc size distributions during the slow mixing stage in flocculation and to some extent, their settling characteristics. The results from analysis of floc properties clearly showed that more mixing energy was expended than necessary in coagulation, which are typically designed at high mixing intensity range of 600-1000 s^{-1} in treatment plants. The key findings from this study have practical implications to water utilities to strategically meet water quality goals while reducing energy demands.

7.1.1 Abstract Art

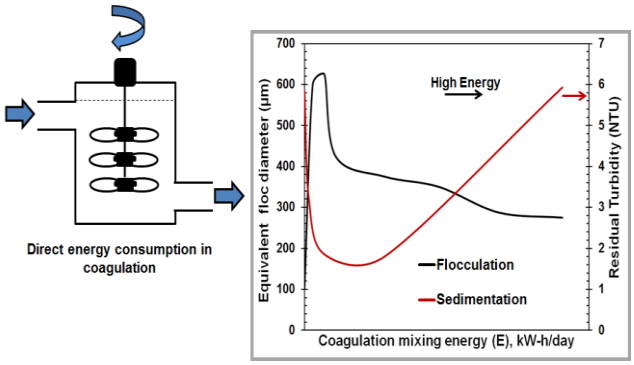

7.2 Introduction

Urban water infrastructure systems require significant amounts of energy for proper operation of major processes, which may include water intake, conveyance, treatment, and distribution systems, to deliver a safe and high-quality drinking water to customers. Life cycle analysis (LCA) are often used to quantify energy usage at each stage[1-3] as measured by energy benchmarks, such as kilowatt-hour of electricity consumed per unit volume of treated water.[4] Accordingly, the predominant use of electricity is directly associated with pumping costs (e.g., low lift and/or high lift pumps), which are connected to the pressure demands and operational characteristics of water distribution networks. This represents a 60-85% of total electricity consumption for surface water treatment plants.[1,5] Rapid mixing in coagulation is described as the second largest consumer of direct energy in a conventional plant.[2,5] A report from the Electric Power Research Institute (EPRI)[5] accounts for an estimated total electricity consumption of approximately 308 kW-h/day during rapid mixing process in a representative surface water treatment plant, with a daily intake of 45 Million liter/day. The primary energy (e.g., fossil fuels, nuclear energy, renewable energy) used in the production of electricity for the operation of these systems is associated with the energy cost and greenhouse gas (GHG) emissions.[6]

In water treatment practice, high energy is expended to ensure instantaneous dispersal of chemicals added during coagulation with the plant influent. Tanks are typically designed for intense mixing with the root mean square velocity gradient (G-value) of 600-1000 s^{-1}.[7] Previous studies have identified several disadvantages in these tank design,[8,9] stating that the practice of intense mixing in coagulation is largely overemphasized. A major shortcoming is that a relatively large amount of energy is utilized to achieve a typical design guideline since the average power supplied varies by the square of G-values. For instance, Edzwald [9] calculated the power requirement to achieve a typical G-value of 750 s^{-1} was 6.25 times greater when compared to 300 s^{-1}. This reflects a proportional increase in the energy cost and associated carbon emissions.

Recent experimental investigations have supported the theory that the coagulation process has a great potential for energy savings with regards to rapid mixing conditions, without sacrificing water quality standards.[10,11] For instance, Vadasarukkai, et al.[11] has proposed a low-mixing intensity range of 110 $s^{-1} < G < 450$ s^{-1} for a combined effective removal of turbidity and

dissolved natural organic matter (DOM). Nevertheless, there has been no study to date that examines how energy utilized in coagulation specifically influences the overall aggregation of metal hydroxide precipitates. Surface hydroxyl groups on these precipitates aid in effective sorption of turbidity, pathogen, inorganic, and DOM to their surfaces. Such surface functional groups can also grow into large sized aggregates by formation of hydroxyl bridges between other metal precipitates,[12] collectively terms as floc aggregates. These aggregates play a vital role in the fate, transport of contaminants incorporated in their structural matrix and their removal in subsequent solid-liquid separation processes.

In efforts to reduce targeted impurities from drinking water supplies, it is essentially important to understand the factors that may affect floc aggregation. The objective of this research is to understand how and to what degree the mixing energy consumed in coagulation influences the overall characteristics of floc, including morphology, size distributions, and their settling characteristics. Surface analyses of flocs formed immediately after the rapid mixing operation (i.e., microflocs) were characterized using Fourier transform infrared (FT-IR) spectroscopy. This was performed to obtain specific information on the mechanism of interaction(s) of sorbed constituents and the metal hydroxide precipitates. Additionally, morphology of microflocs formed during the rapid mixing stage were investigated using a transmission electron microscope (TEM), a scanning electron microscopy (SEM) combined with an energy dispersive X-Ray spectrometry (EDS). A digital in-line holographic microscope (DIHM) was used to measure floc size distributions during slow mixing in the flocculation stage. The results from this present study would provide opportunities for water utilities to strategically meet both water quality goals and energy demands. In particular, it is estimated that an average of 10% reduction in annual energy costs in utilities across the U.S. represents a saving of more than $400 million annually to the water industry.[13] It is anticipated that this study will contribute to the ongoing research and development in implementing technologies for an effective management of energy resources, costs, and carbon footprints.

7.3 Materials and Methods

7.3.1 Water Quality

The Kelly Lake water drawn from the intake at the Louisbourg drinking water treatment plant (Sydney, NS, Canada) was used in this study. This raw water source is characterized with an average specific ultraviolet absorbance (SUVA) of 4-4.2 units of m^{-1} of absorbance per mg/L, indicating a high fraction of aquatic humic matter. Detailed characteristics of this source water are explained elsewhere.[11] The inductively coupled plasma-mass spectrometry (ICP-MS) (Thermo Scientific XSeries II ICP-MS, Waltham, Massachusetts) analysis showed the raw water contained trace elements, including magnesium, sodium, and calcium, as highlighted in Table 7.1.

Table 7.1 Inductively coupled plasma-mass spectrometry (ICP-MS) data of the raw water

Elemental Analysis	Concentration (µg/L)
Magnesium (Mg)	556 ± 2.7
Iron (Fe)	330 ± 2.4
Sodium (Na)	3900 ± 2.8
Aluminum (Al)	111 ± 1.0
Calcium (Ca)	1470 ± 11.3
Potassium (K)	196 ± 5.4

7.3.2 Coagulation-Flocculation Experiments

Coagulation and flocculation experiments were tested at two pH conditions, i.e., at a slightly acidic pH of 4.8 and a near neutral pH of 6.85, following a procedure similar to that of Vadasarukkai, et al..[11] In that study, an iron dose of 0.33 mM and 0.66 mM was determined as optimal coagulant concentration (OCC) of ferric sulphate for 68% removal of turbidity and total organic carbon (TOC) from the raw water at pHs 4.8 and 6.85, respectively. These optimal chemical conditions were used for enhanced coagulation in the present study to form iron-DOM floc aggregates.

All experiments were carried out at a room temperature (21 ± 1 ^{o}C) in a 1-L square jar test beaker, fitted with a flat paddle impeller (76 x 25 mm). A compact digital mixer (Cole-Parmer,

Vernon Hills, Illinois), which had a mixing capacity ranging from 50 to 2500 rpm, was used to mix the water sample. The equivalent G-value for the flat paddle impeller configuration was determined from the laboratory velocity gradient calibration chart (G-curve) of Cornwell and Bishop.[14] The solution was adjusted to the required pH (4.8 or 6.85) by adding a pre-determined volume of the pH adjusting chemicals (i.e., 1 N NaOH or 0.2 HNO_3 solutions). All the reagents used were of analytical grade and stock solutions were prepared using deionized (DI) water.

Energy calculations were based for a representative surface water treatment facility, with an average flow of 120 Million liter/day. Equation 7.1 was used to calculate the daily consumption of energy during the rapid mixing operation in the coagulation process, expressed in kilowatt-hour/day. The average power supplied to stir the mechanical mixer was calculated from the previously determined G-value, assuming at a motor efficiency of 85%. A water temperature of 15°C, a 20 s of retention time in the rapid mixing tanks, and a power cost of $0.12 per kW-h was used as the plant design conditions.[9]

$$\mathbf{E = P_{avg} \times t = \left(\frac{G^2 \times Q_{avg} \times t_m \times \mu}{\eta} \right) \times t} \qquad (7.1)$$

where P_{avg} is the average power supplied in a mixing tank (J/s), t is the operating time period of the mixer (assumed as 24 hour), G is the root mean square velocity gradient (s^{-1}), μ is the dynamic viscosity of water (kg/m.s), η is the motor efficiency, Q_{avg} is the average daily plant flow rate (m^3/s), and t_m is the mean hydraulic retention time (s).

Each coagulation experiment was rotated at a pre-fixed speed ranging from 0 to 750 rpm, which gave an equivalent G-value range from 0 to 1450 s^{-1}. The corresponding energy consumption was calculated from Equation 7.1. An optimized dose of ferric sulphate and a calculated volume of pH adjusting chemicals were added at the start of the rapid mix. Coagulation was conducted for 90 s at a specific rapid mixing G-value. Flocculation was mixed at a fixed 46 s^{-1} for 18 min. The energy consumed in the slow-mixing stage was not included in the total energy consumption of the plant, which accounts for 103 kW-h/day. The operating conditions used in this study were within the recommended standards followed in water treatment plants,[7,15] except for the G-value and 90 s of mixing time specified in the coagulation experiments. Although the use of more than

one chemical (e.g. ferric sulphate, 1 N NaOH or 0.2 HNO_3 solutions) in the present case required this additional detention time to simulate plant conditions.[7]

7.3.3 Characterization of Micro-, Macro- Structures of Iron-DOM Floc Aggregates

7.3.3.1 Rapid Mixing Stage

Analyses of the functional groups in the resulting microflocs was performed using an attenuated total reflectance Fourier transform infrared spectroscopy (FT-IR) in the mid-infrared region of 4000-650 cm^{-1} in the absorption mode (Cary 630 ATR FT-IR, Agilent Technologies, California). A 200 mL of sample was collected immediately after the rapid mixing process, and it was oven dried at 35-40 ^{0}C for at least 3-4 days until the water was evaporated from the sample. An attenuated total reflectance flow cell with a zinc selenide (Zn-Se) crystal was used for this purpose. The Happ-Genzel method was used with 200 scans at a resolution of 2 cm^{-1}. Backgrounds were taken with the crystal alone. Analysis of the spectral data was performed using optical spectroscopy software (Spekwin32, Germany).[16]

The morphology of microflocs was examined using the FEI Tecnai-12 transmission electron microscope (TEM) (Hillsboro, Oregon) equipped with a Gatan 832 CCD camera and Gatan Microscopy suite software. Approximately 20 mL sample was collected from the rapid mixing stage and it was stored at 4 ºC. A droplet of the TEM sample was carefully placed on a 200-mesh copper grid from Electron Microscopy Sciences (Hatfield, Pennsylvania). The grid was then allowed to dry at room temperature for 24 hour. Duplicate samples were prepared for each analysis. A scanning electron microscopy (SEM), along with an energy dispersive x-ray spectroscopy (EDS), was used to analyze the elemental composition of samples from the rapid mixing stage using a Hitachi S-4700 FEG SEM (Hitachi, Tokyo), with an accelerating voltage of 20 kV and an emission current of 8.5 μA. Each EDS spectrum was ran for at least 30s. The SEM samples were prepared in a similar way to the TEM analysis. The samples were coated with gold-palladium using a Polaron SC7620 Mini Sputter Coater (Quorum Technologies, Lewes), with a plasma current of 18 mA for 120s.

7.3.3.2 Flocculation Stage

A digital in-line holographic microscopy (DIHM) from 4deep Inwater Imaging (Halifax, Nova Scotia) was used to measure the dynamic growth of floc sizes during the coagulation-flocculation experiments. The microscope was vertically mounted to one of the corners of the jar beaker, minimizing any interruption to the impeller rotations. Holograms of flocs were recorded continuously at 2 frames per second (fps), and they were stored as digital bitwise images. The formation of microflocs was not recorded at coagulation G-values > 450 s^{-1} due to bubbles formed near the sampling port, which can cause significant errors in size measurements. Numerical reconstruction of holograms was performed to get images of floc aggregates, as described in Vadasarukkai, et al.[17]. Equivalent circular diameter (d) of floc size was calculated from the area of the identified flocs, which was expressed as a volume-based floc equivalent diameter.

7.3.4 Settling Properties

The treated water from the jar test beaker was poured in to an Imhoff cone (Wheaton, Millville, New Jersey) immediately after the slow stirring operation in flocculation. It was allowed to settle at a quiescent period for 24 hours. Samples were collected periodically from 10.3 cm from the water level, using a wide-mouth glass pipette. Residual turbidity measurements were recorded using a HACH 2100AN laboratory turbidimeter (Hach Company, Loveland, Colorado). The volume of settleable solids was recorded at the end of the experiment. This study did not account for a drop in water level height due to the withdrawal of approximately 40 mL of water samples during turbidity measurements, which can result in an estimated 5% discrepancy for the high settling velocity and at approximately a 30% discrepancy for the low settling velocity values.[18] The linear range of the curve was identified, and it was used to determine the sedimentation rate[19], as expressed in Equation 7.2.

$$\mathbf{Slope_{(NTU,min)}} = \frac{y_2 - y_1}{x_2 - x_1} \tag{7.2}$$

where y_1 and y_2 are the values of turbidity in NTU of the linear slope. The slope of the regression line was calculated between the time period 0 (x_1) and 30 (x_2) minutes of the settling period.

7.4 Results and Discussion

7.4.1 Floc Morphology and Size Distributions at Optimal Coagulant Concentrations (OCC)

A high iron to carbon ratio (i.e. > 0.8 mg Fe/mg TOC) used as OCC in the present study resulted in a rapid growth of ferric flocs in the rapid mixing stage itself kept at a G of 175 s^{-1}, which was well within the optimal operating range (i.e., 110 s^{-1} < G < 450 s^{-1}) of mixing energy input recommended for enhanced coagulation.[11] This corresponds to an energy usage of 27 kW-h/day for a 120 Million liter/day representative treatment facility.

TEM micrographs in Figure 7.1 showed a multilevel structural arrangement of flocs, which is consistent with previous investigations.[20] An increase in porosity was evident during the microfloc formation (Figure 7.1a), which signified an increase in water content formed due to possible bridging with other particles or flocs.[21] At least three levels of flocs were formed during the rapid mixing stage. Amongst, two structures were distinct in the colloidal range: dense, spheroid-like or needle-like clusters of 60 -180 nm, and many less dense structures of 50 ± 15 nm, as depicted in Figure 7.1b and 7.1c. The colloidal size range of floc formed was hypothesized as the result of iron-DOM interactions, which is supported by previous microscopic investigations.[22-24] These studies demonstrated the association of coagulant species and humic networks formed similar dark nanoparticles with a variety of shapes, including needle-like, globular or net-like structures. In the present case, many large aggregates were formed from associations of microflocs and discrete flocci. As a resultant, irregular shaped, porous, and less dense floc aggregates ranging up to several microns in size were developed.

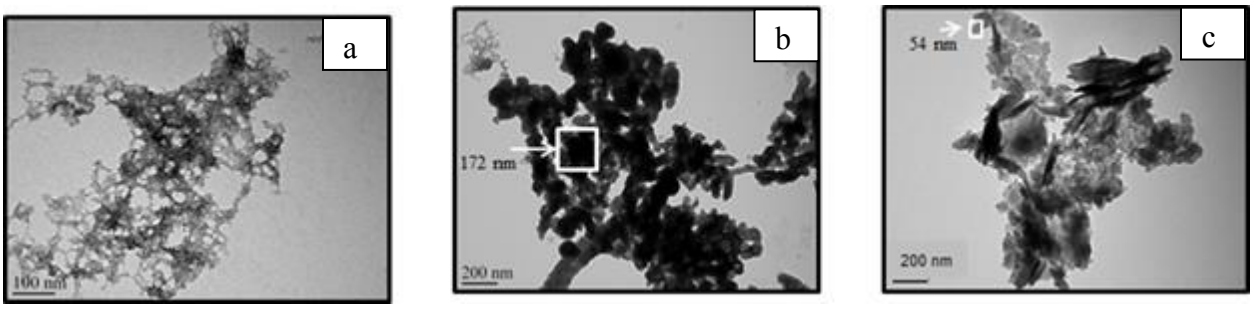

Figure 7.1 TEM images of microfloc formed at a G of 175 s^{-1} for the optimal coagulant concentration of 0.33 mM of Fe and pH = 4.8.

Floc sizes shown in the insert were measured using ImageJ software v1.49.

Changes in the optimal coagulant dose at pH 4.8 and 6.85 resulted in a major difference in the overall floc size distributions between the two experiments, as illustrated in Figure 7.2. A significant difference in the variation of floc size distributions between the two experiments was confirmed using Levene's test (α=0.05; N >30). A high volume fraction of floc sizes, ranging from 100 to 1000 μm, was formed at pH 4.8. It had a median volumetric diameter (D50) at 424 μm. Alternatively, volume of precipitates increased in proportion to the iron dose to 0.66 mM at pH 6.85. This caused a wide variability in floc sizes formed in that case, with a standard deviation of 194 μm. The D50 was increased from 424 to 581 μm at the pH of 6.85.

Unlike distinct differences in floc sizes, it was difficult to interpret the inherent differences in the floc morphology between the two experiments due to complex, multi-level structural formation of aggregates. Details on micrographs are included in the Supporting Information (SI) (i.e. Figures 7.S1 in SI). Most of the TEM micrographs showed similar irregular structures at both the pHs, expect dense flocs were formed at pH 6.85. It was interesting to note the occurrence of bulky and irregular shaped flocs of approximately 100-500 nm at many sections in the TEM grid at pH 6.85 (Figure 7.S1c and 7.S1d in SI), indicating possible enmeshment of DOM structures on the surfaces of amorphous hydroxide precipitates.

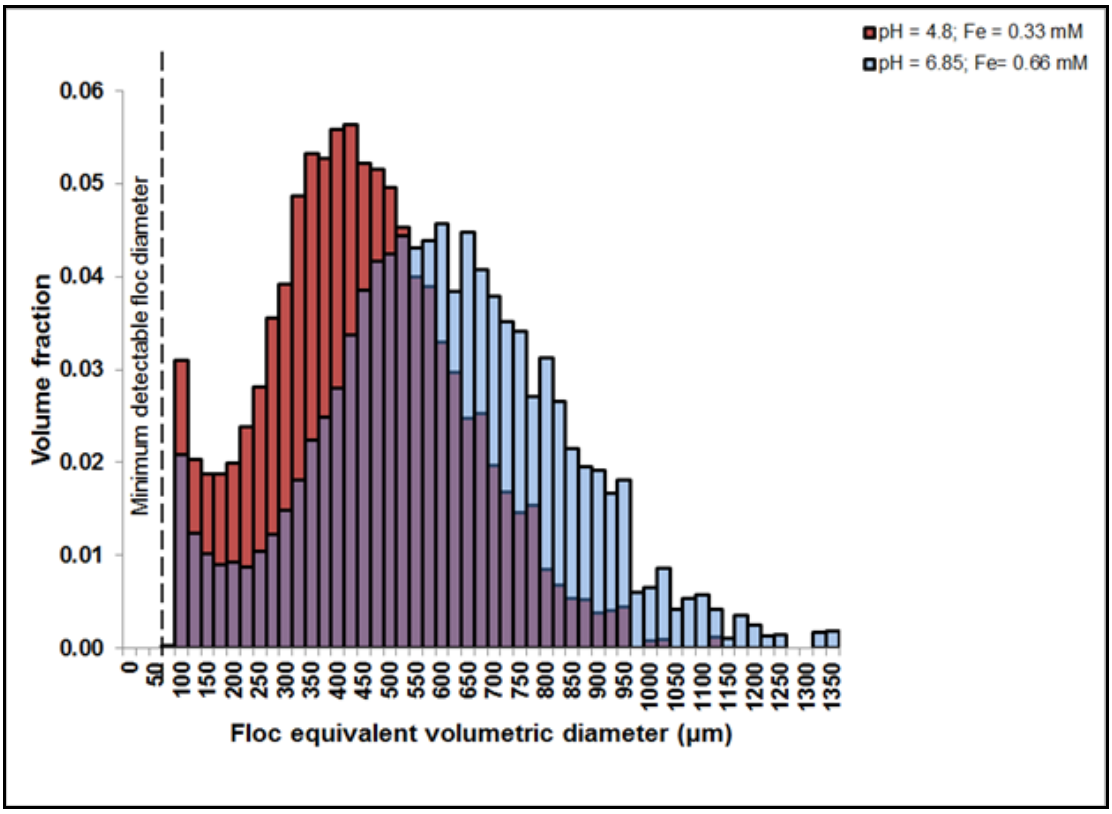

Figure 7.2 Illustration of floc size distributions at a flocculation G-value of 46 s^{-1} for the optimal coagulant concentrations.

The displayed histogram was estimated from three replicate experiments at pH 4.8 and 6.85, respectively.

7.4.2 Influence of Mixing Energy Utilized in Rapid Mixing on Coagulation, Flocculation, and Settling Processes

This section discusses the influence of variation in the mixing energy consumed in coagulation on the overall characteristics of floc properties, including morphology, size distributions, and their settling characteristics. Energy calculations are representative of a 120 Million liter/day surface water treatment facility.

7.4.2.1 Aggregation Behaviour of Primary Particles (DOM) during Coagulation

Initial population has a strong influence on floc size formation.[25] In the present study, a major constituent of primary particles was comprised of dissolved organic matter (DOM), which played an important role in the characteristics of flocs resulting from coagulation. Results from

the FT-IR spectral analyses (Figure 7.S2 in SI) showed similar surface complexation-ligand exchange reactions between DOM and iron hydroxides at both pHs, despite the differences seen in the floc size distributions. This phenomenon of adsorption of DOM on to metal oxide surfaces has been demonstrated previously in natural soil and aqueous systems.[26-28] It resulted in similar IR peaks at 1559 and 1375 cm^{-1} at both the pHs in the present study (spectral results are presented in Figures 7.S2 in SI). These absorption bands represented the stretching vibrations of the carboxylate groups (i.e., COO^-) adsorbed onto the surface active hydroxyl functional groups of iron hydroxides (i.e., Fe-OH_2 and Fe-OH stretches), which has been previously noted for the adsorption process on iron hydroxides.[29]

The adsorption of DOM on iron hydroxides were influenced by the pK_a values of functional groups in the raw water, which had approximate values of 2.85 and 7.03 from acid-base titration curves (data not shown). At pH 4.8, disassociation of protons was expected, favouring the COO^- functional groups to replace the dominant OH_2 groups from surfaces of iron.[30] Therefore, an addition of a 0.33 mM of iron at pH 4.8 resulted in a partial neutralization of the net positive charge on iron hydroxide surfaces and formed insoluble iron-DOM complexes. Alternatively, when the pH was near the pK_a value of 7.03, more protons in the humic networks were disassociated, leading to an increase in the iron dose from 0.33 to 0.66 mM at pH 6.85.

A major difference between the two pHs occurred in the fingerprinting region below 1100 cm^{-1}, which can be explained by the adsorption behaviour of sulphate. Peak, et al.[31] had shown the spectrum of sulfate adsorbed on goethite had a sharply defined peak at 976 cm^{-1} for pH less than 6, forming an inner-sphere sulfate complex with two distinctive splits formed at 1055 and 1133 cm^{-1}. These peaks were similar to the IR peaks formed at pH 4.8 in the current study at 975, 1040, and 1111 cm^{-1}. At pH 6.85, the sharp peak at 975 cm^{-1} was broadened and shifted to 969 cm^{-1}. Aromatic ethers, carbohydrate, and polysaccharide groups also exhibit a broad band near 1120-980 cm^{-1} with a characteristics peak near 1034 cm^{-1}.[32] It is possible that sulphate may have interacted with the co-adsorbed functional groups of DOM macromolecules and formed complexes, instead of directly incorporated on to the surface of iron hydroxides. This observation was previously described for enhanced adsorption of trace metals onto iron oxide

surfaces through the formation of ternary complexes in the presence of high sulphate concentrations.[33]

The relative peak intensity ratios in Table 7.2 provided a quantitative comparison of IR peaks formed at different amount of energy consumed in coagulation. Details on the spectral comparison at different mixing energy input are included in Figure 7.S3 in SI. The ratios for the three prominent peaks of adsorbed constituents (i.e., 1559, 1375 and 1039 cm^{-1}) and the structural O-H vibration (i.e., 3177 cm^{-1}) in the lattice structure of flocs were calculated as I_{1559}/I_{3177}, I_{1375}/I_{3177}, and I_{1039}/I_{3177}. It showed a fairly constant ratio for the adsorbed carboxylate groups (i.e., COO^-) peaks 1559 and 1375 cm^{-1} at different mixing energy input. This suggests iron-DOM complexes formed in the hypothesized colloidal range were less vulnerable to the coagulation G-values. In other words, it implied DOM removal by coagulation can be achieved at reduced energy consumption. Thus, disproves the theory that intense mixing was necessary to bring about particle-particle collision for effective interactions. Although a relatively larger standard deviation for the adsorbed sulphate peak near 1039 cm^{-1} was evident at both the pHs. It implied that the coagulation G-values caused some changes to the shape of absorption spectra of sulphate complexes, indicating changes in their composition.

Table 7.2 Peak intensity ratios calculated from the Infrared spectra at various coagulation mixing intensities (G-value) and the corresponding energy consumed in the coagulation experiments
(a) 0.33 mM of Fe and pH = 4.8 (b) 0.66 mM of Fe and pH= 6.85.

G-values (s^{-1})		**46**	**175**	**452**	**1450**
Energy consumed at 120 MLD (kW-hr/day)		**2**	**27**	**183**	**1879**
Assignment of peak intensity ratios:		**(a) 0.33 mM of Fe and pH = 4.8**			
$\frac{\text{Adsorbed caroboxylate}(\upsilon_{as})}{\text{Structural O}-\text{H}}$	$\frac{\mathbf{I_{1559}}}{\mathbf{I_{3177}}}$	**1.77**	**1.50**	**1.57**	**1.51**
$\frac{\text{Adsorbed caroboxylate}(\upsilon_{s})}{\text{Structural O}-\text{H}}$	$\frac{\mathbf{I_{1375}}}{\mathbf{I_{3177}}}$	**1.61**	**1.32**	**1.46**	**1.33**
$\frac{\text{Adsorbed } SO_4}{\text{Structural O}-\text{H}}$	$\frac{\mathbf{I_{1039}}}{\mathbf{I_{3177}}}$	**2.46**	**1.72**	**1.99**	**1.71**
Assignment of peak intensity ratios:		**(b) 0.66 mM of Fe and pH = 6.85**			
$\frac{\text{Adsorbed caroboxylate}(\upsilon_{as})}{\text{Structural O}-\text{H}}$	$\frac{\mathbf{I_{1558}}}{\mathbf{I_{3177}}}$	**1.29**	**1.44**	**1.34**	**1.32**
$\frac{\text{Adsorbed caroboxylate}(\upsilon_{s})}{\text{Structural O}-\text{H}}$	$\frac{\mathbf{I_{1374}}}{\mathbf{I_{3177}}}$	**1.11**	**1.23**	**1.13**	**1.11**
$\frac{\text{Adsorbed } SO_4}{\text{Structural O}-\text{H}}$	$\frac{\mathbf{I_{1044}}}{\mathbf{I_{3177}}}$	**1.41**	**1.37**	**1.38**	**1.07**

7.4.2.2 Microstructure and their Interactions

The SEM-EDS analysis was used to compare the elemental composition of flocs formed at different mixing energy input in coagulation. Two mixing energies at 2 and 183 kW-h/day are shown for comparison purposes only. In general, most micrographs from SEM had elements of carbon, oxygen, iron, sulphur, and sodium co-existed in their structural matrix. This result, along with the FT-IR analyses, reinforces the interpretation that iron-DOM complexes were formed mainly in the colloidal size range.

Effective contact between iron hydroxides, DOM, and other constituents in the source water matrix was limited at a low energy input of 2 kW-h/day. This may have caused structural rearrangements of DOM macromolecules,[24] which have resulted in a heterogeneous formation of microfloc structures as shown in Figures 7.3a and 7.3b. Flat plate-like structures in a leaf arrangement were formed at pH 4.8; the shape may be an artifact of the natural drying process. On an average, these types of floc structures had less iron (<6 wt %) in their matrix, with a relatively rich source of carbon (21 wt%), oxygen (38 wt%), sulphur (13 wt%), and sodium (7 wt%). This association may have been due to the surface complexation of iron hydroxides with DOM constituents. Even though, the raw water had traces of aluminium, it was not accounted for since Al in the SEM specimen material may have interfered with the analysis. Few aggregates had prominent iron peaks (>14 wt%) with a pin-cushion morphology (not shown), which were the characteristics of Schwertmannite (iron-oxy hydroxy sulfate) precipitates.[34]

The rearrangement of DOM macromolecules was restricted by associations with iron and other particles during a 183 kW-h/day of energy usage, as shown in Figure 7.3b. A relatively smaller size globular aggregate resulted as supposed to flat plate-like arrangements. Previous X-ray microscopic investigations have shown similar shrinkage of anionic humic networks upon binding of cationic coagulant species.[24] Likewise, a bench-scale evaluation of the properties of iron particles by Rahman and Gagnon[35] showed the average (mean) diameter of iron particles reduced from 423 ± 62 nm to 98 ± 0.8 nm in the presence of 2.85 mg/L of DOM. Notably, these globular structures in the present study contained oxygen, carbon, and chlorine in their matrix,

with relatively low peaks of sulphur (< 0.2wt %), and iron (<5 wt %), indicating a possible surface complexation at high mixing intensity.

Floc aggregates formed at pH 6.85 did not have a variety of structural arrangements at different mixing energy. Mostly formed clusters of globular aggregates with a relatively high iron peaks (28 wt%) (data not shown). The presence of iron peaks in inner (K alpha) and outer shells (L alpha) explain an increase in iron concentrations by surface complexation and subsequent adsorption of iron-DOM complexes with other iron hydroxides.

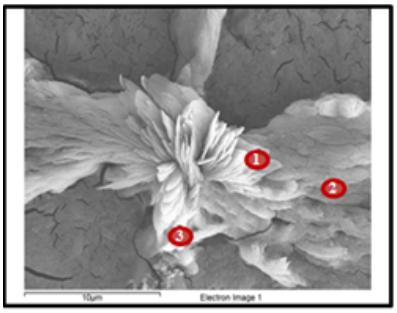

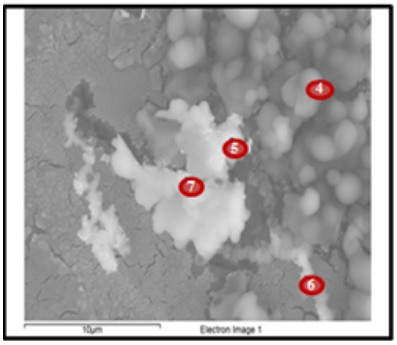

	Normalized weight (%)					
Points	C	O	Na	S	Cl	Fe
At G=46 s^{-1}:	(a) 0.33 mM of Fe and pH = 4.8					
1	19.14	50.89	9.62	7.05	0.57	5.84
2	20.73	25.91	5.48	12.65	1.26	1.72
3	21.62	38.01	6.7	18.34	1.33	2.7
At G=452 s^{-1}:	(b) 0.33 mM of Fe and pH = 4.8					
4	6	76.12	ND	0.1	0.49	0.41
5	12.22	59.42	0.57	0.17	4.81	3.85
6	8.75	66.31	0.47	0.26	3.48	4.43
7	10.42	65.92	0.44	0.1	1.73	3.02

Figure 7.3 SEM-EDS analysis of microfloc structures at different selected points for the coagulation G-values (a) 46 s^{-1} and (b) 452 s^{-1}

7.4.2.3 Floc Size Distribution

Mixing energy input in coagulation governed the floc growth during the slow mixing stage in flocculation, as illustrated in Figure 7.4. Unless stated, the data represents the volume fractions of floc size distributions measured using the in-line holographic microscopy in flocculation at 46 s^{-1}. It was apparent that no mixing energy during coagulation resulted in an obvious decline in the floc size distribution at pH 4.8. On the contrary, a wide range of floc sizes were formed at pH 6.85 even without having a proper mixing condition in coagulation. The slow mixing energy

provided at a 103 kW-h/day in flocculation compensated for the no mixing operation in coagulation and achieved necessary bridging between precipitates in that case. On a similar note, a recent study had shown the overall water treatment performance of a full-scale drinking water treatment plant remained unaffected during the accidental failures of mechanical mixer in the rapid mixing tank.[10]

For an average flow of 120 MLD, the energy consumed to operate at a specified designed G-values of 600-1000 s^{-1} was in the range of 342 to 913 kW-h/day. As seen from Figure 7.4, operating at a mixing energy > 200 kW-h/day did not show any significant improvement in the evolution of floc sizes in flocculation, in terms of median (D50) and 90th percentiles (D90). Conversely, there was a slight drop in the median floc diameter at higher mixing energy. That is, the decrease in the median floc size was from 375 to 275 μm at pH 4.8 and it dropped from 550 to 325 μm at pH 6.85. Likewise, Pivokonsky, et al.[36] found for a pilot-scale set up that a shallow reduction in the average floc diameter was observed at $G \geq 200\ s^{-1}$, with the value of the slope was 0.34. This type of fragmentation of iron hydroxide flocs has been previously indicated for tannery waste samples at > 170 s^{-1}.[37]

A general trend of decrease in floc sizes occurred in the case of higher energy usage, representing aggregate breakage. This phenomenon has been demonstrated previously that, the floc aggregates became more compact and homogeneous in size with increasing G-values.[25,36] Floc breakage can pose an important practical problem by causing resuspension of impurities and increased iron concentrations in settled water. An overall shift in the floc size distributions to the left support this theory of an increase in the volume fractions of smaller flocs less than 100 μm in diameter. Although the minimum detectable size of the instrument was not sufficient to capture the increase in floc sizes of less than 50 μm. Recent work of Yu, et al.[12] suggest that broken flocs may not grow into large aggregates due to a net reduction in the number of active surface hydroxyl groups. This may greatly reduce the effectiveness of separation processes in the present case.

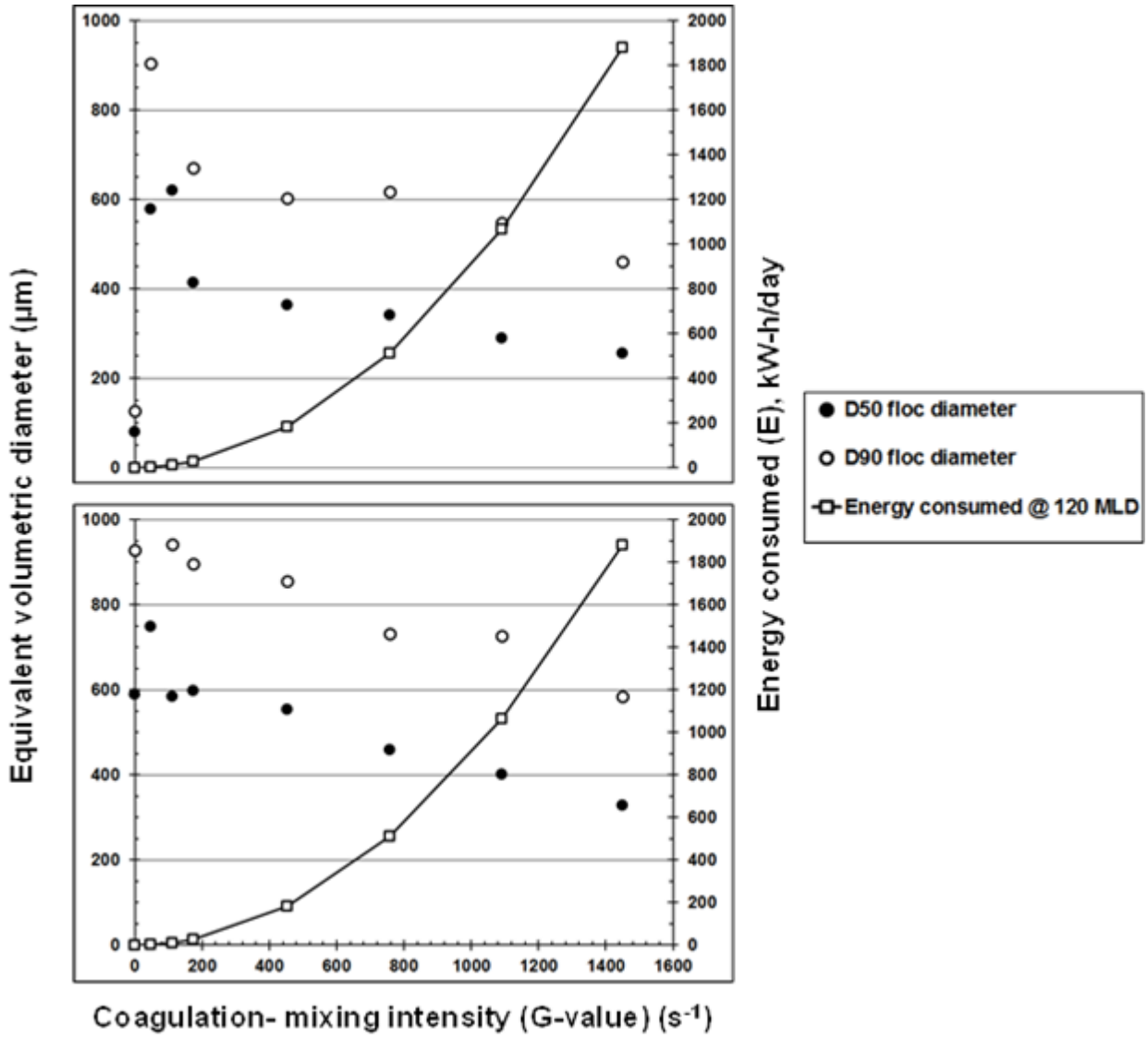

Figure 7.4 Variation in floc size distributions with the change in the coagulation mixing intensities (G-value)

The corresponding energy consumed for the coagulation experiments conducted at 0.33 mM of Fe and pH = 4.8 *(top panel)* and 0.66 mM of Fe and pH= 6.85 *(bottom panel)*.

7.4.2.4 Settling Kinetics of Flocs

Comparison of slope values in Table 7.3 indicated the sedimentation rates were higher for the optimal iron dose of 0.66 mM at pH 6.85 than at 0.33 mM at pH 4.8. This implied a faster rate of floc formation and consequent settling rates were achieved at a relatively high particle concentration,[19] in the case of the near neutral pH.

Table 7.3 Influence of the coagulation mixing intensities (G-value) and the corresponding energy consumed on the sedimentation rate as calculated from the slope

G-values (s^{-1})	0	24	112	452	1450
Energy consumed at 120 MLD (kW-hr/day)	**0**	**0.5**	**11**	**182**	**1879**
Sedimentation rate (NTU/min):*	**(a) 0.33 mM of Fe and pH = 4.8**				
	-0.32	**-0.17**	**-0.17**	**-0.10**	**-0.18**
Sedimentation rate (NTU/min):*	**(b) 0.66 mM of Fe and pH = 6.85**				
	-0.52	**-0.33**	**-0.32**	**-0.25**	**-0.61**

* The slope of the regression line was calculated between the time period 0 (x_1) and 30 (x_2) minutes of the settling period.

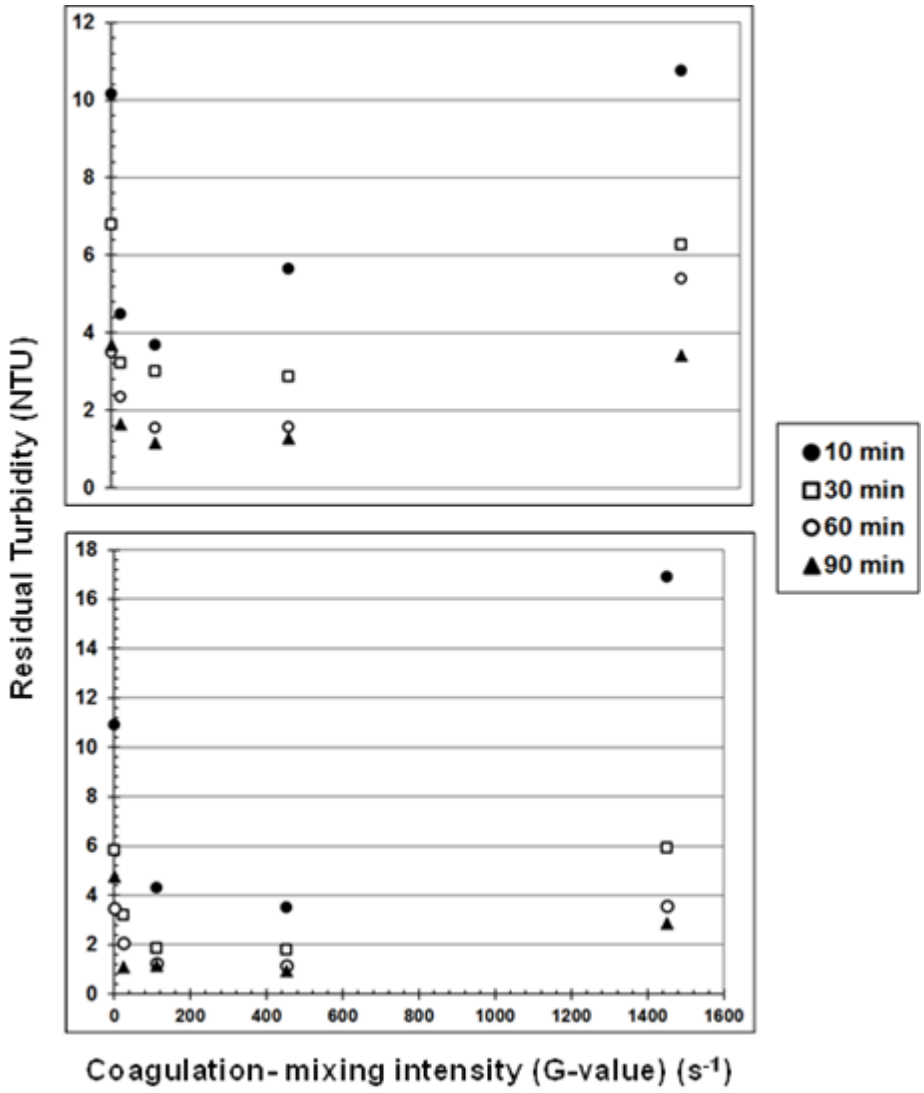

Figure 7.5 Influence of the coagulation mixing intensities (G-value) on settling kinetics
The coagulation experiments conducted at 0.33 mM of Fe and pH = 4.8 *(top panel)* and 0.66 mM of Fe and pH= 6.85 *(bottom panel)*.

The settled water turbidity curve in Figure 7.5 provides a comparative evaluation of the effect of coagulation mixing energy on the settling characteristics of flocs. An overall decreasing trend of residual turbidity with time denoted the sedimentation process offered a dampening effect on the coagulation mixing energy. In other words, there was no significant difference in the settling kinetics after 60 min, particularly in the recommended mixing energy range of 11 to 181 kW-h.[11] Although a gradual rise in residual turbidity of the settled water was projected for the mixing energy between 182 and 1879 kW-h/day. Compact flocs (essentially smaller size particles) that resulted at a higher coagulation mixing energy were able to settle given enough time. Although

the window of opportunity was much narrow for high rate sedimentation at overflow rates of < 0.3 cm/min. As expected, when the coagulation mixing energy was at 0 kW-h/day (i.e. G= 0 s^{-1}) and 1879 kW-h/day (i.e. G= 1450 s^{-1}), the suspended solid concentrations were fairly high (> 2 NTU) even after a quiescent period was provided at an overflow rate of 0.1 cm/min. This demonstrated a minimum amount of energy is necessary to form settleable flocs and for effective separation of those aggregates from the settled water in the subsequent separation processes.

7.5 Practical Implications for Water Treatment

The evaluation of the key findings from the present study is a critical step in the process of intermediate pilot-scale and full-scale implementations. In treatment plants, physicochemical conditions related to the coagulant type and dose, temperature, and pH are routinely optimized at laboratory-scale jar test and pilot-scale analyses. Mixing energy input associated with the tank geometry, impeller types and speed are not often optimized for floc growth in existing infrastructure systems. This shortcoming in the design of rapid mixing system is too big to ignore in the current scenario of rising demands for energy and water, and consequent emissions of carbon. Evidently, more mixing energy is expended than necessary to operate at a recommended design G-values. In the case of a 120 MLD water treatment system, reducing energy consumption from a 502 kW-h/day to less than 200 kW-h/day would result in an annual energy savings of nearly 170 MW-h/year. That is, savings over 90% can be achieved depending on plant flow rate. It is pertinent that stakeholders and decision-makers consider the key results from this study to prioritize energy efficiency opportunities.

Flocs play a significant role in the transportation of dissolved natural organic matter (DOM) and other impurities within engineered treatment systems and their subsequent removal from drinking water supplies. In this study, floc characteristics for a surface water source was investigated at two pHs from within a range commonly associated with drinking water treatment. An important inference drawn is that the mixing energy did not have an influence on the iron-DOM colloidal complexes formed in coagulation. While this phenomenon of complexation of DOM on to the surface of metal oxide is well documented in early mechanistic studies,[26] it is expected the impact of the reported finding is applicable to other water sources and coagulant types. Further investigations on different particle concentrations are recommended.

A major difference in the overall floc size distributions resulting at the optimal coagulant concentrations would have potential implications for a number of treatment plants. Prior investigation on the spatial distribution of floc sizes at a direct filtration plant suggests large, irregular shaped floc aggregates can reduce the effective filter run times.[17] The data acquired from the present study on floc sizes can be calibrated to a treatment plant requirement by operating at a definite pH, coagulant dose and mixing energy. For plants requiring dense and pin-point flocs, for example in a direct filtration facility, a small standard deviation in floc sizes will be beneficial. This can be achieved at a slightly acidic pH condition. Whereas in treatment plants with slow clarification processes it may be more desirable at a higher pH as it resulted in a relatively high standard deviation in floc size distributions.

7.6 Associated Content

Supporting Information
Three figures (TEM micrographs, Figure 7.S1; FT-IR spectral data, Figures 7.S2 and 7.S3) addressing additional experimental data are included.

7.7 Acknowledgements

The authors acknowledge the financial support of both NSERC and Halifax Water through the NSERC/Halifax Water Industrial Research Chair program. The authors acknowledge the Institute for Research in Materials (IRM) at Dalhousie University. The authors thank the technical and in-kind supports of Patricia Scallion (IRM, Dalhousie University) during SEM analysis and Dr. Ping Li (Biology Dept., Dalhousie University) in executing TEM analysis. We thank Jon-Paul Sun (Ph.D. Student) from the department of Physics at Dalhousie University for allowing us to use the FTIR instrument. The authors also acknowledge the technical support of Heather Daurie at Dalhousie University's Clean Water lab. We would like to thank the Louisbourg water treatment plant authority, Nova Scotia, Canada for providing access to the water treatment for sampling.

7.8 References

1. Santana, M. V. E.; Zhang, Q.; Mihelcic, J. R. Influence of water quality on the embodied energy of drinking water treatment. *Environ. Sci. Technol.* **2014***, 48 (5)*, 3084-3091.

2. Plappally, A. K.; Lienhard, J. H. Energy requirements for water production, treatment, end use, reclamation, and disposal. *Renewable & Sustainable Energy Reviews* **2012***, 16 (7)*, 4818-4848.

3. Stokes, J.; Horvath, A. Life cycle energy assessment of alternative water supply systems. *International Journal of Life Cycle Assessment* **2006***, 11 (5)*, 335-343.

4. New York State Energy Research & Development Authority, *Water and Wastewater Energy Management Best Practices Handbook*; New York State Energy Research & Development Authority: Albany, New York, 2010.

5. Electric Power Research Institute, *Water & Sustainability (Volume 4): U.S. Electricity Consumption for Water Supply & Treatment- The Next Half Century;* Electric Power Research Institute Inc.: Palo Alto, CA, 2002.

6. Mo, W.; Wang, R.; Zimmerman, J. B. Energy-water nexus analysis of enhanced water supply scenarios: A regional comparison of Tampa Bay, Florida, and San Diego, California. *Environ. Sci. Technol.* **2014***, 48 (10)*, 5883-5891.

7. American Water Works Association; American Society of Civil Engineering. Mixing, Coagulation, and Flocculation. *In: Water Treatment Design; Fifth edition; Randtke, S.J., Horsley, M.B., Eds;* McGraw Hill, AWWA and ASCE: New York, 2012.

8. Kawamura, S. *Integrated Design and Operation of Water Treatment Facilities; Second edition;* John Wiley & Sons: New York, 2000.

9. Edzwald, J. K. Coagulant mixing revisited: theory and practice. *Journal of Water Supply Research and Technology-Aqua* **2013***, 62 (2)*, 67-77.

10. Allerdings, D.; Foerster, G.; Vasyukova, E.; Uhl, W. The practical influence of rapid mixing on coagulation in a full-scale water treatment plant. *Water Science and Technology* **2015***, 71 (4)*, 566-571.

11. Vadasarukkai, Y. S.; Gagnon, G. A. Application of low-mixing energy input for the coagulation process. *Water Res.* **2015***, 84*, 333-341.

12. Yu, W.; Gregory, J.; Graham, N. Regrowth of broken hydroxide flocs: Effect of Added Fluoride. *Environ. Sci. Technol.* **2016***, 50 (4)*, 1828-1833.

13. U.S Environmental Protection Agency, *Ensuring a Sustainable Future: An Energy Management Guidebook for Wastewater and Water Utilities;* Environmental Protection Agency: Washington, D.C., 2008.

14. Cornwell, D. A.; Bishop, M. M. Determining velocity-gradients in laboratory and full-scale systems. *Journal American Water Works Association* **1983***, 75 (9)*, 470-475.

15. Ten State Standards of the Great Lakes-Upper Mississippi River Board of State and Provincial Public Health and Environmental Managers, *Recommended Standards for Water Works;* Health Research Inc., Health Education Services Division: Albany, New York, 2012.

16. Menges, F. Spekwin32 - Optical Spectroscopy Software, Version *v1.72.0,* 2016*;* http://www.effemm2.de/spekwin/.

17. Vadasarukkai, Y. S.; Gagnon, G. A. Characterization, fate and transport of floc aggregates in full-scale flocculation tanks. *Environmental Science-Water Research & Technology* **2016***, 2 (1)*, 223-232.

18. Wong, K. B.; Piedrahita, R. H. Settling velocity characterization of aquacultural solids. *Aquacult. Eng.* **2000***, 21 (4)*, 233-246.

19. Tassinari, B.; Conaghan, S.; Freeland, B.; Marison, I. W. Application of turbidity meters for the quantitative analysis of flocculation in a jar test apparatus. *J. Environ. Eng.* **2015***, 141 (9)*, 04015015-1-04015015-8.

20. Gorczyca, B.; Ganczarczyk, J. Structure and porosity of alum coagulation flocs. *Water Qual. Res. J. Can.* **1999***, 34 (4)*, 653-666.

21. Droppo, I. G.; Leppard, G. G.; Flannigan, D. T.; Liss, S. N. The freshwater floc: A functional relationship of water and organic and inorganic floc constituents affecting suspended sediment properties. *Water Air and Soil Pollution* **1997***, 99 (1-4)*, 43-53.

22. Lin, J.; Huang, C.; Dempsey, B. A.; Hu, J. Fate of hydrolyzed Al species in humic acid coagulation. *Water Res.* **2014***, 56*, 314-324.

23. Myneni, S. C. B.; Brown, J. T.; Martinez, G. A.; Meyer-Ilse, W. Imaging of humic substance macromolecular structures in water and soils. *Science* **1999***, 286 (5443)*, 1335-1337.

24. Sieliechi, J. M.; Lartiges, B. S.; Kayem, G. J.; Hupont, S.; Frochot, C.; Thieme, J.; Ghanbaja, J.; de la Caillerie, J. B. D.; Barres, O.; Kamga, R.; Levitz, P.; Michot, L. J. Changes in humic acid conformation during coagulation with ferric chloride: Implications for drinking water treatment. *Water Res.* **2008***, 42 (8-9)*, 2111-2123.

25. Coufort, C.; Bouyer, D.; Line, A. Flocculation related to local hydrodynamics in a Taylor-Couette reactor and in a jar. *Chemical Engineering Science* **2005***, 60 (8-9)*, 2179-2192.

26. Gu, B. H.; Schmitt, J.; Chen, Z.; Liang, L. Y.; Mccarthy, J. F. Adsorption and desorption of different organic-matter fractions on iron-oxide. *Geochim. Cosmochim. Acta* **1995***, 59 (2)*, 219-229.

27. Guan, X.; Shang, C.; Chen, G. ATR-FTIR investigation of the role of phenolic groups in the interaction of some NOM model compounds with aluminum hydroxide. *Chemosphere* **2006***, 65 (11)*, 2074-2081.

28. Vinkler, P.; Lakatos, B.; Meisel, J. Infrared spectroscopic investigations of humic Substances and their metal-complexes. *Geoderma* **1976***, 15 (3)*, 231-242.

29. Rout, K.; Mohapatra, M.; Anand, S. 2-Line ferrihydrite: synthesis, characterization and its adsorption behaviour for removal of Pb(II), Cd(II), Cu(II) and Zn(II) from aqueous solutions. *Dalton Transactions* **2012***, 41 (11)*, 3302-3312.

30. Liu, C., Huang, P. M. The influence of catechol humification on surface properties of metal oxides. In *Humic substances structures, models and functions;* Ghabbour, E. A.; Davies, G., Eds.; The Royal Society of Chemistry: Cambridge, UK, 2001; pp 253-270.

31. Peak, D.; Ford, R. G.; Sparks, D. L. An in situ ATR-FTIR investigation of sulfate bonding mechanisms on goethite. *J. Colloid Interface Sci.* **1999***, 218 (1)*, 289-299.

32. Amir, S.; Jouraiphy, A.; Meddich, A.; El Gharous, M.; Winterton, P.; Hafidi, M. Structural study of humic acids during composting of activated sludge-green waste: Elemental analysis, FTIR and C-13 NMR. *J. Hazard. Mater.* **2010***, 177 (1-3)*, 524-529.

33. Webster, J. G.; Swedlund, P. J.; Webster, K. S. Trace metal adsorption onto an acid mine drainage iron(III) oxy hydroxy sulfate. *Environ. Sci. Technol.* **1998***, 32 (10)*, 1361-1368.

34. Bigham, J. M.; Carlson, L.; Murad, E. Schwertmannite, a new iron oxyhydroxysulphate from Pyhasalmi, Finland, and other localities. *Mineralogical Magazine* **1994***, 58 (393)*, 641-648.

35. Rahman, M. S.; Gagnon, G. A. Bench-scale evaluation of drinking water treatment parameters on iron particles and water quality. *Water Res.* **2014***, 48*, 137-147.

36. Pivokonsky, M.; Bubakova, P.; Pivokonska, L.; Hnatukova, P. The effect of global velocity gradient on the character and filterability of aggregates formed during the coagulation/flocculation process. *Environ. Technol.* **2011***, 32 (12)*, 1355-1366.

37. Rossini, M.; Garrido, J. G.; Galluzzo, M. Optimization of the coagulation-flocculation treatment: Influence of rapid mix parameters. *Water Res.* **1999***, 33 (8)*, 1817-1826.

7.A Supporting Information

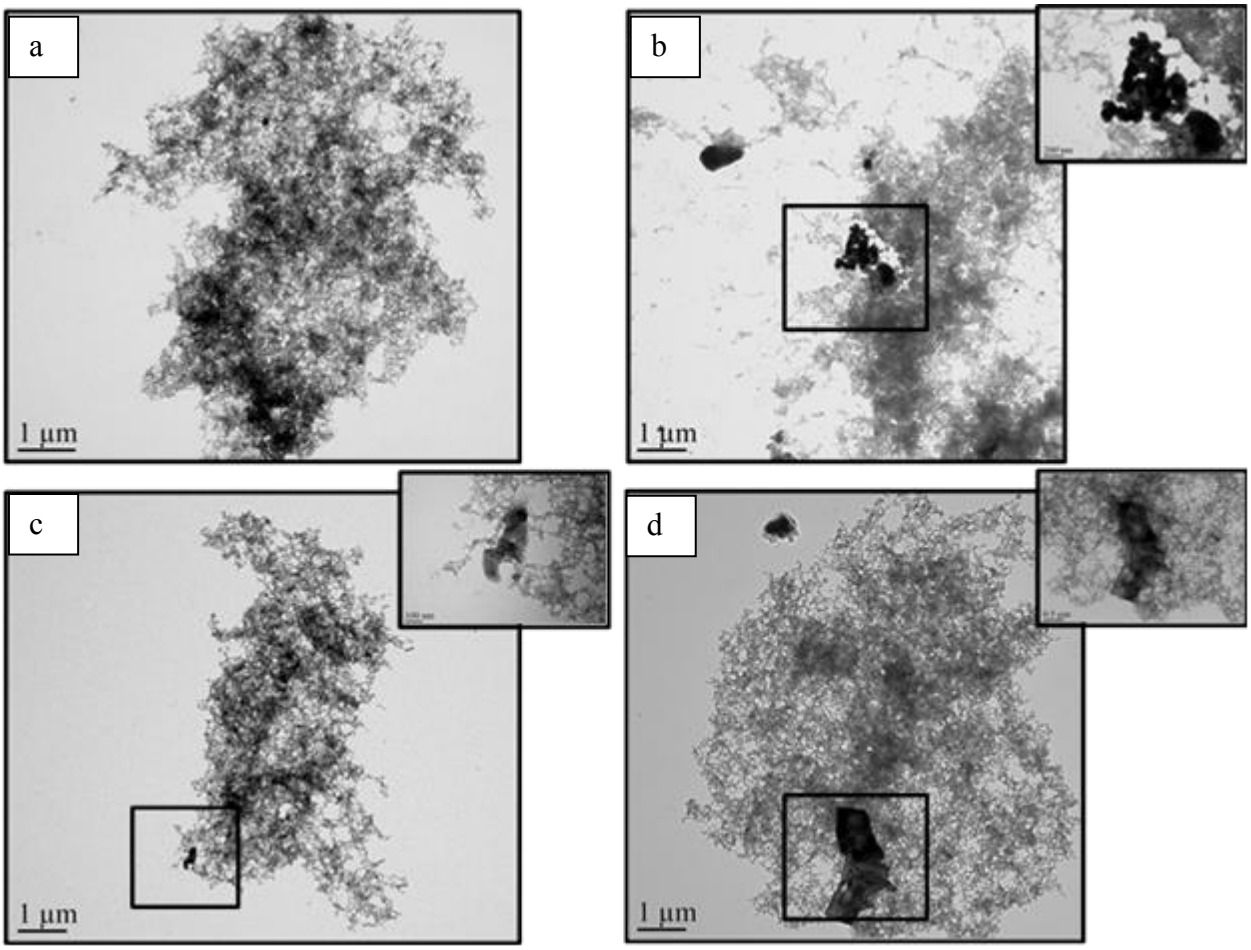

Figure 7.S1 TEM images of microflocs formed at G of 175 s-1 for the optimal coagulant concentration
(a,b) 0.33 mM of Fe and pH = 4.8 (c,d) 0.66 mM of Fe and pH= 6.85. Insert shows the zoomed area.

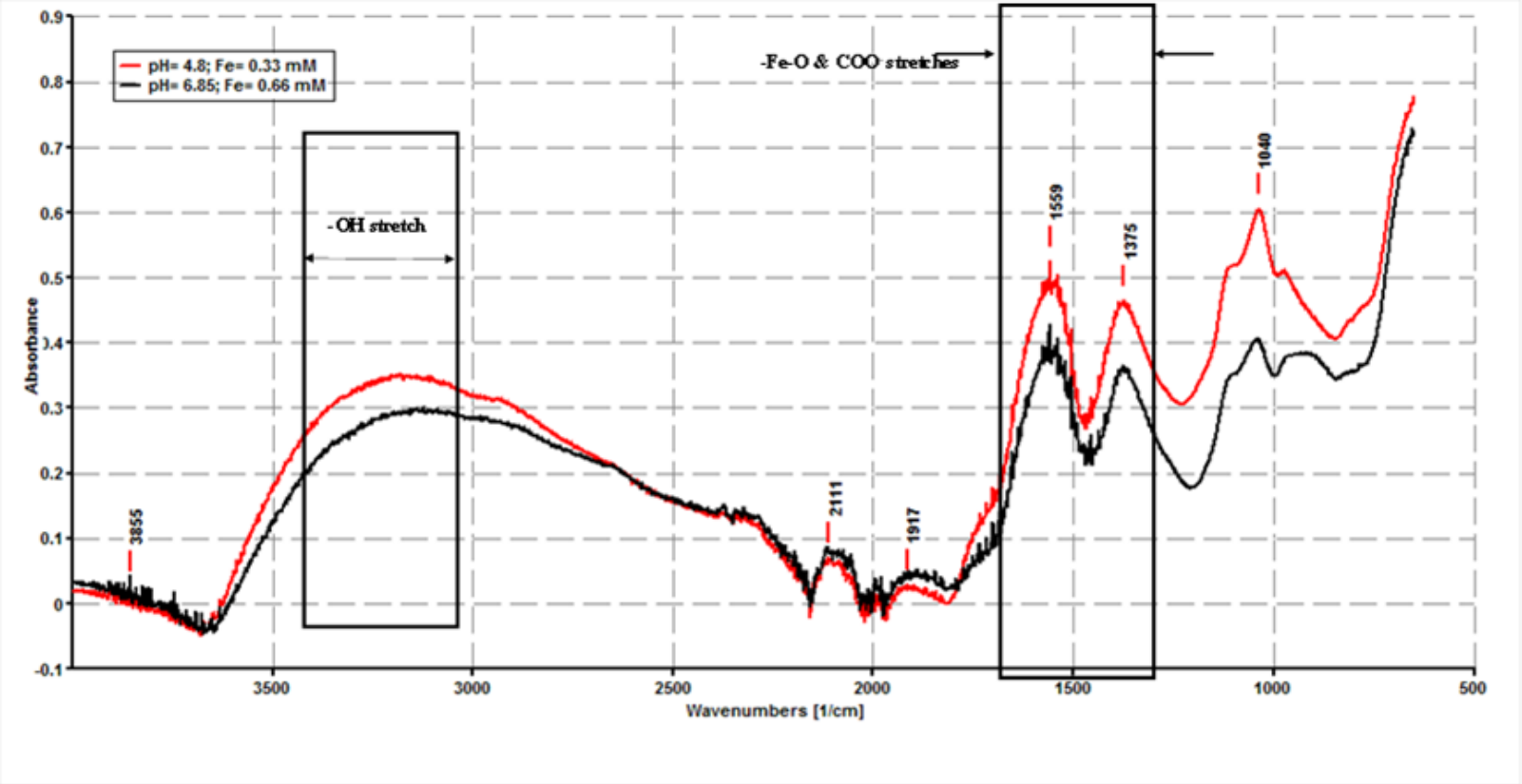

Figure 7.S2 Mid-infrared spectra of DOM-Fe flocs formed at a G of 175 s-1 (a) 0.33 mM of Fe and pH = 4.8 (b) 0.66 mM of Fe and pH= 6.85.

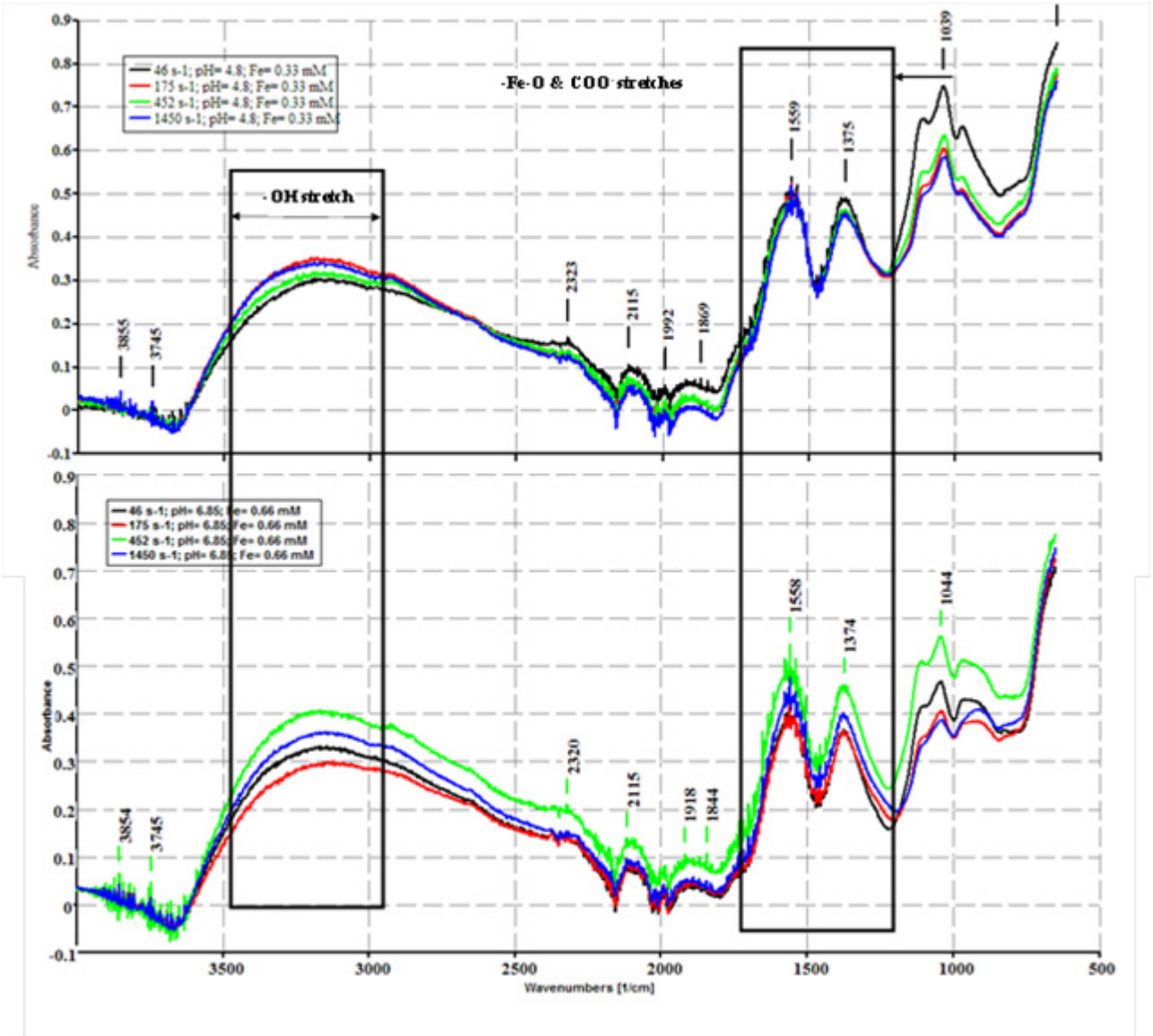

Figure 7.S3 Influence of the coagulation mixing intensities (G-value) on the FT-IR spectra (a) 0.33 mM of Fe and pH = 4.8 (b) 0.66 mM of Fe and pH= 6.85.

Chapter 8 Discussion

8.1 Introduction

The influence of mixing energy consumed during coagulation was examined for two water types in this present study: synthetic humic water and raw water from a lake source. Both waters were characterized by a high organic content, with a specific ultraviolet absorbance (SUVA) of at least 2-2.5 units of m^{-1} of absorbance per mg/L. A batch reactor was used to represent a continuous-flow, stirred tank reactor (CSTR) design that is conventionally used in a coagulation, flocculation, and sedimentation process train (Figure 8.1). A square beaker of a fixed capacity (1 L) was used at a laboratory workbench as a batch reactor design to simulate the coagulation and flocculation processes. Samples were collected for water quality analysis from a sampling port located at ~10.3 cm from the water level. Using a modified mixing arrangement, rapid mixing was examined for a range of the root mean square velocity gradient ((i.e., the G-value) from 0 to 1450 s^{-1}. A hydraulic residence time of 90 s was fixed during rapid mixing and 20 minutes in flocculation, with a calculated overflow rate of 0.17 cm/min was simulated for settling purposes.

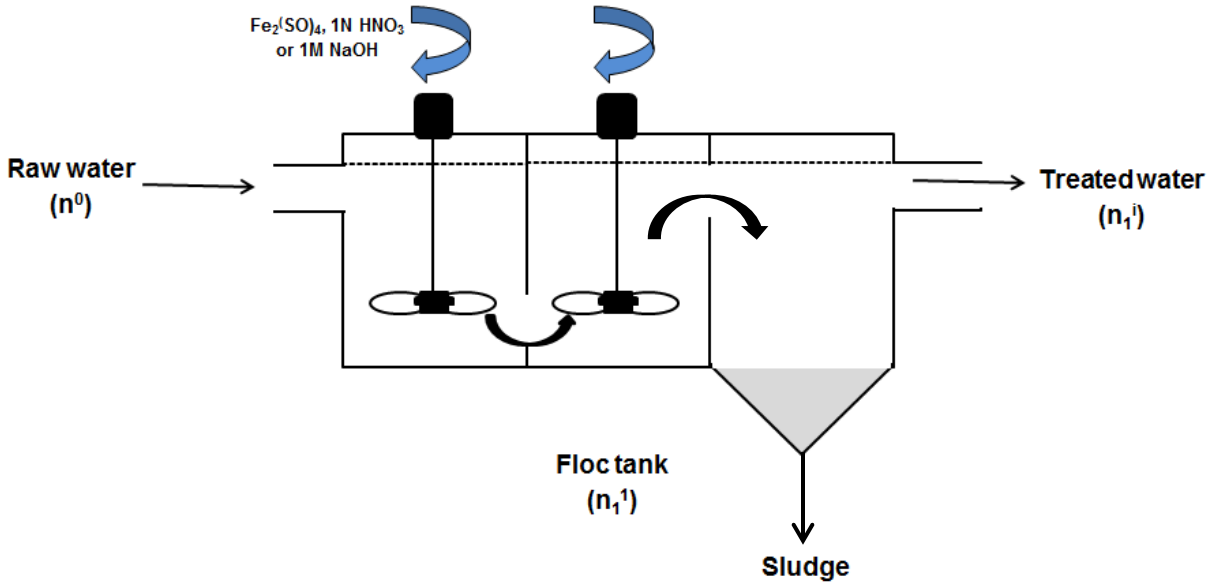

Figure 8.1 Schematic diagram of a continuous-flow, stirred tank reactor (CSTR) design of a conventional treatment process
(n^0 is the initial number of particle; $n_1^{1..i}$ is the number concentrations in subsequent processes)

The major findings from the experiments carried out suggest coagulation mixing energy (measure in terms of the G-value) was not an important parameter for organic matter removal and lower coagulation mixing energy produced flocs of larger size following flocculation. The evaluation of coagulation mixing energy for particle-particle and particle-water interactions is discussed in this Chapter. The floc size distribution data obtained from the lake water experiment is used as an example case, as shown in Figure 8.2.

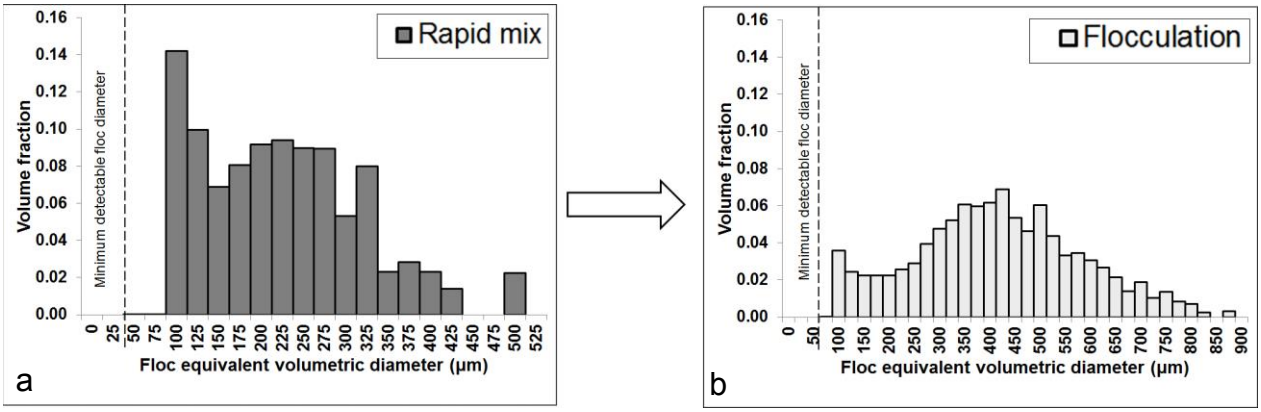

Figure 8.2 Evolution of floc size distributions measured during coagulation and flocculation

(a) 90 s of the rapid mixing stage at 175 s^{-1} (b) 20 minutes during flocculation process at 46 s^{-1}

The addition of ferric sulphate coagulant and pH adjusting chemicals caused an expected increase in the number of particles, which led to collisions between hydrolysed ferric species and primary particles (e.g., initial particles in the lake water). As expected, this phenomenon resulted in a large volume fraction of flocs with diameters ranging from 100 to 1000 μm at the end of 90 s of rapid mixing at 175 s^{-1}. In other words, small particles aggregated over the time of 90 s, resulting in an increase in the number of larger particles in rapid mixing. The observed trend is in accordance to the modified Smoluchowski Equation 8.1 (Li 1996), which describes mathematically the rate of formation of a new particle k resulting from collision and subsequent aggregation between two particles of sizes i and j in flocculation.

$$\frac{dn_k}{dt} = \alpha\left[\frac{1}{2}\sum_{i+j\to k}\beta(i,j)n_i n_j - n_k\sum_{k=1}^{\infty}\beta(i,k)n_i\right] \qquad (8.1)$$

where, subscripts i, j, k refers to discrete particle sizes, n refers to the number concentration of particles in a sample volume (m^{-3}), t is the time of flocculation (s), $\beta(i,j)$ is a collision frequency function which describes the frequency of collisions between i and j particles caused by different transport mechanisms (m^3/s), α is the collision efficiency factor ($0 < \alpha < 1$), whose magnitude ranges between 0 (completely stable suspension) and 1 (neutralized particles that can remain attached after collision).

The term $\left(\mathbf{dn_k}/\mathbf{dt}\right)$ on the left hand side represents the change in the number concentration of size k particles with time in a batch reactor. The first term on the right hand side represents an increase in the number of particles of size k by aggregation between i and j-sized particles and the second term describes the loss of particles of size k by virtue of their aggregation with any other particles. In Equation 8.1, it is assumed that the particle volume is conserved in every collision (Oyegbile et al. 2016). That is, the total volumes of i and j-size particles is assumed to be equal to the volume of resulting particle of size k. A factor of one half in the first term is used to negate the possibility of counting twice the collision between sizes i and j.

Three main transport mechanisms can cause particle motions that can lead to collisions between particles in an unstable suspension (e.g., particles resulting from the addition of coagulant). It is possible for all three of the mechanisms to occur together; however, the importance of a mechanism in promoting collisions become important for a particular size range of particles (Benjamin and Lawler 2013; Han and Lawler 1992). That is, thermal activity arising from random Brownian motion is only important for very small particles less than 1μm (perikinetic flocculation), mixing results in difference in velocities, which causes velocity gradients (e.g., measured as the G-value) that can cause collisions of particles in the diameter range of 1-40 μm (orthokinetic flocculation), and unequal settling velocities arise typically for particles with diameter larger than 40 μm that can cause collisions due to differential sedimentation (Oyegbile et al. 2016).

Collision frequency functions (β) for perikinetic, orthokinetic, and differential sedimentation can be expressed as follows (Benjamin and Lawler 2013, Li and Logan 1997, Oyegbile et al. 2016, Thomas et al. 1999):

For perikinetic flocculation:

$$\beta_{Br}(i,j) = \frac{2KT}{3\mu}\left(\frac{1}{d_i} + \frac{1}{dj}\right)\left(d_i + d_j\right) \tag{8.2}$$

For orthokinetic flocculation:

$$\beta_{Sh}(i,j) = AG\left(d_i + d_j\right)^3 \tag{8.3}$$

For differential sedimentation:

$$\beta_{DS}(i,j) = \frac{\pi g}{72\mu}\left(\rho_p - \rho_w\right)\left(d_i + d_j\right)^3 \left|\left(d_i - d_j\right)\right| \tag{8.4}$$

where, subscripts i and j refers to discrete particle sizes of diameters d_i and d_j, respectively (μm), ρ_p and ρ_w are the densities of particles and water, respectively (kg m^{-3}), μ is the dynamic viscosity of water (kg $m^{-1}s^{-1}$), K is Boltzmann's constant (1.3807 x 10^{-23} J/K), T is the absolute temperature (K), A is a numerical non-dimensional coefficient that has a predicted value of 0.162 for laminar and 0.167 for turbulent flows (Li and Logan 1997), G is the root mean square velocity gradient (G-value in s^{-1}), π is the numerical constant (3.1416), and g is the gravitational constant (9.81 m s^{-2}). The total collision frequency often represented as the summation of the three mechanisms of particle collisions (Han and Lawler 1992), wherein each mechanism is assumed to be independent, i.e.

$$\beta(i,j) = \beta_{Br}(i,j) + \beta_{Sh}(i,j) + \beta_{DS}(i,j) \tag{8.5}$$

Equations 8.2 to 8.5 describe the rectilinear model of predicting particle collisions. In this rectilinear modelling approach, particles are assumed to travel in a linear fashion such that the effects of changes in water motion and short-range forces are ignored as the particles come in close contact (Han and Lawler 1992, Thomas et al. 1999). The results of this rectilinear approach have shown orthokinetic flocculation as the dominant transport mechanism for collisions between particles larger than 10μm (Benjamin and Lawler 2013, Crittenden et al. 2005).

Accordingly, Equation 8.3 suggests increasing the mixing energy input (G-value) is favourable for particles to collide with one another. It also indicates from a rectilinear standpoint, that mixing is of a prime importance for collisions that may result in successful attachment of particles. This notion has probably led to the widely accepted practice of considering the G-value as the principal design component in municipal water treatment.

In practical applications, as particles approach one another by any of the three transport mechanisms, water between the particles gets squeezed out of their way. This water movement influences the motion of the approaching particles to slightly rotate around one another, such that they deviate from the linear path that is assumed in the classical approach (Thomas et al. 1999). This phenomenon of particle-water interactions is termed as hydrodynamic interactions (Han and Lawler 1992). Other short range forces can exist between two particles and their role become significant at smaller separation distances (Han and Lawler, 1992; Li 1996). These forces may include van der Waals attractive forces that promote attachment of particles, and electrostatic repulsive forces that can exist between particles of similar charge, by which particles tend to repel each other and therefore do not collide. Thus, only a fraction of the total number of interactions may result in a successful collision and attachment (Li 1996), which needs to be accounted for in the collision efficiency factor (α).

Previous studies have looked into an alternative approach called the curvilinear approach, wherein corrections were applied to the collision efficiency factor (α) by accounting for hydrodynamic and particle-particle interaction forces in each mechanism (Benjamin and Lawler 2013, Han and Lawler 1992). Details on the collision efficiency factor (α) for collision by the three mechanisms can be found in the literature (Benjamin and Lawler 2013, Han and Lawler 1992). These correction factors are included in the classic rectilinear approach as expressed below:

$$\beta(i,j) = \alpha_{Br}(i,j)\beta_{Br}(i,j) + \alpha_{Sh}(i,j)\beta_{Sh}(i,j) + \alpha_{DS}(i,j)\beta_{DS}(i,j) \quad (8.6)$$

where, subscripts i and j represents discrete particle sizes, subscripts Br, Sh, and DS represents perikinetic, orthorkinetic, and differential sedimentation mechanisms, respectively, β is the

curvilinear collision frequency function ($m^3\ s^{-1}$), α is the collision efficiency factor (dimensionless) for each mechanisms.

8.2 The Role of Coagulation G-value

Mixing energy has shown to have less influence on floc aggregations in suspensions that vary greatly in size (Benjamin and Lawler 2013, Han and Lawler 1992, Li 1996). The experimental findings from Chapters 5 and 7 also support the contention that mixing energy can be kept at low G-values without a significant penalty in turbidity and organic removal. Han and Lawler (1992) applied the collision efficiency factor (α) calculated from the curvilinear approach to the rectilinear model (i.e., Equations 8.2-8.4) for various size ratios of colliding particles (λ, the ratio of smaller to larger diameter) and concluded that G-value has a far less significance in enhancing the collision rate for different size ranges of particles. The authors also showed that orthokinetic flocculation was the dominant mechanism only for similar sizes of colliding particles and inferred that a minimum G was required to keep particles in suspension in flocculation. In the present study, the collision efficiency values from Han and Lawler (1992) was extended to coagulation in order to understand the role of coagulation G-value on particle collisions. Figure 8.3 was developed using similar conditions as used by Han and Lawler (1992). That is, one particle size was held constant (d_i=2 μm) while the size of j particle was varied from 0.1 to 100 μm. Additional details on the calculation of collision frequency function can be found in Appendix A3. This model is applicable for G-values > 0 s^{-1} since the dimensionless attraction group, Hamaker constant (H_A in Table A.2), tends to infinity at no mixing condition.

It was clearly evident from the results in Figure 8.3 that the G-value had a minimum influence on collision frequency for particles greater than 10 μm, which is consistent with the previous findings (e.g., Benjamin and Lawler 2013, Han and Lawler 1992). As shown in Figure 8.3, the dominant mechanism was perikinetic flocculation for collision of 2 μm with particles less than 0.1 μm, which agrees with the rectilinear approach. Differential sedimentation became significant when a particle was relatively larger than the other. In the above example case, collisions due to differential sedimentation was significantly increased for collisions between 2 μm and particles larger than 10 μm.

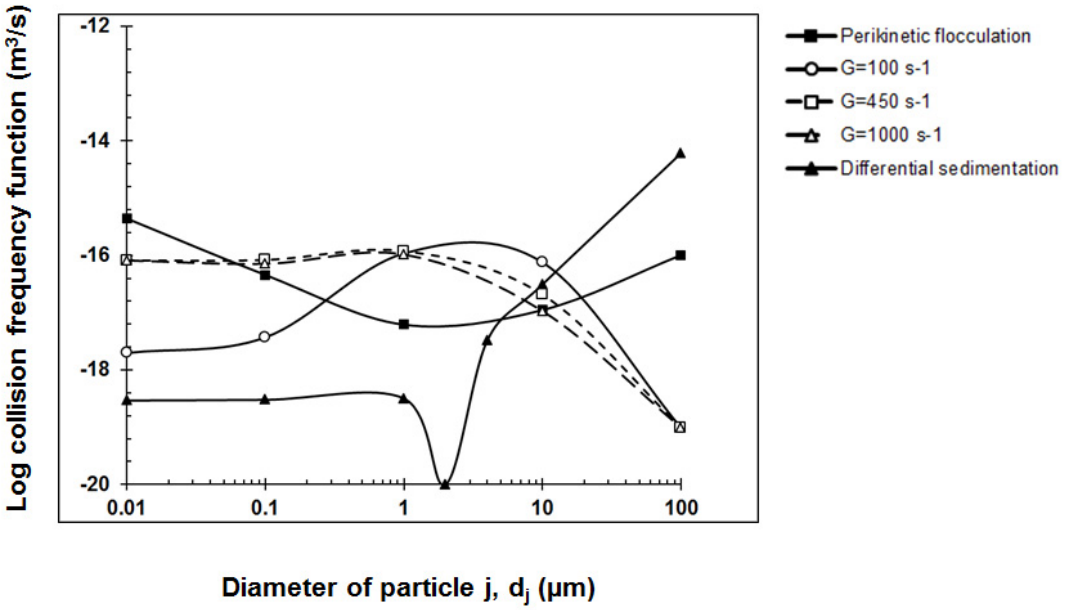

Figure 8.3 Total collision frequency function predicted using the curvilinear approach (Figure is specific to the conditions: d_i=2 µm; temperature T= 20 ^{0}C; density of particle ρ_p=1100 kg/m^3)

Figure 8.3 also showed that increasing the coagulation G-value from 100 s^{-1} to 450 s^{-1} and 1000 s^{-1} did not lead to any significant changes in the predicted collision frequency function. Although for collisions between 2 µm and particles in the range of 0.01-0.1 µm, it showed an appreciable increase in the predicted collision frequency at G-values of 450 s^{-1} and 1000 s^{-1}. It also implies higher coagulation mixing G-values for a shorter time may initiate the process when particles are small. Alternatively, when two particles were of very different size, for example collisions between 2 µm and particles greater than 10 µm, the predicted collision frequency due to orthokinetic flocculation was drastically reduced. Perikinetic and differential sedimentation seemed to dominate particle collisions in that size range.

Han and Lawler (1992) conducted a similar analysis for different particle size combinations and showed orthokinetic flocculation was dominant only when two particle diameters were within a factor of approximately 10. A substantial reduction in orthokinetic flocculation for collision between large and small particles (low λ, the ratio of smaller to larger diameter) was mainly due to the hydrodynamic corrections that were incorporated in the curvilinear model (Benjamin and Lawler 2013). High G-values produce high relative velocity gradients between two approaching

particles of different sizes. It is argued that the time available to overcome hydrodynamic effects becomes shorter at high G-values (Han and Lawler 1992). Thereby, the opportunity for attractive forces to keep the particles together was partially hindered by less contact time available between those particles.

8.3 Effects of Initial Particle Size Distribution on Particle Collisions

In the case of an initial size distribution less than 1μm in the present study, it is likely that perikinetic or Brownian diffusion mechanism initially controlled transport and collision between hydrolysed ferric species and particles during rapid mixing. Primary particles (e.g., original particles in raw water) was mainly natural dissolved organic matter (DOM) in the colloidal size range of 44-68 nm for lake water while synthetic humic water had at a slightly higher size range of 122-220 nm. On the other hand, sizes of 1 g/L of ferric sulfate stock solution was around 255-531 nm, which was relatively larger in diameter than both water types. This formed a heterodisperse colloidal suspension in water during rapid mixing. In other words, particles of slightly different size ranges were available during coagulation.

Table 8.1 Total collision frequency function predicted using the curvilinear approach for colliding pair of primary particles and ferric sulphate coagulant

G-values (s^{-1})	Collision Pairs nm	Perikinetic (m^3/s)	Orthokinetic (m^3/s)	Differential Sedimentation (m^3/s)	Total Collision Frequency (m^3/s)	Dominant Collision Mechanism
100	43-255	1.63E-17	2.45E-19	8.38E-23	1.65E-17	Brownian
	43-531	2.98E-17	8.68E-19	1.53E-21	3.07E-17	Brownian
	164-255	7.00E-18	9.29E-19	7.98E-23	7.93E-18	Brownian
	164-531	9.62E-18	2.62E-18	1.60E-21	1.22E-17	Brownian
450	43-255	1.63E-17	1.87E-19	8.38E-23	1.65E-17	Brownian
	43-531	2.98E-17	5.09E-19	1.53E-21	3.03E-17	Brownian
	164-255	7.00E-18	7.41E-19	7.98E-23	7.74E-18	Brownian
	164-531	9.62E-18	1.78E-18	1.60E-21	1.14E-17	Brownian
1000	43-255	1.63E-17	1.53E-19	8.38E-23	1.64E-17	Brownian
	43-531	2.98E-17	3.27E-19	1.53E-21	3.01E-17	Brownian
	164-255	7.00E-18	6.46E-19	7.98E-23	7.65E-18	Brownian
	164-531	9.62E-18	1.42E-18	1.60E-21	1.10E-17	Brownian

The research hypothesis of the insignificant role of G-value was examined for the heterodisperse suspension that was initially present at time zero (i.e., t=0) in water during rapid mixing. Table 8.1 depicts the predicted collision frequency between each pair of primary particles and ferric sulphate particles for different coagulation G-values. The ratio of smaller to larger diameter (λ) was less than 0.64 for the colliding pairs, implying the corrections to rectilinear model was less severe (Han and Lawler, 1992). As expected, Perikinetic flocculation involving Brownian diffusion was predicted as the dominant mechanism for all colliding pairs within the size range of 44 – 531 nm. Notably, for collisions between primary particles in the synthetic humic water and ferric sulphate, i.e., for 164 and 531 nm particle diameters, increasing G-value was observed to have a slight influence on their collision frequency. This may be explained due to similar size range of colliding particles for which mixing was shown as an important transport mechanism in previous studies (e.g., Benjamin and Lawler 2013, Han and Lawler 1992).

8.4 Energy Dissipation in Turbulent Flow and Floc Breakage

High mixing energy calculated from the G-value was shown to not be necessary for particle collisions and subsequent attachment in coagulation, which could be favoured for two reasons. Firstly, some of the turbulent kinetic energy supplied to the impeller may have been directly dissipated into heat at the surfaces (friction) of the impeller and the beaker wall (Letterman et al. 1999). Secondly, in turbulent flow conditions, collisions between particles are suggested to be promoted by eddies of a size similar to those of colliding particles (Oyegbile et al. 2016, Stanley and Smith 1995, Thomas et al. 1999). The G-value ranging from 46 to 1450 s^{-1} was estimated to produce Kolmogorov microscales of 146 to 26 μm, respectively. The range of floc aggregate sizes examined following coagulation and flocculation was slightly larger than this scale. For particles larger than Kolmogorov scale, the mechanism can be viewed similar to Brownian diffusion, except diffusivity caused by turbulent eddies are considered important rather than molecular diffusion (Benjamin and Lawler 2013). This is the inertial convective subrange of the energy spectrum. This scale is also suggested to cause fragmentation to floc structures as a result of fluctuating dynamic pressure (Thomas et al., 1996), which may explains the breakage mechanism in the present case. It would also be interesting to observe if any differences exist in

smaller floc sizes as a result of mixing regimes, which were likely to experience viscous stress in viscous sub-range.

Breakage of floc aggregates are neither dealt with in the rectilinear nor curvilinear modelling approach. As number of larger particle increases, which was observed at the 90 s of rapid mixing, the collision frequency should reach a maximum and then reduce (Han and Lawler, 1992). This observation was comparable to the concept of floc formation process, which is understood as a balance between the rate of collision induced aggregation and the rate of breakage (e.g., Argaman 1971, Bridgeman et al. 2008). Many experimental works have looked in to floc breakage during flocculation (Coufort et al. 2005, Pivokonsky et al. 2011); however, they failed to consider breakage of aggregates during rapid mixing. It is often assumed that neutralization of charges on particle surfaces occurs, followed by aggregation (attachment) of those unstable particles during rapid mixing. Few studies have shown breakage of flocs formed during rapid mixing in sweep coagulation (e.g., Kan et al. 2002). In Chapter 7, the phenomenon of floc breakage was demonstrated by a decrease in floc size distributions following flocculation, which was attributed to the consumption of high energy at coagulation G-values > 450 s^{-1}.

The role of turbulence was not directly evaluated in the present study as spatial variation in local G-values was not accounted for. However, there are major limitations of using the average G-values that needs to be addressed. Spatial heterogeneity in floc size distributions is shown to exist due to variations in turbulent dissipation rate in a tank (Hopkins and Ducoste 2003, Prat and Ducoste 2006, Samaras et al. 2010). Experimental floc measurements done by Hopkins and Ducose (2003) have found large flocs in bulk region which had a relatively lower velocity gradient than the impeller zone. Furthermore, the numerical model of Prat and Ducoste (2006) has shown floc growth rate to increase with increasing the average G-value while a lower steady-state floc sizes was achieved due to high breakage rates. In the present case, it is likely that larger flocs following flocculation may have experienced breakage near the impeller region at high average G-values (>450 s^{-1}).

While the mixing energy is primarily used to disperse chemicals into water, adequate time is required for the transfer of energy from macro-scale of production to micro scale, reaction time

for chemicals to interact with particles, and a total residence time in rapid mix tanks (Benjamin and Lawler 2013). Most rapid tanks are designed for a theoretical hydraulic residence time in the range of 10-60 s (AWWA and ASCE 2012), which is at least 10^4 times greater than $\tau_{Kolmogorov}$ (i.e., 0.0017 - 0.001 s. Also, the characteristics reaction times for the formation of monomeric hydrolysis products are expected at less than 10^{-4} s (Dempsey et al. 1984), which is substantially lesser than the total residence time. While precipitation was expected approximately 2 to 5 minutes depending on the process conditions (Francois 1988). Specifically for organic flocs, Jarvis 2004a) showed iron-DOM flocs reached a steady-state distribution within 3-5 minutes.

Another aspect that plays an important role is the time-scale for which a floc resides in a tank. In real systems, the length of time a particle resides in a tank can be shorter or longer than the theoretical residence time (Vadasarukkai et al. 2011). Thus, the length of time a floc spends on high or low G-values is also an important factor to understand floc breakage. Bridgeman et al. (2008) estimated a particle of 500 μm diameter was subjected to 9.4 times the average G-value of 165 s^{-1} at every 5 seconds for the 60 s of mixing in a jar test. This suggests the frequency at which flocs are exposed to a maximum (peak) local velocity gradient are expected to increase with the mixing energy in the present case, which was also identified by the author (Bridgeman et al. 2008). This may have caused rupture to floc structures; additional experiments involving floc size measurements at different time interval are required to ascertain this theory.

8.5 Effect of Chemical Conditions and Mechanistic Understanding of DOM Removal

Floc breakage is measured by its strength to resist external forces. Floc strength tests have been measured as a function of coagulant mechanism, pH, type and dose of coagulant, as noted from the review of (Jarvis et al. 2005a). Although a mechanistic understanding of breakage has not been conclusively identified, internal composition and bonding mechanism subjective to chemical conditions are thought to withstand such forces (Parsons et al. 2007,Yeung and Pelton 1996). Ferric coagulant that was used in the present study is a considerably stronger acid than alum coagulant (Stumm and Morgan 1962). As discussed in the literature review (Chapter 2), floc sizes may vary from one study to another depending on the experimental conditions and techniques used to measure floc properties. A general consensus can be drawn from previous investigations that ferric flocs have consistently shown to result in larger floc size distributions

(e.g., Gonzalez-Torres et al. 2014, Jarvis et al. 2005b, Zhong et al. 2011). For example, Gonzalez-Torres (2014) reported the average ferric floc size ranged between 871 and 954 μm while for alum the size was around 492-661 μm. This difference in size distributions between the coagulants can be related to the initial floc growth rates, which from previous review indicate that ferric flocs grew faster in size than alum (Jarvis et al. 2005a).

The dose ratio was shown as the driving factor for higher floc growth as opposed to coagulant type (Jarvis et al. 2005b, Sharp et al. 2006), which was at a high iron to carbon ratio (i.e. > 0.8 mg Fe/mg TOC) as determined from the optimal coagulant concentration in Chapter 3 and 5. At such sufficiently high dose ratio, it was very likely to result in bulk precipitation of amorphous iron hydroxides (Duan and Gregory 2003). Using the acid-base pH titration curves, the formation of ferric hydroxide precipitates was estimated at a relatively lower pH value of 5.5 in the absence of any organic impurities. This equivalence point was between the two pHs of 4.5 ± 0.3 and 6.7 ± 0.3 that was selected for the batch experimental conditions. This study did not identify hydrolysis species resulting from adding iron to water. It was assumed that a possible combination of charge neutralization of DOM, followed by precipitation of complexes and strong adsorption onto (solid) iron precipitates were the mechanisms responsible for DOM removal at both the selected pHs presented in this thesis.

Infrared spectral analyses in Chapter 6 suggest surface hydroxyl functional groups on hydrolyzed iron surfaces to have interacted with DOM particles, resulting in DOM-iron complexes. Such complexes were shown to result from the surface adsorption by ligand exchange between iron and DOM, which has been well documented in earlier mechanistic studies (e.g., Guan et al. 2006). A conceptual model was developed for this present study based on an adsorption model that was carried out for an iron oxide- dihydroxybenzene system (Liu and Huang 2001), as illustrated in Figure 8.4. When iron was initially added to water it reacted with the OH^- ligand in water, resulting in surface active hydroxyl groups (e.g., Fe-OH and $Fe\text{-}OH_2$ functional groups). Functional groups such as carboxylic COOH and/or phenolic OH groups of DOM disassociated depending on the pK_a values. The protonation of weaker acids replaced some of the bound -OH and $-OH_2$ groups from the surfaces of iron, resulting in a partial neutralization of the positive charge on iron hydroxide surfaces (Liu and Huang 2001). The resulting iron-DOM complexes

from a site specific adsorption via ligand exchange are suggested to form inner-sphere complexes (Guan et al., 2006). This complexation was followed by precipitation and chemical bridging between other iron hydroxide sites, containing at least one water molecule in their structure (i.e., HOH···OH). Future work on adsorption studies are recommended to validate this theory for different pH and DOM concentrations.

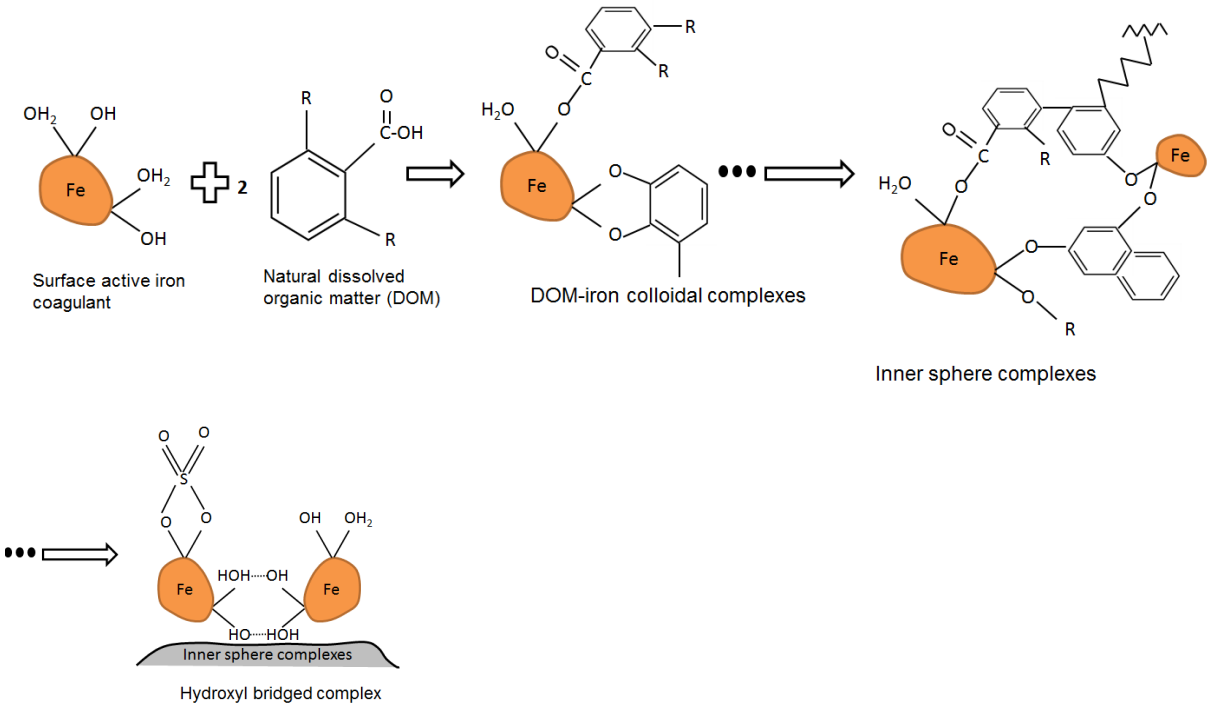

Figure 8.4 Schematic illustration of aggregation of DOM with hydrolyzed iron coagulant

The hydroxyl bridging may have caused flocs to grow in size during the coagulation and flocculation experiments. At high G-values, the water molecule was expected to be pushed out of the permeable structure of floc aggregates, resulting in more compact structures. This may have caused breakage at the hydroxyl bridges (Yu et al. 2016), which was evident from a rise in residual turbidity and not residual organic carbon (assumed as inner-sphere complexes) in the experiments conducted in Chapter 7. Previous studies have consistently shown hydroxide flocs to not fully regrow when they are broken at high G-values (e.g., Jarvis et al. 2004b, Yu et al. 2016). This implies floc breakage as an irreversible phenomenon. In other words, the effect of bond breakage would leave two flocs of same charge that would not form any hydroxyl bridges again.

Chapter 9 Conclusion and Recommendations

This chapter summarizes key findings of this dissertation work, and describe implications of the findings to municipal water treatment. Furthermore potential significance of the work are discussed, and directions for future work are proposed.

9.1 Summary and Conclusions

This thesis integrates water quality and floc characterization techniques to evaluate the influence of mixing energy expended during coagulation. The central hypothesis of this thesis was that removal of natural dissolved organic matter (DOM) is achievable at a much lower mixing energy during rapid mixing stage of coagulation. To test the hypothesis, coagulation experiments were examined at different values of the root mean square velocity gradient (i.e., the G-value), while all other chemical (e.g., coagulant dose, pH) and physical conditions (e.g., temperature) were kept similar. A modified mixing arrangement was used to set the coagulation G-value ranging from 0 to 1450 s^{-1}. An in-line holographic microscopy technique was used for a non-destructive, direct measurement of floc characteristics (e.g., floc counts, sizes, relative floc velocities) in a laboratory workbench and in a full-scale flocculation tank. The two water types selected were characterized by a high organic content, with a specific ultraviolet absorbance (SUVA) of at least 2-2.5 units of m^{-1} of absorbance per mg/L.

The key experimental findings from water quality and floc measurement analyses presented in this thesis confirmed that reduced coagulation mixing energy was effective for DOM removal from the water types examined. Notably, floc aggregates resulting from a low mixing intensity were effectively removed during settling process. Specifically, the results presented offered a new range of reduced mixing intensities ($110\ s^{-1} < G < 450\ s^{-1}$) during rapid mixing for a combined effective removal of total organic carbon, turbidity, and floc aggregates.
Specific conclusions that can be drawn from individual Chapters presented in this dissertation are outlined.

1. **Bench-scale floc size measurements:** The present study has demonstrated the applicability of an inline digital holographic microscopic (DIHM) technique for

characterization of DOM flocs resulting from coagulation and flocculation processes in a jar test apparatus.

- Repeatability of the experimental data was shown possible using the DIHM technique at a significant level of α=0.05.
- In general, differences in floc size distribution were observed at the selected pHs for both the water types. Flocs formed at an acidic pH (4.5 ± 0.3) were characterized with a slightly narrow distribution; while an obvious increase with a higher variability was observed at a near neutral pH (6.7 ± 0.3).
- A broad distribution of floc sizes ranging between 100 to1400 μm was measured, following flocculation for pH 4.8 and 6.85 experiments at 175 s^{-1}, a coagulation G-value of within the proposed range (Figure 6.2).
- While reduction in floc sizes was clearly indicated at the recommended design G-values of 600-1000 s^{-1} (Figure 6.4). This was observed at both the pHs.

2. **Full-scale floc size measurements:** The application of an in-line holographic technique was successfully implemented to measure spatial variations in floc sizes in a full-scale flocculation tank.
    - The results indicated characteristics of larger, more open (bulky) aggregates being formed as a consequence of inadequate flocculation mixing energy ($G < 40\ s^{-1}$).
    - Flocs residing in those stagnant zones were less likely to have sufficient particle-particle interactions and therefore, resulted in a median floc diameter values between 175 and 200 μm.
    - Median floc sizes of 200-225 μm were formed in the regions that had the local velocity range of 0.035 to 0.07 m/s.
    - At large, the predicted fluid velocities (0.02 to 0.055 m/s) from the CFD analysis were approximately an order of magnitude larger than the DIHM calculated particle velocity (0.002 to 0.008 m/s).
3. **Water quality analysis:** A low-mixing intensity range of $110\ s^{-1} < G < 450\ s^{-1}$ was shown as the optimal operating range of the mixing energy input required in the coagulation process for two types of water examined in this study.

- The jar test analysis at an acidic pH (4.5 ± 0.3) required an iron dose <0.3 mM to arrive at an optimal coagulant concentration and resulted in at least 75% of total organic removal (TOC) removal.
- Notably, coagulation operated at G greater than 450 s^{-1} showed negligible improvement in TOC removal. This implies high mixing energy was not essential for organic removal.
- Minimizing energy consumption in enhanced coagulation is feasible at the proposed mixing intensity range (i.e., 110 s^{-1} < G < 450 s^{-1}), without sacrificing the effectiveness of DOM removal by coagulation.

4. **Sorption mechanism of DOM:** the characteristics of DOM floc aggregates were analyzed at two pH set points using a Fourier transform infrared spectroscopy (FT-IR), and a scanning electron microscopy (SEM) combined with an energy dispersive X-Ray spectrometry (EDS).
    - Sample preparation played a key role in both the analysis. It was shown any drying procedures applied had some influence on the FT-IR spectra. Dehydration may cause distortion to their arrangements. This is partly attributed to the presence of water molecules within floc structures.
    - Nevertheless, the results from surface analyses were comparable to the phenomenon of complexation of DOM on to hydrolyzed iron surfaces during coagulation, which is well documented in early mechanistic studies (Guan et al. 2006).

9.2 Practical Implications and Significance:

The coagulation process is routinely optimized for a substantial removal of total organic carbon (TOC) and particles in treatment plants; however, the operational use of the G-value remains unexplored in the water sector. This design concept is based on a relatively older process design approach, and it is plausible that the energy input in the tanks is not optimized for an effective organic and particle removal. An important inference drawn from this presented thesis is that high mixing energy was not essential for aggregation; Perikinetic flocculation involving Brownian diffusion was predicted as the dominant mechanism for all colliding pairs within the size ranges examined. One approach proposed in this study was to reduce the average

coagulation mixing intensity in those tanks. Several design options are available to minimize the energy supplied to an entire tank, for instance use of a plug flow mixing reactor has an advantage of mixing of chemicals to a relatively smaller section of water and therefore, requires a small power input, about 0.05 to 0.1 hp/mgd (Lang 2000). In-line pressurized pipe static mixers or open channel static mixers are other alternative low energy requirement system, wherein mixing occurs when water and coagulant passes through their static blades (Edzwald 2013).

The optimized rapid mix processes that simultaneously achieve water quality goals and reduced energy consumption will help in providing utilities with guidance for improving energy efficiency and creating cost savings for utilities. From a research standpoint, this study will expand the current knowledge base on the coagulation mixing. It will facilitate the continuation of research into the chemical and physical interactions between the added coagulant, particles, organic and other constituents in the water matrix.

9.3 Future Directions:

This dissertation on floc aggregation at different mixing energy has raised a number of interesting research opportunities for future work in this area. The following highlights few suggestions for future work.

1. **Pilot- and full-scale studies:** Jar tests are widely used by the utility operators and researchers to simulate the plant conditions and to determine the optimal coagulant doses. The evaluation of the key findings from the present study is a key step in the process of intermediate pilot- and full-scale implementation. Previous studies have shown similar insignificant role of mixing energy at a full-scale (Allerdings 2015) and pilot-scale (Pivokonsky 2011) studies. In terms of evaluation of direct energy consumption, future studies on optimization of mixing energy for particle and organic removal are recommended at a pilot-scale by conducting similar water quality and floc size analysis at different mixing velocities.
2. **Particle size distributions (< 50 μm):** Floc breakage was indicated by an overall shift in floc size distributions to smaller scale (< 100 μm). Although the size detection limit of DIHM was set to measure floc diameters above 17 μm, it is suggested to result in an

obvious increase in smaller flocs sizes. It is recommended to examine any difference in the small floc size distributions as a result of the different coagulation mixing regimes and pH as carryover of these flocs can pose significant challenges on downstream separation processes (e.g., turbidity breakthrough in filters, reduced filter runtimes, increased organic loading etc.).

3. **Adsorption studies:** The sorption mechanism proposed from the experimental findings from this work has to be verified for different coagulant coagulation and types. A well-controlled adsorption study is recommended for this purpose. Use of wet procedures for understanding the mechanism of floc formation is recommended, instead of applying drying methods.
4. **Particle concentrations:** The work presented is applicable to achieve targeted removal of DOM for low turbidity and alkalinity conditions, which pose significant challenges in terms of optimizing chemicals and energy consumptions. Most surface waters in Nova Scotia is generally characterized as having a low alkalinity (<5 mg/L as $CaCO_3$), low pH (5.5-6.5), low turbidity (<2.0 NTU), and moderate to high in color and organic carbon. Since complexation and adsorption was indicated for a pH range used in water treatment at a high SUVA values, it would be interesting to conduct mixing experiments for a low to moderate SUVA values to understand their interactions and effects of coagulation mixing energy.

   Although this work was focused on low turbidity waters, the results are applicable for a high turbidity condition. An increase in particle concentrations at a high turbidity condition will results in a higher rate of collision between particles (Equation 8.1). The resulting floc sizes may reach a steady-state at a shorter mixing time during coagulation. The impact of shortening the time while maintaining the coagulation G-value must be investigated to ensure whether 60-90 s of coagulation mixing time is necessary to improve floc growth.
5. **Numerical modelling:** There are some serious limitations when using average G values to describe mixing intensity. One of the major limitations of this study was the spatial variation in the G-values was not accounted. High mixing energy may contain maximum local G-values in several orders higher in magnitude than the average G. The maximum

velocity gradient experienced by a floc or the length of time a floc spends in any particular G value requires numerical modelling approach (e.g., computational fluid dynamics).

References

Alberts, J.J. and Filip, Z. (1998) Metal binding in estuarine humic and fulvic acids: FTIR analysis of humic acid-metal complexes. Environmental Technology 19(9), 923-931.

Allen, T. (1997) Particle Size Measurement, Chapmann & Hall, London.

Allerdings, D., Foerster, G., Vasyukova, E. and Uhl, W. (2015) The practical influence of rapid mixing on coagulation in a full-scale water treatment plant. Water Science and Technology 71(4), 566-571.

Amirtharajah, A. and Mills, K.M. (1982) Rapid-mix design for mechanisms of alum coagulation. Journal American Water Works Association 74(4), 210-216.

Argaman, Y.A. (1971) Pilot-plant studies of flocculation. Journal American Water Works Association 63(12), 775-&.

American Water Works Association (AWWA), American Society of Civil Engineering (ASCE), 2012. Mixing, coagulation, and flocculation. In: Water Treatment Design. 5th ed. (S.J. Randtke and M.B. Horsley, editors). McGraw Hill, American Water Works Association and American Society of Civil Engineering, New York.

Baidoo, E., Ephraim, J.H., Darko, G. and Akoto, O. (2014) Potentiometric studies of the acid-base properties of tropical humic acids. Geoderma 217, 18-25.

Bellamy, L.J. (1968) Advances in infrared group frequencies Barnes & Noble Inc.,, London : Methuen.

Benjamin, M.M. and Lawler, D.F. (2013) Water quality engineering: physical/chemical treatment processes, John Wiley & Sons, New Jersey.

Biggs, C.A. and Lant, P.A. (2000) Activated sludge flocculation: On-line determination of floc size and the effect of shear. Water Research 34(9), 2542-2550.

Bigham, J.M., Carlson, L. and Murad, E. (1994) Schwertmannite, a new iron oxyhydroxysulphate from pyhasalmi, finland, and other localities. Mineralogical Magazine 58(393), 641-648.

Bose, P. and Reckhow, D.A. (1998) Adsorption of natural organic matter on preformed aluminum hydroxide flocs. Journal of Environmental Engineering-Asce 124(9), 803-811.

Bridgeman, J., Jefferson, B. and Parsons, S. (2008) Assessing floc strength using CFD to improve organics removal. Chemical Engineering Research & Design 86(8A), 941-950.

BSI (1963) BS3406: Methods for determination of particle size distribution. , BSI, London.

Chakraborti, R.K., Atkinson, J.F. and Van Benschoten, J.E. (2000) Characterization of alum floc by image analysis. Environmental Science & Technology 34(18), 3969-3976.

Chakraborti, R.K., Gardner, K.H., Atkinson, J.F. and Van Benschoten, J.E. (2003) Changes in fractal dimension during aggregation. Water Research 37(4), 873-883.

Chen, P., Cui, L. and Zhang, K. (2015) Surface-enhanced Raman spectroscopy monitoring the development of dual-species biofouling on membrane surfaces. Journal of Membrane Science 473, 36-44.

Coufort, C., Bouyer, D. and Line, A. (2005) Flocculation related to local hydrodynamics in a Taylor-Couette reactor and in a jar. Chemical Engineering Science 60(8-9), 2179-2192.

Crittenden, J.C., Trussell, R.R., Hand, D.W., Howe, K.J. and Tchobanoglous, G. (2005) Water Treatment Principles and Design, John Wiley & Sons, New Jersey.

Davis, C.C. and Edwards, M. (2014) Coagulation With Hydrolyzing Metal Salts: Mechanisms and Water Quality Impacts. Critical Reviews in Environmental Science and Technology 44(4), 303-347.

de Oliveira, A.L., Moreno, P., da Silva, P.A.G., De Julio, M. and Moruzzi, R.B. (2015) Effects of the fractal structure and size distribution of flocs on the removal of particulate matter. Desalination and Water Treatment, 1-12.

Dempsey, B.A., Ganho, R.M. and Omelia, C.R. (1984) The coagulation of humic substances by means of aluminum salts. Journal American Water Works Association 76(4), 141-150.

Droppo, I.G., Leppard, G.G., Flannigan, D.T. and Liss, S.N. (1997) The freshwater floc: A functional relationship of water and organic and inorganic floc constituents affecting suspended sediment properties. Water Air and Soil Pollution 99(1-4), 43-53.

Duan, J.M. and Gregory, J. (2003) Coagulation by hydrolysing metal salts. Advances in Colloid and Interface Science 100, 475-502.

Ducoste, J.J., Clark, M.M. and Weetman, R.J. (1997) Turbulence in flocculators: Effects of tank size and impeller type. Aiche Journal 43(2), 328-338.

Electric Power Research Institute, 2002. Water & Sustainability (Volume 4): U.S. Electricity Consumption for Water Supply & Treatment- The Next Half Century; Electric Power Research Institute Inc.: Palo Alto, CA.

Edzwald, J.K. (1993) Coagulation in drinking-water treatment - particles, organics and coagulants. Water Science and Technology 27(11), 21-35.

Edzwald, J.K. (2013) Coagulant mixing revisited: theory and practice. Journal of Water Supply Research and Technology-Aqua 62(2), 67-77.

El Samrani, A.G., Lartiges, B.S., Montarges-Pelletier, E., Kazpard, V., Barres, O. and Ghanbaja, J. (2004) Clarification of municipal sewage with ferric chloride: the nature of coagulant species. Water Research 38(3), 756-768.

Francois, R.J. (1988) Growth-kinetics of hydroxide flocs. Journal American Water Works Association 80(6), 92-96.

Garcia-Sucerquia, J., Xu, W.B., Jericho, S.K., Klages, P., Jericho, M.H. and Kreuzer, H.J. (2006) Digital in-line holographic microscopy. Applied Optics 45(5), 836-850.

Gibbs, R.J. and Konwar, L.N. (1982) Effect of pipetting on mineral flocs. Environmental Science & Technology 16(2), 119-121.

Goldberg, S. (2013) Surface Complexation Modeling. Reference Module in Earth Systems and Environmental Sciences.

Gonzalez-Torres, A., Putnam, J., Jefferson, B., Stuetz, R.M. and Henderson, R.K. (2014) Examination of the physical properties of Microcystis aeruginosa flocs produced on coagulation with metal salts. Water Research 60, 197-209.

Goodwill, J.E., Jiang, Y., Reckhow, D.A., Gikonyo, J. and Tobiason, J.E. (2015) Characterization of Particles from Ferrate Preoxidation. Environmental Science & Technology 49(8), 4955-4962.

Gorczyca, B. and Ganczarczyk, J. (1999) Structure and porosity of alum coagulation flocs. Water Quality Research Journal of Canada 34(4), 653-666.

Gorczyca, B. and Klassen, P. (2008) Optimization of Solids Separation in Dissolved Air Flotation. Water Quality Research Journal of Canada 43(2-3), 239-247.

Govoreanu, R., Saveyn, H., Van der Meeren, P. and Vanrolleghem, P.A. (2004) Simultaneous determination of activated sludge floc size distribution by different techniques. Water Science and Technology 50(12), 39-46.

Gu, B.H., Schmitt, J., Chen, Z., Liang, L.Y. and McCarthy, J.F. (1995) Adsorption and desorption of different organic-matter fractions on iron-oxide. Geochimica Et Cosmochimica Acta 59(2), 219-229.

Guan, X.-h., Chen, G.-h. and Shang, C. (2007) ATR-FTIR and XPS study on the structure of complexes formed upon the adsorption of simple organic acids on aluminum hydroxide. Journal of Environmental Sciences 19(4), 438-443.

Guan, X.-H., Shang, C. and Chen, G.-H. (2006) ATR-FTIR investigation of the role of phenolic groups in the interaction of some NOM model compounds with aluminum hydroxide. Chemosphere 65(11), 2074-2081.

Han, M.Y. and Lawler, D.F. (1992) The (relative) insignificance of g in flocculation. Journal American Water Works Association 84(10), 79-91.

Hedges, J.I. and Oades, J.M. (1997) Comparative organic geochemistries of soils and marine sediments. Organic Geochemistry 27(7-8), 319-361.

Hong, S.K. and Elimelech, M. (1997) Chemical and physical aspects of natural organic matter (NOM) fouling of nanofiltration membranes. Journal of Membrane Science 132(2), 159-181.

Hopkins, D.C. and Ducoste, J.J. (2003) Characterizing flocculation under heterogeneous turbulence. Journal of Colloid and Interface Science 264(1), 184-194.

Jarvis, P. 2004a The impact of natural organic matter on floc structure. PhD. thesis, Cranfield University, School of Water Sciences, United Kingdom.

Jarvis, P., Jefferson, B. and Parsons, S. (2004b) The duplicity of floc strength. Water Science and Technology 50(12), 63-70.

Jarvis, P., Jefferson, B., Gregory, J. and Parsons, S.A. (2005a) A review of floc strength and breakage. Water Research 39(14), 3121-3137.

Jarvis, P., Jefferson, B. and Parsons, S.A. (2005b) How the natural organic matter to coagulant ratio impacts on floc structural properties. Environmental Science & Technology 39(22), 8919-8924.

Jarvis, P., Jefferson, B. and Parsons, S.A. (2006) Floc structural characteristics using conventional coagulation for a high doc, low alkalinity surface water source. Water Research 40(14), 2727-2737.

Jarvis, P., Jefferson, B., Dixon, D. and Parsons, S.A. (2008) Treatment options and their effect on NOM-coagulant floc structures. Journal American Water Works Association 100(1), 64-73.

Jiang, J.Q. and Graham, N.J.D. (1998) Pre-polymerised inorganic coagulants and phosphorus removal by coagulation - A review. Water Sa 24(3), 237-244.

Jung, A.V., Chanudet, V., Ghanbaja, J., Lartiges, B.S. and Bersillon, J.L. (2005) Coagulation of humic substances and dissolved organic matter with a ferric salt: An electron energy loss spectroscopy investigation. Water Research 39(16), 3849-3862.

Kan, C.C., Huang, C.P. and Pan, J.R.S. (2002) Time requirement for rapid-mixing in coagulation. Colloids and Surfaces a-Physicochemical and Engineering Aspects 203(1-3), 1-9.

Kim, S.H., Moon, B.H. and Lee, H.I. (2001) Effects of pH and dosage on pollutant removal and floc structure during coagulation. Microchemical Journal 68(2-3), 197-203.

Lang, S. J., 2002. Optimize initial mixing with plug-flow reactors. J. Am. Water Works Assoc. 28 (12), 12-13, 22.

Leenheer, J.A. (1981) Comprehensive approach to preparative isolation and fractionation of dissolved organic-carbon from natural-waters and wastewaters. Environmental Science & Technology 15(5), 578-587.

Leenheer, J.A. and Croue, J.P. (2003) Characterizing aquatic dissolved organic matter. Environmental Science & Technology 37(1), 18A-26A.

Leiby, V., M., Burke, M., E., 2011. Energy efficiency best practices for North American drinking water utilities. ISBN 978-1-60573-159-9. Water Research Foundation and New York State Energy Research and Development Authority, U.S.A.

Letterman, R.D., Amirtharajah, A. and O'Melia, C.R. (1999) Coagulation and flocculation., American Water Works Association, McGraw Hill,New York.

Li, D.H. and Ganczarczyk, J. (1991) Size distribution of activated-sludge flocs. Research Journal of the Water Pollution Control Federation 63(5), 806-814.

Li, J. (1996) Rectilinear Vs. Curvilinear Models of Flocculation: Experimental Tests, The University of Texas, Austin.

Li, T., Zhu, Z., Wang, D., Yao, C. and Tang, H. (2006) Characterization of floc size, strength and structure under various coagulation mechanisms. Powder Technology 168(2), 104-110.

Li, X.Y. and Logan, B.E. (1997) Collision frequencies between fractal aggregates acid small particles in a turbulently sheared fluid. Environmental Science & Technology 31(4), 1237-1242.

Lin, J.L., Huang, C., Dempsey, B.A. and Hu, J.Y. (2014) Fate of hydrolyzed Al species in humic acid coagulation. Water Research 56, 314-324.

Ling, Z.C. and Wang, A. (2010) A systematic spectroscopic study of eight hydrous ferric sulfates relevant to Mars. Icarus 209(2), 422-433.

Lin-Vien, D., Colthup, N.B., Fateley, W.G. and Grasselli, J.G. (1963) The Handbook of Infrared and Raman Characteristic Frequencies of Organic Molecules, Academic Press, California.

Liu, C. and Huang, P.M. (2001) The influence of catechol humification on surface properties of metal oxides, In Humic substances structures, models and functions; Ghabbour, E. A.; Davies, G., Eds.; The Royal Society of Chemistry: Cambridge, UK, pp 253-270.

Lu, X.Q., Vassallo, A.M. and Johnson, W.D. (1997) Thermal stability of humic substances and their metal forms: an investigation using FTIR emission spectroscopy. Journal of Analytical and Applied Pyrolysis 43(2), 103-113.

Maas, C., 2010. Ontario's water-energy nexus: Will we find ourselves in hot water… or tap into opportunity? POLIS Research Report 10-01. POLIS Project on Ecological Governance, Canada. <http://poliswaterproject.org/nexus>.

Manning, A.J. and Dyer, K.R. (1999) A laboratory examination of floc characteristics with regard to turbulent shearing. Marine Geology 160(1-2), 147-170.

Matilainen, A., Vepsalainen, M. and Sillanpaa, M. (2010) Natural organic matter removal by coagulation during drinking water treatment: A review. Advances in Colloid and Interface Science 159(2), 189-197.

MFI™ micro-flow imaging. (2011). Technology overview- Area, ECD and intensity. mfitech.com. 30 May 2012. <http://www.mfitech.com/technology-overview/size-and-morphology/area-ecd-and-intensity/ >

Minor, E.C., Swenson, M.M., Mattson, B.M. and Oyler, A.R. (2014) Structural characterization of dissolved organic matter: a review of current techniques for isolation and analysis. Environmental Science-Processes & Impacts 16(9), 2064-2079.

Missan, S. and Hrytsenko, O. (2015) Using digital inline holographic microscopy and quantitative phase contrast imaging to assess viability of cultured mammalian cells, San Francisco, CA.

Mo, W., Wang, R. and Zimmerman, J.B. (2014) Energy-water nexus analysis of enhanced water supply scenarios: a regional comparison of Tampa bay, Florida, and San diego, California. Environmental Science & Technology 48(10), 5883-5891.

Myneni, S.C.B., Brown, J.T., Martinez, G.A. and Meyer-Ilse, W. (1999) Imaging of humic substance macromolecular structures in water and soils. Science 286(5443), 1335-1337.

Nakamoto, K. (1963) Infrared and Raman Spectra of Inorganic and Coordination Compounds, John Wiley & Sons, New York.

Narkis, N. and Rebhun, M. (1977) Stoichiometric relationship between humic and fulvic acids and flocculants. Journal American Water Works Association 69(6), 325-328.

New York State Energy Research & Development Authority (NYSERDA), 2010. Water and Wastewater Energy Management Best Practices Handbook. New York State Energy Research & Development Authority, Albany, New York.

Niemeyer, J., Chen, Y. and Bollag, J.M. (1992) Characterization of humic acids, composts, and peat by diffuse reflectance fourier-transform infrared-spectroscopy. Soil Science Society of America Journal 56(1), 135-140.

Nopens, I., Biggs, C.A., De Clercq, B., Govoreanu, R., Wilen, B.M., Lant, P. and Vanrolleghem, P.A. (2002) Modelling the activated sludge flocculation process combining laser light diffraction particle sizing and population balance modelling (PBM). Water Science and Technology 45(6), 41-49.

Owen, D.M., Amy, G.L., Chowdhury, Z.K., Paode, R., McCoy, G. and Viscosil, K. (1995) Nom - characterization and treatability. Journal American Water Works Association 87(1), 46-63.

Oyegbile, B., Ay, P. and Narra, S. (2016) Flocculation kinetics and hydrodynamic interactions in natural and engineered flow systems: A review. Environmental Engineering Research 21(1), 413-428.
Parker, D.S., Asce, A.M., Kaufman, W.J. and Jenkins, D. (1972) Floc breakup in turbulent flocculation processes. Journal of the Sanitary Engineering Division-Asce 98(NSA1), 79-&.

Parsons, S.A., Jefferson, B., Jarvis, P.J., Sharp, E., Dixon, D.W., Bolto, B. & Scale, P.J. 2007.Treatment of waters with elevated organic content. AwwaRF, Denver.

Pernitsky, D.J. and Edzwald, J.K. (2006) Selection of alum and polyaluminum coagulants: principles and applications. Journal of Water Supply Research and Technology-Aqua 55(2), 121-141.

Pivokonsky, M., Bubakova, P., Pivokonska, L. and Hnatukova, P. (2011) The effect of global velocity gradient on the character and filterability of aggregates formed during the coagulation/flocculation process. Environmental Technology 32(12), 1355-1366.

Plappally, A.K. and Lienhard, J.H. (2012) Energy requirements for water production, treatment, end use, reclamation, and disposal. renewable & sustainable energy reviews. 16(7), 4818-4848.

Prat, O.P. and Ducoste, J.J. (2006) Modeling spatial distribution of floc size in turbulent processes using the quadrature method of moment and computational fluid dynamics. Chemical Engineering Science 61(1), 75-86.

Ramimoghadam, D., Bagheri, S. and Hamid, S.B.A. (2014) Progress in electrochemical synthesis of magnetic iron oxide nanoparticles. Journal of Magnetism and Magnetic Materials 368, 207-229.

Ribeiro, J.S., Ok, S.S., Garrigues, S. and de la Guardia, M. (2001) FTIR tentative characterization of humic acids extracted from organic materials. Spectroscopy Letters 34(2), 179-190.

Rustad, J.R. and Casey, W.H. (2006) A molecular dynamics investigation of hydrolytic polymerization in a metal-hydroxide gel. Journal of Physical Chemistry B 110(14), 7107-7112.

Sari, M.A. and Chellam, S. (2015) Mechanisms of boron removal from hydraulic fracturing wastewater by aluminum electrocoagulation. Journal of Colloid and Interface Science 458, 103-111.

Samaras, K., Zouboulis, A., Karapantsios, T. and Kostoglou, M. (2010) A CFD-based simulation study of a large scale flocculation tank for potable water treatment. Chemical Engineering Journal 162(1), 208-216.

Santana, M.V.E., Zhang, Q. and Mihelcic, J.R. (2014) Influence of Water Quality on the Embodied Energy of Drinking Water Treatment. Environmental Science & Technology 48(5), 3084-3091.

Scott, M.J., Jones, M.N., Woof, C., Simon, B. and Tipping, E. (2001) The molecular properties of humic substances isolated from a UK upland peat system - A temporal investigation. Environment International 27(6), 449-462.

Sharp, E.L., Parsons, S.A. and Jefferson, B. (2006) Seasonal variations in natural organic matter and its impact on coagulation in water treatment. Science of the Total Environment 363(1-3), 183-194.

Sheng, J., Malkiel, E. and Katz, J. (2006) Digital holographic microscope for measuring three-dimensional particle distributions and motions. Applied Optics 45(16), 3893-3901.

Sieliechi, J.M., Lartiges, B.S., Kayem, G.J., Hupont, S., Frochot, C., Thieme, J., Ghanbaja, J., de la Caillerie, J.B.D., Barres, O., Kamga, R., Levitz, P. and Michot, L.J. (2008) Changes in humic acid conformation during coagulation with ferric chloride: Implications for drinking water treatment. Water Research 42(8-9), 2111-2123.

Smith, B. (1999) Infrared Spectral Interpretation: A Systematic Approach, CRC Press, Baco Raton, London, New York, Washington D.C.

Spicer, P.T. and Pratsinis, S.E. (1996) Shear-induced flocculation: The evolution of floc structure and the shape of the size distribution at steady state. Water Research 30(5), 1049-1056.

Spicer, P.T., Keller, W. and Pratsinis, S.E. (1996) The effect of impeller type on floc size and structure during shear-induced flocculation. Journal of Colloid and Interface Science 184(1), 112-122.

Spicer, P.T., Pratsinis, S.E., Raper, J., Amal, R., Bushell, G. and Meesters, G. (1998) Effect of shear schedule on particle size, density, and structure during flocculation in stirred tanks. Powder Technology 97(1), 26-34.

Stanley, S.J. and Smith, D.W. (1995) Measurement of turbulent-flow in standard jar test apparatus. Journal of Environmental Engineering-Asce 121(12), 902-910.

Stokes, J. and Horvath, A. (2006) Life cycle energy assessment of alternative water supply systems. International Journal of Life Cycle Assessment 11(5), 335-343.

Stumm, W. and Morgan, J.J. (1962) Chemical Aspects of Coagulation. Journal American Water Works Association 54(8), 971-992.

Stumm, W. and Morgan, J.J. (1995) Aquatic Chemistry: Chemical Equilibria and Rates in Natural Waters, John Wiley & Sons, New York.

Tejedor-Tejedor, M.I., Yost, E.C. and Anderson, M.A. (1990) Characterization of benzoic and phenolic complexes at the goethite/aqueous solution interface using cylindrical internal reflection Fourier transform infrared spectroscopy. Part 1. Methodology. Langmuir 6 (- 5), 979-987.

Ten State Standards of the Great Lakes-Upper Mississippi River Board of State and Provincial Public Health and Environmental Managers, 2012. Recommended standards for water works. Health Research Inc., Health Education Services Division, Albany, New York.

Thomas, D.N., Judd, S.J. and Fawcett, N. (1999) Flocculation modelling: A review. Water Research 33(7), 1579-1592.

Thurman, E. M., 1985. Organic geochemistry of natural waters. ISBN: 978-94-010-8752-0. Martinus Nijhoff/Dr W. Junk Publishers, Dordrecht.

Tremblay, L., Alaoui, G. and Leger, M.N. (2011) Characterization of Aquatic Particles by Direct FTIR Analysis of Filters and Quantification of Elemental and Molecular Compositions. Environmental Science & Technology 45(22), 9671-9679.

U.S. Environmental Protection Agency (USEPA), 2008. Ensuring a sustainable future: an energy management guidebook for wastewater and water utilities. U.S. Environmental Protection Agency, Washington, D.C.

U.S. Environmental Protection Agency (USEPA), (1999). Enhanced coagulation and enhanced precipitative softening guidance manual. EPA 815-R-99-012. U.S. Environmental Protection Agency, U.S.A.

Vadasarukkai, Y.S. and Gagnon, G.A. (2010) Determination of conventional velocity gradient (G) using CFD technique for a pilot-scale flocculation system. Journal of Water Supply Research and Technology-Aqua 59(8), 459-470.

Vadasarukkai, Y.S., Gagnon, G.A., Campbell, D.R. and Clark, S.C. (2011) Assessment of hydraulic flocculation processes using CFD. Journal American Water Works Association 103(11), 66-+.

Vadasarukkai, Y.S. and Gagnon, G.A. (2015) Application of low-mixing energy input for the coagulation process. Water Research 84, 333-341.

Vanbenschoten, J.E. and Edzwald, J.K. (1990) Chemical aspects of coagulation using aluminum salts .2. coagulation of fulvic-acid using alum and polyaluminum chloride. Water Research 24(12), 1527-1535.

Varsanyi, G., Szoke, S. 1969. Vibrational spectra of benzene derivatives, Academic Press, New York; London.

Vilge-Ritter, A., Rose, J., Masion, A., Bottero, J.Y. and Laine, J.M. (1999) Chemistry and structure of aggregates formed with Fe-salts and natural organic matter. Colloids and Surfaces a-Physicochemical and Engineering Aspects 147(3), 297-308.

Vinkler, P., Lakatos, B. and Meisel, J. (1976) Infrared spectroscopic investigations of humic substances and their metal-complexes. Geoderma 15(3), 231-242.

Webster, J.G., Swedlund, P.J. and Webster, K.S. (1998) Trace metal adsorption onto an acid mine drainage iron(III) oxy hydroxy sulfate. Environmental Science & Technology 32(10), 1361-1368.

West, J., 2015. Creating a culture of water and energy efficiency in Nova Scotia communities. Ecological Action Centre. <http://ecologyaction.ca>.

Wu, J. and Wheatley, A. (2010) Assessing activated sludge morphology by laser and image analysis. Proceedings of the Institution of Civil Engineers-Water Management 163(3), 139-145.

Xiao, F., Yi, P., Pan, X.-R., Zhang, B.-J. and Lee, C. (2010) Comparative study of the effects of experimental variables on growth rates of aluminum and iron hydroxide flocs during coagulation and their structural characteristics. Desalination 250(3), 902-907.

Xie, J.K., Wang, D.S., van Leeuwen, J., Zhao, Y.M., Xing, L.N. and Chow, C.W.K. (2012) pH modeling for maximum dissolved organic matter removal by enhanced coagulation. Journal of Environmental Sciences-China 24(2), 276-283.

Yao, M., Nan, J. and Chen, T. (2014) Effect of particle size distribution on turbidity under various water quality levels during flocculation processes. Desalination 354, 116-124.

Yeung, A.K.C. and Pelton, R. (1996) Micromechanics: A new approach to studying the strength and breakup of flocs. Journal of Colloid and Interface Science 184(2), 579-585.

Yu, W.-Z., Gregory, J. and Graham, N. (2016) Regrowth of Broken Hydroxide Flocs: Effect of Added Fluoride. Environmental Science & Technology 50(4), 1828-1833.

Yu, W.-z., Gregory, J., Liu, H.-j. and Qu, J.-h. (2014) Investigation of the property of kaolin-alum flocs at acidic pH. Colloids and Surfaces a-Physicochemical and Engineering Aspects 443, 177-181.

Yukselen, M.A. & Gregory, J. 2004 The reversibility of floc breakage. Int. J. Miner. Process 73(2-4), 251-259.

Zeng, T., Wilson, C.J. and Mitch, W.A. (2014) Effect of Chemical Oxidation on the Sorption Tendency of Dissolved Organic Matter to a Model Hydrophobic Surface. Environmental Science & Technology 48(9), 5118-5126.

Zhong, R., Zhang, X., Xiao, F., Li, X. and Cai, Z. (2011) Effects of humic acid on physical and hydrodynamic properties of kaolin flocs by particle image velocimetry. Water Research 45(13), 3981-3990.

Appendix A FT-IR Sample Preparation, pKa Determination, and Curvilinear Sample Calculations

A.1 Sample Preparation for the Fourier Transform Infrared Spectroscopy (FT-IR) Analysis

An attenuated total reflectance module (ATR) of the Fourier Transform Infrared Spectroscopy (FT-IR) was used to identify possible functional groups present in floc aggregates, following coagulation and flocculation experiments. All the infrared analysis was carried out using the Cary 630 ATR FT-IR (Agilent Technologies, Santa Clara, California) in the absorption mode. It had two modules: an ATR stage for both solid and liquid samples; a dialpath stage, specifically for liquid samples. The dialpath of the FT-IR module had a particle size restriction to 30, 50 and 100 µm, which was less than floc sizes measured in the present study. Hence, an ATR module with a zinc selenide (Zn-Se) crystal was used for this purpose.

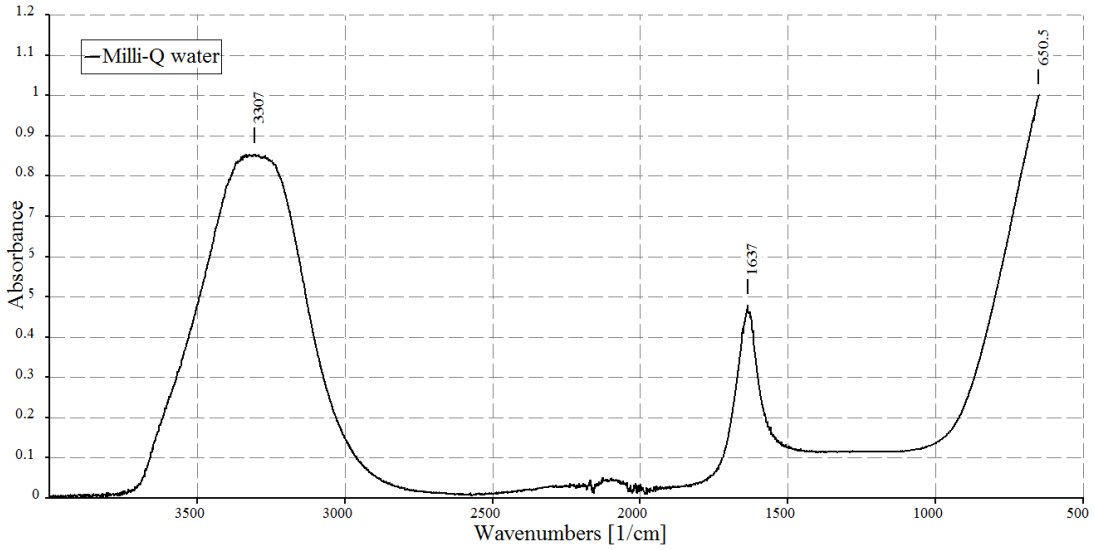

Figure A.1 FTIR spectra of a deionized (DI) water sample

An approximate volume of floc aggregates was collected following coagulation (~150 mL) and settling experiments (~850 mL). Samples were then allowed to settle for at least an hour; while water was carefully discarded from the surface level using a 25 mL glass pipette. Three sampling procedures were tested to concentrate and collect humic floc aggregates: a direct freeze-drying at -20 ^{0}C (El Samrani et al. 2004), an oven-drying method at 35-40 ^{0}C, and a filtration method on a glass fiber filter (glass microfibers, 0.7 μm porosity, Whatman Co.) (Tremblay et al. 2011). Samples were preserved at -70 ^{0}C before freeze drying. While for filtration method, glass fiber filters were initially combusted at 500 ^{0}C for 16 h, following a procedure from Tremblay et al. (2011) to remove any organic impurities. Floc sample was then filtered through a pre-combusted glass filter at room temperature using a vacuum pump.

Moisture or water content from the filtered samples was removed at two different temperatures: air-dried at room temperature (21 ± 1°C), and vacuum dried. These two methods were chosen as it prevents crystallinity development that occurs at high temperature Sari and Chellam 2015). An attempt to collect floc samples by centrifugation for 20 min at 6000 rpm (Sari and Chellam 2015) was not always successful. As the vacuum dried samples used to stick to the container walls, which caused very less amount of sample to cover the crystal surface. This type of sampling issue occurred during the direct freeze drying method as well.

A.1.1 FT-IR Results of Drying Methods

As illustrated in Figure A.2, filtration on a glass fiber filter produced similar IR spectra for air- and vacuum-dried samples. It had the two distinct peaks at 2920 and 2850 cm^{-1}, which represented the C-H stretch of aliphatic hydrocarbon with the iron addition. The two metal-COO$^-$ stretching peaks were also identified. Although the glass fiber filter was opaque to IR spectra (Tremblay et al., 2011), it produced a strong background noise near 1000 cm^{-1}, which overlapped with the assigned vibrational mode of S-O of sulphate in iron-DOM complexes. Notably, this region varied among other methods (refer *bottom panel* in Figure A.2). Centrifuged and filtration method showed a single strong peak; while the oven and freeze dried samples experienced two splits in that region. One possible explanation for this is related to drying methods employed. It has been noted previously that the degree of dehydration (prolonged exposure to high or low temperatures) caused a large distortion to SO_4 tetrahedra in ferric sulfate structure (Ling and

Wang, 2010). On a similar note, Lu et al. (1997) showed iron humate complexes are less stable and decompose at a faster rate as temperature was varied from 150 to 400 ^{0}C temperatures, with a release of carbon monoxide (band identified at 2180 cm^{-1}). Notably, this band was prominent for most of the FT-IR peaks observed in this study at temperatures below 40 ^{0}C.

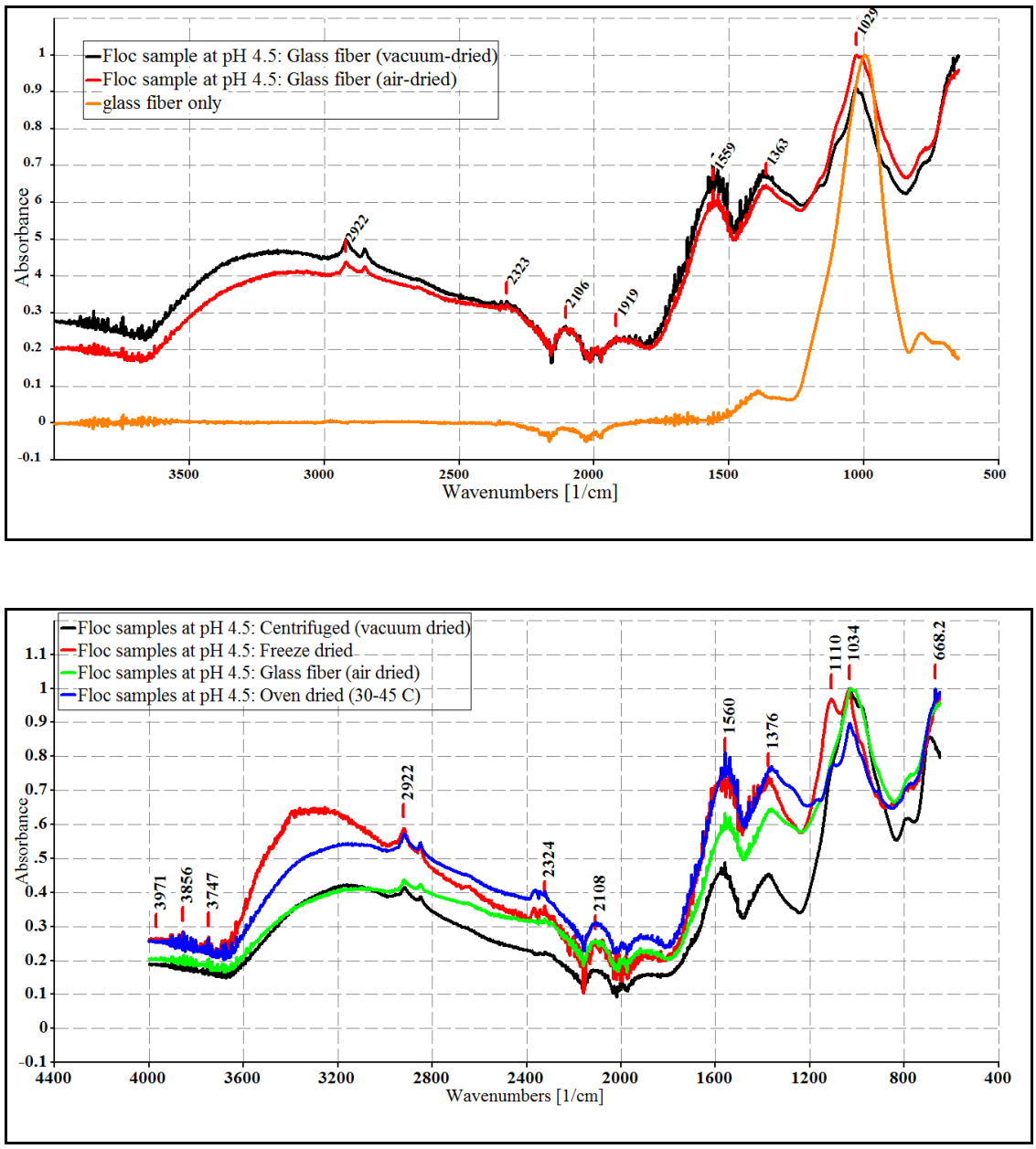

Figure A.2 Comparison of FT-IR spectra from different sample preparation methods

(a) Filtration on glass fiber filters (*top panel*) (b) all methods (*bottom panel*)

It was found from the preliminary investigation of spectral data that all the four drying procedures examined in this present study had some influence on the FT-IR spectra generated for DOM-metal complexes. Highest intensity of most spectral region was obtained by oven-drying method at 35-40 ^{0}C. The findings from oven-dried samples showed comparable results to the freeze-dried samples, which has been commonly used to preserve coagulated sediments (El Samrani et al. 2004). The oven-dried floc aggregates in the crucibles were scraped and placed it on the surface of the crystal, and the dial was lowered to lock into place. The Happ-Genzel method was used with 200 scans at a resolution of 2 cm^{-1} was collected from a spectral range of 650-4000 cm^{-1}. Backgrounds were taken with the crystal alone.

A.1.2 FT-IR Results of Ferric Sulphate

When ferric sulphate was added to water, the IR profile varied significantly for pH 4.8 and 6.8. Although the stretching and bending modes of water molecules were quite similar to ferric sulphate, it was interesting to note the asymmetrical vibrational mode of S-O in sulphate experienced severe changes in their spectra. As noted previously, peak splitting indicates variation in distortion to SO_4 tetrahedra in ferric sulfate structure during the process of dehydration (Ling et al. 2010). In that study, amorphous phase was suggested to have a broad peak at 1032 cm^{-1}, which was observed at 1100 cm^{-1} for the case of pH 6.8; while multiple peaks caused at pH 4.8 was possibly due to degree of distortion caused by water molecules in their structure.

A quantitative analysis of various iron hydrolyses species that may have formed during hydrolysis was not conducted in this study. However, the surfaces of iron hydrolysis species, in particular iron hydroxide, were assumed to be covered with surface hydroxyl groups. In the FT-IR spectra for pH 6.8, the –OH stretch at 3173 cm^{-1} of ferric sulfate was shifted to a higher wavenumber, approximately 3300 cm^{-1}, which signified the participation of hydroxyl group in the adsorption process (Rout et al., 2012). Free hydroxyl ions are characterized by a sharp stretching band at 3700-3500 cm^{-1} (Nakamoto, 1986), which may arise from the surface hydroxyl groups of iron hydrolyzed precipitates as shown in Figure A.3 for the absorption bands above 3500 cm^{-1}. The active surface functional groups at ferrihydrite edges, Fe-O and Fe-OH, were reported to have corresponding peaks at 1572 and 1392 cm^{-1} based on the information from

other researchers (Rout et al., 2012). Two bands were identified at 1472 and 1374 cm^{-1} at pH 6.8 that may corresponds to Fe-O and Fe-OH, respectively; however, these assigned bands were at a slightly different wavenumber than the reported values probably due to sulphate interferences.

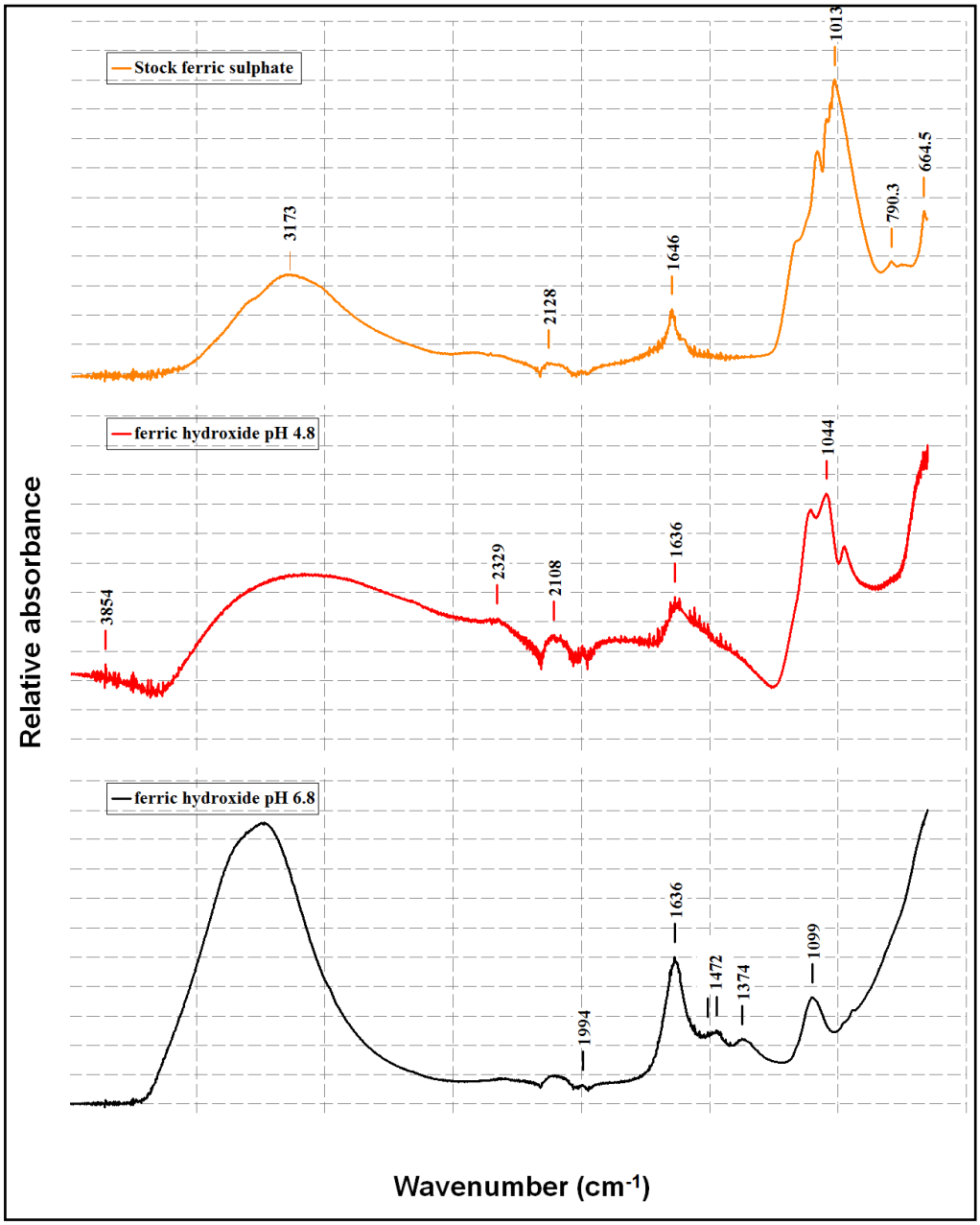

Figure A.3 Comparison of FT-IR spectra for ferric sulphate at pH 4.8 and 6.8

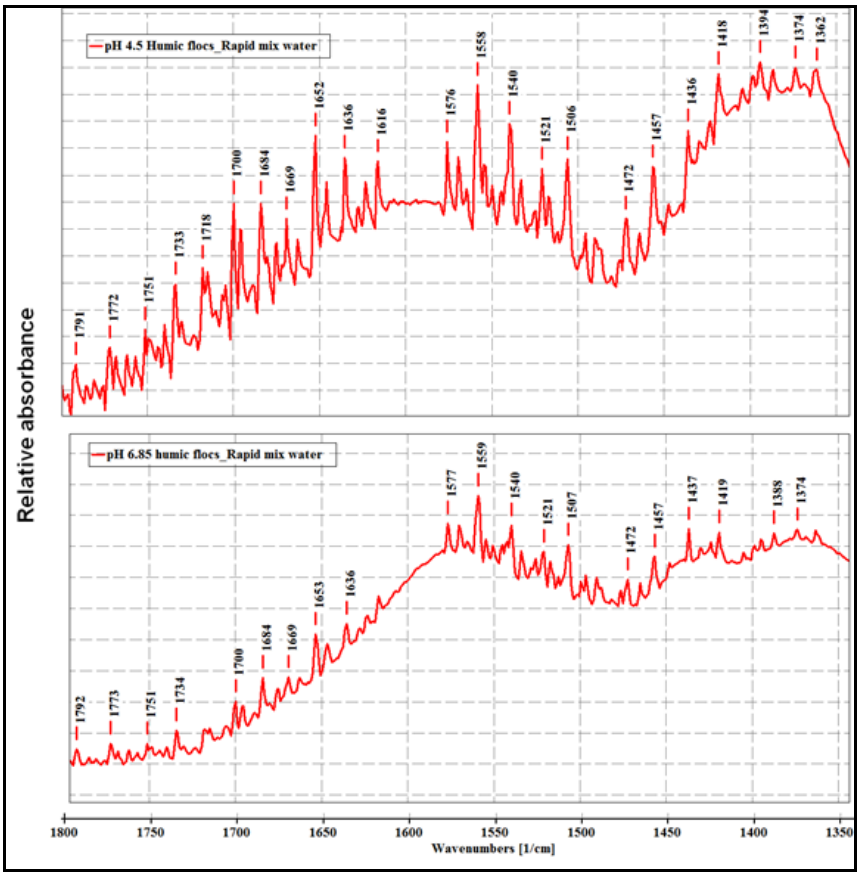

Figure A.4 Comparison of the FT-IR region between 1800 and 1350 cm^{-1} for humic flocs formed at the two selected pHs

(a) an acidic pH of 4.5 and an optimal coagulant iron dose of 8 mg/L (b) a near neutral pH of 6.8 and an optimal coagulant iron dose of 14 mg/L of Fe

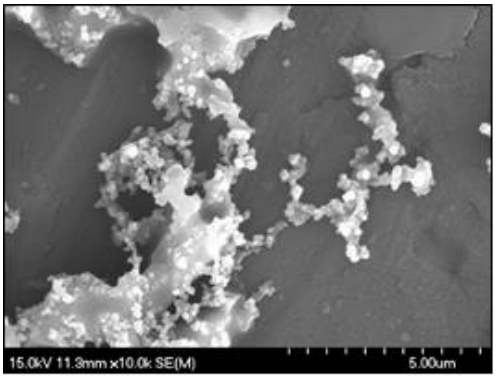

Element	Weight%
C K	22.15
O K	40.16
Na K	3.89
Mg K	2.5
Al K	27.16
S K	1.47
Ca K	1.07
Fe L	1.6
Totals	100.00

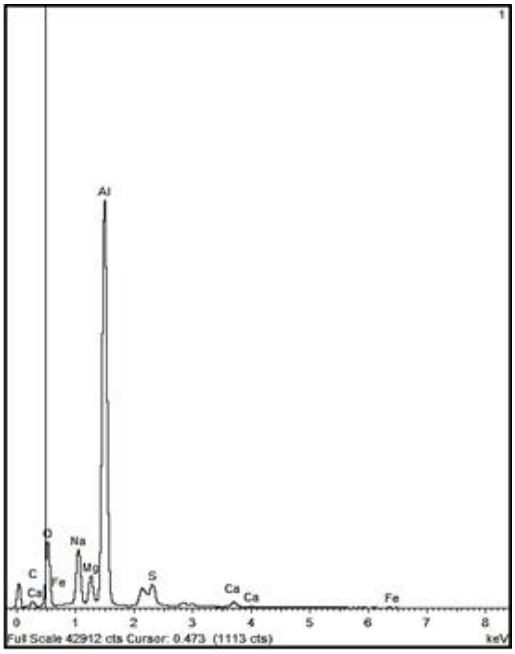

Figure A.5 Micrograph image and EDS analysis of a portion of humic macromolecules that remained after settling process (i.e., supernatant) at pH 6.8

A2. Determination of pK_a

The disassociation of functional groups is shown to strongly depend on both pH and ionic strength (Baidoo et al. 2014). Acid-base pH titration curves were used to estimate the acid dissociation constant (pK_a). Stock solution of a strong base, 1N NaOH, solution was used as a titrant in the titration procedure. The change in pH with a small addition of base (i.e., 1N NaOH) was noted down, starting from an initial pH of 2.5. The equivalence point was noted as the point where the weak acid in the solution was neutralized by the base added, which was indicated by a change in the slope direction. The pK_a was determined at half the equivalence point using Henderson-Hasselbach equation as given below:

$$\mathbf{pK_a = pH - \log\left(\frac{\alpha}{1-\alpha}\right)} \qquad \text{(A.1)}$$

where, α was the degree of disassociation and it is equal to 0.5 at pK_a (i.e., 50% disassociation of acid groups). All titrations were carried out at room temperature.

The pK_a value provides a quantitative explanation for understanding the formation of soluble and insoluble complexes in aqueous solution. This value is important to estimate protonation of a ligand depending on the pH of a solution. For example, by using the pK_a value for benzoic acid, Xiao-hong et al., (2006) identified possible species of benzoic acid at different pHs. That is, disassociation of benzoic acid to benzoate ions ($C_6H_5COO^-$) was indicated at a pH value of 4.12 (since pK_a = pH). A mixture of benzoate ions and benzoic acid was suggested at pH 4; while at pH 7, the solution corresponds more to benzoate anions ($C_6H_6COO^-$).

Acid-base pH titration was carried out for three sets of solution, consisting of 1L of 5 mM of stock ferric sulphate only, 1L of synthetic humic water only, and a liter containing a mixture of 0.3 mM of iron and humic water. Figure A.6 shows a comparison of the three titration curves. In the titration containing only iron, the change in slope of the curve started at 1.85 mM of NaOH, which was marked by an equivalence point or "end point" at a pH of 5.5. The corresponding pK_a value was at 2.72, which indicates hydrolysis of ferric ion resulting in different soluble and insoluble hydrolysis species. For titration curve having only humic water, disassociation of weak acids was indicated at two pK_a values of 2.8 and 6.4. This indicates presence of more than one functional group in humic water. The first inflection point may depict protonation of a weak carboxylic acid in the source water and the second may reflect the presence of a phenolic group.

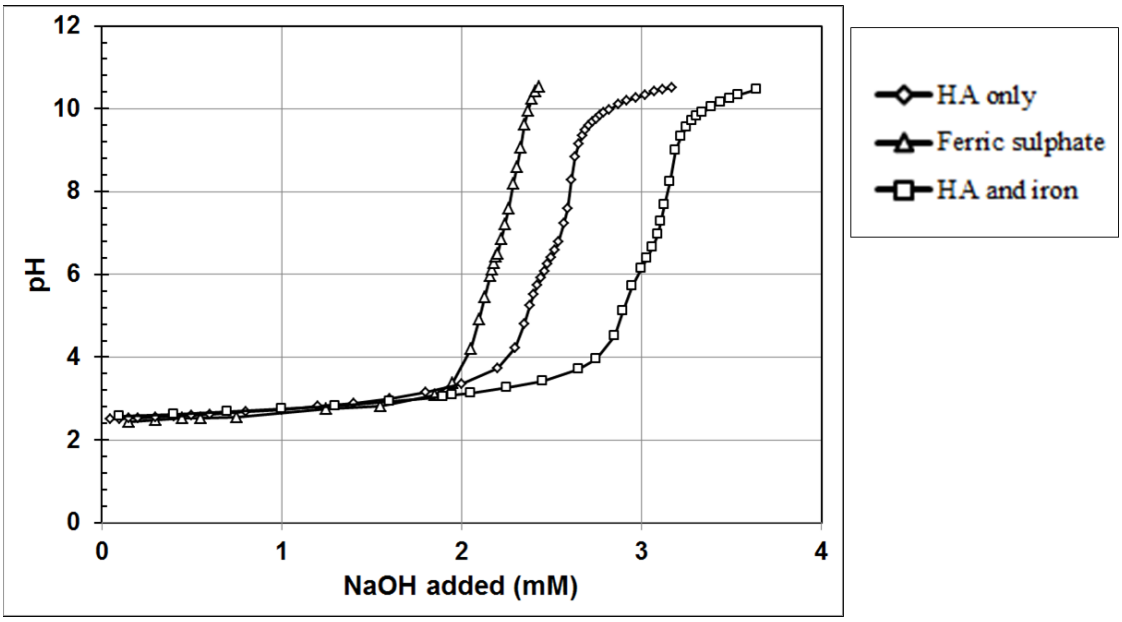

Figure A.6 Acid-base pH titration curves for humic acid, iron, and an iron-humic mixture

Titration of humic water with iron showed an increased amount of NaOH required to reach the equivalence point at 5.76. This suggests possible complexation reaction of iron with anionic ligands in the humic water (Stumm and Morgan 1962). Complex formed may be soluble depending on the charge of the complex formed. It has been shown by Stumm and Morgan (1962) that precipitation does not take place until all surface charges on complex are neutralized by equivalents OH^-, in their example calculation it was shown precipitation of hydroxo-oxalate aluminum complex was approximately at 5.8. When all weak acids reacted, it reached an equivalence point. After this point, a steep incline in the pH was observed, which was essentially due to an increase in the concentration of hydroxyl ions with the addition of base. This change in slope was observed near pH 5.1 and 9, suggesting precipitation of soluble complexes to insoluble precipitates.

A3. Calculation Equations for Collision Efficiency Function

Table A3.1 Collision efficiency for Brownian motion, shear, and differential sedimentation (Benjamin and Lawler 2013)

Table A-1. Collision Efficiency for Brownian Motion

Diameter	a	b	c	d
0.1	1.025	-0.626	0.516	-0.152
0.2	1.007	-0.86	0.87	-0.322
0.6	0.976	-1.155	1.342	-0.554
1	0.962	-1.263	1.522	-0.645
2	0.943	-1.383	1.725	-0.748
6	0.916	-1.533	1.991	-0.887
10	0.905	-1.587	2.087	-0.936
20	0.891	-1.658	2.221	-1.009
60	0.871	-1.739	2.371	-1.09
200	0.863	-1.775	2.439	-1.125
β_{Br}=	$a+b\lambda+c\lambda 2+d\lambda 3$			

Table A-2 Collision Efficiency for Fluid Shear

Log HA	a	b	c	d
1	-1.128	2.498	-2.042	0.671
0	-1.128	2.498	-2.042	0.671
-1	-1.482	3.189	3.468	1.581
-2	-1.704	3.116	-2.881	1.121
-3	-2.523	5.55	-6.098	2.553
-4	-3.723	10.039	-12.569	5.557
-5	-5.775	18.267	24.344	10.992
-6	-7.037	20.829	-25.589	10.755
-7	-8.773	25.663	-30.703	12.555
-8	-9.733	-11.466	-13.199	14.555
H_A=	$A/18.\mu.(d_i)^3.G$			
$Sh_{\alpha i,j}$ =	$8/(1+\lambda)^3.10^{a+b\lambda+c\lambda 2+d\lambda 3}$			

Table A-3 Collision Efficiency for Differential Sedimentation

long Ng	a	b	c	d
1	-0.3184	-0.548	0.0865	0.501
0	-0.84	0.423	-1.069	0.93
-1	-1.32	1.318	-2.17	1.361
-2	-1.757	2.137	-3.229	1.794
-3	-2.152	2.88	-4.232	2.23
-4	-2.505	3.547	-5.186	2.668
-5	-2.815	4.137	-6.088	3.108
-6	-3.084	4.652	-6.94	3.551
-7	-3.31	5.09	-7.742	3.996
-∞	-3.928	6.423	-9.449	4.614
N_B=	$48A/\pi.(\rho p-\rho L)\cdot g\cdot dl^4$			
$DS_{\alpha i,j}$ =	$10^{a+b\lambda+c\lambda 2+d\lambda 3}$			

Appendix B Copyright Permissions

B1. Copyright Permissions from the Journal of Environmental Science: Water Research & Technology (Royal Society of Chemistry)

Dear Mr Vadasarukkai

Thank you for your e-mail. This will be fine as long as the article is embedded in the thesis and is not reproduced as a separate document. There should also be a link back to the article on our website - http://dx.doi.org/10.1039/C5EW00259A.

Yours sincerely

Environmental Science: Water Research & Technology Editorial Office
Royal Society of Chemistry
Thomas Graham House,
Science Park, Milton Road
Cambridge, CB4 0WF, UK

COPYRIGHT NOTES FOR THE AUTHORS

Characterization, fate and transport of floc aggregates in full-scale flocculation tanks
Y. S. Vadasarukkai and G. A. Gagnon, Environ. Sci.: Water Res. Technol., 2016, 2, 223
DOI: 10.1039/C5EW00259A

If you are not the author of this article and you wish to reproduce material from it in a third party non-RSC publication you must formally request permission using RightsLink. Go to our Instructions for using RightsLink page for details.

Authors contributing to RSC publications (journal articles, books or book chapters) do not need to formally request permission to reproduce material contained in this article provided that the correct acknowledgement is given with the reproduced material.

Reproduced material should be attributed as follows:

For reproduction of material from NJC:

Reproduced from Ref. XX with permission from the Centre National de la Recherche Scientifique (CNRS) and The Royal Society of Chemistry.

For reproduction of material from PCCP:
Reproduced from Ref. XX with permission from the PCCP Owner Societies.

For reproduction of material from PPS:
Reproduced from Ref. XX with permission from the European Society for Photobiology, the European Photochemistry Association, and The Royal Society of Chemistry.

For reproduction of material from all other RSC journals and books:
Reproduced from Ref. XX with permission from The Royal Society of Chemistry.
If the material has been adapted instead of reproduced from the original RSC publication "Reproduced from" can be substituted with "Adapted from".

In all cases the Ref. XX is the XXth reference in the list of references.

If you are the author of this article you do not need to formally request permission to reproduce figures, diagrams etc. contained in this article in third party publications or in a thesis or dissertation provided that the correct acknowledgement is given with the reproduced material.

Reproduced material should be attributed as follows:

For reproduction of material from NJC:
[Original citation] - Reproduced by permission of The Royal Society of Chemistry (RSC) on behalf of the Centre National de la Recherche Scientifique (CNRS) and the RSC

For reproduction of material from PCCP:
[Original citation] - Reproduced by permission of the PCCP Owner Societies

For reproduction of material from PPS:
[Original citation] - Reproduced by permission of The Royal Society of Chemistry (RSC) on behalf of the European Society for Photobiology, the European Photochemistry Association, and RSC

For reproduction of material from all other RSC journals:
[Original citation] - Reproduced by permission of The Royal Society of Chemistry
If you are the author of this article you still need to obtain permission to reproduce the whole article in a third party publication with the exception of reproduction of the whole article in a thesis or dissertation.

Information about reproducing material from RSC articles with different licences is available on our Permission Requests page.

B2. Copyright Permissions from Water Research (Elesevier)

ELSEVIER LICENSE
TERMS AND CONDITIONS
Jul 04, 2016

This Agreement between Yamuna S. Vadasarukkai ("You") and Elsevier ("Elsevier") consists of your license details and the terms and conditions provided by Elsevier and Copyright Clearance Center.

License Number
3901911310337
License date
Jul 04, 2016
Licensed Content Publisher
Elsevier
Licensed Content Publication
Water Research
Licensed Content Title
Application of low-mixing energy input for the coagulation process
Licensed Content Author
Yamuna S. Vadasarukkai,Graham A. Gagnon
Licensed Content Date
1 November 2015
Licensed Content Volume Number
84
Licensed Content Issue Number
n/a
Licensed Content Pages
9
Start Page
333
End Page
341
Type of Use
reuse in a thesis/dissertation
Portion

full article
Format
both print and electronic
Are you the author of this Elsevier article?
Yes
Will you be translating?
No
Order reference number
Title of your thesis/dissertation
Investigation of the Mixing Energy Consumption Affecting Coagulation and Floc Aggregation
Expected completion date
Aug 2016
Estimated size (number of pages)
202
Elsevier VAT number
GB 494 6272 12
Requestor Location
Yamuna S. Vadasarukkai
1360 Barrington Street
Office D-514, Dalhousie University

Halifax, NS B3H 4R2
Canada
Attn: Yamuna S. Vadasarukkai
Total
0.00 CAD
Terms and Conditions

INTRODUCTION

1. The publisher for this copyrighted material is Elsevier. By clicking "accept" in connection with completing this licensing transaction, you agree that the following terms and conditions apply to this transaction (along with the Billing and Payment terms and conditions established by Copyright Clearance Center, Inc. ("CCC"), at the time that you opened your Rightslink account and that are available at any time at http://myaccount.copyright.com).

GENERAL TERMS

2. Elsevier hereby grants you permission to reproduce the aforementioned material subject to the terms and conditions indicated.

3. Acknowledgement: If any part of the material to be used (for example, figures) has appeared in our publication with credit or acknowledgement to another source, permission must also be sought from that source. If such permission is not obtained then that material may not be included in your publication/copies. Suitable acknowledgement to the source must be made, either as a footnote or in a reference list at the end of your publication, as follows:
"Reprinted from Publication title, Vol /edition number, Author(s), Title of article / title of chapter, Pages No., Copyright (Year), with permission from Elsevier [OR APPLICABLE

SOCIETY COPYRIGHT OWNER]." Also Lancet special credit - "Reprinted from The Lancet, Vol. number, Author(s), Title of article, Pages No., Copyright (Year), with permission from Elsevier."

4. Reproduction of this material is confined to the purpose and/or media for which permission is hereby given.

5. Altering/Modifying Material: Not Permitted. However figures and illustrations may be altered/adapted minimally to serve your work. Any other abbreviations, additions, deletions and/or any other alterations shall be made only with prior written authorization of Elsevier Ltd. (Please contact Elsevier at permissions@elsevier.com)

6. If the permission fee for the requested use of our material is waived in this instance, please be advised that your future requests for Elsevier materials may attract a fee.

7. Reservation of Rights: Publisher reserves all rights not specifically granted in the combination of (i) the license details provided by you and accepted in the course of this licensing transaction, (ii) these terms and conditions and (iii) CCC's Billing and Payment terms and conditions.

8. License Contingent Upon Payment: While you may exercise the rights licensed immediately upon issuance of the license at the end of the licensing process for the transaction, provided that you have disclosed complete and accurate details of your proposed use, no license is finally effective unless and until full payment is received from you (either by publisher or by CCC) as provided in CCC's Billing and Payment terms and conditions. If full payment is not received on a timely basis, then any license preliminarily granted shall be deemed automatically revoked and shall be void as if never granted. Further, in the event that you breach any of these terms and conditions or any of CCC's Billing and Payment terms and conditions, the license is automatically revoked and shall be void as if never granted. Use of materials as described in a revoked license, as well as any use of the materials beyond the scope of an unrevoked license, may constitute copyright infringement and publisher reserves the right to take any and all action to protect its copyright in the materials.

9. Warranties: Publisher makes no representations or warranties with respect to the licensed material.

10. Indemnity: You hereby indemnify and agree to hold harmless publisher and CCC, and their respective officers, directors, employees and agents, from and against any and all claims arising out of your use of the licensed material other than as specifically authorized pursuant to this license.

11. No Transfer of License: This license is personal to you and may not be sublicensed, assigned, or transferred by you to any other person without publisher's written permission.

12. No Amendment Except in Writing: This license may not be amended except in a writing signed by both parties (or, in the case of publisher, by CCC on publisher's behalf).

13. Objection to Contrary Terms: Publisher hereby objects to any terms contained in any purchase order, acknowledgment, check endorsement or other writing prepared by you, which terms are inconsistent with these terms and conditions or CCC's Billing and Payment terms and conditions. These terms and conditions, together with CCC's Billing and Payment terms and conditions (which are incorporated herein), comprise the entire agreement between you and publisher (and CCC) concerning this licensing transaction. In the event of any conflict between your obligations established by these terms and conditions and those established by CCC's Billing and Payment terms and conditions, these terms and conditions shall control.

14. Revocation: Elsevier or Copyright Clearance Center may deny the permissions described in this License at their sole discretion, for any reason or no reason, with a full refund payable to you. Notice of such denial will be made using the contact information provided by you. Failure to receive such notice will not alter or invalidate the denial. In no event will Elsevier or Copyright Clearance Center be responsible or liable for any costs, expenses or damage incurred by you as a result of a denial of your permission request, other than a refund of the amount(s) paid by you to Elsevier and/or Copyright Clearance Center for denied permissions.

LIMITED LICENSE

The following terms and conditions apply only to specific license types:
15. **Translation**: This permission is granted for non-exclusive world **English** rights only unless your license was granted for translation rights. If you licensed translation rights you may only translate this content into the languages you requested. A professional translator must perform all translations and reproduce the content word for word preserving the integrity of the article.

16. **Posting licensed content on any Website**: The following terms and conditions apply as follows: Licensing material from an Elsevier journal: All content posted to the web site must maintain the copyright information line on the bottom of each image; A hyper-text must be included to the Homepage of the journal from which you are licensing athttp://www.sciencedirect.com/science/journal/xxxxx or the Elsevier homepage for books athttp://www.elsevier.com; Central Storage: This license does not include permission for a scanned version of the material to be stored in a central repository such as that provided by Heron/XanEdu.
Licensing material from an Elsevier book: A hyper-text link must be included to the Elsevier homepage at http://www.elsevier.com . All content posted to the web site must maintain the copyright information line on the bottom of each image.

Posting licensed content on Electronic reserve: In addition to the above the following clauses are applicable: The web site must be password-protected and made available only to bona fide students registered on a relevant course. This permission is granted for 1 year only. You may obtain a new license for future website posting.

17. **For journal authors:** the following clauses are applicable in addition to the above:
Preprints:
A preprint is an author's own write-up of research results and analysis, it has not been peer-reviewed, nor has it had any other value added to it by a publisher (such as formatting, copyright, technical enhancement etc.).

Authors can share their preprints anywhere at any time. Preprints should not be added to or enhanced in any way in order to appear more like, or to substitute for, the final versions of articles however authors can update their preprints on arXiv or RePEc with their Accepted Author Manuscript (see below).

If accepted for publication, we encourage authors to link from the preprint to their formal publication via its DOI. Millions of researchers have access to the formal publications on ScienceDirect, and so links will help users to find, access, cite and use the best available version. Please note that Cell Press, The Lancet and some society-owned have different preprint policies. Information on these policies is available on the journal homepage.

Accepted Author Manuscripts: An accepted author manuscript is the manuscript of an article that has been accepted for publication and which typically includes author-incorporated changes suggested during submission, peer review and editor-author communications.
Authors can share their accepted author manuscript:

- - immediately
    - via their non-commercial person homepage or blog
    - by updating a preprint in arXiv or RePEc with the accepted manuscript
    - via their research institute or institutional repository for internal institutional uses or as part of an invitation-only research collaboration work-group
    - directly by providing copies to their students or to research collaborators for their personal use
    - for private scholarly sharing as part of an invitation-only work group on commercial sites with which Elsevier has an agreement

- - after the embargo period
    - via non-commercial hosting platforms such as their institutional repository
    - via commercial sites with which Elsevier has an agreement

In all cases accepted manuscripts should:

- - link to the formal publication via its DOI
- - bear a CC-BY-NC-ND license - this is easy to do
- - if aggregated with other manuscripts, for example in a repository or other site, be shared in alignment with our hosting policy not be added to or enhanced in any way to appear more like, or to substitute for, the published journal article.

Published journal article (JPA): A published journal article (PJA) is the definitive final record of published research that appears or will appear in the journal and embodies all value-adding publishing activities including peer review co-ordination, copy-editing, formatting, (if relevant) pagination and online enrichment.

Policies for sharing publishing journal articles differ for subscription and gold open access articles:

Subscription Articles: If you are an author, please share a link to your article rather than the full-text. Millions of researchers have access to the formal publications on ScienceDirect, and so links will help your users to find, access, cite, and use the best available version.
Theses and dissertations which contain embedded PJAs as part of the formal submission can be posted publicly by the awarding institution with DOI links back to the formal publications on ScienceDirect.
If you are affiliated with a library that subscribes to ScienceDirect you have additional private sharing rights for others' research accessed under that agreement. This includes use for classroom teaching and internal training at the institution (including use in course packs and courseware programs), and inclusion of the article for grant funding purposes.

Gold Open Access Articles: May be shared according to the author-selected end-user license and should contain a CrossMark logo, the end user license, and a DOI link to the formal publication on ScienceDirect.
Please refer to Elsevier's posting policy for further information.

18. **For book authors** the following clauses are applicable in addition to the above: Authors are permitted to place a brief summary of their work online only. You are not allowed to download and post the published electronic version of your chapter, nor may you scan the printed edition to create an electronic version. **Posting to a repository:** Authors are permitted to post a summary of their chapter only in their institution's repository.

19. **Thesis/Dissertation**: If your license is for use in a thesis/dissertation your thesis may be submitted to your institution in either print or electronic form. Should your thesis be published commercially, please reapply for permission. These requirements include permission for the Library and Archives of Canada to supply single copies, on demand, of the complete thesis and include permission for Proquest/UMI to supply single copies, on demand, of the complete thesis. Should your thesis be published commercially, please reapply for permission. Theses and dissertations which contain embedded PJAs as part of the formal submission can be posted publicly by the awarding institution with DOI links back to the formal publications on ScienceDirect.

Elsevier Open Access Terms and Conditions
You can publish open access with Elsevier in hundreds of open access journals or in nearly 2000 established subscription journals that support open access publishing. Permitted third party re-use of these open access articles is defined by the author's choice of Creative Commons user license. See our open access license policy for more information.

Terms & Conditions applicable to all Open Access articles published with Elsevier:
Any reuse of the article must not represent the author as endorsing the adaptation of the article nor should the article be modified in such a way as to damage the author's honour or reputation. If any changes have been made, such changes must be clearly indicated.
The author(s) must be appropriately credited and we ask that you include the end user license and a DOI link to the formal publication on ScienceDirect.

If any part of the material to be used (for example, figures) has appeared in our publication with credit or acknowledgement to another source it is the responsibility of the user to ensure their reuse complies with the terms and conditions determined by the rights holder.

Additional Terms & Conditions applicable to each Creative Commons user license:
CC BY: The CC-BY license allows users to copy, to create extracts, abstracts and new works from the Article, to alter and revise the Article and to make commercial use of the Article (including reuse and/or resale of the Article by commercial entities), provided the user gives appropriate credit (with a link to the formal publication through the relevant DOI), provides a link to the license, indicates if changes were made and the licensor is not represented as endorsing the use made of the work. The full details of the license are available at http://creativecommons.org/licenses/by/4.0.

CC BY NC SA: The CC BY-NC-SA license allows users to copy, to create extracts, abstracts and new works from the Article, to alter and revise the Article, provided this is not done for commercial purposes, and that the user gives appropriate credit (with a link to the formal publication through the relevant DOI), provides a link to the license, indicates if changes were made and the licensor is not represented as endorsing the use made of the work. Further, any new works must be made available on the same conditions. The full details of the license are available at http://creativecommons.org/licenses/by-nc-sa/4.0.

CC BY NC ND: The CC BY-NC-ND license allows users to copy and distribute the Article, provided this is not done for commercial purposes and further does not permit distribution of the Article if it is changed or edited in any way, and provided the user gives appropriate credit (with a link to the formal publication through the relevant DOI), provides a link to the license, and that the licensor is not represented as endorsing the use made of the work. The full details of the license are available at http://creativecommons.org/licenses/by-nc-nd/4.0. Any commercial reuse of Open Access articles published with a CC BY NC SA or CC BY NC ND license requires permission from Elsevier and will be subject to a fee.
Commercial reuse includes:

- - Associating advertising with the full text of the Article
- - Charging fees for document delivery or access
- - Article aggregation
- - Systematic distribution via e-mail lists or share buttons

Posting or linking by commercial companies for use by customers of those companies.

20. **Other Conditions**:

v1.8
Questions? customercare@copyright.com or +1-855-239-3415 (toll free in the US) or +1-978-646-2777.
